

**Robotic Minimally Invasive Tools for Restricted Access
Confined Spaces**

By

Jason Hon Wei Liu

Submitted in accordance with the requirements for the degree of
Doctor of Philosophy

The University of Leeds
Institute of Design, Robotics and Optimisation
School of Mechanical Engineering

April 2016

The candidate confirms that the work submitted is his/her own and that appropriate credit has been given where reference has been made to the work of others.

This copy has been supplied on the understanding that it is copyright material and that no quotation from the thesis may be published without proper acknowledgement.

Acknowledgements

I would like to thank my supervisor, Professor Robert Richardson for his support, guidance, and encouragement during the research and preparation of this thesis. I am deeply grateful to Andrew Pickering for his invaluable support and advice during this and previous work.

I am deeply indebted to Shaun Whitehead from Scoutek Ltd for giving me the opportunity to continue my passion for designing and building robotic systems. I would like to express my gratitude to all members of the School of Mechanical Engineering who aided my course of study since the year 2007.

A special mention to Gard Pin Grace Lee for her care, support and delicious cakes.

Furthermore, I would like to thank my family for their support and all the friends I made throughout my period of study; especially, William Mayfield, Bing Yin Ma, Tama Single-Liertz and Lemuel Valdez for making these years so memorable.

Abstract

A study has been performed in the design and fabrication of deployable borehole robots into confined spaces. Three robot systems have been developed to perform a visual survey of a subterranean space where for any reason humans could not enter.

A 12mm diameter snake arm was designed with a focus on the cable tensions and the failure modes for the components that make the snake arm. An iterative solver was developed to model the snake arm and algorithmically calculate the snake arms optimal length with consideration of the failure modes.

A robot was developed to extend the range capabilities of borehole robots using reconfigurable borehole robots based around established actuation and manufacturing techniques. The expected distance and weight requirements of the robot are calculated alongside the forces the robot is required to generate in order to achieve them. The whegged design incorporated into the tracks is also analysed to measure the capability of the robot over rough terrain. Finally, the experiments to find the actual driving forces of the tracks are performed and used to calculate the actual range of the robot in comparison to the target range.

The potential of reconfigurable mobile robots for deployment through boreholes is limited by the requirement for conventional gears, motors, and joints. This chapter explores the use of smart materials and innovative manufacturing techniques to form a novel concept of a self-folding robotic joint for a self-assembling robotic system. The design uses shape memory alloys fabricated in laminate structures with heaters to create folding structures.

Table of Contents

Acknowledgements.....	iii
Abstract.....	iv
Table of Contents	v
List of Tables	x
List of Figures	xii
List of Abbreviations.....	xviii
Chapter 1 Introduction	1
1.1 Background.....	1
1.2 Motivation for Research	3
1.3 Research Objectives	4
1.4 Statement of Contribution.....	4
1.4.1 Published Documents (Appendix A).....	5
1.5 Structure of Thesis	5
Chapter 2 Literature Review	8
2.1 Introduction	8
2.2 Methods of entry	8
2.3 Void entry ground robots.....	10
2.3.1 Tracked	13
2.3.2 Legged	18
2.3.3 Wheel-Legged.....	21
2.4 Borehole Inspection	26
2.4.1 Static and Dry.....	26
2.4.2 Static and Wet.....	27
2.4.3 Mobile and Dry	27
2.4.4 Mobile and Wet	27
2.1.1 Reconfigurable robots	28
2.4.4.1 Modular reconfigurable robots	28
2.4.4.2 Non-modular reconfigurable robots.....	31
2.1.2 Self-folding robots	32
2.1.3 Snake robots	36
2.1.3.1 Snake arms.....	38
2.2 Discussion and conclusion	43
Chapter 3 System Specifications	46
3.1 Introduction	46

3.2	Environment 1	46
3.3	Environment 2	47
3.4	Locomotion method selection.....	48
3.5	Refining the specifications.....	53
3.5.1	Snake arm specifications	53
3.5.2	Reconfigurable specifications.....	53
3.6	Discussion and conclusion	55
Chapter 4	Snake arm theory and analysis.....	57
4.1	Introduction	57
4.2	Kinematics and statics.....	59
4.3	Link buckling.....	66
4.3.1	Flexural buckling	66
4.3.2	Local buckling	67
4.4	Cable tensions.....	68
4.5	Tension experiments	71
4.5.1	Joint variations	71
4.5.2	Friction	74
4.6	Discussion and conclusion	80
Chapter 5	Mechanical design of snake arm prototype	82
5.1	Introduction	82
5.2	Prototype design	82
5.3	Joint design	83
5.3.1	Shear forces.....	84
5.3.2	Finite Element Analysis of joint assembly	87
5.4	Cable properties.....	90
5.5	Base actuation design.....	96
5.5.1	Tendon forces and control.....	97
5.5.2	Actuator frame.....	101
5.5.1.1	Force supplied.....	103
5.5.1.2	Beam bending.....	105
5.5.1.3	Arm angle.....	108
5.5.1.4	Gearing selection	109
5.6	Iterative solver	110
5.6.1	Optimisation strategy.....	111
5.6.2	Solver results	114

5.6.3	Further strategies	118
5.7	Experiment	126
5.7.1	Methodology	126
5.7.2	Results	128
5.8	Discussion and conclusion	131
Chapter 6	Reconfigurable Dual Track Robot	133
6.1	Introduction	133
6.2	Specifications	133
6.3	Design theory	134
6.3.1	Robot Mass	135
6.3.2	Driving Force	137
6.4	Robot design	138
6.4.1	Locomotion Module	140
6.1.1.1	Gearbox	141
6.1.1.2	Step-Climbing	144
6.4.2	Deployment Module	145
6.5	Experimentation	151
6.5.1	Speed	151
6.5.2	Track force	152
6.6	Discussion and conclusion	154
Chapter 7	Feasibility of Self-Folding Robots	156
7.1	Introduction	156
7.2	Specifications	157
7.3	Layer design	157
7.3.1	Bend radius	160
7.3.2	Active Af Experiment	161
7.3.3	Thermal Layer	164
7.3.3.1	Thermal Analysis	165
7.4	Experiment	169
7.4.1	Methodology	169
7.4.2	Results	171
7.5	Discussion and conclusion	176
Chapter 8	Conclusions and future work	178
8.1	Assessment of research objectives	178
8.1.1	Investigate the length limitations to snake arms	178

8.1.2	Develop an algorithmic approach to producing a snake arm of optimal length.....	178
8.1.3	Extend the range capabilities of borehole robots using reconfigurable robot techniques	178
8.1.4	Investigate advanced actuation and fabrication technologies	179
8.2	Conclusions.....	179
8.2.1	Snake arm.....	179
8.2.2	Reconfigurable Dual Track Robot	181
8.2.3	Self-Folding Robot.....	182
8.3	Future work	183
8.3.1	Snake arm.....	183
8.3.2	Reconfigurable dual track robot.....	184
8.3.3	Self-folding robot	185
List of References		186
Appendix A Papers published		194
Appendix B Results for Tension Experiments		207
B.1	Theoretical Results of a Single Cable on Single Joint.....	207
B.2	Experimental Results of a Single Cable on Single Joint	208
B.3	Theoretical and Experimental Results of a Double Cable on Double Joint	209
Appendix C Results for Friction Experiments		211
C.1	Experimental Results of the Friction Test	211
C.2	Force Applied Against Friction for Cable 1 and Cable 2	213
C.3	Theoretical and Corrected Experimental Results of a Double Cable on Double Joint.....	215
Appendix D Matlab .m files.....		217
D.1	Algorithmic solver for snake arm length.....	217
D.2	run_me.m.....	217
D.3	test_code.m	218
D.3	calc_tube_buckling.m	229
D.4	joint_torque_check.m.....	231
D.5	calc_tendon_weight.m	238
D.6	calc_tube_weight.m	238
D.7	calc_wire_weight.m	238
Appendix E Results from the snake arm cable length changes		239
E.1	Joint 1	239

E.2 Joint 2	239
E.3 Joint 3	240
Appendix F Results from the reconfigurable robot design	241
F.1 Maximum torque generated and torque required for the deployment module.....	241
F.2 Reduced torque generated and torque required for the deployment module.....	242
Appendix G Results from transient thermal study.....	243

List of Tables

Table 2.1 Review of locomotion methods for USAR [21].	12
Table 2.2 Snake arm specifications.	39
Table 3.1 Environmental specifications.	46
Table 3.2 Environmental specifications.	47
Table 3.3 Decision matrix criteria for locomotion designs.	48
Table 3.4 Decision matrix for locomotion designs.	52
Table 4.1 Denavit-Hartenberg notation for each snake arm link.	60
Table 4.2 Specifications of the simplified snake arm.	62
Table 5.1 Steel grade 303S31 specification for the joint pin.	86
Table 5.2 Stainless Steel material for joint used for FEA simulations.	87
Table 5.3 Supplier stated average break loads.	91
Table 5.4 Coordinates of each actuation cable w.r.t the centroid.	99
Table 5.5 Sample cable lengths for joint angles $\theta_1=15$ and $\theta_2=20$.	100
Table 5.6 Firgelli Automation Light Duty Linear Actuator [115].	103
Table 5.7 Cable lengths in actuator frame.	109
Table 5.8 Known variables for iterative solver.	110
Table 5.9 Unknown variables for iterative solver.	111
Table 5.10 Factors of safety.	113
Table 5.11 Actuation cable tension results.	115
Table 5.12 Joint compression results.	116
Table 5.13 Joint shear results.	116
Table 5.14 Maximum torque twist at joint 1.	116
Table 5.15 Flexural buckling results.	116
Table 5.16 Local buckling results.	116
Table 5.17 Actuation cable tension results.	119
Table 5.18 Joint compression results.	119
Table 5.19 Joint shear results.	119
Table 5.20 Maximum torque twist at joint 1.	119
Table 5.21 Flexural buckling results.	120
Table 5.22 Local buckling results.	120
Table 5.23 Actuation cable tension results.	120
Table 5.24 Joint compression results.	121
Table 5.25 Joint shear results.	121

Table 5.26 Maximum torque twist at joint 1.	121
Table 5.27 Flexural buckling results.....	121
Table 5.28 Local buckling results.	121
Table 5.29 Actuation cable tension results.....	122
Table 5.30 Joint compression results.	122
Table 5.31 Joint shear results.	123
Table 5.32 Maximum torque twist at joint 1.	123
Table 5.33 Flexural buckling results.....	123
Table 5.34 Local buckling results.	123
Table 5.35 Experimental accuracy.....	130
Table 6.1 Mine exploration robot specifications.....	139
Table 6.2 Maxon motor specification.....	141
Table 6.3 Maxon motor planetary gearbox specification.....	142
Table 6.4 Maximum torque from track gearbox.....	142
Table 6.5 Maximum speed from track gearbox.....	144
Table 6.6 Deployment module properties.	146
Table 6.7 Locomotion module properties.	146
Table 6.8 Power screw properties.....	148
Table 6.9 Velocity results.	152
Table 6.10 Testing robot at 2° incline.	153
Table 7.1 Layer roles.....	158
Table 7.2 Layer parts sourced.....	159
Table 7.3 Active Af measurement experiment 1.	162
Table 7.4 Polyimide thermal properties at 25°C	164
Table 7.5 Air thermal properties at 25°C	164
Table 7.6 Thermal Analysis Parameters.....	165
Table 7.7 Thermal analysis results comparison.....	168
Table 7.8 Different sized SMA strips used.	169
Table 7.9 Experimental checks.	170
Table 7.10 Experimental results for SMA strip 1.	171
Table 7.11 Experimental results for SMA strip 2.	171
Table 7.12 Experimental results for SMA strip 3.	172
Table 7.13 Experimental results for SMA strip 4.	173
Table 7.14 Experimental results for SMA strip 5.	174

List of Figures

Figure 1.1 Graphical design of thesis structure.	7
Figure 2.1 Illustration of the restricted access entrance where entrance depth and diameter can both be varied.....	9
Figure 2.2 Shaw tool 41mm OD drill kit [14].....	10
Figure 2.3 Geometry of four standard obstacles. (a) gradient (b) ditch (c) vertical step (d) isolated wall [20].	11
Figure 2.4 Resquake mobile rescue robot [28].	14
Figure 2.5 Completed Switchblade prototype [18].	15
Figure 2.6 USAR robot RAPOSA [29].....	16
Figure 2.7 iRobot 510 PackBot [8].	17
Figure 2.8 iRobot 110 FirstLook [31].....	17
Figure 2.9 Six-legged Abagaille-I robot [33].....	19
Figure 2.10 Hexapod robot Sprawlita [34].	20
Figure 2.11 mini-hexapod with the simplified mechanism for leg automation [35].....	20
Figure 2.12 (a) mini-hexapod climbing over step obstacle [35] (b) mini-hexapod climbing over ramp obstacle [35].	21
Figure 2.13 ASGUARD robot climbing stairs [36].....	21
Figure 2.14 Wheel-leg robots (a) can obtain a foothold on higher obstacles than wheels (b) of equal radius [16].....	22
Figure 2.15 (Left) RHex hexapod robot [37], (Right) RHex posed atop section of obstacle course [37].	23
Figure 2.16 Size comparison of the Mini-Wheg IV and a Blaberus giganteus cockroach [39].	24
Figure 2.17 The Mini-Wheg 4J in action reaching heights of 220mm [39].....	24
Figure 2.18 Mini-Wheg 7 can climb obstacles 25% greater in size than the length of each leg spoke [40].	25
Figure 2.19 Mini Wheg 9J jumps over a 90mm obstacle [40].	26
Figure 2.20 Close up of a single module from the 1st gen. PolyBot with protruding motor [48].	29
Figure 2.21 2nd gen. PolyBot with nine modules. A micro camera and battery is attached at the front [48].	29
Figure 2.22 2nd gen. PolyBot in its 3 configurations, (top-left) rolling track, (bottom-left) snake-like, (bottom-right) four-legged spider [47].....	29
Figure 2.23 SuperBot module with 3DOF [49].....	30
Figure 2.24 Multiple configurations of the SuperBot [49].	30

Figure 2.25 Houdini robot deployment system at different stages of deployment [50]. (a) the robot is first deployed vertically from above (b) the robot begins reconfiguring stage (c) robot is fully deployed on ground.....	31
Figure 2.26 Hitachi and HGNE shape-changing robot [52].....	32
Figure 2.27 (a) The robot before the structure is self-folded. (b) The folded robot after the servo and battery is manually attached [55].....	33
Figure 2.28 Two positions of the single direction SMA actuated fold [59]. (Left) unfolded position (Right) folded position.....	34
Figure 2.29 Bi-directional fold. (a) & (b) Before activation occurs. (c) Single fold activated. (d) Both folds activated [60].	35
Figure 2.30 Small Active Cord Mechanism [72].	37
Figure 2.31 OmniTread in cantilever-lift position [51].....	37
Figure 2.32 Cable-driven dexterous robotic arm prototype [76].	40
Figure 2.33 Prototype of the search and rescue apparatus [94].	41
Figure 2.34 PAC long reach robotic carrier [101].	41
Figure 2.35 (left) Robot kinematic model. (right) Forces through the parallelogram [101].	42
Figure 2.36 Features of robotic arm with one module [102].....	42
Figure 2.37 USAR elephant-trunk-like robot (ETR) [104].	43
Figure 4.1 First prototype from OC Robotics [108].	57
Figure 4.2 (Top) rigid snake arm, (Bottom) continuous snake arm.	58
Figure 4.3 Snake arm cross section of 12mm diameter.....	59
Figure 4.4 Denavit-Hartenberg notation for snake arm.....	60
Figure 4.5 (Top left) Snake arm at start position, (Top right) Snake arm at middle position, (Bottom left) Snake arm at end position, (Bottom right) Path of the snake arm end effector.....	63
Figure 4.6 Change in pitch torque per joint as joint angle is incremented.....	64
Figure 4.7 Change in yaw torque per joint as joint angle is incremented.....	65
Figure 4.8 Buckling modes of circular sections [111].....	67
Figure 4.9 Simplified snake arm with single joint and single tendon.	69
Figure 4.10 Simplified snake arm with two joints and two tendons.	69
Figure 4.11 Double jointed variant of snake arm test rig.....	71
Figure 4.12 Single jointed variant of snake arm test rig.	72

Figure 4.13 Comparison of the theoretical and experimental tendon tensions for a single joint snake arm controlled by a single tendon. The dotted lines represent the theoretical values for tendon tension for each value of D_y and the points represent the experimental data.	72
Figure 4.14 Comparison between a sample of theoretical and experimental tendon tensions for a double-jointed snake arm with two tendons. This graph compares the values for T1, the tendon constraining the first joint as shown in Figure 4.10.....	73
Figure 4.15 Comparison between a sample of theoretical and experimental tendon tensions for a double-jointed snake arm with two tendons. This graph compares the values for T2, the tendon constraining the second joint as shown in Figure 4.10.	74
Figure 4.16 Friction test rig with illustrated forces and length.	75
Figure 4.17 Experimental results from friction test.....	76
Figure 4.18 Force applied against friction for cable 1.....	77
Figure 4.19 Force applied against friction for cable 2.....	77
Figure 4.20 Comparison between a sample of theoretical and corrected experimental tendon tensions for a double-jointed snake arm with two tendons. This graph compares the values for T1, the tendon constraining the first joint as shown in Figure 4.9.	78
Figure 4.21 Comparison between a sample of theoretical and corrected experimental tendon tensions for a double-jointed snake arm with two tendons. This graph compares the values for T2, the tendon constraining the first joint as shown in Figure 4.9.	79
Figure 5.1 Snake arm links and joints.	83
Figure 5.2 A 2-DOF universal joint with collinear axis of rotation.	84
Figure 5.3 Exploded view of a single joint assembly.	85
Figure 5.4 Manufactured joint.	85
Figure 5.5 Shearing of the joint pin occurs at two locations (in red).	86
Figure 5.6 Iteration of 2DOF snake arm joint undergoing a FEA simulation.	87
Figure 5.7 Iteration of 2DOF snake arm joint, FEA results can reveal the site for highest stress points. The above shows where the local stresses exceed the material yield stress.....	88
Figure 5.8 Results of multiple FEA simulations, linear trend reveals an axial load of approximately 1350N to be the absolute maximum the 2DOF joint should be subjected too.....	88

Figure 5.9 FEA simulation with 0.8Nm torque axial torque applied to joint.	89
Figure 5.10 FEA simulation plot.....	90
Figure 5.11 Tensile testing machine.....	92
Figure 5.12 Figure-eight loop knot.....	92
Figure 5.13 Seven specimens before testing.....	92
Figure 5.14 Seven specimens after testing.	93
Figure 5.15 BPL 1.5mm diameter Dyneema rope.	93
Figure 5.16 Marlow Excel Racing Dyneema rope with SK75 core and 16 plait polyester cover.	94
Figure 5.17 BPL 1.5mm diameter Dyneema rope.	94
Figure 5.18 Marlow Excel Racing Dyneema rope with SK75 core and 16 plait polyester cover.	95
Figure 5.19 Proposed cable length control method.	96
Figure 5.20 Complete snake arm assembly with base mechanism on left.	96
Figure 5.21 Simplified kinematic model of the 2DOF joint.	97
Figure 5.22 Arrangement of actuation cables in the joint vertebrae. Dxi denotes the horizontal position and Dyi denotes the vertical position of the ith cable.	98
Figure 5.23 Illustration of the different part lengths required to calculate each cable length.....	100
Figure 5.24 The three groups of cables and where each is expected to span the snake arm.	101
Figure 5.25 The base actuator frame assembly.....	102
Figure 5.26 Illustration of change in actuation cable length. (left) The red actuation cable will be at its shortest length, (right) the blue actuation will be at its longest length.	102
Figure 5.27 Graphical model of the actuator frame assembly as seen in Figure 5.26.....	104
Figure 5.28 Maximum possible cable tension changes with the arm angle in the actuator frame.	105
Figure 5.29 Actuator frame beams and cable path.....	105
Figure 5.30 Actuator frame beam bending.....	106
Figure 5.31 Actuator frame loading condition simplifies to beam bending problem.	106
Figure 5.32 Moment of inertia for square aluminium beam.....	107
Figure 5.33 Graphical model of the actuator frame assembly without a linear actuator.....	108
Figure 5.34 Gear assembly on the actuator frame.	110

Figure 5.35 Graphical representation of MATLAB code to determine the maximum length of the snake arm.	114
Figure 5.36 Snake arm lengths.....	115
Figure 5.37 Snake arm lengths.....	118
Figure 5.38 Snake arm lengths.....	120
Figure 5.39 Snake arm lengths.....	122
Figure 5.40 Workspace for snake arms of different link materials.	125
Figure 5.41 Experimental test rig set up.....	127
Figure 5.42 Results of actuating only Cable 1.	127
Figure 5.43 Experimental results for Joint 1.	128
Figure 5.44 Experimental results for Joint 2.	129
Figure 5.45 Experimental results for Joint 3.	129
Figure 6.1 Illustrating track width and wheelbase.	135
Figure 6.2 Free body diagram of robot and tether on an incline.....	135
Figure 6.3 Free body diagram of the robot on an incline.....	137
Figure 6.4 The mine exploration robot in the deployed configuration.	139
Figure 6.5 The mine exploration robot in the un-deployment configuration.	139
Figure 6.6 Front view of the locomotion module and the diameter limits.....	140
Figure 6.7 Locomotion module.	140
Figure 6.8 Motor and gearbox section for locomotion module.	141
Figure 6.9 Track gear train.....	142
Figure 6.10 Side view of the track.....	143
Figure 6.11 Whegged tracks climbing steps.....	145
Figure 6.12 Two modules as a two-link arm at both angle extremes.	146
Figure 6.13 Change in joint torque versus arm angle.	147
Figure 6.14 Inside deployment module.	147
Figure 6.15 Power screw components.	148
Figure 6.16 Deployment mechanism.	149
Figure 6.17 Torque results.....	150
Figure 6.18 0.25Nm Gearbox output torque results.	151
Figure 6.19 Experimental set up for timed distances.....	151
Figure 6.20 Track force experimental set up.....	153
Figure 7.1 Layer composition.....	158

Figure 7.2 Selectively heating one side changes fold direction.....	158
Figure 7.3 Proposed self-folding inchworm mechanism.....	159
Figure 7.4 SMA strain.....	160
Figure 7.5 Active Af-test.	161
Figure 7.6 Active Af measurement results.....	163
Figure 7.7 Thermal damping range.....	164
Figure 7.8 Different sized air pockets.....	165
Figure 7.9 SolidWorks thermal analysis heating curve maintains the temperature at 70°C.	166
Figure 7.10 Thermal analysis results.....	166
Figure 7.11 Thermal analysis results.....	167
Figure 7.12 Thermal analysis results.....	167
Figure 7.13 Several samples of different sized embedded SMA sheets.....	169
Figure 7.14 Flexible heating layer failure.	175

List of Abbreviations

UAV	Unmanned aerial vehicles
VTOL	Vertical take-off and landing
SAR	Search and rescue
GPR	Ground penetrating radar
MAV	Micro aerial vehicles
MUAV	Mini unmanned aerial vehicles
LOS	Line of sight
USAR	Urban search and rescue
UGV	Unmanned ground vehicle
SMP	Smart memory polymers
SMA	Shape memory alloys
NiTi	Nickel titanium
DOF	Degree of freedom
OD	Outer diameter
ID	Inner diameter
RNE	Recursive Newton-Euler
ESDU	Engineering sciences data unit
FEA	Finite element analysis
UHMwPE	Ultra-High molecular weight polyethylene
BPL	Backpacking light
FOS	Factors of safety

Chapter 1 Introduction

This chapter details the background, aims and objectives of this research.

1.1 Background

In our modern technological world, it is surprising that there are many locations that cannot be characterised through remote scanning via satellite or other remote sensing technologies. These spaces are often too small or unsafe for human to explore [1].

There are three methods available for mapping and surveying underground spaces as outlined by Morris, A., et al. [2]. These are:

- **Direct Observation**, which requires the direct presence of personnel to produce irrefutable first-hand observations on the state and geometry of underground spaces.
- **Borehole Observation** where a borehole is drilled to allow a down-hole camera probe to be deployed, this can produce satisfactory results in certain circumstances.
- **Remote Sensing** that employs non-intrusive techniques to measure geophysical features using electromagnetic waves and assumed soil compositions to locate voids without the need for drilling. Other techniques also involve the use of ground penetrating radar and seismic reflection/refraction. These techniques cannot match the fidelity and sampling densities of direct observation.

Robots have the potential to be deployed within those spaces and provide crucial sensor data. Robotic exploration can be classified into three scenarios, i) Space exploration, ii) Subsea exploration, iii) on Land exploration. This research focuses on land exploration robotics.

The Fukushima nuclear power plant incident (2011), whilst was a terrible accident, provided an opportunity for companies to showcase state-of-the-art robotic devices. Two PackBot ground robots from iRobot were granted the opportunity to enter the Fukushima reactor in order to monitor oxygen levels, temperature and radioactivity. The results successfully revealed high levels of

radiation at Unit 1 and Unit 3, too high for humans to safely access the facilities [3].

Other unexplored spaces, such as unmapped subterranean voids (caves, sewers and mines) are well suited to robotic exploration [2]. Knowledge of these subterranean features are vital for prevention and mitigation of mining disasters [4] [5] and play a key role in the design and planning of new mines, sewer lines and surface structures.

Lack of accurate documentation has led to accidents and deaths such as the Quecreek Mine Rescue in July 2002 [4] where miners accidentally dug into a poorly documented coal mine leading to flooding and trapping of 9 miners. In March 2010 similar events occurred at the Wangjialing coal mine trapping 153 miners [5]. In fact, from 1900 to 2007 in the United States alone, there have been 12,823 fatalities which mostly involves mine rescue teams working in the harsh extremely hostile environments [6].

Subterranean robots enhance the capabilities of traditional borehole camera probes (cameras on sticks) as they are capable of locomotion beyond the initial entry point to survey a larger space.

The research and application challenges for robotic underground mapping and surveying are varied; the PackBot ground robot (by iRobot) highlighted some problems during the exploration of the Fukushima power plant. Officials described that the robot was impeded by broken chunks of ceiling and walls blown off during hydrogen blasts [7]. Although, the PackBot was specifically designed and built to navigate difficult terrain - including the capability to open doors and defuse roadside bombs [8].

Subterranean mines generally consist of several tunnels acting as accesses, haulages, production levels, and airways [9]. Most shafts constructed in the 1900's were of a rectangular cross section due to the shape of the equipment brought into the shafts. However, in hard rock mines, it is common to see circular cross sections because the geometry provides good airflow, rock support characteristics and also ease of construction. Furthermore, elliptical shafts were implemented as an alternative to the large circular shafts which had the effect of reducing the amount of rock required to be excavated and therefore also the cost, which is an important aspect of mining projects. As all

these shafts can run great distances into the hundreds of metres the range of all robotic systems must be considered.

The condition of the mine opening is dependent on whether the mine is still in use or disused. Disused mines can be sealed voluntarily (filled and capped) or by accident. Obviously, entry into well maintained and operating mine shafts will provide the easiest method of mine ingress allowing for large systems such as the 1500 pound Groundhog to be deployed [10]. However, deploying systems into sealed shafts do require additional costs and effort.

In August 2007, a vertical shaft of 6m diameter costed USD \$12,857 per metre to excavate, and a 5x4m declining shaft at 8° costed USD \$5,714 per metre [9]. To breach a sealed mineshaft from the surface is a costly endeavour hence the use of small diameter borehole drop cameras with less than 15.2cm (6 inches) diameter to reduce costs.

The small borehole also has the benefit of reduced damage resulting in the reduced likelihood of compromising the structural integrity of a subterranean void. Subterranean voids are often speculated to contain historical artefacts that are fragile and irreplaceable. The Sphinx in Egypt was speculated to contain secret tunnels and chambers beneath it. Due to raised subterranean water levels, boreholes were drilled around the site to allow the ground water to be pumped away to protect the Sphinx. Dr Zahi Hawass lowered borehole deployable cameras to show no such hidden structures exist [11]. Furthermore, if the subterranean void is also of historical importance such as the underground city in Cappadocia region of Turkey [12] or the tomb of William Shakespeare [13] then despite the size differences the preservation by minimising damage is a priority.

1.2 Motivation for Research

The motivation for this research is to undertake research and development into minimally invasive tools, for deployment through small diameter boreholes, in order to expand the capabilities of current borehole deployable systems. These new capabilities will create viable solutions for exploration robotics across a broad range of application areas including urban search and

rescue, mine rescue, robot archaeology, and nuclear power station inspection and decommission.

Despite a compelling case for restricted access exploration robotics, relatively little attention has been paid to the borehole robotics area by the robotics community. As a field, robotics has thoroughly researched applications on land, in water and in the air; but few have concentrated on developing fully capable robots to be deployed through small-restricted access boreholes.

This thesis discusses the path taken from this problem to analysis and experimentation of robotic tools capable of exploring subterranean expanses of different sizes yet producing minimal damage to preserve the condition and integrity of the explored space.

1.3 Research Objectives

The overall aim of this study is to undertake research into ground based robotic systems capable of deployment, and subsequent visual survey, through restricted access entrances into two confined spaces of different sizes. To fulfil the project aim, the following objectives were outlined:

1. To investigate the fundamental length limitations of self-supported snake arms.
2. To create an algorithmic approach to designing the self-supporting snake arms of optimal length for a given borehole diameter and current material properties.
3. To extend the range capabilities of borehole robots using reconfigurable borehole robots based around established actuation and manufacturing techniques.
4. To investigate advanced actuation and fabrication technologies towards miniature mobile borehole exploration robots.

1.4 Statement of Contribution

The main areas of original work carried out during this research are highlighted below.

1. The methodology to algorithmically determine the maximum length of a long reach small diameter snake arm is conducted and implemented to produce a long reach snake arm. (Published paper 2)
2. A reconfigurable dual track robot has been designed and built to be deployed through small 41mm boreholes. (Published paper 1)
3. A novel bi-directional self-folding joint has been presented that is unique using compound layers of shape memory alloys, thermally insulating layers and heat generating layers.

1.4.1 Published Documents (Appendix A)

1. Liu, J., et al., Exploration Robots for Harsh Environments and Safety. IFAC-PapersOnLine, 2015. 48(10): p. 41-45.
2. Liu, J., et al., Mechanical Design of Long Reach Super Thin Discrete Manipulator for Inspections in Fragile Historical Environments, in Towards Autonomous Robotic Systems: 16th Annual Conference, TAROS 2015, Liverpool, UK, September 8-10, 2015, Proceedings, C. Dixon and K. Tuyls, Editors. 2015, Springer International Publishing: Cham. p. 155-160.

1.5 Structure of Thesis

The main body of this thesis consists of eight chapters. A breakdown of each chapter is given below.

Chapter 1: Introduction

This chapter describes the context, objectives and methodology of the reported research.

Chapter 2: Literature review

This chapter reviews research into the locomotion of exploration robots and the suitability of the system for borehole deployment and confined space explorations.

Chapter 3: System specifications

This chapter introduces two environmental scenarios for inspection and builds the system specifications to cover the overall aims.

Chapter 4: Snake arm theory and analysis

This chapter develops the method to calculate the cable tensions of a snake arm and analyses the buckling failure modes of each component comprising the snake arm. The experiments to verify the cable tensions are also performed with the inclusion of friction analysed for the experimental test rig.

Chapter 5: Mechanical design of snake arm prototype

This chapter details the design of the 12mm snake arm building towards a model for algorithmically calculating the optimal snake arm length. The forces where part failure occurs using FEA software and buckling theory is performed and the effects they have on snake arm length analysed.

Chapter 6: Reconfigurable dual track robot

This chapter details the design of the reconfigurable robot with whegged profiles. The expected distance and weight requirements of the robot are calculated alongside the forces the robot is required to generate in order to achieve them. The whegged design incorporated into the tracks is also analysed to measure the capability of the robot over rough terrain. Finally, the experiments to find the actual driving forces of the tracks are performed to calculate the actual range of the robot in comparison to the target range.

Chapter 7: Self-folding robot

This chapter explores the novel concept of a self-folding robotic joint for a self-assembling robotic system. The generation of a thermal barrier isolating two parallel layers of heat activated shape memory alloys is developed using heat transfer studies. Alongside experiments to characterise the transformation curve of the shape memory alloy and effect of length and width on the torque generated at each joint.

Chapter 8: Conclusions

This chapter presents and discusses the finding from the three case studies conducted to evaluate the applicability of each system for the exploration of restricted access confined spaces. Before finally summarising the research and its findings. It discusses benefits of using the proposed systems and make recommendations for further research.

A flow chart of the overall thesis structure is shown in Figure 1.1.

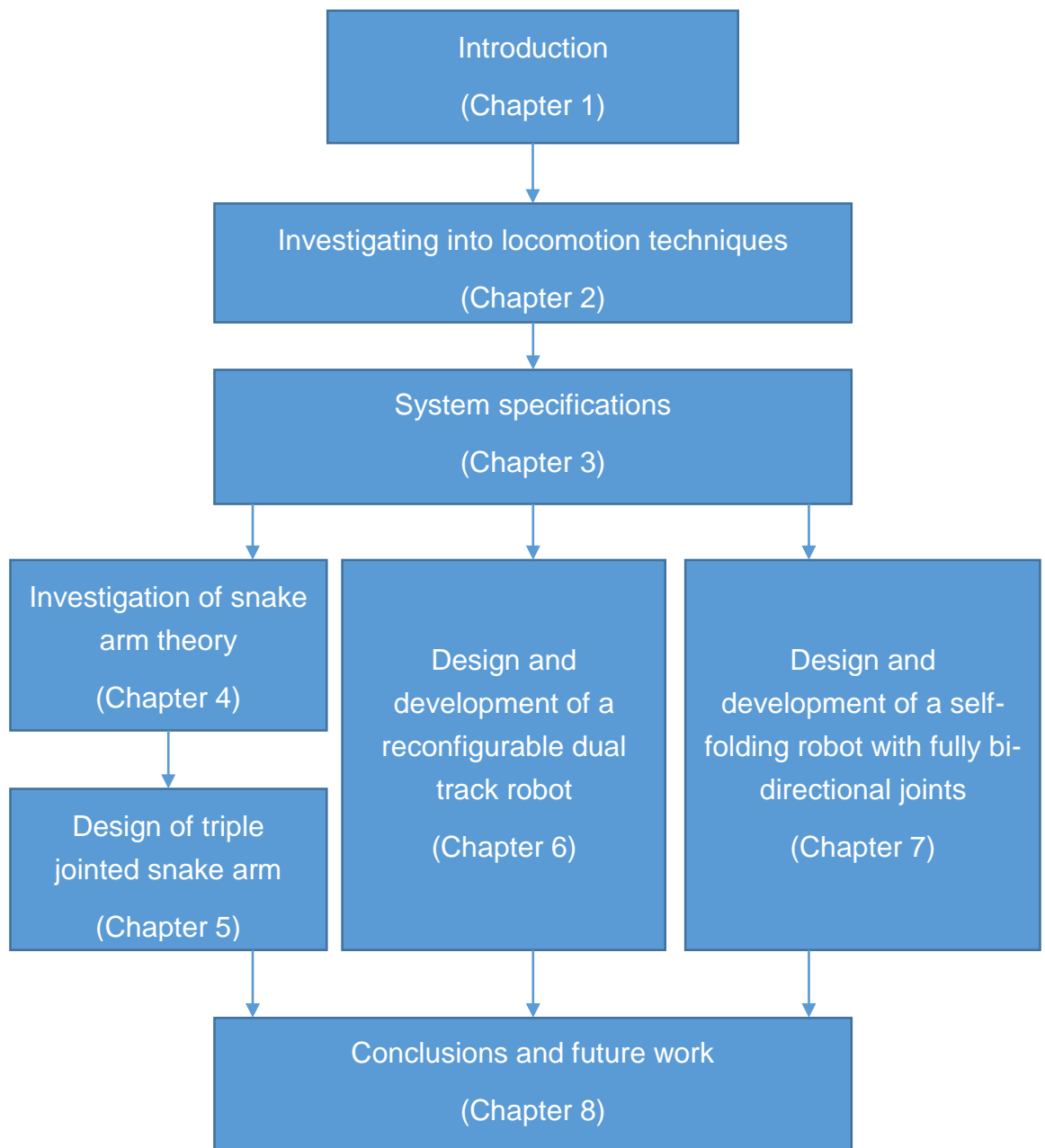


Figure 1.1 Graphical design of thesis structure.

Chapter 2

Literature Review

This chapter reviews research into the locomotion of exploration robots and the suitability of the system for borehole deployment and confined space explorations. Gaps in knowledge are identified that form the basis of this research.

2.1 Introduction

Methods of locomotion can be characterised by the environmental medium the robot will traverse through; air, land and water. Locomotion methods on land are viable approaches for restricted access robotic exploration and are explored within this literature review. Whilst there are many spaces to explore that are flooded – this is a specific problem for which solutions are not generally applicable, therefore this class of technology is not covered within this review.

Locomotion enhances the capabilities of a robot for remote mapping and surveying underground spaces by improving observational detail and expanding the explored workspace. The benefits incurred from including methods of locomotion can be measured in endurance, distance and detail, which each locomotion method will score differently.

2.2 Methods of entry

There are generally two types of entrances for accessing subterranean spaces i) existing void like openings as primary entrances to mine shafts and caves ii) new entrances such as boreholes.

Primary entrances are designed and constructed to be large enough for humans and machinery resulting in relatively easy access for large commercial mobile robots such as the Groundhog [10]. However, in most exploration scenarios, the subterranean spaces are difficult or impossible for humans to enter due to the small entrance or the requirement to drill an entrance path. Minimisation of the drill diameter increases the speed that the hole can be created, reduces the energy required to make the hole and minimises the risk of structural collapse or damage to important structures.

Therefore, from a void perspective, the aim is to minimise the size of the drilled hole. This places strict limits on the cross section and payload of a deployed robot. For long vertical drill depths of approximately 300m and greater, horizontal drift can occur causing deployment issues and affecting the orientation of a borehole robot [2].

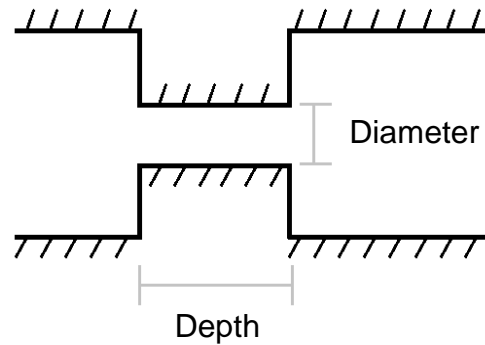


Figure 2.1 Illustration of the restricted access entrance where entrance depth and diameter can both be varied.

The use of portable borehole drilling equipment has the capability of drilling boreholes from one intact mine shaft to another adjacent shaft therefore drastically reducing the long distances involved if the shaft was to be reached from the surface. The Shaw tool (Figure 2.2) [14] is a uniquely designed handheld drilling tool that is easy to use, portable, fast penetrating and self-contained. Commonly used for initial metal ore prospecting, academic applications have used the Shaw portable drill for projects including petroleum source, paleomagnetic investigations and monitoring well installations. The diameters available for the Shaw tool are 25mm, 41mm and 51mm and can achieve drill depths of up to 23m depending on the materials involved.



Figure 2.2 Shaw tool 41mm OD drill kit [14].

2.3 Void entry ground robots

Ground-based systems for exploration is a well-established area with a large range of applications and can assume many forms. Ground-based robots do not require constant power to maintain position allowing for a natural increase in endurance for explorations into restricted access voids.

Locomotion over cluttered and unstructured terrain can be a significant challenge for robots. Traditional approaches use wheeled locomotion [15] that lack the capability of climbing over obstacles of equal height [16]. Alternative approaches such as legged robots [17] and tracked robots [18] can increase the capability of the robot to navigate over difficult terrain.

The implementation of land locomotion for use in an unknown environment presents several complications as the size constraint of the restricted access way affects the size of the robot and the effectiveness of the locomotion. For these reasons wheeled locomotion [15], legged robots [17] and tracked robots [18] are studied as they can increase the capability of the robot to navigate over difficult terrain.

Although borehole entrances can vary greatly in size and impose strict limits on the cross section and payload of a robot, void entrances can readily lead into subterranean spaces from the surface, which can offer a reduced constraint on size. Past the entrance, the workspace can range from a few centimetres to metres in width and height. This cross-sectional size, therefore,

does constrain a robot's physical size; the length of the subterranean space in the range of kilometres will also constrain a robot's mobility and operational range.

Larger and less complex robots are more commonly found in literature and commercially in comparison to a small self-reconfigurable robot for a borehole deployment. Void entrance robots commonly have greater abilities to overcome rough terrains and gaps on the floor, more resistance to low levels of water and most importantly can carry a larger payload.

Once inside the void, the floor on which the robots will locomote can vary significantly. Manmade sites such as underground tombs that have since been sealed are likely to find some flat ground and steps such as in the ZhangHuai Prince's Tomb near the city Xi'an in China. Though built 1300 years ago, an exploration robot was able to travel on its flat floor and steps, all of which were on a slight slope incline of 15° [19]. Uneven terrain can occur when floor sections of buildings have collapsed creating a constrained and layered environment.

Whether it is rough, irregular, uneven, difficult or complex terrain, these terms all describe an environment where there is no clear path for a robot to travel. It is said that the variety of irregular terrain is unlimited and it is difficult to cover all the different cases for navigating over irregular terrain [20]. Terrain features can be simplified into four different features that are commonly found in rough terrain and these are gradient, ditch, vertical step and isolated wall as shown in Figure 2.3 where each obstacle can be described by only one or two parameters [20].

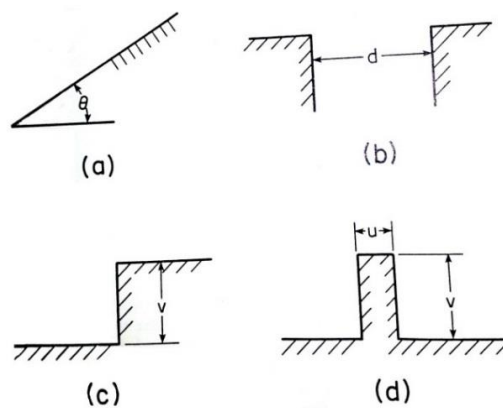


Figure 2.3 Geometry of four standard obstacles. (a) gradient (b) ditch (c) vertical step (d) isolated wall [20].

Subterranean spaces both natural and manmade have environments that greatly vary from one to another, this brings about a level of uncertainty that greatly influences the design and construction of a robot [2, 6]. Additional features can be introduced into the operating environment such as low crumbled ceilings and roofs that are an obstacle in itself. This constraint will restrict the height of any deployed vehicles and altitude of flying aircraft.

Robots used for Urban Search and Rescue (USAR) are commonly found to use land-based locomotion with wheels or tracks. A report that reviews locomotion mechanisms for USAR scenarios by Wang, Z. and H. Gu, conclude that current robots are incapable of practically and autonomously carrying out any sort of rescue work in irregular, complex, and unstructured environments [21]. They argue how the specific downfalls of each locomotion method analysed would stop the robots in their tracks as seen at Table 2.1 that sums up their conclusions.

Table 2.1 Review of locomotion methods for USAR [21].

Locomotion Method	Examples	Advantages	Disadvantages
Wheeled	<ul style="list-style-type: none">• CUL [22]	<ul style="list-style-type: none">• Compact designs• Easy to use	<ul style="list-style-type: none">• Difficult to adapt to uneven/complicated terrain• The wheel can be caught on pieces of clothing and loose electrical wiring etc.• More prone to slip and fall over
Tracked	<ul style="list-style-type: none">• Micro VGTV [21]• PackBot [23]	<ul style="list-style-type: none">• Works in unstructured terrain	<ul style="list-style-type: none">• Not competent at tackling vertical voids or inclined walls• More prone to slip and fall over

Legged	<ul style="list-style-type: none">• Robug III [24]	<ul style="list-style-type: none">• Can walk over uneven rugged terrain	<ul style="list-style-type: none">• Difficult to function in narrow voids• Not competent at tackling vertical voids or inclined walls
Serpentine	<ul style="list-style-type: none">• Serpentine robot by Carnegie Mellon University [25]• Serpentine robot by Erkmen [26]	<ul style="list-style-type: none">• Good for navigating voids	<ul style="list-style-type: none">• Difficult to adapt to uneven/complicated terrain

Other characteristics found in subterranean spaces that can influence the design of a robot are:

- The amount of debris the robot must navigate. A large build-up of debris will favour locomotion choices such as tracks or legs and will affect whether the robot is teleoperated or acting autonomously.
- How wet or dry the spaces are. Increasing depth of liquid impacts locomotion and design of the robot.
- What composition of the air within the space is, the possibility of flammable gases would require no exposed wiring for the robot and a corrosive atmosphere will affect the material of the exposed robot.
- The level of illumination in the subterranean space. Generally, these voids are incredibly dark and therefore must contain its own source of illumination or employ other sensors such as sonar.

2.3.1 Tracked

Robots for USAR purposes can use wheel or tracks for its locomotion system, however uneven terrain creates problems for wheels due to an inevitable loss of traction. Larger more bulky wheels can be used to increase surface contact however the change to tracked robots is a more capable choice despite the

higher costs. If the environment is flat, wheels are effective and the lowest-priced solution. Obstacles of different sizes present an extreme challenge, as the diameter of the wheels is proportional to its ability to navigate them. Tracks on the other hand smooths out bumps in the terrain and can allow a robot to glide over small obstacles, unlike wheels, tracks cannot be punctured or torn and effectively distribute the weight of a robot over a larger area to aid locomotion over soft ground like mud or snow [27].

Moosavian, S.A.A., et al. discussed the compromises a USAR robot must overcome, on one hand the robot must be small enough to bypass small openings and voids but on the other hand, the same robot needs the ability to climb over obstacles which calls for a larger size [28]. The minimum length of their mobile rescue robot was decided at 730mm, the minimum length for a tracked robot to span two steps on stairs. The large length of 730mm creates a large turning circle, a space that cannot be afforded in a destructed environment, therefore Moosavian, S.A.A., et al. compromises by implementing a robot with extendable tracks. This ensures the length required for climbing stairs yet has the capacity to alter its structure to produce a smaller profile for better manoeuvrability.

The actuated and tracked sections of the robots also add the benefit of allowing these robots to navigate higher obstacles; it is no coincidence that this design improvement is commonly seen elsewhere with commercial robots.



Figure 2.4 Resquake mobile rescue robot [28].

Switchblade is an unmanned ground vehicle (UGV) with a small form factor for navigating confined spaces. By Morozovsky, N. et al. the Switchblade is a treaded rover capable of transversing rough terrain by use of its two treads pivotally attached on either side of the central torso [18]. This unique design allows the UGV to transverse terrain other generic treaded rovers may struggle with such as chasms longer than the rovers length or inclined stairs. The length of the Switchblade in its most compact configuration is approximately 300-400mm and its ability to continue to function upside down is beneficial to reduce risks of failure during any mission deployment.

The Switchblade was mainly demonstrated to advertise its ability to balance itself in the 'V-balance mode' (Figure 2.5); a mode which provides the robot with the ability to overcome obstacles nearly as high as its treads length [18]. This ability was not tested in the paper; therefore, it is unknown whether the Switchblade V-balance mode successfully functions to allow the robot to climb over any high uneven obstacles.



Figure 2.5 Completed Switchblade prototype [18].

A similar design approach to the Switchblade can be found in the USAR robot RAPOSA by Marques, C., et al., [29]. It is intended for outdoor use in environments hostile to human presence. A unique component of this robot is the ability to disconnect and reattach its tether while being remotely controlled. Other similar USAR robots have the option to draw its power from the tether or onboard batteries, they cannot, however, switch between the two without changing the robot structure [29]. The robot that measures 175mm tall,

370mm wide, 750 long and weighs 27kg is claimed to have the ability to allow deployment into a deep hole by lowering it down via the tether. The ability to disconnect and reconnect the tether remotely improves the mission duration and search area of the robot, at the cost of increased complexity. Wang, Z. and H. Gu [21] state that tracked robots are incompetent in navigating inclined walls and are prone to slip and flip; the RAPOSA is therefore built to climb 45° inclinations and also function upside down.



Figure 2.6 USAR robot RAPOSA [29].

The iRobot 510 PackBot is the most successful robot in its class and has reached commercial success with over 4500 robots delivered worldwide [8]. Described as mobile, expandable, portable and easy to use the military applications of the robot have aided its success [30]. With the detachable front flippers the robot measures at 178mm high, 521mm wide and 889mm long weighing at 10.89kg (without batteries), it can climb inclines of 60° and submersible in 914mm water [8]. The specifications of the PackBot are certainly impressive in comparison to its competition. Unfortunately, the sizes of these front flipper tracked robots make it extremely difficult or impossible to navigate small voids.



Figure 2.7 iRobot 510 PackBot [8].

In the military, there is a requirement for a tool that can provide situational awareness fast. The iRobot 510 PackBot is much too large and heavy to be transported by a person; therefore, a smaller version was created by iRobot. Named the iRobot 110 FirstLook, the smaller version had to be in a smaller and lighter package yet retain some advantages from its larger model that made it popular. Weighing only 2.45kg with dimensions 254 x 229 x 102mm (L x W x H) the FirstLook can be carried in a backpack and be thrown for deployment purposes which reflect the ruggedness of the design. Crawl spaces present less of a problem for this robot and the ability to climb over steps 178mm high means this robot is suitable for investigating unknown environments despite its small size.



Figure 2.8 iRobot 110 FirstLook [31].

2.3.2 Legged

It is said that legged robots have an advantage in walking through uneven terrain but not through narrow and inclined voids [21, 32]. Though not so important for USAR operations, the fact that the legs in contact with the floor are static means there is a reduced chance of scratching the surface when moving. However, as the contact area of legged robots is largely reduced compared to tracked robots, the chance of slip is increased, which can create scratches on a surface. This risk is reduced due to legged robots usually having multiple degrees of freedom (DOF) which allows the robot to shift its weight and thus its own centre of mass.

If a wheeled or tracked robot is deployed, the consequences of failure of a wheel or track could result in the complete loss of mobility. Not for legged robots though if the design incorporated redundant legs [32] although these robots require more complex mechanisms thus achieving a larger chance of a part failure.

Drawing inspiration from a spider the Abigaille-I robot has six legs (each with 10 DOF) and 18 actively controlled joints and only weighs 0.131kg. Featuring specially designed feet that can integrate synthetic dry adhesives the Abigaille-I by Menon, C., et al. can adhere onto a slope of almost 50° on a smooth plastic surface [33]. The dimensions of this robot was not reported nor was a demonstration of the robot walking, however what is gained from this paper is lightweight legged robots can hold their own ground on inclines contrary to what was reported by Wang, Z. and H. Gu in their review of locomotion methods [21]. Therefore the material coating the feet plays a role alongside the surface area of the foot that aids in providing the traction needed for the robot.

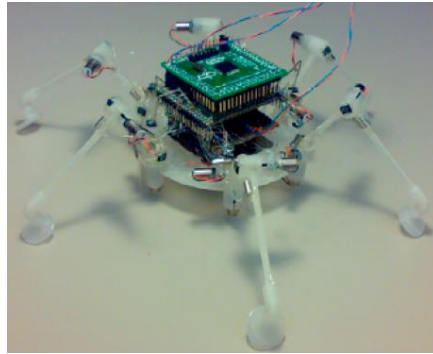


Figure 2.9 Six-legged Abigail-I robot [33].

Just as the Abigail-I used small electric motors to actuate each leg joint other components can also be utilised to automate the legs of a robot. An important measure of whether the mechanism is applicable depends on several aspects such as size, scalability and reliability. Another six-legged robot by Clark, J.E., et al. finds its inspiration from nature and the authors attempt to fabricate a robot with passive mechanical properties like those found in small invertebrates [34].

For a small-legged robot to transverse over uneven and uncertain terrain Clark, J.E., et al. closely observed the cockroach that can achieve great speed and stability. The authors note how many hexapod designs maintain its centre of mass within the support polygon provided by at least three feet to ensure static stability, it was noted however that these designs limit many of those robots to very slow, near static speeds. Aiming for a hexapod built for the simple task of running straight ahead through rough terrain, their first prototype named the Sprawlita (Figure 2.10) was a 160mm long robot with its legs in a sprawled posture to provide a wide base of support [34]. From studying the anatomy of a cockroach, the authors decide to use pneumatic pistons for the leg functions to greatly accelerate and decelerate the robot faster than the electrical component alternatives could have provided. The disadvantage of using the pneumatic pistons is obviously the need for the robot to be tethered in order to supply pressurised air to the pistons.

Overall, the Sprawlita was said to have managed to clear obstacles 35mm high and achieve speeds of 0.42m/s on the smooth level ground. Whilst the robot was capable of moving across different soils such as sand the authors noted that foot design was important to prevent miring [34].

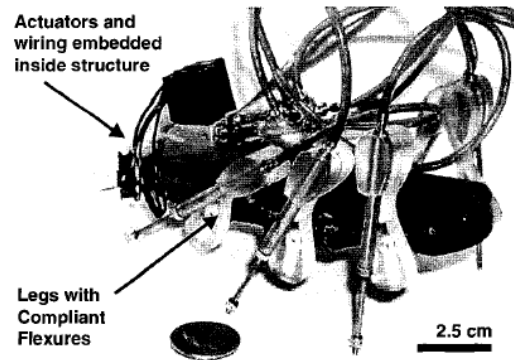


Figure 2.10 Hexapod robot Sprawlita [34].

Solutions that will enable the miniaturising of legged robots would be beneficial for the exploration of a historical chamber where its small size will allow for the robot to transverse small voids. Reducing the amount of legs and/or simplifying the mechanism that automates the legs will reduce the complexity of the design and should aid in the miniaturisation effort.

A mini-hexapod robot produced by Arena, P., et al. has a simple design by only providing each of the six legs just two DOF (Figure 2.11), this results in only 12 servos in place which has the benefit of reducing power consumption, complexity and also weight [35]. The mini-hexapod robot has dimensions 150 x 100 x 100mm (L x W x H), weighs 0.826kg and is powered by four AA batteries and two additional 9v batteries, the duration the robot can function is not mentioned. Experimentation with the robot has revealed the robot to be capable of walking on flat surfaces, small slopes and small size obstacles (Figure 2.12).



Figure 2.11 mini-hexapod with the simplified mechanism for leg automation [35].



Figure 2.12 (a) mini-hexapod climbing over step obstacle [35] (b) mini-hexapod climbing over ramp obstacle [35].

The maximum height of an obstacle this robot could climb over was not provided nor was information regarding length of void the robot could bridge over. The duration the robot could continuously function was said to be range between 0.5-1 hour on flat terrain and it has a speed ranging from 1 cm/s to 10 cm/s [35].

2.3.3 Wheel-Legged

Further simplifying the mechanism of the legs can imply a reduction in the degrees of freedom per leg. The mini-hexapod by Arena, P., et al. had 2 DOF per legs thus has two servo motors per leg. Reducing the DOF to just one per leg would therefore half the amount of servomotors required. An example of a robot with this set up is the ASGUARD (Figure 2.13) by Eich, M., F. Grimmering, and F. Kirchner [36]. Designed for harsh outdoor environments and USAR missions the ASGUARD makes use of multiple rotating legs to navigate the difficult terrain. As the legs are rotating, the category these robots fit under is a hybrid between wheels and legged, sometimes referred to as 'whegs'.



Figure 2.13 ASGUARD robot climbing stairs [36].

The ASGUARD robot has dimensions 0.95 x 0.5 x 44m (L x W x H) and demonstrates ability to climb stairs in an outdoor test track. The authors noted that at times the robot did perform undesired backflips during some tests that was later fixed using program changes. Unlike the legged robots reviewed previously, ASGUARD robot should continue to function also when upside down, although not explicitly stated.

An in-depth analysis of benefits for using wheel-legs for USAR has already been done [16] and proves to be more advantageous than wheels alone. One reason is that wheel-legs are able to obtain a foothold on obstacles that are taller than the wheel-leg radius.



Figure 2.14 Wheel-leg robots (a) can obtain a foothold on higher obstacles than wheels (b) of equal radius [16].

The number of spokes per wheel-leg and the number of wheel-legs per robot can still be altered for each robot designed and produced. A hexapod named RHex [37] is a whegged robot despite only having one spoke per wheel-leg as each of the six legs rotate a full circle when walking. The simplicity of the RHex produced a robust robot with demonstrated capabilities on an obstacle course specially designed for great difficulty and a sense of uncertainty (Figure 2.15). The number of spokes does affect the design of the robot. RHex is an example that six legs must remain in coordination where the stable triangular stance could be maintained. However, with the ASGUARD robot the use of several spokes allows the robot to manoeuvre in a similar manner with only four wheel-legs yet still maintaining the triangular stance. The actual benefits of the two additional wheel-legs then are in the hexapods capability to have redundancy on its movement, increased stability [38] and the ability to bridge larger voids.



Figure 2.15 (Left) RHex hexapod robot [37], (Right) RHex posed atop section of obstacle course [37].

Miniaturisation of a robot using the simplified wheel-leg type locomotion is possible and has already been proposed and studied, but problems occur with capabilities of the legged robot that strongly affect the usefulness of the robot in USAR missions. Though these robots could be assembled to navigate the smallest of holes and crevices, the downscaled wheel-legs obviously affect the ability to scale over tall obstacles.

The Mini-Wheg IV (Figure 2.16) is a highly mobile small robot using the wheel-leg locomotion method. Two versions were built; one to present its miniature design and the other to demonstrate an ability to jump in order to clear obstacles it is not able to climb otherwise. The physical dimensions of the Mini-Wheg IV chassis are 0.09 x 0.068 x 0.036m (L x W x H). It is controlled by radio control signals, drawing power from onboard lithium batteries [39]. Capable of reaching speeds of 0.9m/s, the Mini-Wheg IV is fast in comparison with previously reviewed legged and whegged robots, yet only has one motor driving the two axles of the four wheel-legs. Problems were found during testing with the whegs being caught in slated surfaces or tangled surfaces. The robot is also incapable of turning on the spot, a useful ability when navigating through tight confined crevices. This is due to the Mini-Wheg IV using traditional steering like those found in cars, providing the Mini-Wheg IV with a turning circle between 178 – 27.9mm or between 2 and 3.1 body lengths [39].



Figure 2.16 Size comparison of the Mini-Wheg IV and a *Blaberus giganteus* cockroach [39].

The Mini-Wheg IV at its current form would not be able to climb stairs or any other obstacles approximately more than twice its height. The novel solution to this by Morrey, J.M., et al. was to design the Mini-Wheg 4J as proof of concept. Sacrificing the steering and radio controlling system, a spring-loaded four-bar jumping mechanism was introduced powered by the same motor running the whegs, which meant both systems were not independent. Though a prototype the Mini-Wheg 4J performed admirably reaching heights of 220mm, however as acknowledged by the authors the controlling aspects of the robot had to be reinstated in future versions of the Jumping Mini-Wheg [62].



Figure 2.17 The Mini-Wheg 4J in action reaching heights of 220mm [39].

A later iteration of the Mini-Wheg was built to incorporate several design improvements to both the Mini-Wheg IV and the Mini-Wheg 4J [40]. The Mini-Wheg 7 was fitted with improved wheel-legs that included wider feet and

rubber coating to aid traction and modification of the shape to eliminate tangling with terrain. Slight alterations were made to the steering mechanism to reduce weight where possible, overall the chassis of the Mini-Wheg 7 measures 0.089 x 0.054m (L x W) making it smaller than its predecessor [40]. Experiments with the newer version revealed the robot to still be able of achieving speeds of almost four times its body length when carrying additional batteries onboard yet the climbing ability remained unchanged from the previous design (due to leg length remaining unchanged). When attempting to climb over obstacles of 38mm the robot begins to tumble over and inclines of 25° are its limit on a unmentioned surface [40]. The lightweight steering mechanism in the Mini-Wheg 7 provided the robot with a turning circle of three to four body lengths which is an increase in comparison to the Mini-Wheg IV [39].



Figure 2.18 Mini-Wheg 7 can climb obstacles 25% greater in size than the length of each leg spoke [40].

The prototype Mini-Wheg 4J was only a proof of concept lacking the capability to steer and jump independently while driving forwards. The Mini-Wheg 9J was an attempt to realise a fully functional model building upon the improvements from the Mini-Wheg 7. Separating the mechanism driving the four wheel-legs and the jumping mechanism a separate motor had to be introduced thus increasing the size of the chassis to 0.104 x 0.076m (L x W). Figure 2.19 shows the robot jumping over a 90mm high obstacle reaching a height of 150-180mm [40], this is less than the height achieved by the prototype model which achieved 220mm yet the newer version weighs less at 191g. Regardless the jumping height would still allow the robot to climb atop obstacles higher than the 38mm found from the Mini-Wheg 7.



Figure 2.19 Mini Wheg 9J jumps over a 90mm obstacle [40].

2.4 Borehole Inspection

Borehole entrances can vary greatly in size and impose strict limits on the cross section and payload of a robot. They do not benefit from the same freedoms a void entry robot enjoys and must be designed for restricted access deployments.

A dry subterranean environment allows a device to be designed and constructed with ease and operated with a minimum number of personnel. Often tethered and deployed by raising/lowering the device from the surface, these devices can only offer a linear form of mobility.

2.4.1 Static and Dry

A static borehole device similar to the Ferret [41] is a very simple yet effective device for its task. Often tethered and deployed by raising/lowering the device from the surface these can only offer a linear form of mobility. A dry subterranean environment allows the device to be designed and constructed with ease and operated with a minimum number of personnel. The Ferret carries onboard a surveying laser on a two-axis mechanism to allow for a more detail analysis once deployed alongside a camera and two small lamps to provide visual feedback to the operator.

A common issue that arises with these systems is that they are highly constrained to the line of sight. Obstructions such as supporting pillars in a mineshaft can greatly obstruct a sensors view and therefore warrant the need for careful and accurate placement of boreholes.

2.4.2 Static and Wet

The borehole camera system for imaging the deep interior of ice sheets [42] is designed to house two cameras (one side and one facing down) with halogen bulbs to provide illumination. Tethered via a fibre-optic cable this device was deployed into a 1000 -1200m deep borehole where water is assumed present, the presence of water and pressure was addressed in the design. In this case, the borehole camera system never navigates beyond the bored shaft in the ice, had the system entered an underwater cavern with any water current, then the analysis would not have produced the same quality images as the camera system contains no method of stabilisation.

2.4.3 Mobile and Dry

The cost of drilling a hole is proportional to the volume of material removed; therefore, it will be costly for a static camera system to find there is a large obstruction adjacent to the breach in the subterranean space. Rather than repositioning and re-drilling the borehole, a mobile system that can navigate the space beyond the borehole would be advantageous. A more detailed analysis of the subterranean space is possible with additional vantage points and the TerminatorBot [43] is an example of one. Utilising two three-degree of freedom arms that retract into a cylindrical body, the tethered robot can be deployed into a borehole and continue to navigate beyond the entrance by crawling.

The use of tracks can also supplement the locomotion system to improve the ability to overcome rough terrains [6]. Inkutun Mine Crawler robot contains two sets of tracks that can tilt to allow the robot to compact and transverse the borehole. Comparisons between the TerminatorBot and Inkutun Mine Crawler reveal that both have the ability to self-reconfigure after deployment into the borehole, a capable locomotion system to overcome expected obstacles and a form of steering appropriate for navigation in narrow passages [2].

2.4.4 Mobile and Wet

The wet subterranean environment may contain water currents that affect the detail of images and other sensory data. The inclusion of underwater locomotion provides the deployed system with the capability to navigate and stabilise itself throughout a deployment. Just as an obstacle can obstruct

sensors' view for a static and dry device, the ability to navigate around them greatly improves the capabilities of such system [2].

2.1.1 Reconfigurable robots

2.4.4.1 Modular reconfigurable robots

Modular reconfigurable robots have received attention that mainly focuses on a modular design [44-46]. The PolyBot G2 (short for generation 2) promised great versatility and robustness with its modular design. The ability to self-reconfigure into three modes allows it to use three different land-based locomotion methods [45]. By utilising up to a maximum of 32 modules, the PolyBot G2 has the capacity to rearrange its own structure to create a snake-like gait for easy navigation of obstacles, rolling track for efficient travel over flat terrain and a four-legged configuration to stride over uncertain rough terrains (Figure 2.22).

The PolyBot self-reconfigurable robot appears to be a logical choice for exploration purposes, as it can be deployed in its slender snake-like mode to minimise the size of the chamber entrance and once deployed there are three locomotion options to allow for different terrain scenarios. Therefore, the PolyBot can be subject to the same scrutiny as the snake robots in regards to the size of such robots and the ease of scalability in the design (Figure 2.21).

The design goal of the PolyBot G2 is for each module to fit within a 50mm cube on a side (Figure 2.20). Unfortunately the inclusion of a brushless DC motor protrudes from the cube destroying the sleek looks of the robot, increases its physical size and creates interference with some of its own functions [45]. The third generation version, the PolyBot G3 promises a redesign where the protruding motor is absent by replacing the component with a pancake DC motor and planetary gears [47]. Further papers of the PolyBot G3 have yet to be published at the time of writing.

Demonstrations of the PolyBot G2 capabilities revealed its ability to clear a variety of obstacles including "crawling in a 4" diameter aluminium ducting pipes, up ramps (up to 30 degrees), over chicken wire, climbing 1.75" steps, over loose debris and wooden pallets" [48] using the snake-like configuration. Due to the complexity of introducing an individual power source into each module, the authors opt to supply power to the robot via a tether.

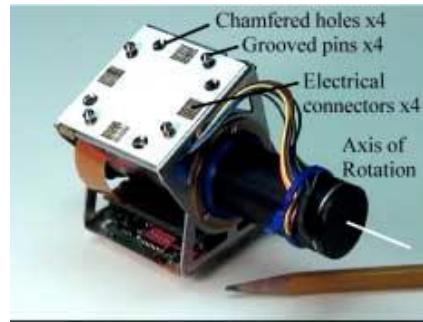


Figure 2.20 Close up of a single module from the 1st gen. PolyBot with protruding motor [48].

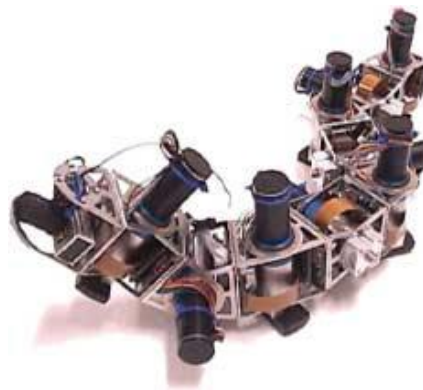


Figure 2.21 2nd gen. PolyBot with nine modules. A micro camera and battery is attached at the front [48].

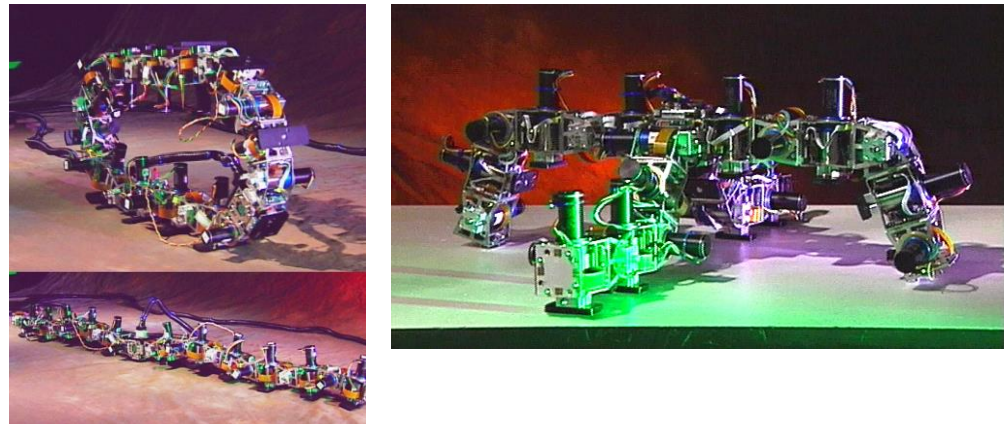


Figure 2.22 2nd gen. PolyBot in its 3 configurations, (top-left) rolling track, (bottom-left) snake-like, (bottom-right) four-legged spider [47].

A single module of the PolyBot contains just 1DOF yet the SuperBot [49] module contains 3DOF (Figure 2.23). The extra DOF drastically increase the robot's mobility and flexibility. Designed to be operated in uncontrolled harsh rough terrain, a design requirement of the SuperBot was for each module to be sealed from outside contaminants and incorporate an abrasion resistant

outer casing [46]. In essence, the SuperBot robots are designed for real outdoor applications by distancing itself from proof of concept hardware in controlled environment. This transition introduces many new challenges for the robot such as the ability to share power amongst its own modules, a full list can be found in the same paper [46].

The dimensions of each prototype cube for the SuperBot is 84mm thus each module is 168mm long, limited to 180° for yaw/pitch and 270° roll. Torque from each module is capable of reliably lifting two neighbouring modules, granting the robot with the capacity to travel 1km using the rolling track configuration on a single battery charge or climb 45° inclines on hard surfaces using the legged configuration [49].



Figure 2.23 SuperBot module with 3DOF [49].

Unlike the PolyBot G2, the SuperBot is currently unable to self-reconfigure and relies on external aid for setting up. This is due to manual connectors between each module and will be addressed in future designs. On a positive note, each module contains its own power supply meaning the SuperBot robots are autonomous and untethered [49].



Figure 2.24 Multiple configurations of the SuperBot [49].

Docking of each module is an important milestone for self-reconfiguration for robots such as the PolyBot or the SuperBot. The creators of the PolyBot experimented with docking procedures and found the problem to be complex due to compounding errors in kinematics from one module to another. In order to reduce errors and to aid positioning of modules, the creators introduced a three-step guide for accurate alignment using additional sensors before a latch is closed to secure a module [47].

2.4.4.2 Non-modular reconfigurable robots

Robots that are designed for configurability and are compatible with small diameter boreholes incorporate mechanisms to maintain high levels of functionality post-deployment into subterranean spaces.

Houdini is a tethered reconfigurable and collapsible machine for remotely cleaning hazardous waste and petroleum storage tanks [50]. The tethered robot system is designed for deployments into boreholes as small as 0.51m in diameter. Capable of a variable aspect ratio (ratio between wheelbase and track width) this is achieved using a collapsible diamond shaped frame powered by dual rotary hydraulic actuation to separate two parallel track modules.

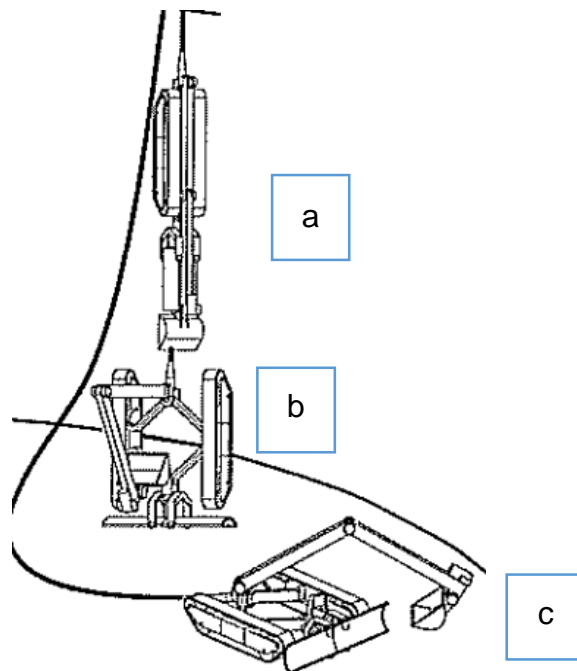


Figure 2.25 Houdini robot deployment system at different stages of deployment [50]. (a) the robot is first deployed vertically from above (b) the robot begins reconfiguring stage (c) robot is fully deployed on ground.

Deploying the tracks of the reconfigurable robot in series will assist with reducing the borehole diameter for entry. Like the OmniTread robot [51] as reviewed in Chapter 2.4.3, the combination of in-line tracks connected by actuated joints allows the robot an option to drive through boreholes and can reconfigure post-deployment to assume a wider aspect ratio for enhanced stability.

This form is adopted with the shape changing robot by Hitachi and Hitachi-GE Nuclear Energy (HGNE) for inspection of the Fukushima Daiichi nuclear plant [52]. The robot is composed of the main body and two compact tracked modules that can be rotated 90° in relation to the main body (Figure 2.28). It can travel through pipes of 100mm diameter and has the dimensions 90 x 250 x 272mm (h x l x w) when moving along flat surfaces or 90 x 640 x 65mm when moving within pipes. Weighing 7.5kg, the robot is operated via a 40m cable.

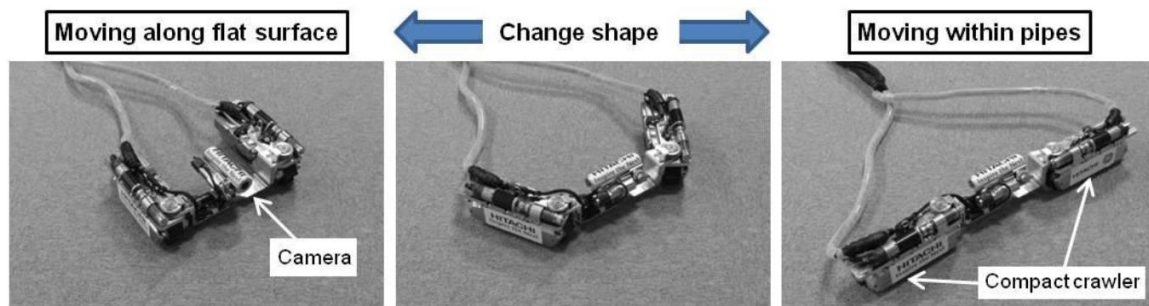


Figure 2.26 Hitachi and HGNE shape-changing robot [52].

In terms of performance, the Hitachi shape changing robot ‘died’ exploring the tsunami-hit Fukushima Daiichi nuclear power plant within 3 hours due to loss of control, however, the robot did succeed in examining 14 out of 18 planned inspection spots [53]. The Houdini robot however only concludes the robot is well suited for a wide range of clean-up tasks and will be able to drive in expected silo wastes with minimum sinkage [54].

2.1.2 Self-folding robots

Origami inspired self-folding robots rely on the shape memory effect of smart memory polymers (SMP) or shape memory alloys (SMA). Shape memory materials are stimuli-responsive materials and have the capability of changing their shape upon application of an external stimulus. The widely used form of stimulus is the application of heat.

Applications from the ability to change shape on command can be useful for self-assembling of robotic machines. Creating complex geometries and mechanisms by manual folding requires a significant amount of time and effort. Self-folding to construct three-dimensional structures from two-dimensional materials without external manipulation is, therefore, desirable as it reduces work required and aids storage of such robots when not required [55].

Use of SMP materials was demonstrated by Felton, S.M., et al. by building a self-folding lamp [56], origami cranes [57] and also the self-assembly printed inchworm robot [55]. The actuated folds of the inchworm robot are heat activated via a joule heating copper circuit layer for localised heating laminated to a layer of pre-stretched polystyrene (PSPS) that permanently shrinks when activated. The ability to localise the heating and activation of the PSPS layer allows the printed robot to sequential and simultaneous folding to assemble the structure of the inchworm robot. Only after completion of the folding process does the manual addition of servos and batteries take place to finish the inchworm mechanism (Figure 2.27).

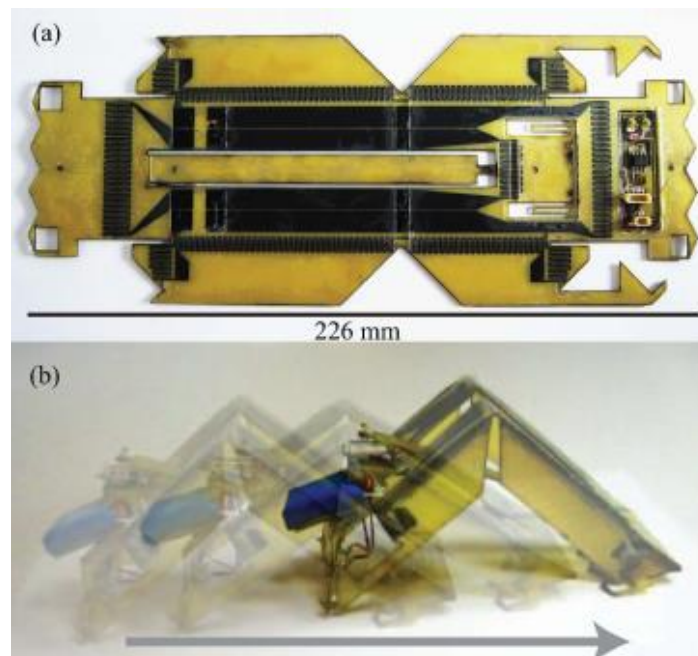


Figure 2.27 (a) The robot before the structure is self-folded. (b) The folded robot after the servo and battery is manually attached [55].

The method for building these self-folding machines is further demonstrated with a four-legged robot demonstrating potential for complex, autonomous and

self-controlled assembly [58]. Once the PSPS material is activated and shrunk to create the folds, the change to the material is irreversible and the robot cannot be unfolded and reused. If a benefit of the self-folding robot is the easy storage when not in use, that benefit will be lost as the additional servos and battery must be stored elsewhere.

The different approach using nickel titanium (NiTi) SMA materials can allow the folds to be unfolded and reused. This research was demonstrated by Paik, J.K., E. Hawkes, and R.J. Wood with their low-profile SMA torsional actuator [59]. With pre-programmed SMA sheets bound to passive sheets, a heating coil was bonded to each SMA actuator with non-conductive thermal epoxy. The heated coils activate each fold when the SMA transition temperature is reached and the 180° fold is achieved (Figure 2.28). Like the SMP folds, the direction of the folds for the SMA can only occur in one direction. Unlike the SMP folds, the SMA fold can be manually undone due to the ductile material properties.

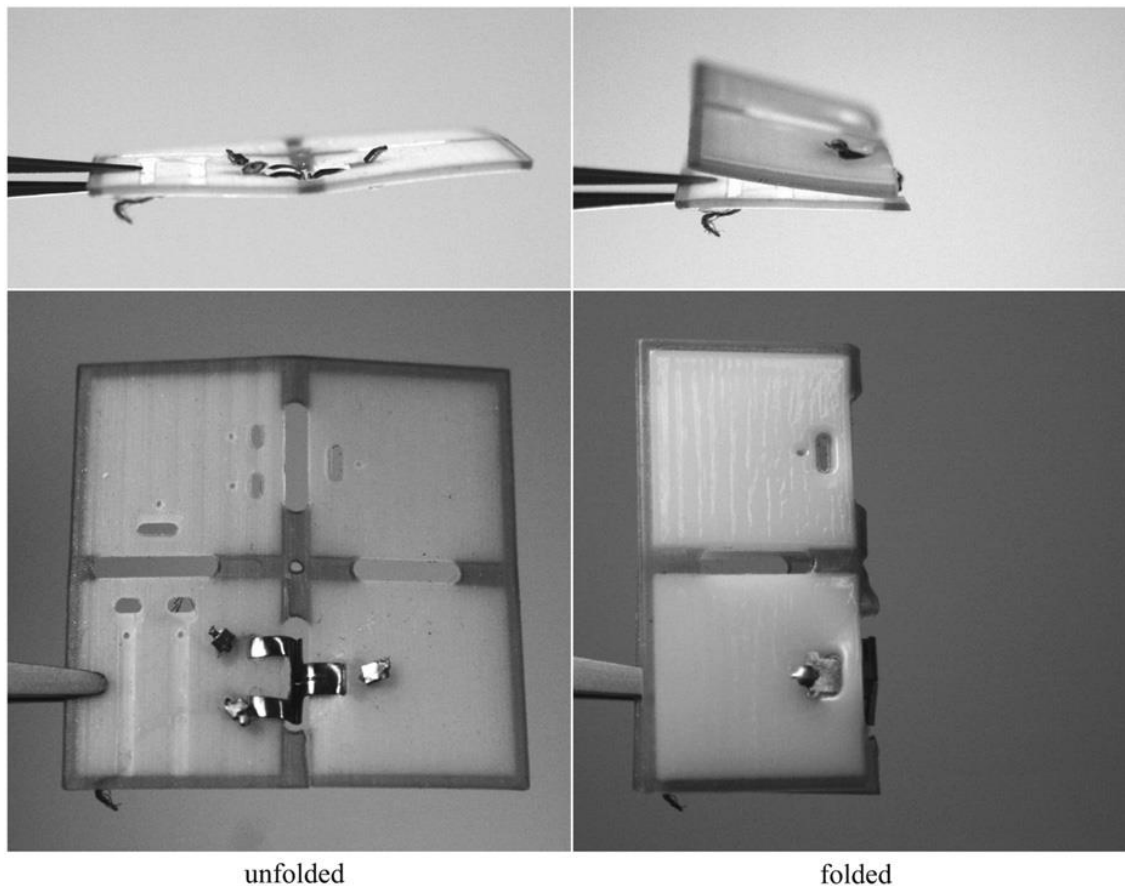


Figure 2.28 Two positions of the single direction SMA actuated fold [59]. (Left) unfolded position (Right) folded position.

In an attempt to increase the capabilities of each fold, Paik, J.K. and R.J. Wood introduce the bi-directional SMA folding actuator [60]. The changes made over the previous single directional fold is the SMA sheet is now pre-programmed to fold either direction (Figure 2.29) and the heating element is replaced with a 'printed-on' flexible heater that is micro laser welded and epoxied.

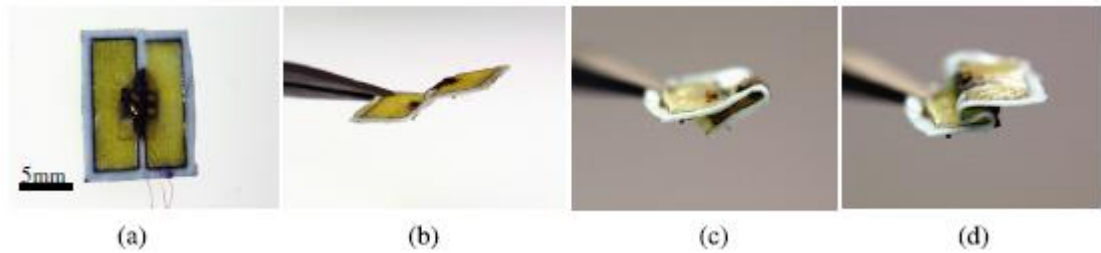


Figure 2.29 Bi-directional fold. (a) & (b) Before activation occurs. (c) Single fold activated. (d) Both folds activated [60].

It was reported the critical element for producing the independent motions is isolating the heated regions from one another, which was challenging due to the close proximity to mimic collinear rotation [60]. It can be seen the bi-directional fold suffers from the same issue as the single fold, as the unfolding process remains irreversible without external manipulation. In comparison to the SMP folds by Felton, S.M., et al. the use of SMA can perform the same role but offers greater flexibility with the option to be reactivated once manually reset.

Without the capability for each fold to unfold itself without external aid, the single use folds can only be assigned to performing structural folds and any actuation requirements reliant on servos or other actuators. The use of SMA materials have allowed dedicated SMA actuators to be utilised for worm robots [61, 62] and biomimetic inchworm robots [63-65], but those applications lose the capability for self-assembly and disassembly.

To the knowledge of the author, there has been no attempt to construct a self-folding robot where each fold is self-reversible and bi-directional. For a self-folding robot to be applicable for borehole deployment into restricted spaces, it is crucial to reduce the need for bulky externally embedded actuators and sensors so the remaining flexible materials used for construction can be utilised to conform to the geometry of the borehole. A benefit to a fully

reversible SMA fold is the fold itself will then be capable to of both being structural folds and actuated folds, therefore, bypassing the need for externally embedded servos.

2.1.3 Snake robots

Land systems reviewed so far has shown the locomotion mechanisms can take a large amount of space that creates a large robot. The performance of each system varies according to the design and the more novel techniques such as hopping [66, 67] are created in an attempt to overcome the limitations of its inherent design. Using nature for inspiration, there are methods animals use to avoid the ground when avoiding predators or scouring for food. A snake is able to navigate difficult terrain despite having no external limbs and is also capable of climbing trees by reaching from branch to branch [68].

Snake robots have been in circulation around researchers for years. Shigeo Hirose has achieved awards for contributions to robotic mechanisms at the Tokyo Institute of Technology [69] began development of snake-like robots in 1972 [70]. Through several iterations, Hirose eventually built an impressive dust and waterproof snake robot named the ACM-R5 [71] which had eight joints, was 1.7m long, 0.08m diameter and weighed at 6.5kg and is capable of replicating the creeping motions of a live snake on the ground and in water. This ability is due to 2 degree of freedom (DOF) joints Hirose proposed in his paper [72]. For a tree snake to cross a gap between tree branches, the snake must first secure its tail to support its dead weight as it lifts and lengthens its main body and head towards the target branch like a girder. For a snake robot to achieve the same, the individual joints must produce a torque capable of lifting sections of its body unsupported. The ACM-R5 is capable of only lifting two of seven joint units and with a link length of 0.17m that means it can cross a horizontal gap of 0.34m at most. The distance of this horizontal gap a snake robot is capable of crossing is important as it is representative of the distance this snake robot can be deployed into restricted access spaces without touching any surfaces past the initial borehole.



Figure 2.30 Small Active Cord Mechanism [72].

The OmniTread is a serpentine robot by Granosik [51], this is slightly different to the usual snake robots because it derives propulsion from tracks located around its outer body rather than the relative motion of the joints like in the ACM-R5 [72]. At 1.27m length, 0.186m diameter and at 13.6kg the OmniTread is much larger than Hirose's ACM-R5, the larger volume allows for its four joints to be powered by pneumatic bellows which Granosik discusses its benefits over electric motors and hydraulics in another article [73]. The greater torque produced by using pneumatics over electric power is revealed when they are described as capable of lifting two lead sections to allow the robot to navigate gaps more than half its length long, making the gap approximately 0.65m wide.



Figure 2.31 OmniTread in cantilever-lift position [51].

On the snake robot over half the body weight is used to counter the weight of the head and body to stop the snake robot from tilting over, this means the tail section of the robot is wasted whereas a dedicated counterweight can fulfil the same role.

2.1.3.1 Snake arms

The snake arm is essentially a snake robot with its tail-anchored to a base section, used as a highly dexterous and redundant system snake arms have had focus in the industry to successful effect [74, 75]. Snake arms have shown that they can be built to have a large variance in diameter; snake arms can be sufficiently small to be used for minimally invasive surgery [75] or large to make repairs on nuclear power plant sites [74]. It seems apparent the diameter of the snake-arm is highly dependent on the environment the product is to be deployed in, also a correlation between the diameter and length can be deduced which will affect the performance of the snake arm.

Lum, G.Z., et al. breaks down the design of snake arms further by stating how there are currently two categories for dexterous robotic arms, those being discrete and continuum [76]. Discrete robots consist of a series of short rigid links connected to one another with the use of discrete joints (such as universal joints), continuum robots, on the other hand, replaces the discrete joints for an elastic deformable body. The authors mention this will decrease the weight of the snake arm, however, it makes calculating the motion of the continuum robot more complex [76].

The base of the snake arm would contain the components necessary for the function of the snake arm, but not required for deployment through a restricted access entrance. This results in the base of the snake arm to benefit from less restrictive specifications allowing room for mounting large actuators and sensors if required. The diameter of the snake arm, on the other hand, is subject to the borehole diameter.

If there is a large range of available borehole diameters, there is also a large selection of options for actuating the snake arms. These can be categorised as a motor driven [77], pneumatically driven [78] or cable driven [79]. A larger snake arm diameter generally results in a snake arm capable of further horizontal reach. The specifications and type of a range of snake arms illustrate this in Table 2.2.

Table 2.2 Snake arm specifications.

Type	Backbone	Diameter (mm)	Length (mm)	D/L ratio	Reference
Motor	Discrete	6.35	14.5	0.438	[80]
Motor	Discrete	100	1130	0.088	[77]
Pneumatic	Continuous	10	150	0.066	[81]
Pneumatic	Continuous	80	300	0.267	[82]
Pneumatic	Continuous	~150	1480	0.101	[78]
Cable	Continuous	3.8	770	0.005	[83]
Cable	Continuous	4.2	28	0.150	[84]
Cable	Continuous	4.8	800	0.006	[85]
Cable	Continuous	8.8	77.4	0.114	[86]
Cable	Continuous	15	150	0.100	[87]
Cable	Continuous	15	300	0.050	[88]
Cable	Continuous	15	450	0.033	[89]
Cable	Continuous	16	150	0.107	[90]
Cable	Continuous	30	355	0.085	[91]
Cable	Continuous	-	750	-	[92]
Cable	Continuous	40	-	-	[74]
Cable	Continuous	60	-	-	[74]
Cable	Continuous	100	1200	0.083	[93]
Cable	Discrete	12.5	2200	0.006	[74]
Cable	Discrete	~40	~700	0.057	[94]
Cable	Discrete	100	6000	0.017	[95, 96]
Cable	Discrete	150	2400	0.063	[97]
Cable	Discrete	160	8200	0.020	[98]

Lum, G.Z., et al. constructed a discrete robotic arm to verify their kinematic formulations and motion control algorithms [76]. Using three cables to actuate each discrete joint, the feasibility of using the lightweight tendons proved to be successful and the authors suggested the use of cables as opposed to heavy actuators in each section which provided a larger workspace, larger payload to weight ratio and lower production costs [76].



Figure 2.32 Cable-driven dexterous robotic arm prototype [76].

A successful example of a product that uses cables would be by a company known as OC Robotics [99]. As described in their case study the authors Buckingham, R.O. and A.C. Graham describe the event where their discrete snake arm was used to repair a vital pipe at a nuclear power plant site, the snake arm has a diameter 60mm and length of 800mm. In place of the general universal joint and link configuration, the authors designed and patented their own link assemblies which go away with the mechanical joints in place of plates with elastomers sandwiched between them [100]. The environment which the snake arm was deployed was too small and too dangerous for a human worker to reach, the fact that the snake arms would not require any access holes practically guaranteed the job to them. This has shown that snake arms are capable of reaching into difficult to reach spaces using limited space, yet still have the dexterity to allow it to function in the severely constrained spaces.

Practical applications for the use of snake arms can be found in search and rescue operations at disaster sites. To search through piles of rubble, the use of a thin elongated snake arm could be capable of navigating around the small gaps in the rubble to reach a destination, this will be less labour intensive than digging the site and also much safer for anyone buried under the rubble. With this scenario was the research conducted by Lu, C., et al. [94] where a portable discrete snake arm was manufactured. Using only manual power for controlling the snake arm, the lack or limited use of electricity at disaster sites was overcome as the only power source required was for the cameras and lights, a small resource in comparison to several high power linear actuators. The paper makes no mention of the products total diameter or length, however

from approximate scaling on images the diameter is approx. 40mm and length approx. 700mm. Unfortunately, only the 'head' section was actuated by cables and the majority of the body is composed of flexible hollow segments. Whilst the length of the actuated segments is short, by lengthening the unactuated flexible segments the authors essentially drastically improved the effective range of their snake arm in a simple manner.



Figure 2.33 Prototype of the search and rescue apparatus [94].

Issues with unsupported links for long reach snake arms is the arm cannot hold the horizontal cantilever posture without being supported externally. At small diameters where space is a premium this issue is difficult to overcome without large forces for torque production, however, with larger diameters, there are options to compensate for the gravity effect. Using a special mechanical parallelogram structure, Perrot, Y., et al. was able to reduce the size of the actuators needed to operate the snake arm (Figure 2.34) with the inclusion of an equilibrium spring to counter the gravity effect on the elevation (pitch) actuators (Figure 2.35) [101].



Figure 2.34 PAC long reach robotic carrier [101].

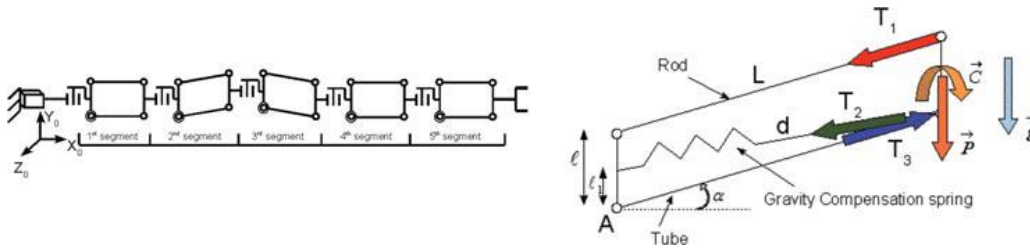


Figure 2.35 (left) Robot kinematic model. (right) Forces through the parallelogram [101].

It is advantageous to use discrete robots as the motion can be predictable, however, they cannot produce high output speeds. On the other hand, continuum robots can achieve higher speeds but the predictability of the motion is sacrificed [102]. Attempting to combine the advantages of both Tran, L.D., et al. built a test rig for a cable driven snake arm with a flexible backbone. The backbone material was chosen to be elastic, inextensible and rigid in torsion with the cables made of steel. The author's conclusions indicate they are capable of achieving good position control and tracking ability with the flexible backbone such that it is comparable to a discrete universal joint [102]. Tran, L.D., et al. however makes no mention of the flexible backbone possibly buckling under the pull of the steel cables, it is common knowledge that struts will buckle under sufficient axial compression, therefore the low stiffness of the system could pose to be an issue.

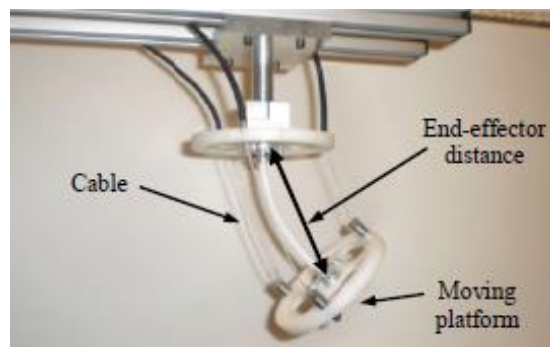


Figure 2.36 Features of robotic arm with one module [102].

An area where the short flexible backbone is shown to be suitable is found in tools for minimally invasive surgery. Although the buckling of the flexible backbone still occurs on the snake-like unit built by Simaan, the author prevents the failure by replacing the thin cables for the same material as the primary backbone [103]. This improved design allows the actuating cables to

be used in a push/pull manner as opposed to the larger snake arm designs where the actuating cables can only pull; essentially the actuating cables are now secondary backbones that reduce the load on the primary backbone. In the author's conclusion, Simaan states the multiple backbone method could be miniaturised, the author does not however mention about upscaling the method to possibly improve systems such as that created by Tran, L.D., et al [102].

The joints of a snake-like robot have been an important focus for literature, the greater torque a joint can produce, the greater the ability to cantilever-lift (lift when extended horizontally) [104]. The snake arm built by Wolf, A., et al. has the capability to cantilever-lift six joints, this is achieved not through cables but by designing a 1DOF joint with a motor and ball screw assembly. By limiting the joints of their design to 1DOF, the single segment has a less complex mechanism and more room to accommodate larger motors. Overall the authors introduce the concept to be capable of inspecting unreachable areas by searching through small cracks and pipes alike. No specifications to the snake arms size nor length were provided.



Figure 2.37 USAR elephant-trunk-like robot (ETR) [104].

2.2 Discussion and conclusion

A selection of literature regarding methods of locomotion was reviewed for deploying instruments for exploring a restricted access space. It can be beneficial for explorations to be conducted through a small borehole that can be quickly bored and the damage is minimal. The implications of this on the design of a purpose-built robot are it would need to be able to fit through that very same small diameter borehole. Once a robot is deployed beyond the

restricted opening and into a larger expanse beyond, the robot would then require the capacity to travel around unaided through unpredictable and possibly uneven rough terrain.

On the process of selecting the appropriate robot design, Li, B., et al. [105] mentions how the selection demands trade-offs related to:

- System size to access through the smallest possible voids and openings.
- The system's ability to climb over large obstacles which are directly related to size for land locomotion.
- The ability to adapt to the uneven terrain and the need to probe to varying depths.

Therefore, a robot that can access entrances of the smallest possible diameter is not expected to overcome large obstacles (with respect to the robot) unless a novel solution exists to overcome those barriers.

Snake robots are in a unique position where their design inherently requires the design of the robot to have a slender profile i.e. large length to diameter ratio. This makes these snake robots suited for deployment through a bored hole of equal or larger diameter than the snake robot. The disadvantage of using snake robots has been their large chassis required to house the many actuators within the body of the snake robot and for snake arms even though all the motors can be relocated to a base platform, the reach of the snake-arm is limited to the design so exploration beyond its length would not be possible. An advantage of using a snake arm is the ability to support its own weight and not require contact with any internal surfaces nor structures for any length of time.

The design for a self-reconfigurable robot is similar to a snake robot with greater capabilities, one that requires an additional layer of complexity over an already complex design. Simplification of a reconfigurable robot would be beneficial to reduce chances of failure. Reconfigurable robots can be restructured to adapt to the terrain encountered, however its legged configuration is still capable of crossing flat areas and slopes at the cost of efficiency. The strength of a reconfigurable robot in our case was found in its ability to alter its cross section area before and after deployment.

Self-folding systems are still in the early development stage, however, their flexible construction and ability to function without traditional motors demonstrates potential for a new class of novel robotics. A printed inchworm robot is capable of self-assembly and motion using external servo-motors by Felton, S.M., et al. [55], whilst actuated joints using SMA are already functional though limited by Paik, J.K. and R.J. Wood introduce the bi-directional SMA folding actuator [60]. A fusion of bi-directional SMA folds forming an inchworm mechanism will produce a lightweight and compact system capable of self-reconfiguration and locomotion. This fusion of technologies can assist towards creating miniature mobile borehole exploration robots.

Chapter 3

System Specifications

This chapter develops the specifications for the two robotic tools covered in this research that will be deployed into two different environmental scenarios.

3.1 Introduction

The literature review in Chapter 2 explored the use of several locomotion techniques for ground robots. To apply the techniques into this research and fulfil the research aims, the specifications for two borehole inspection robotic tools for two different environmental scenarios are expanded upon and developed.

Before deploying robotic tools into the subterranean spaces, the composition of the two environments was investigated further. Factors such as the boreholes diameter and depth, and the size of the chamber after, are important factors for deciding on the type of robot to be deployed.

3.2 Environment 1

Environment 1 has the attributes of an underground tomb with great historical significance. Access into the subterranean chamber must be conducted through the smallest and least damaging hole possible and capable of visually observing the chamber. Table 3.1 details the environmental specifications that affects the robot chosen for this task.

Table 3.1 Environmental specifications.

Borehole diameter	The suggested diameter for the borehole is 14mm, based on available drill sizes.
Borehole depth	From the surface to the subterranean space is a distance of approximately 200mm.
Chamber size	The subterranean space assumed to be 2m width x 2m long x 1-4m deep.

Provided with the information in Table 3.1, the environment describes a scenario where a robotic tool must be deployed through a small borehole of

14mm diameter and 200mm in length. Thereafter, the robot enters a chamber of volume between 4m^3 to 16m^3 . The additional information suggesting the chamber is of historical importance further suggests preservation of the site has priority and ideally, the explored chamber will be kept unmarked and undamaged. This results in the robots locomotive options being restrictive.

3.3 Environment 2

Environment 2 has the attributes of a disused mineshaft. Accessing the mineshaft is possible through a small diameter borehole using the Shaw portable drill. In comparison to Environment 1 (Section 3.2), entry into the mineshaft requires travelling through a borehole of longer length into a subterranean space of much greater proportions. Table 3.2 details the environmental specifications that affects the robot chosen to explore this space.

Table 3.2 Environmental specifications.

Borehole diameter	Based on the Shaw portable drill [14], the diameter of the borehole is 41mm.
Borehole Depth	The Shaw portable drill can achieve borehole depths of up to 23m in some circumstances. In this case, the robot will be deployed vertically downwards in a borehole of length 30ft (9.144m).
Chamber size	After penetrating the borehole and entering the confined subterranean space. The geometry of the mineshaft is assumed 2.5m wide x 2.5 m high with a length of up to 200m on a slight 2° incline.

Provided with the information in Table 3.2, the environment describes a scenario where a robotic tool must be deployed through a larger borehole of 41mm diameter and approximately 9m in length. Thereafter, the robot enters a chamber of 1250m^3 in volume. Without the requirement for historical preservation of the mineshaft beyond not compromising the structural integrity of the mineshaft, more locomotive options are available for the design of the

robotic system. As the mineshaft was at some point active, it is expected the terrain to be rough and uneven.

3.4 Locomotion method selection

Subject to the two environments of different specifications to be inspected by two robotic systems. It was necessary to select a suitable locomotion system inspired by those examined in the literature review in Chapter 2. The decision was aided using a decision matrix (Table 3.4) and the criteria shown in Table 3.3. Scoring was completed by scoring each locomotion method against each criteria with a score between 1 and 5, with a score of 1 being low and a 5 being high.

Table 3.3 Decision matrix criteria for locomotion designs.

Criteria	Score		
	1 - low	3 - medium	5 - high
Size of chamber entrance	The locomotion method requires a large chamber entrance.	The locomotion method requires a medium chamber entrance.	The locomotion method requires a small chamber entrance.
Deployed size of robot	The deployed robot is large and difficult to control in an enclosed space.	The deployed robot is of medium size and can cause controlling issues in an enclosed space.	The deployed robot is small and will be simple to control in an enclosed space.
Robust design	The design is not robust and is difficult to disassemble and repair.	The design is quite robust and can be repaired with replacement parts but is difficult to disassemble.	The design is robust and is easily repaired and disassembled.

Feasibility through a 14mm bore	The locomotion method cannot be scaled down for the 14mm diameter borehole.	It is possible with minor modifications for the locomotion method to be deployed through the 14mm borehole.	The locomotion method can easily be deployed through 14mm borehole entrances.
Feasibility through a 41mm bore	The locomotion method cannot be scaled down for the 41mm diameter boreholes.	It is possible with minor modifications for the locomotion method to be deployed through the 41mm borehole.	The locomotion method can easily be deployed through 41mm borehole entrances.
Range	If tethered, the locomotion system is not expected to travel great distances.	If tethered, the locomotion system is expected to produce travel distances adequate for a brief exploration.	If tethered, the locomotion system is suitable for long distance explorations.
Survivability from impacts	The mechanism driving the locomotion is complex and prone to complications.	The mechanism driving the locomotion is complicated but reliable.	The mechanism driving the locomotion is simple and very reliable.
Ability to climb over obstacles	The robot cannot climb over obstacles.	The robot will not be impeded by minor obstacles	The robot displays the ability to climb over obstacles.

		but will find larger steps difficult.	
Ability to navigate through voids	Once deployed the robot will be too large to pass through further voids due to a large cross section.	Once deployed the robot will be able to pass through voids due to a smaller cross section.	Once deployed the robot will retain a small cross section or has the ability to reconfigure its cross sectional area to navigate through voids.
Ability to climb slopes	The robot locomotion does not produce enough driving force to climb inclines.	The robot locomotion does produce enough driving force to climb inclines, but at a reduced range.	The robot locomotion is unhindered by slopes.
Ability to navigate unpredictable rough terrain	The robot is incapable of handling terrain composed of multiple obstacles such as steps, ramps and gaps.	The robot is impeded when handling terrain composed of multiple obstacles such as steps, ramps and gaps.	The robot is capable of handling terrain composed of multiple obstacles such as steps, ramps and gaps.

From Table 3.4, wheeled and tracked robots underperform due to their large size and limited ability to navigate obstacles. However, snake arms, wheel-leg robots and reconfigurable robots rank amongst the highest. Reconfigurable robots and wheel-leg robots rank similar in their abilities and size, however, the reconfigurable robots naturally benefits in tackling voids and obstacles.

Wheel-leg robots have demonstrated the ability to climb over rough terrain, hence the larger feasibility scores. Although, merging both to create a wheel-

leg robot that can be reconfigured will draw upon the strength of both is possible. Furthermore, this merger will result in the reconfigurable robot losing its modular design in place of a simplified design as wheel-legs have been shown to be capable on both flat and rough terrain, so the capabilities and feasibility of the robot can only improve in that regard.

Snake arms have demonstrated ability to function through small diameter entrances in minimally invasive surgery [75] or for USAR operations [94]. Therefore snake arms scored highly for its size and feasibility. A snake arm can be designed to continuously operate in a horizontal cantilever position the snake arm, hence its ability to navigate obstacles and voids is a strength for the snake arm as is its capability to function over rough terrain. In fact the snake arms only low scoring criteria was the short reach normally associated with small diameters. A small diameter snake arm with long length would be a useful tool for exploration with minimal damage.

Table 3.4 Decision matrix for locomotion designs.

	Size of chamber entrance	Deployed size of robot	Robust design	Feasibility through a 14mm bore	Feasibility through a 41mm bore	Range	Survivability from impacts	Ability to climb over obstacles	Ability to navigate through voids	Ability to scale slopes	Ability to navigate unpredictable rough terrain	Total
Snake-Arm	5	5	4	4	4	2	3	5	4	5	5	46
Wheel-Leg	4	4	5	3	3	4	4	4	4	4	5	44
Reconfigurable	4	4	4	2	4	4	3	5	4	5	5	44
Legs	3	3	4	2	2	3	3	5	3	4	5	37
Snake-like	3	3	4	2	2	3	3	4	4	5	4	37
Wheels	2	2	5	3	3	5	5	1	4	1	1	32
Tracked	1	1	5	1	3	5	3	3	3	3	3	31
Self-folding	4	3	2	4	4	1	5	1	1	1	1	27

3.5 Refining the specifications

Integrating the results of the decision matrix (Table 3.4) and the environmental specifications (Section 3.2 and 3.3) produces the most suited locomotion solution for each environmental layout.

3.5.1 Snake arm specifications

Environment 1 revealed a situation where the inspection of an underground tomb was required. The borehole entrance had to be small at 14mm diameter and the length of the borehole was short at approximately 200mm, the borehole then expanded into a small chamber 2m width x 2m long x 1-4m deep.

Comparing the results of the snake arm to environment 1, the snake arm scores high with feasibility through the small diameter boreholes and ability to overcome the terrain within the chamber. The main disadvantage of the snake arm was the range, however, as the chamber is relatively small the drawback from this issue is minimised. The ability to hold the horizontal cantilever position without external supports will additionally encourage the use of the snake arm as the tomb does hold historical significance. This results in a system that can explore the internal volume without the need to make contact with any chamber surfaces.

A snake arm designed to explore environment 1 must therefore:

- Be 12mm in diameter for portable borehole deployment (1mm clearance each side through borehole).
- Be designed for maximum reach to perform a visual exploration.
- Be capable of self-supporting in the horizontal cantilever position to minimise risk of internal damage to the chamber.

3.5.2 Reconfigurable specifications

Environment 2 revealed a situation where the inspection of a sealed mineshaft was required. The diameter of the borehole entrance was taken from the size of the Shaw tool at 41mm and the length of the borehole is expected to be approximately 9m long. The mineshaft is assumed 2.5m wide x 2.5m high with a length of up to 200m on a slight 2° incline.

Although the snake arm scored highly in the decision matrix, the dimensions of the mineshaft and the short range of a snake arm meant it was not feasible to deploy a snake arm for this case. The use of a wheel leg robot would grant it the capability to explore the mineshaft at a much greater distance than the snake arm. However, complications would arise in deploying such robotic systems through a small 41mm diameter entrance without some method of reconfiguring the shape of the robot from an unstable slender profile to a more stable wide gait.

A reconfigurable robot utilising wheel leg techniques for locomotion is ideal for exploring environment 2. The Houdini [50] and Hitachi robot [52] demonstrates the ability for a robot to conform to two configurations, one whilst deploying and another during the exploration. Therefore, implementing wheel leg profiles onto the tracks of the reconfigurable robot will increase the capability of the robot to overcome obstacles and terrain.

A method of controlled decent and retrieval is also vital for any remote exploration. This is possible with a tether for a physical connection between the surface and the robot. The tether can also be used to supply electrical power and communications between a user and the robot and this system is also found for the Houdini [50] and Hitachi robot [52].

Combining the information for environment 2 and the decision to use a reconfigurable robot with wheel leg profiles for locomotion, the following specifications are formed.

- The diameter of the robot must be less than 41mm.
- The robot is expected to travel 200m on a slight 2° incline.
- The robot must be tethered to transmit power and assist in extraction of the device
- Illumination from a small light, such as a single Cree XLamp module to provide sufficient illumination [106].
- Tapered at rear for withdrawal.
- The robot weight needs to be sufficiently high to generate traction forces sufficient to pull the cable.

3.6 Discussion and conclusion

Environmental information is essential when planning any inspections. Information on the access routes, size, obstacles on the ground (debris, voids, steps, inclines etc.) and any other dangers will aid in the selection of an appropriate robotic platform. In cases where a subterranean chamber remains unexplored, ground penetrating radar (GPR) is capable of detecting subsurface objects, changes in material properties, and map subsurface archaeological artefacts, features, and patterning [107]. A more detailed preliminary inspection can then be conducted using drop down borehole cameras to gather visual information on the immediate surrounding area. This will provide further information on the terrain and state of the subterranean space for selecting the next tool to be deployed for an in-depth exploration.

In sections 3.2 and 3.3, two opposing environments is introduced, one environment is small and the other a magnitude larger. To select the appropriate tool to inspect each environment, a decision matrix was utilised using criteria scoring on performance over different terrain and feasibility through small diameter boreholes of different sizes. The results show snake arms robots scoring highest and wheel-leg and reconfigurable scoring equally below snake arms.

Snake arms suffer from a limited range due to the base platform housing the motors and electronics actuating the cables within the arm being larger than the diameter of the arm. This benefits the snake arm as all forward movement is provided directly from the surface and if the snake arm is capable of maintaining a horizontal cantilever position then it would not be affected by terrain inside the chamber. Therefore, this makes it suitable for inspecting the smaller environment (environment 1).

With a range of up to 200m for environment 2, the deployment of a snake arm is unsuitable for exploring this space. From literature, reconfigurable robots can be designed to assume many forms to aid with deployment and locomotion. These creations are complex and modular, increasing the risk of complications and failure. To deploy through a small diameter borehole of 9m in length, a reconfigurable robot must assume a long and slender posture,

then upon entering, a locomotive configuration can be used to overcome any terrain and obstacles.

A wheel-leg platform is demonstrated to be capable of overcoming rough terrain and obstacles. These systems are also much simpler and more robust than modular reconfigurable robots. Although, four whegged robot cannot be easily deployed through small diameter boreholes. Fortunately, it is possible to combine the reconfigurable robot together with a whegged platform, forming a platform capable of forming a slender configuration through a borehole and reconfigure into an alternate configuration for exploration of the mineshaft.

From the decisions formed from the environmental specifications and the decision matrix, the specifications for two robotics platforms are created. This demonstrates how different environments will require different robotic systems to perform the inspection and there is no single solution to every scenario.

Chapter 4

Snake arm theory and analysis

This chapter develops the method to calculate the cable tensions of a snake arm and analyses the buckling failure modes of each component comprising the snake arm. The experiments to verify the cable tensions are also performed with the inclusion of friction analysed for the experimental test rig.

4.1 Introduction

A snake arm is an self-supporting (can lift its weight against gravity) articulated series manipulator. It often contains large numbers of joints that enable positioning of a payload as well as the ability to define the path taken to the desired sensor deployment co-ordinates. A snake arm is anchored at a base point opposed to snake robots that are self-contained and not grounded.



Figure 4.1 First prototype from OC Robotics [108].

A discrete backbone snake arm structure is formed from a series of long rigid links and joints while a continuous one formed is from multiple continuous curving short vertebrae interconnected with a flexible backbone (Figure 4.2).

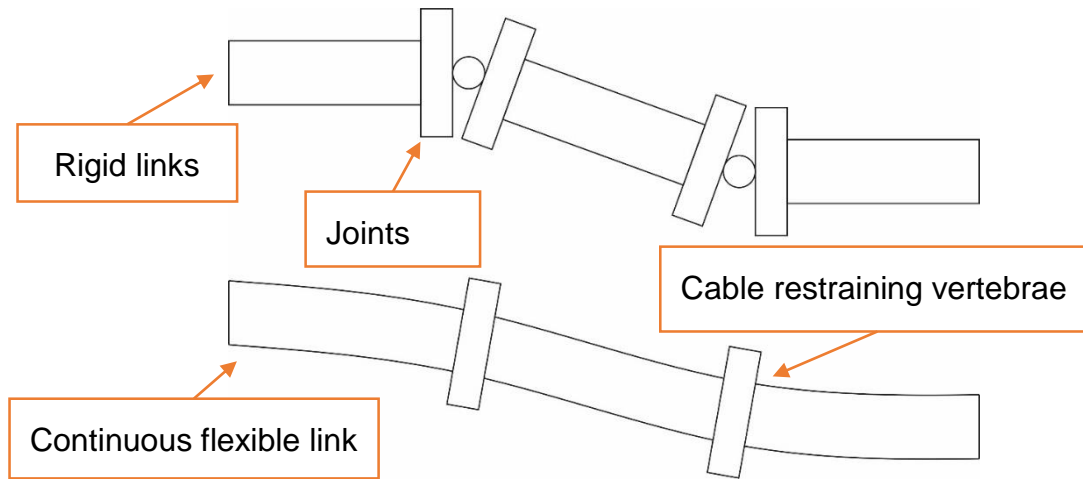


Figure 4.2 (Top) rigid snake arm, (Bottom) continuous snake arm.

Motors within each joint can actuate a snake arm, or as the arm is supported at a fixed point motors can drive cables attached to each joint and remotely operate them. For a self-supporting snake arm it is important to minimise the weight in each joint, therefore cables (tendons) offer the lightest solution. However, the internal space must accommodate tendons for each joint and additional cables for the end effector. The diameter of each tendon is determined by the tension required and the properties of the tendon material. There is a physical limit to the number of tendons that will fit in a given diameter of snake arm and this, in turn, places a physical limit on the number of joints achievable.

Cables can only exert tension but not compression i.e. forces applied are unidirectional. Morecki, A., et al. stated that a manipulator with n -DOF requires at least $n+1$ tendons to achieve complete control of all degrees of freedom [109].

Figure 4.3 illustrates how a 12mm diameter cross section is used for a thin cylindrical link, cables and a 2-DOF joint located at the centre. The specific values of this example are determined in Chapter 3. Using a cable of 1.5mm diameter with a cylindrical link of 1mm wall thickness allows the cables to be spaced radially at 7mm diameter. Leaving at least 1mm space between each cable allows space for only 10 cables. Allocating a single cable for a camera end effector, the nine remaining cables are divided by three (the minimum amount of cables required to fully constrain the joints) to reveal the capacity

of a 12mm diameter snake arm to be only three joints with 2DOF each. The remaining space can then be allocated for the joints.

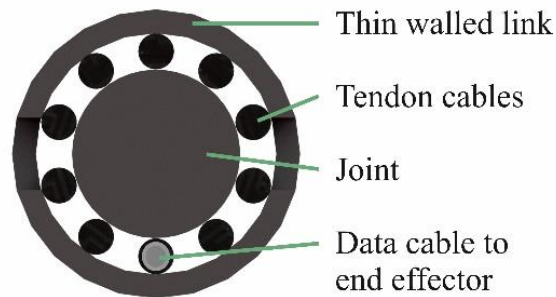


Figure 4.3 Snake arm cross section of 12mm diameter.

For a snake arm to increase its workspace, the length of the snake arm and the range of motion at each joint should be maximised. However, there is a physical limit to these properties that, if exceeded will cause the snake arm to fail. The remainder of this chapter considers how these properties can be maximised.

4.2 Kinematics and statics

It is important to calculate the forces required at each joint and the forces acting on the structure. To find this information the torque required at each joint is needed. Kinematics of a three jointed snake arm can be characterised using Denavit-Hartenberg parameters as shown in Table 4.1.

Link length J denotes the offset distance between the two axes of rotation in a 2DOF universal joint. In most cases, the axes are collinear resulting in the value of zero. In Chapter 4, it is shown that by offsetting the axes a smaller diameter joint is possible with larger diameter pins and is represented in Figure 5.3. This effectively splits each universal joint into two individual joints. For purposes of simplification and continuation, each combination of adjacent pitch and yaw joints will be regarded as a single joint.

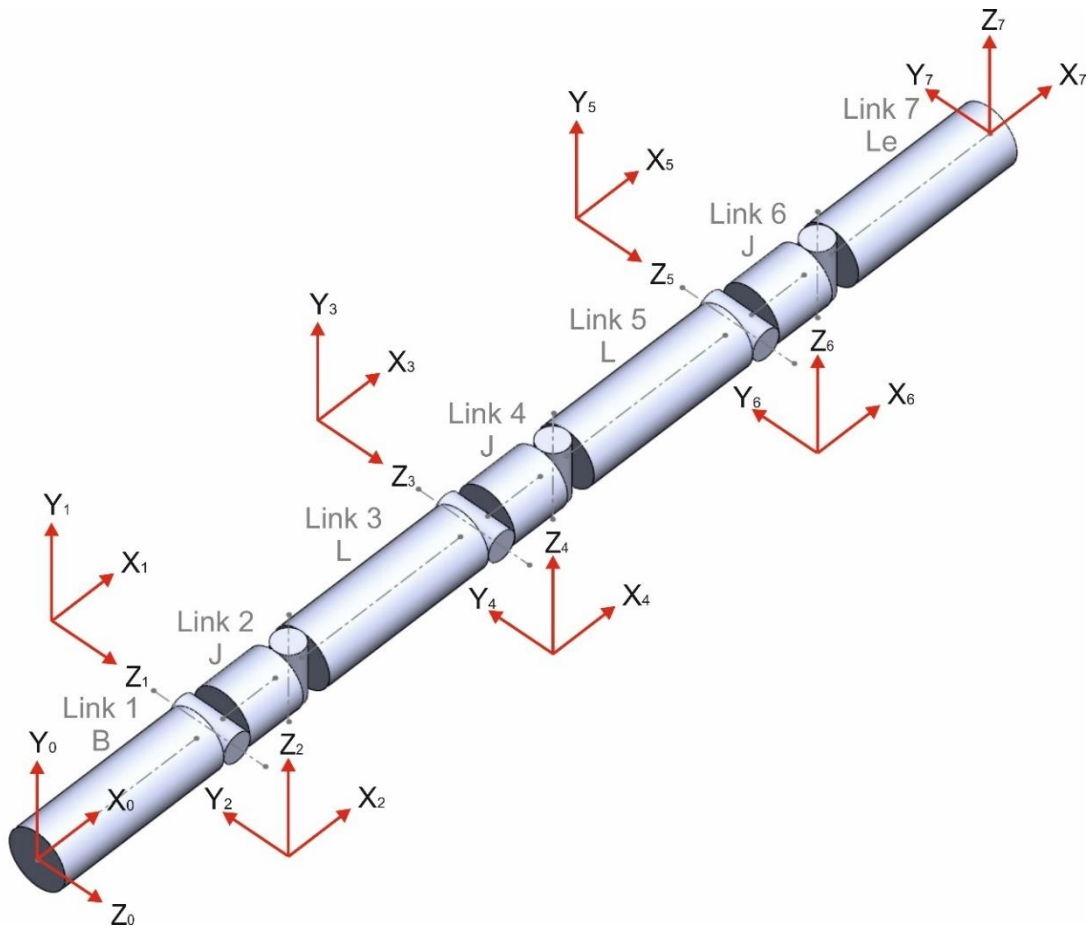


Figure 4.4 Denavit-Hartenberg notation for snake arm.

Table 4.1 Denavit-Hartenberg notation for each snake arm link.

Link	α	A	θ	D
1	0	B	0	0
2	0	J	θ_1	0
3	$-\pi/2$	L	θ_2	0
4	$\pi/2$	J	θ_3	0
5	$-\pi/2$	L	θ_4	0
6	$\pi/2$	J	θ_5	0
7	$-\pi/2$	Le	θ_6	0

Using these parameters, the position at each joint and the end effector can be computed as the product of the transformation matrices. The solution to the forward kinematic problem is given by:

$${}^0T_{18} = {}^0T_1 {}^1T_2 {}^2T_3 {}^3T_4 {}^4T_5 {}^5T_6 {}^6T_7 {}^7T_8 {}^8T_9 {}^9T_{10} {}^{10}T_{11} {}^{11}T_{12} {}^{12}T_{13} {}^{13}T_{14} {}^{14}T_{15} {}^{15}T_{16} {}^{16}T_{17} {}^{17}T_{18} \quad 4.1$$

$$\begin{aligned} {}^0T_{18} = & \text{tran}(B, 0, 0) \cdot \text{rot}(Z, \theta_1) \cdot \text{tran}(J, 0, 0) \cdot \text{rot}\left(X, -\frac{\pi}{2}\right) \cdot \text{rot}(Z, \theta_2) \\ & \cdot \text{tran}(L, 0, 0) \cdot \text{rot}\left(X, \frac{\pi}{2}\right) \cdot \text{rot}(Z, \theta_3) \cdot \text{tran}(J, 0, 0) \\ & \cdot \text{rot}\left(X, -\frac{\pi}{2}\right) \cdot \text{rot}(Z, \theta_4) \cdot \text{tran}(L, 0, 0) \cdot \text{rot}\left(X, \frac{\pi}{2}\right) \\ & \cdot \text{rot}(Z, \theta_5) \cdot \text{tran}(J, 0, 0) \cdot \text{rot}\left(X, -\frac{\pi}{2}\right) \cdot \text{rot}(Z, \theta_6) \\ & \cdot \text{tran}(Le, 0, 0) \cdot \text{rot}\left(X, \frac{\pi}{2}\right) \end{aligned} \quad 4.2$$

Where the operators are given by:

$$\text{tran}(x, y, z) = \begin{bmatrix} 1 & 0 & 0 & x \\ 0 & 1 & 0 & y \\ 0 & 0 & 1 & z \\ 0 & 0 & 0 & 0 \end{bmatrix} \quad 4.3$$

$$\text{rot}(x, \theta) = \begin{bmatrix} 1 & 0 & 0 & 0 \\ 0 & \cos \theta & -\sin \theta & 0 \\ 0 & \sin \theta & \cos \theta & 0 \\ 0 & 0 & 0 & 1 \end{bmatrix} \quad 4.4$$

The unknown variables of link lengths B, L and J are required to calculate the position and orientation of the end effector at any joint angle. Calculating the torques required at each joint to maintain the joint angles will assist in solving for the unknown link length, which would maximise the workspace, and length. This is possible using the recursive Newton-Euler (RNE) formulations to calculate joint torques for rigid link arms. The formulations are derived directly from Newton's Second Law of Motion, which describes dynamic systems in terms of force and momentum. Incorporating all the forces and moments acting on individual links including the coupling forces and moments between links, the resulting equations provides a closed-form expression in terms of joint torques and joint displacements [110].

This is achieved in two steps, the outward recursion and the inwards recursion.

Outward recursion

For link $i=1:n$

- 1) Angular velocity of link: $\omega_i = \omega_{i-1} + \dot{\theta}_i$
- 2) Angular acceleration of link: $\dot{\omega}_i = \dot{\omega}_{i-1} + \ddot{\theta}_i$
- 3) Linear acceleration of link at frame origin: ${}^i\dot{v}_{i-1} = {}^iR_{i-1}{}^{i-1}\dot{v}_{i-1}$

$${}^i\dot{v}_i = {}^i\dot{v}_{i-1}L_i \begin{bmatrix} -\omega_i^2 \\ \dot{\omega}_i \end{bmatrix}$$

- 4) Linear acceleration of link at centroid: ${}^i a_i = {}^i\dot{v}_{i-1} + c_i \begin{bmatrix} -\omega_i^2 \\ \dot{\omega}_i \end{bmatrix}$
- 5) Resultant force acting on link at centroid: ${}^i F_i = m_i {}^i a_i$
- 6) Resultant moment acting on link around centroid: $N_i = I_i \omega_i$

Inward Recursion

For link $i=n:1$

- 1) Force exerted on link i by link $i-1$: ${}^i f_{i+1} = {}^i R_{i+1} {}^{i+1} f_{i+1}$

$${}^i f_i = {}^i F_i + {}^i f_{i+1}$$

- 2) Torque exerted on link i by link $i-1$:

$$\tau_i = N_i + \tau_{i+1} + {}^i f_{i,y} c_i + {}^i f_{i+1,y} (L_i - c_i)$$

Assuming we have a simplified snake arm with the specifications listed in Table 4.2, by applying the above RNE formulations, a torque required for each joint displacement is calculated.

Table 4.2 Specifications of the simplified snake arm.

Number of links	4
Number of joints	3
Length of each link	1 m
Mass of each link	1 kg
Joint angle limit	-90° to 90°

Using Matlab software to perform the RNE formulations the torque at each of the three joints of the simplified snake arm (as shown in Figure 4.4) is iteratively computed in one-degree increments. Assuming the arm is static (no inertia), a torque required to hold the snake arm at each step is recorded and

plotted to illustrate the joint angle at which a peak torque occurs. Figures 4.6 and 4.7 show that the peak torque occurs at a joint angle of 0° , otherwise known as the horizontal cantilever position. This is where the focus of the snake arm will be aimed as the relationship between torques required and cable tensions will contribute to the axial compressive forces acting through the snake arm structure.

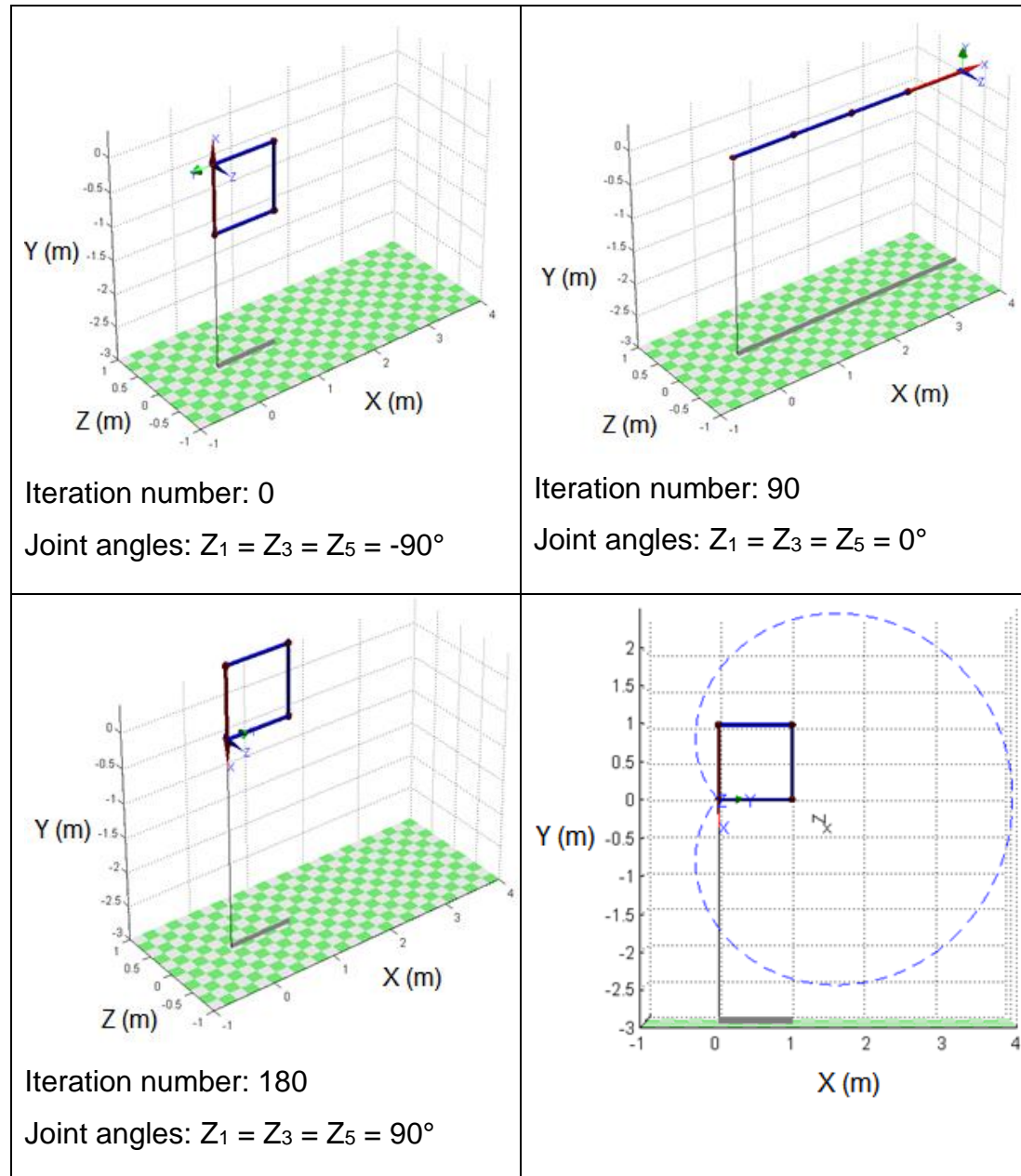


Figure 4.5 (Top left) Snake arm at start position, (Top right) Snake arm at middle position, (Bottom left) Snake arm at end position, (Bottom right) Path of the snake arm end effector.

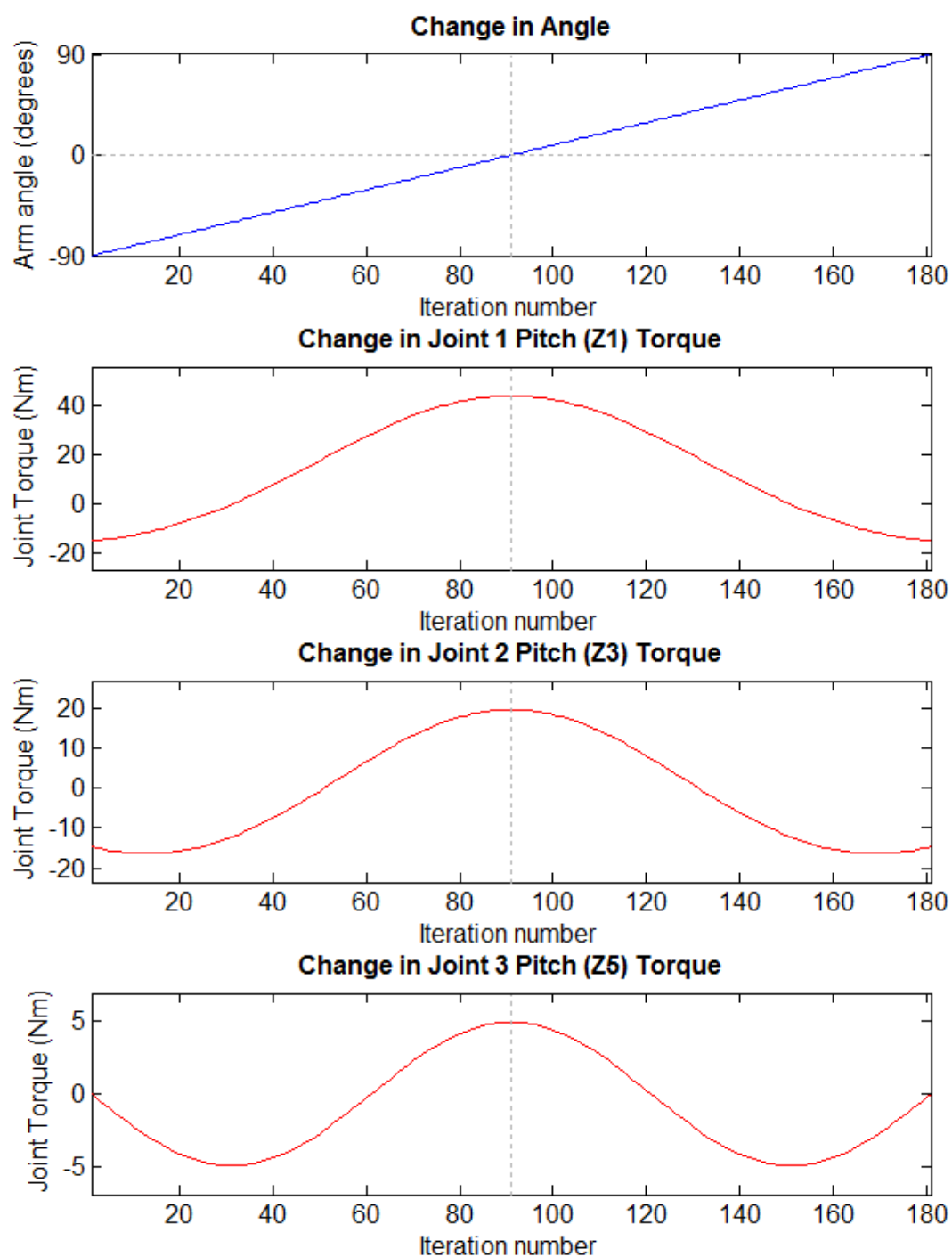


Figure 4.6 Change in pitch torque per joint as joint angle is incremented.

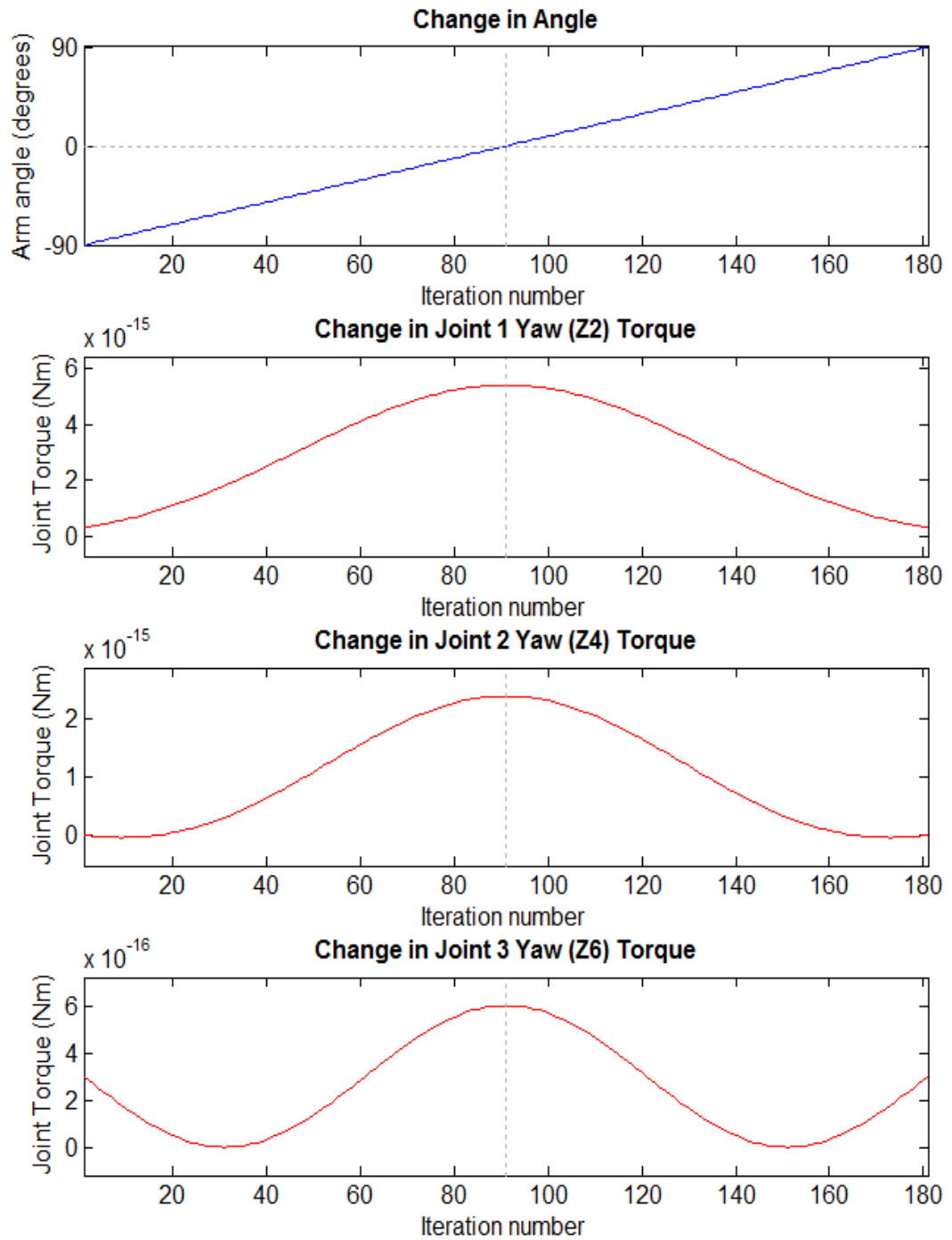


Figure 4.7 Change in yaw torque per joint as joint angle is incremented.

4.3 Link buckling

The composition of the tubing that makes up the links for the snake arm is a long, thin-walled cylinder. For the control of a discrete snake arm, it is important that the link remains rigid as axial loading induced bending affects the RNE torque formulations. Links under axial compression can deflect and deform through two types of buckling modes, flexural and local buckling. Both are independent and each must be investigated to avoid buckling failure.

4.3.1 Flexural buckling

Flexural buckling occurs when a load causes an extreme fibre of the cylinder to reach a prescribed stress. The Engineering Sciences Data Unit (ESDU) who is an engineering advisory organisation based in the United Kingdom contains many datasheets which is assessed and peer-reviewed and some containing information on the buckling of thin-walled cylinders. The formula to find the stress at which flexural buckling occurs is stated as [111]:

$$\frac{f_b}{f_E} = \frac{1}{2} \left(\frac{f_P}{f_E} + (1 + \eta) \right) - \left[\frac{1}{4} \left(\frac{f_P}{f_E} + (1 + \eta) \right)^2 - \frac{f_P}{f_E} \right]^{\frac{1}{2}} \quad 4.5$$

$$f_E = \pi^2 E \left(\frac{k}{l'} \right)^2 \quad 4.6$$

$$\eta = 0.003 \left(\frac{l'}{k} \right) \quad 4.7$$

$$k = \frac{(D^2 + d^2)^{\frac{1}{2}}}{4} \quad 4.8$$

Where:

f_b = Elastic buckling stress [N/m²]

f_E = Euler buckling stress [N/m²]

f_P = 0.2% proof stress or yield stress of material [N/m²]

η = Empirically determined factor accounting for imperfections

k = Radius of gyration of section [m]

E = Modulus of elasticity of material [N/m²]

l' = Equivalent length of strut, $2 \times l$ [m]

D = Outer diameter of cylinder [m]

d = Inner diameter of cylinder [m]

Torsional buckling can be characterised using the equations

$$f_T = \frac{GJ}{I_p} + \frac{\pi^2 E \Gamma}{2 I_p l'} \quad 4.9$$

$$J = 2I = \frac{\pi}{2} [D^4 - (D - 2t)^4] \quad 4.10$$

Where:

G = Shear modulus of material [N/m²]

J = Torsion constant of section [m⁴]

I_p = Polar second moment of area about shear centre [m⁴]

E = Modulus of elasticity of material [N/m²]

l' = Equivalent length of strut, fixed ends $2 \times l$ [m]

Γ = Warping constant of section

D = Outer diameter of cylinder [m]

t = Wall thickness of cylinder [m]

4.3.2 Local buckling

When a cylindrical shell is subjected to an axial compression, local buckling in the small deflection range can occur in two possible modes. The first mode is in the form of waves or bellows and is known as symmetrical, ring, or bellows buckling mode (Figure 4.8). The other mode is in the form of waves in both the longitudinal and transverse direction which post-buckling snaps into another state of equilibrium known as the depressed diamond shape [111, 112].

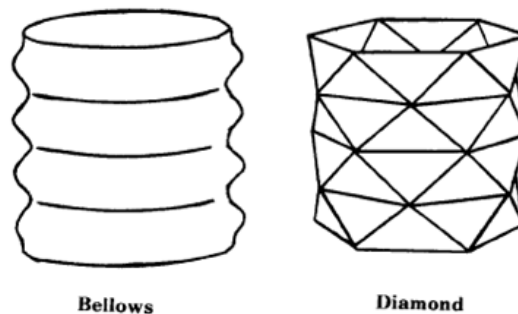


Figure 4.8 Buckling modes of circular sections [111].

Local buckling occurs in two modes, diamond and bellows, the critical stress for when initial buckling occurs for an ideal cylinder is given as:

$$f_{bt} = \frac{QE}{[3(1 - \nu)^2]^{\frac{1}{2}}} \left(\frac{t}{R} \right) \quad 4.11$$

Where:

Q = Empirically found constants for tube end states

E = Modulus of elasticity of material [N/m²]

ν = Poisson's ratio

t = Wall thickness of cylinder [m]

R = Outer radius of cylinder, $D/2$ [m]

4.4 Cable tensions

Table 4.1 shows the parameters used to specify the kinematics of the snake arm assuming the links do not bend or twist. The position of the end effector with respect to the base frame is computed with forward kinematics from the transformation matrices produced. Combined with the Recursive Newton-Euler (RNE) method, the torque at each joint is computed and is carried over to calculate the cable tensions.

The RNE joint torques reach a maximum when the snake arm is at a horizontal cantilever position without additional external forces other than gravity acting upon it; therefore at this point, it is assumed the closely associated tendon tensions are also at its maximum. This horizontal state should then be where the failure of the snake-arm is most likely to occur and is where this analysis is focused on.

Calculating the cable tensions from the joint torques can be performed if the cables are assumed to have constant length and tension with negligible friction and all joint angles are known. Simplifying the snake arm into a single joint system of length L , weight W , payload weight P and perpendicular tendon distance of D_y as shown in Figure 4.9 the single tendon tension T must be equal to the moment about the joint, assuming no friction or other external forces.

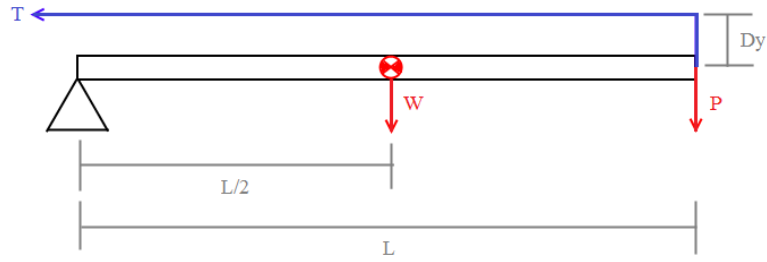


Figure 4.9 Simplified snake arm with single joint and single tendon.

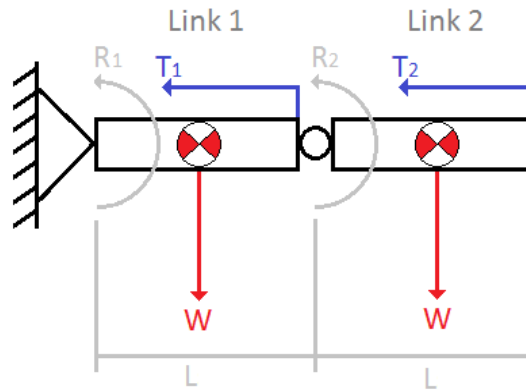


Figure 4.10 Simplified snake arm with two joints and two tendons.

As multiple tendons cannot occupy the same space for all joints, some tendons are displaced radially about the centre. This creates an undesirable lateral load and the introduction of additional tendons to counteract the loads. As snake arms generally include multiple joints, Figure 4.10 represents a snake arm with two joints and two tendons at different heights of D_y for a more accurate representation. The RNE method is used to calculate the joint torques R_1 and R_2 and the tendon tensions calculated for the i th joint is expressed as:

$$R_{xyi} = \sum_{j=i}^N T_j D_{xyj} \quad 4.12$$

Where R_{xyi} is the torque generated at joint i for both yaw (R_x) and pitch (R_y) joint directions. T_j is the tension of each tendon that passes through or terminates at joint j . D_{xyj} is defined as the distance between tendon j and the neutral axis of joint i , it can also be a negative value dependent on the direction the tendon j transmits its force on joint i .

Applying the equation to the double-jointed snake arm as shown in Figure 4.10 the equations relating torques to tensions can be produced and solved using matrices.

$$\begin{bmatrix} 0 & D_{y2} \\ D_{y1} & D_{y2} \end{bmatrix} \begin{bmatrix} T_1 \\ T_2 \end{bmatrix} = \begin{bmatrix} R_{y2} \\ R_{y1} \end{bmatrix} \quad 4.13$$

Where the tensions T_1 and T_2 can be solved as:

$$\begin{bmatrix} T_1 \\ T_2 \end{bmatrix} = \begin{bmatrix} \frac{R_{y1}}{D_{y1}} - \frac{R_{y2}}{D_{y1}} \\ \frac{R_{p2}}{D_{y2}} \end{bmatrix} \quad 4.14$$

For a three jointed snake arm with six DOF and nine control tendons, the calculations to determine tendon tensions cannot be readily solved as this creates a system of linear equations with infinite solutions.

$$\begin{bmatrix} 0 & 0 & D_{x3} & 0 & 0 & D_{x6} & 0 & 0 & D_{x9} \\ 0 & 0 & D_{y3} & 0 & 0 & D_{y6} & 0 & 0 & D_{y9} \\ 0 & D_{x2} & D_{x3} & 0 & D_{x5} & D_{x6} & 0 & D_{x8} & D_{x9} \\ 0 & D_{y2} & D_{y3} & 0 & D_{y5} & D_{y6} & 0 & D_{y8} & D_{y9} \\ D_{x1} & D_{x2} & D_{x3} & D_{x4} & D_{x5} & D_{x6} & D_{x7} & D_{x8} & D_{x9} \\ D_{y1} & D_{y2} & D_{y3} & D_{y4} & D_{y5} & D_{y6} & D_{y7} & D_{y8} & D_{y9} \end{bmatrix} \begin{bmatrix} T_1 \\ T_2 \\ T_3 \\ T_4 \\ T_5 \\ T_6 \\ T_7 \\ T_8 \\ T_9 \end{bmatrix} = \begin{bmatrix} R_{y3} \\ R_{x3} \\ R_{y2} \\ R_{x2} \\ R_{y1} \\ R_{x1} \end{bmatrix} \quad 4.15$$

To assist in finding a solution to the above, the tendons with a negative D_y would not contribute any torque to overcoming the gravity acting on the snake arm and can be allocated pre-tension values depending on the snake arm design. This action results in a solvable matrix and the necessary equations for a theoretical tendon tensions.

$$\begin{bmatrix} 0 & 0 & D_{x3} & 0 & 0 & D_{x9} \\ 0 & 0 & D_{y3} & 0 & 0 & D_{y9} \\ 0 & D_{x2} & D_{x3} & 0 & D_{x8} & D_{x9} \\ 0 & D_{y2} & D_{y3} & 0 & D_{y8} & D_{y9} \\ D_{x1} & D_{x2} & D_{x3} & D_{x4} & D_{x8} & D_{x9} \\ D_{y1} & D_{y2} & D_{y3} & D_{y4} & D_{y8} & D_{y9} \end{bmatrix} \begin{bmatrix} T_1 \\ T_2 \\ T_3 \\ T_4 \\ T_8 \\ T_9 \end{bmatrix} = \begin{bmatrix} R_{y3} - T_6 D_{x6} \\ R_{x3} - T_6 D_{y6} \\ R_{y2} - T_5 D_{x5} - T_6 D_{x6} \\ R_{x2} - T_5 D_{y5} - T_6 D_{y6} \\ R_{y1} - T_5 D_{x5} - T_6 D_{x6} - T_7 D_{x7} \\ R_{x1} - T_5 D_{y5} - T_6 D_{y6} - T_7 D_{y7} \end{bmatrix} \quad 4.16$$

The tensions T_5 , T_6 and T_7 are the pre-tension values assigned, and a value of zero represents the tendon left slack.

4.5 Tension experiments

Designed for easy and fast modification, the test rig illustrated in Figure 4.11 uses one DOF joints with capacity for fifteen Dyneema tendons to be mounted at three different diameters for a variable value of D_y and D_x . Given three tendons to constrain each joint, the test rig is able to accommodate up to five joints for experimentation. The links are composed of 6mm aluminium or carbon fibre dowel attached to a rapid prototyped vertebra. The end vertebra contains a hook where additional payload weights can be attached. The test rig was assembled to examine the ability to accurately predict the tension of the tendons in multiple configurations.

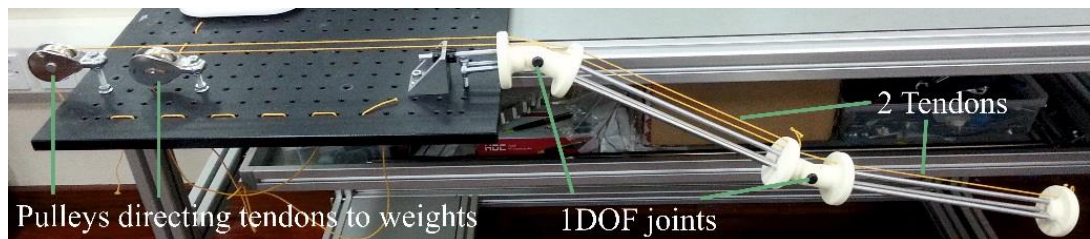


Figure 4.11 Double jointed variant of snake arm test rig.

The experimental method consisted of holding the arm at a horizontal cantilever position and attaching weights to each tendon in increments of 1kg, 0.5kg or 0.1kg. As the load on the tendon is assumed to equal the tension in the tendon, when the arm is released and maintains its position afterwards with no change to the joint angles, the weight is recorded and repeated for accuracy. If inadequate tension were supplied to the tendons, the arms would collapse and if too much tension were supplied, the arm would rise beyond the horizontal starting position. The recorded tensions are then taken and plotted against the theoretical tension values for further analysis. To alter the torque required at each joint to maintain its position, the payload is also incrementally increased and the experimental method repeated.

4.5.1 Joint variations

Equation (1) is used to calculate the tension of a single tendon with three different heights of D_y and five selections of payload weight. The experiment to test the equation uses a single joint configuration of the rig shown in Figure 4.11 with a length of 934mm and carbon fibre links.

The experimental results on Figure 4.13 display a strong correlation between the theoretical and experimental values; this implies (1) is suitable predicting the tendon tensions for simple single joint snake arms in the horizontal cantilever position.

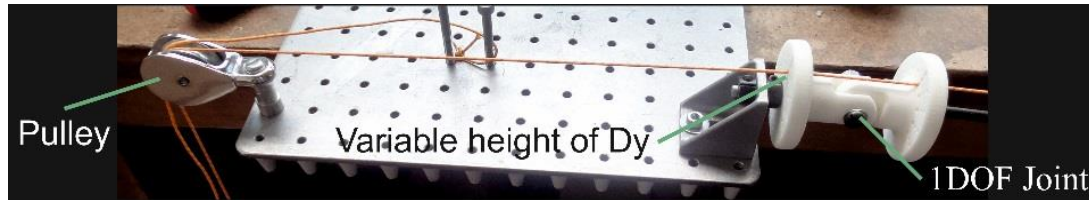


Figure 4.12 Single jointed variant of snake arm test rig.

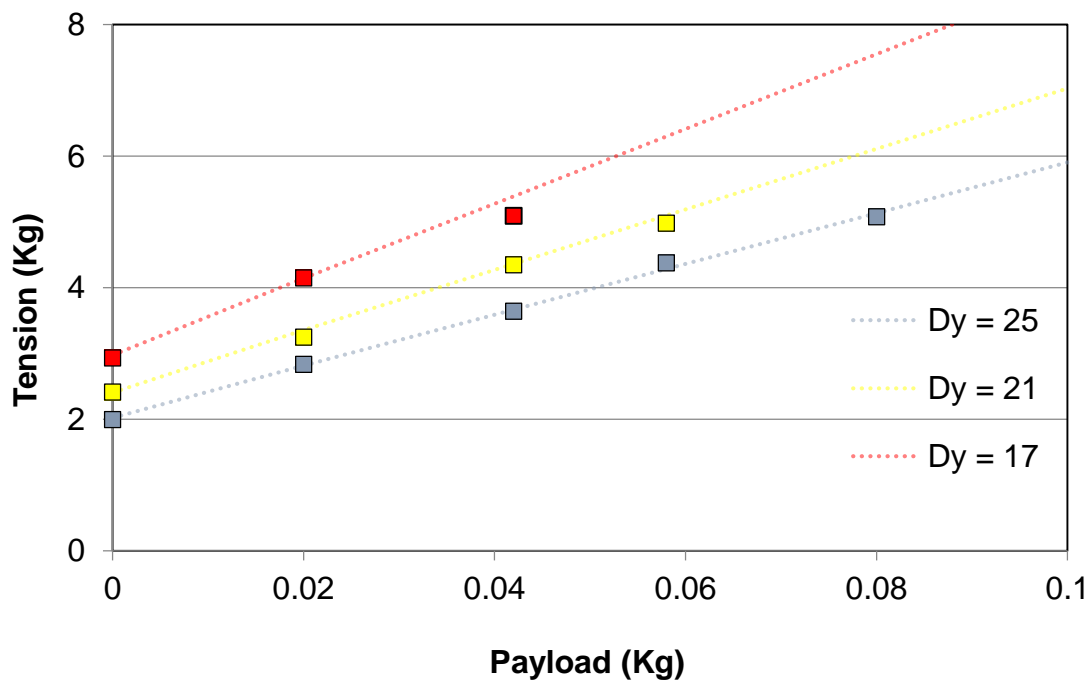


Figure 4.13 Comparison of the theoretical and experimental tendon tensions for a single joint snake arm controlled by a single tendon. The dotted lines represent the theoretical values for tendon tension for each value of D_y and the points represent the experimental data.

The interaction between two tendons and the distribution of tension between two joints was tested using the configuration shown in Figure 4.11. In this experiment, the link lengths and values of D_y for both tendons remained constant and only the payload was incremented. Four tests were completed for each payload weight and the full experimental results can be found in Appendix B.3. The results shown in Figure 4.14 and Figure 4.15 show a similar form between the theoretical equation (3) and the experimental results of T_1

and T2. Although the zero-shift in the results reveals a difference between the theoretical equations and the experimental results as a result of external influences not present in the theoretical calculations.

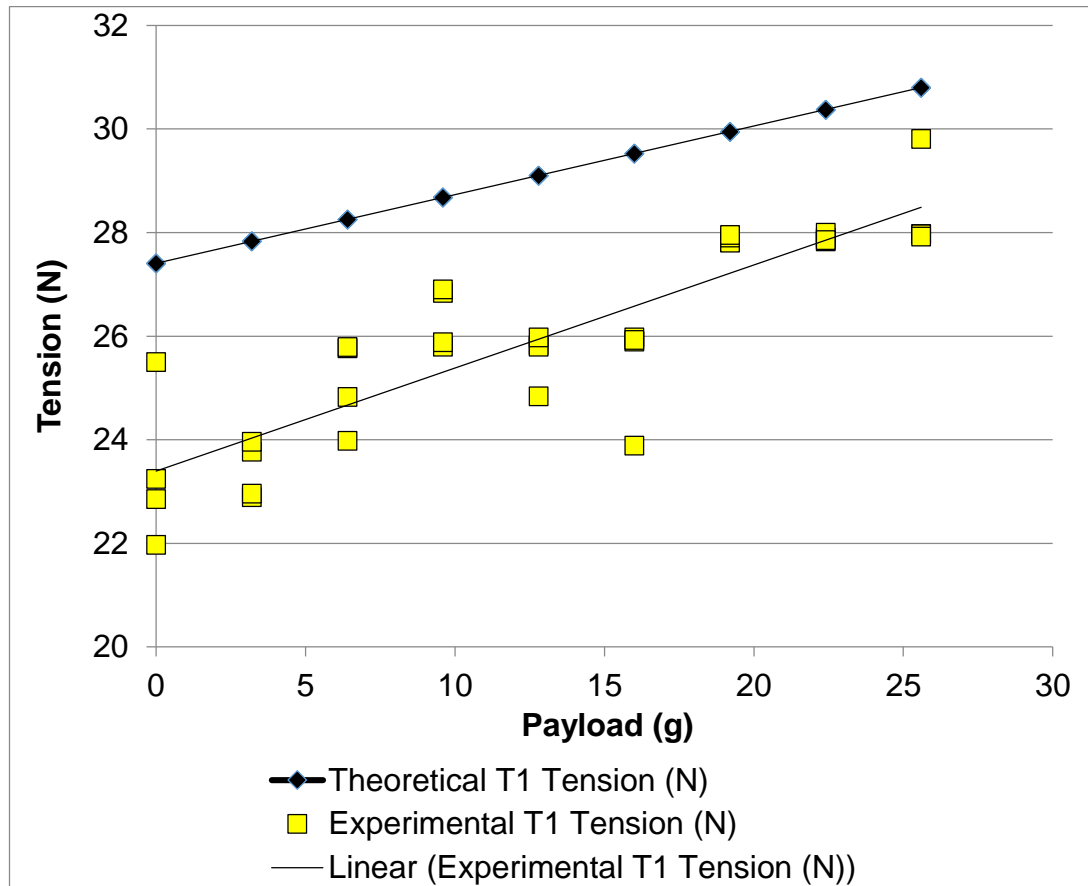


Figure 4.14 Comparison between a sample of theoretical and experimental tendon tensions for a double-jointed snake arm with two tendons. This graph compares the values for T1, the tendon constraining the first joint as shown in Figure 4.10.

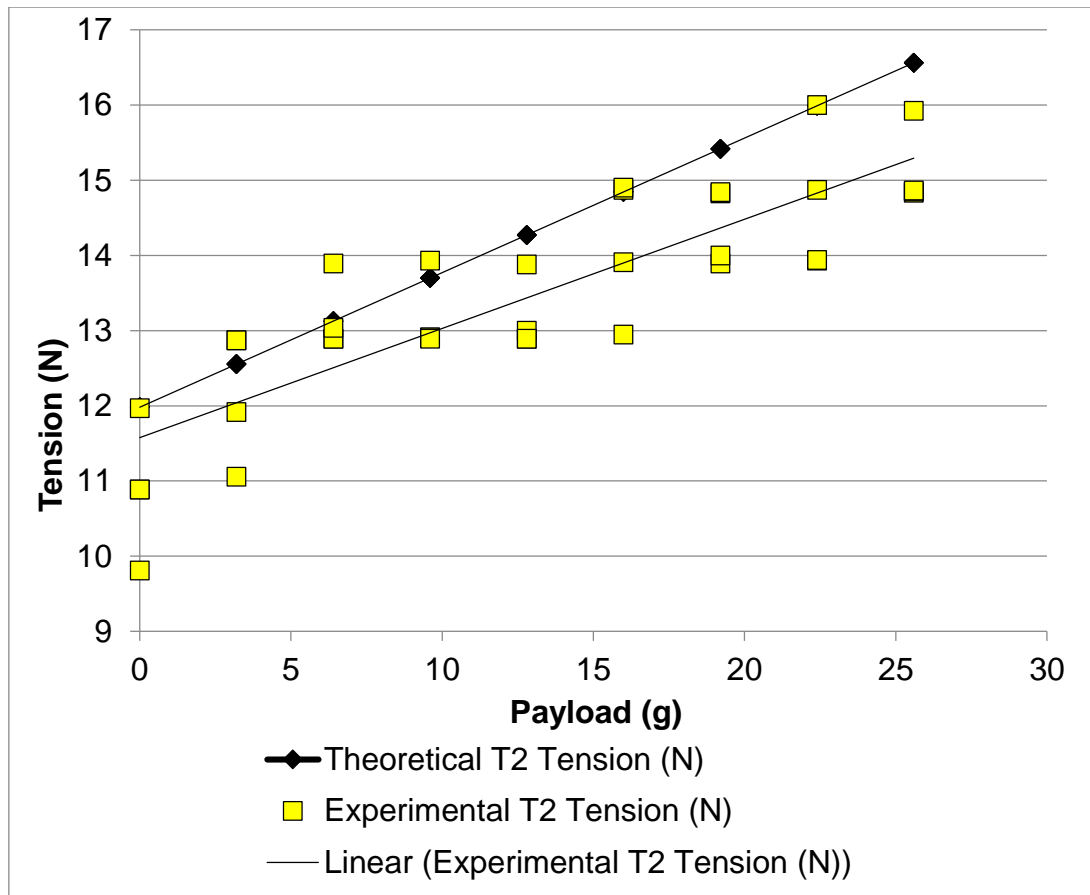


Figure 4.15 Comparison between a sample of theoretical and experimental tendon tensions for a double-jointed snake arm with two tendons. This graph compares the values for T2, the tendon constraining the second joint as shown in Figure 4.10.

4.5.2 Friction

Further investigation revealed this was the result of friction in the test rig between the tendon, vertebra and pulleys and the theoretical calculations that were assumed to have negligible friction in the system. To compensate for the error, the relationship between the load acting on the tendons and friction for the test rig was developed and implemented with the experimental values adjusted for the additional friction forces dependent on the load on the tendons.

The test rig was modified as illustrated in Figure 4.16 where force F is opposed with friction forces acting on the cable where it is in contact with the pulley and joint vertebrae. Rather than have the cables terminate at the usual joint, the cable was extended and attached to a linear stiffness spring, which is then anchored to an immovable platform.

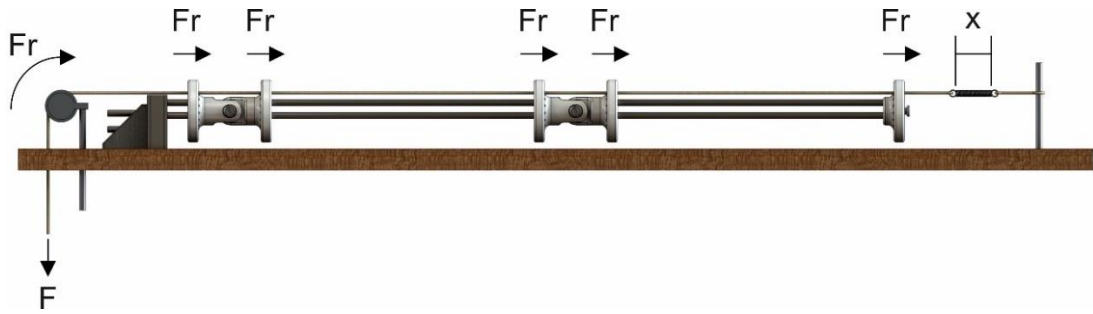


Figure 4.16 Friction test rig with illustrated forces and length.

Calculating the friction force per cable was done by careful measurement of the spring's length and known force acting on each cable. If there would be zero friction acting throughout the cable, it would be possible to find the calculated spring stiffness from Equation 4.17 to be equal to the actual spring stiffness, which is also found experimentally.

$$F = kx$$

4.17

Where,

F = Normal force acting on spring

k = Spring stiffness

x = spring length

With the introduction of friction into the system, a change will be found in the recalculated spring stiffness and the difference between the actual spring stiffness and new spring stiffness will allow the friction force to be calculated.

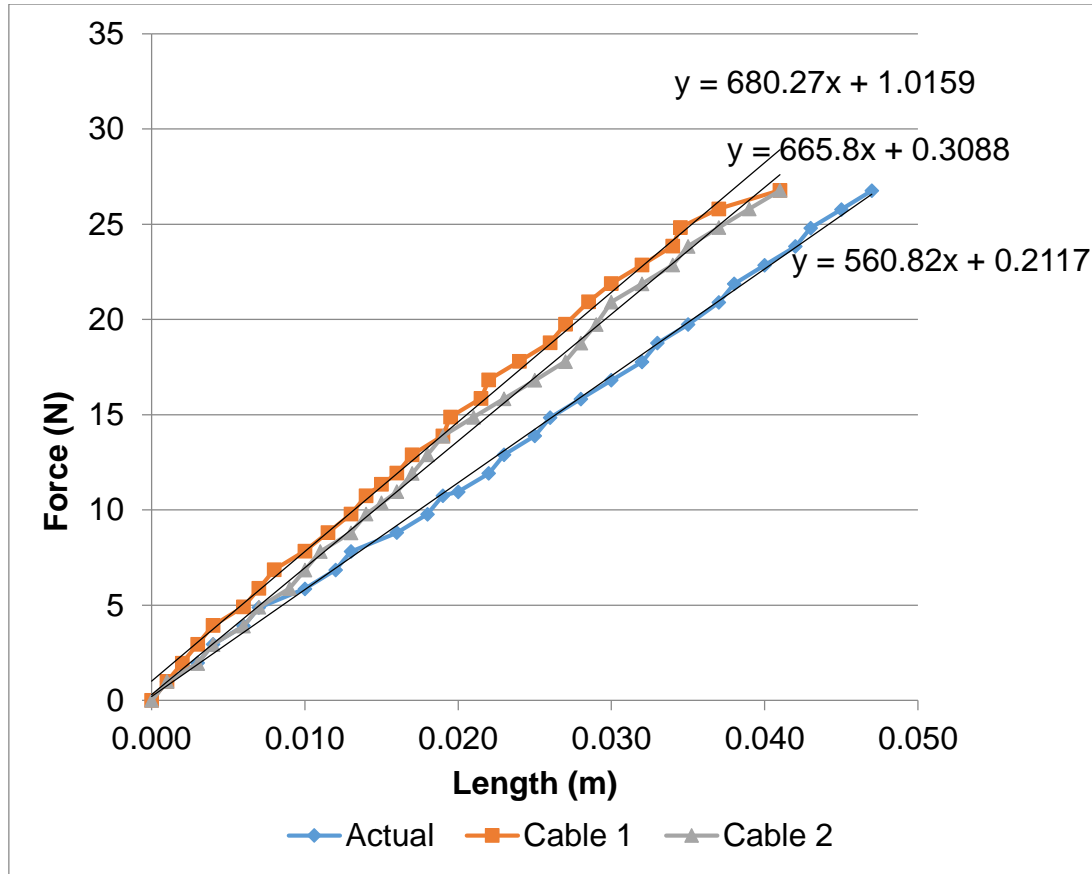


Figure 4.17 Experimental results from friction test.

The results on Figure 4.17 show the length the of spring (x) in response to the load acting on the cable (F) and displays a clear difference on the levels of friction acting on each cable. For cable 2, the larger gradient correctly indicates the presence of larger friction forces as expected due to the increase in surface contact with respect to cable 1.

Modifying equation to include friction provides the following equation:

$$F - Fr = kx \quad 4.18$$

Where,

F = Normal force acting on spring

Fr = Friction

k = Spring stiffness

x = spring length

Rearranging for friction,

$$Fr = F - kx \quad 4.19$$

As the actual spring stiffness was experimentally determined to be 560.82 N/m from the gradient from Figure 4.17, equation 4.19 can then be applied to find the relationship between the force applied and the friction.

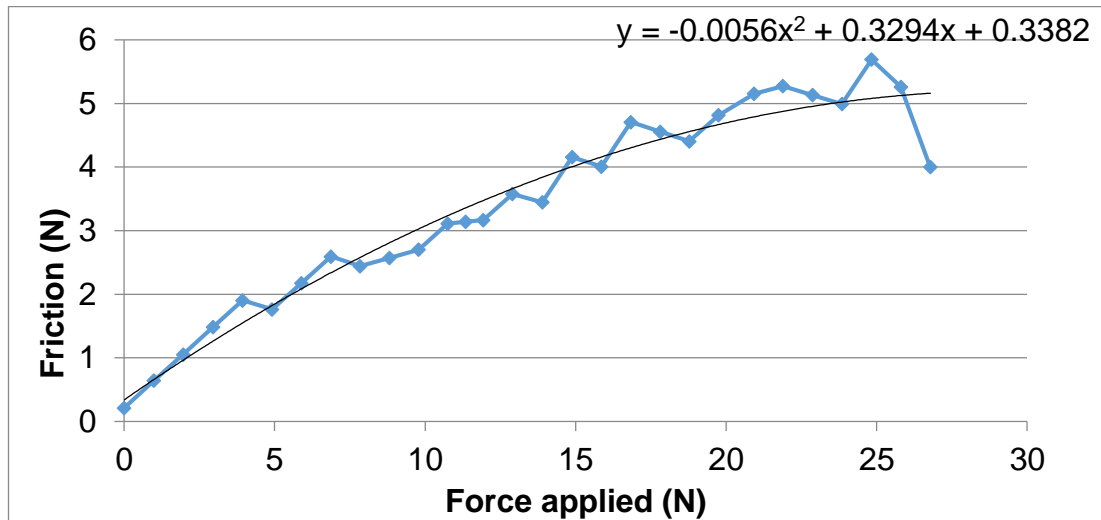


Figure 4.18 Force applied against friction for cable 1.

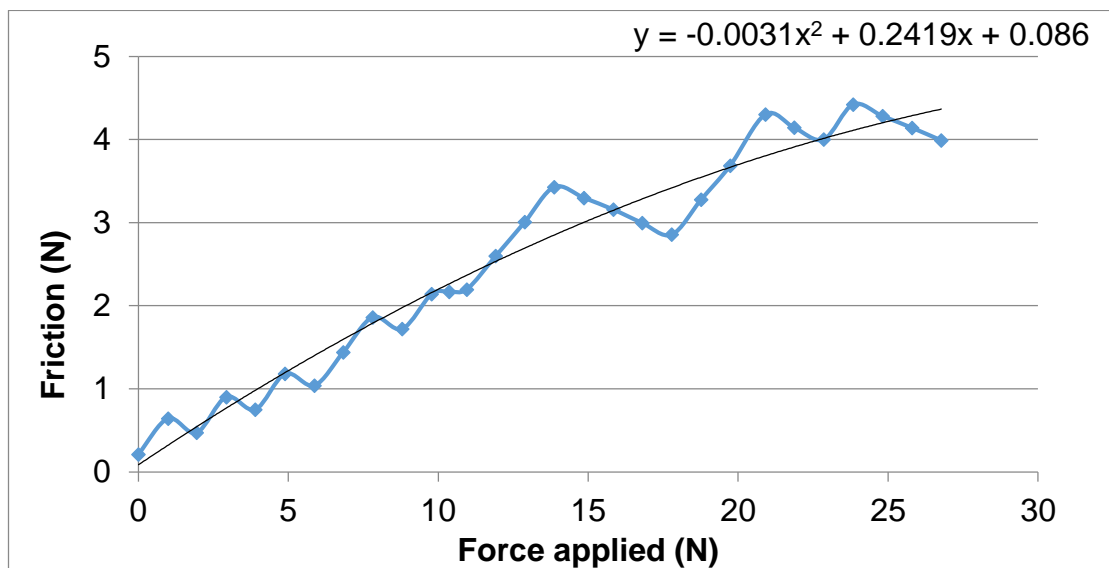


Figure 4.19 Force applied against friction for cable 2.

An equation is derived from Figure 4.18 and Figure 4.19 representing the relationship between the tension acting through the cable and the friction encountered. It can be seen the friction acting on each cable is non-linear and will eventually plateau. Since the friction test is a measure of static friction on the cables these results are expected as once the static friction forces peak the cables will be under kinetic friction and must be moving.

Cable 1: $Fr = -0.0056F^2 + 0.3294F + 0.3382$ 4.20

Cable 2: $Fr = -0.0031F^2 + 0.2419F + 0.086$ 4.21

For each case in the original experiment the tension (F) is already known, substituting each value into equations and the unique friction force is calculated. Therefore, we can correct each experimental value by compensating for friction for a clearer comparison to the theoretical values by using:

$$F_{new} = F_{exp} + Fr$$
 4.22

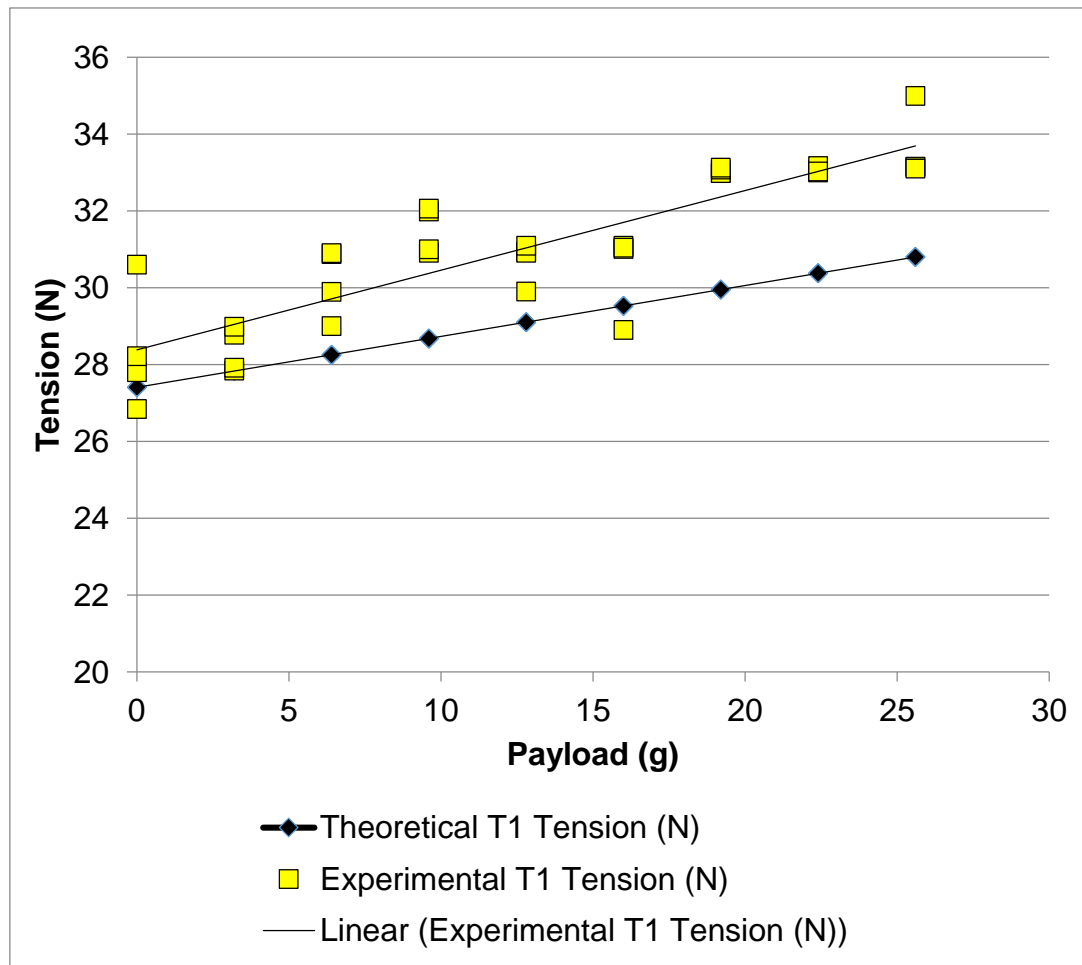


Figure 4.20 Comparison between a sample of theoretical and corrected experimental tendon tensions for a double-jointed snake arm with two tendons. This graph compares the values for T1, the tendon constraining the first joint as shown in Figure 4.9.

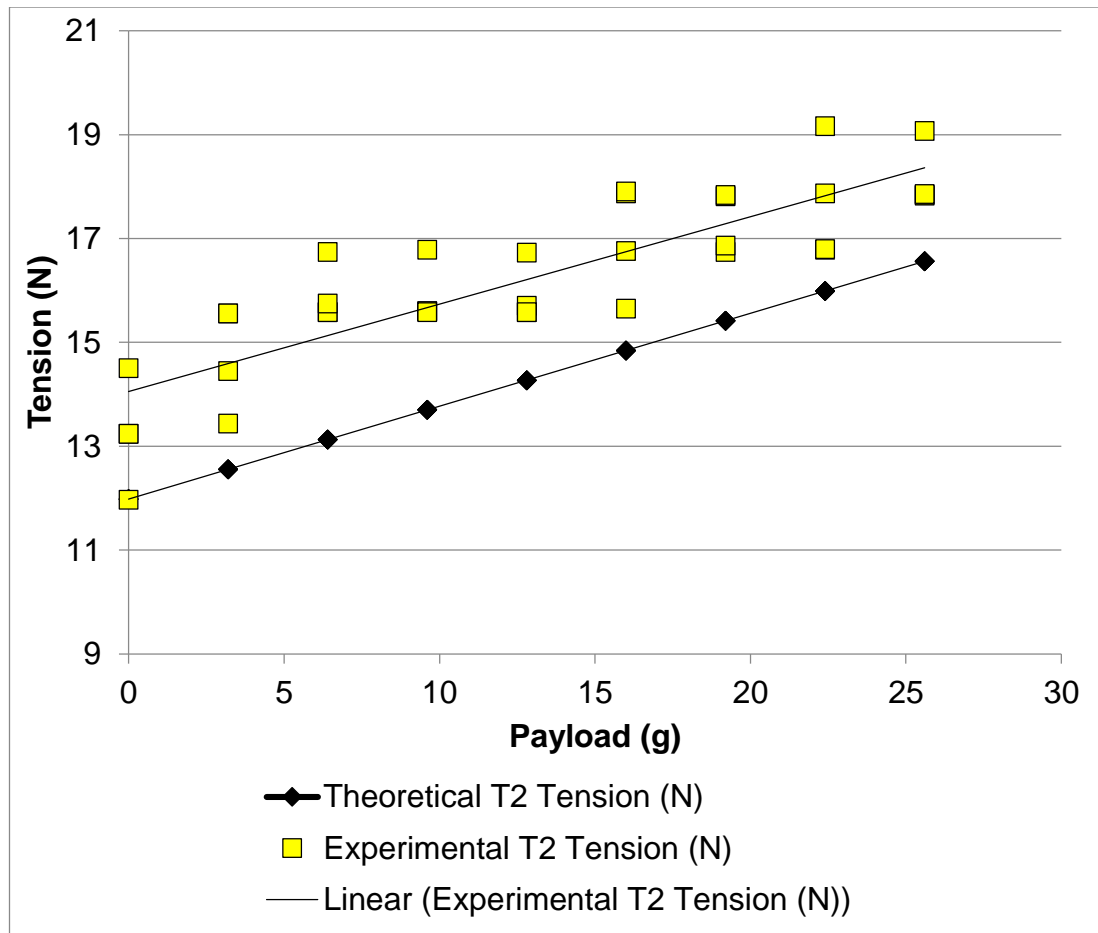


Figure 4.21 Comparison between a sample of theoretical and corrected experimental tendon tensions for a double-jointed snake arm with two tendons. This graph compares the values for T2, the tendon constraining the first joint as shown in Figure 4.9.

Accounting for friction for the experimental results as illustrated in Figure 4.20 and Figure 4.21, the differences between the theoretical and experimental results have been reduced. The amount the experimental values can be adjusted for static friction is dependent on the experimentally calculated value of spring stiffness (k), if the stiffness value was recorded larger the resulting static friction will be assumed larger due to Equation 4.18 and therefore further affecting the unique friction force acting on each cable as the payload changes.

The remaining discrepancy between the theoretical and experimental results is assumed the result of the imperfect joint angles during the experiments as the snake arm is manually held in the horizontal cantilever position. Slight deviations to the joint angle affects the horizontal distance and torque

requirements. Likewise, the friction tests also assumes the snake arm is held at the exact same joint angles throughout original experiment, however any small deviations in the joint angle will affect the friction force between the cable and test rig.

4.6 Discussion and conclusion

Predicting the magnitude of the forces acting through a snake arm is important for preventing the failure of structural components. The arrangement of links and joints forming the snake arm can be tabulated using the Denavit-Hartenberg notation. The DH parameters can then be used with the RNE formulations to calculate the torque requirements at each joint axis. Torque at each joint is produced using actuation cables running from each joint to a base platform located at the root of the arm where the length of each cable can be controlled, pulled taught and relaxed.

Assuming gravity is the only external force acting on the snake arm, holding an unsupported arm in the horizontal cantilever position generates the largest torque requirements. Accordingly, in this position, the actuation cable tensions and the resulting axial compressive forces is also at its peak.

Knowing the torque requirements and the layout and position of each actuation cable enables the tension of each cable to be generated. To safeguard the snake arm links against the cable tensions and axial compressive forces, the behaviour of the thin walled cylinders under axial compression was studied and incorporated using ESDU resources.

Therefore, the prevention of all component failures begin from the cable tension calculations. Experiments were conducted to examine the accuracy of those cable tension predictions using two test rigs. The results of a single joint and single cable experiment revealed the theoretical and experimental values were close almost identical. However, the addition of another joint and cable created some complications in the experiment. An offset between the theoretical and experimental values revealed additional forces needed to be considered. The presence of friction was measured in the test rig leading to a method of incorporating frictional forces into the experimental data, resulting in a closer approximation.

It was not possible, however, to predict the cable tensions as accurately as in the case for a single joint and single cable without redesigning the test rig for better control of the joint angles, without which would affect the tensions and the torques at each joint and create discrepancy with the ideal theoretical values.

Chapter 5

Mechanical design of snake arm prototype

This chapter develops an algorithmic approach to the design and fabrication of snake arms to optimise the maximum length. To this end, failure points are analysed using finite element analysis software and algorithmic buckling theory is implemented. Specific experimental designs are developed at a 12mm diameter scale in line with the primary scope of the research.

5.1 Introduction

The rigid snake arm, at its most basic form, is just a series of links and joints. If each joint length were the same, the only method of altering the length of the snake arm would be through the length of the links or increasing the number of links. However, cable tension theory (Section 4.4) demonstrated that cable tension dramatically increases with the length of the snake arm. Therefore, it is important to analyse the forces and failure modes of the links and cables to maximise the length.

5.2 Prototype design

Section 3.5 developed the fundamental specifications for a snake arm in this research:

- 12mm diameter for portable borehole deployment.
- Long reach to perform a visual exploration.
- Must be self-supporting in the horizontal cantilever position.

The construction of a discrete snake arm relies on a series of joints and rigid links as shown in Figure 5.1.

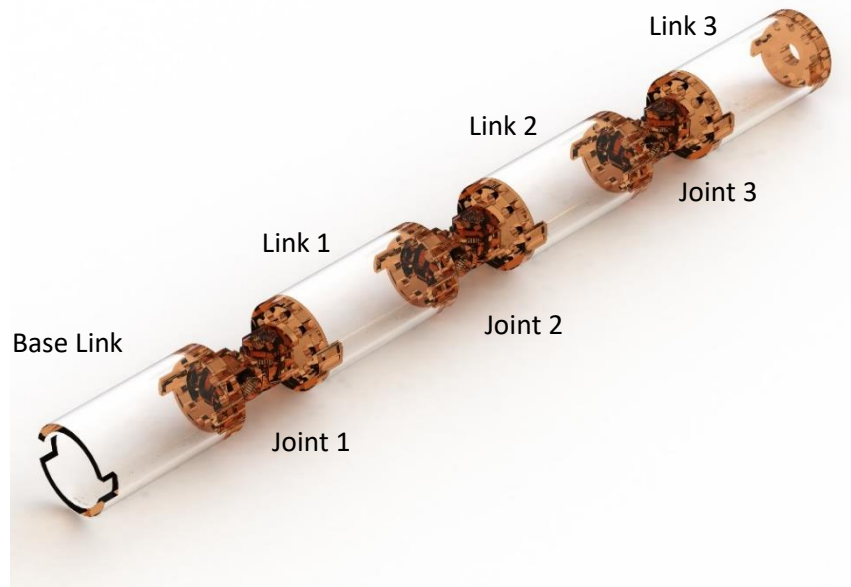


Figure 5.1 Snake arm links and joints.

As established in Section 4.1 with Morecki, A., et al. stating a manipulator with n -DOF requires at least $n+1$ tendons to achieve complete control of all degrees of freedom [109]. The limit of nine, 1.5mm diameter cables, results in a snake arm that has just three 2-DOF joints and four links of unknown length. The sum of the tension running through the actuation cables will exhibit an axial compressive force throughout the entire structure of the snake arm.

An axial compressive force of sufficient magnitude could result in failure of components on the snake arm, including:

- The actuation cable could fail due to exceeding its yield limit.
- Joints at the connection of links could fail due to either the shear of the pins that hold the joint to the link or plastic deformation of material.
- The links could fail due to the three buckling modes.

Each of the proposed failure modes is to be investigated separately.

5.3 Joint design

Joints join links together and enable them to be constrained longitudinally whilst allowing relative rotation through actuation. Therefore, the joint is a highly critical component of the snake arm that provides a range of movement and also anchors termination cables so that forces can be applied to the end

of links for actuation. Ordinary 2-DOF joints can be readily purchased (Figure 5.2). Universal joints are designed to transmit torque between two shafts while the angle between the shafts varies.

If a universal joint is to be used to join links to create a snake arm, outer diameter is required to be as small as possible to allow room for cables whilst keeping the diameter small. For example, to conform to the specifications for an outer diameter of 12mm, a universal joint is limited to a maximum outer diameter of just 7mm (diameter remaining after accommodating for link wall thickness and cable thickness). Commercial universal joints have both axis of rotations intersecting at a mid-point as illustrated in Figure 5.2 that results in joint with smaller diameter pins and smaller arms. This, therefore, reduces the maximum axial force and torque that can be exerted on the joint.

There are three joint specific failure modes in this scenario, these are:

- Shearing, where the pins at the pivot shear and break.
- Axial compression, where the joint undergoes plastic deformation.
- Torque twisting, where the joint twists and plastically deforms.

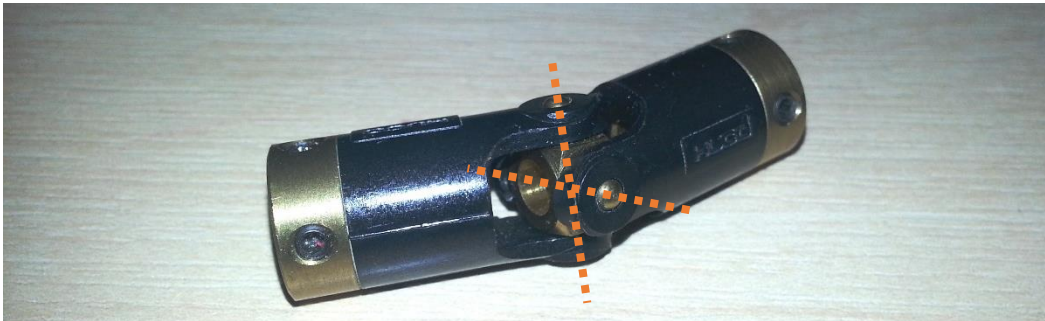


Figure 5.2 A 2-DOF universal joint with collinear axis of rotation.

5.3.1 Shear forces

Shearing failure of the joints (Figure 5.4) can occur at the arms or the pins of the joint (as illustrated in Figure 5.5) and is calculated as:

$$\tau = \frac{F}{A} \quad 5.1$$

Failure occurs when:

$$\tau = 0.58 \cdot TS \quad 5.2$$

Where:

τ = Shear stress

F = Force

A = Cross-sectional area of material with area perpendicular to the applied force vector

TS = Tensile strength

The value of 0.58 is the result of the Von Mises yield criterion [113] and is an approximation for the relationship between the Tensile Yield Strength and Shear yield point for wrought steel and alloy steel.

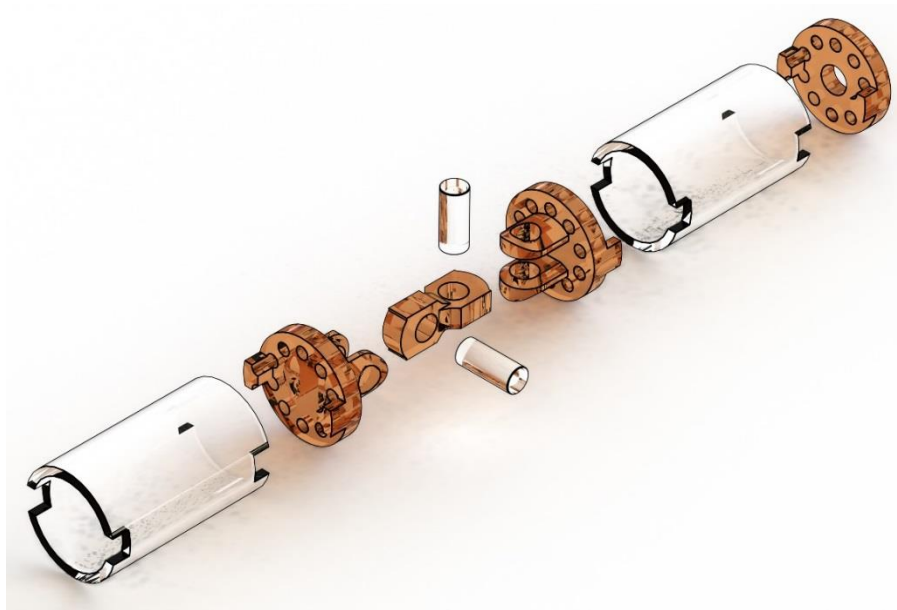


Figure 5.3 Exploded view of a single joint assembly.



Figure 5.4 Manufactured joint.

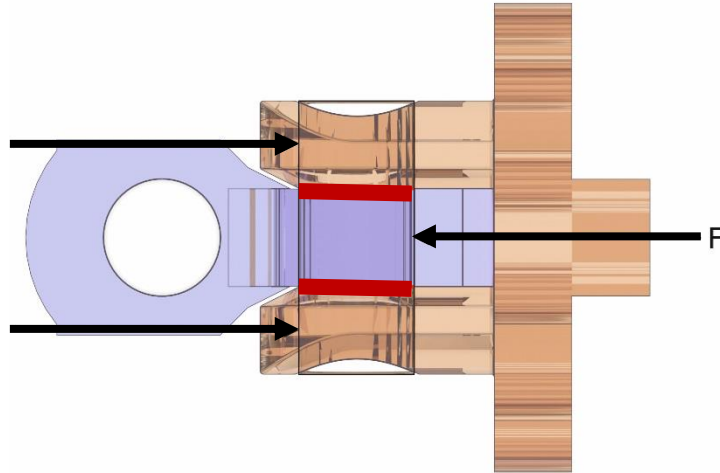


Figure 5.5 Shearing of the joint pin occurs at two locations (in red).

The proposed joints in Figure 5.3 uses stainless steel with the following specifications:

Table 5.1 Steel grade 303S31 specification for the joint pin.

Grade		303	Stainless steel
Diameter	D	mm	3
Young's Modulus	E	GPa	193
Tensile Strength	TS	N/mm ²	517.1067
Yield Strength	YS	N/mm ²	206.8427

The force required to shear the pin can be approximated through the diameter of the pin and the material tensile yield strength.

$$F = \tau A = 0.58 \cdot TS \cdot 2 \cdot \pi \cdot \left(\frac{D}{2}\right)^2 \quad 5.3$$

$$F = 0.58 \cdot 206.843 \cdot 2 \cdot \pi \cdot \left(\frac{3}{2}\right)^2 \quad 5.4$$

$$F = 4240 \text{ N} \quad 5.5$$

Figure 5.5 shows shearing of the pin at two locations and was reflected in the previous calculations as double the area resisting the shear force. The approximated value of 4240N represents the maximum combined shear force from the sum of the cable tensions.

5.3.2 Finite Element Analysis of joint assembly

Finite element analysis (FEA) was used to evaluate the joint as a non-destructive testing method, unlike the shear force calculations in Chapter 5.3.1 the structure of the joint can fail wherever stress concentrations form. The location of the stress concentrations can be found during the FEA process that allows preventative measures to be implemented in the joint design before manufacture takes place. This includes elements of adding fillets to sharp edges or increasing the material thicknesses at some parts.

SolidWorks software was used to perform the FE analysis with a model of the 2DOF joint (Figure 5.6) under applied axial forces. Given the joint will fail when the stresses exceed the material yield strength (Figure 5.7) the maximum stress for each simulation was recorded and plotted in order to find the load value where joint failure starts to occur (Figure 5.8).

Table 5.2 Stainless Steel material for joint used for FEA simulations.

Young's Modulus	E	GPa	210
Tensile Strength	TS	N/mm ²	723.83
Yield Strength	YS	N/mm ²	620.42

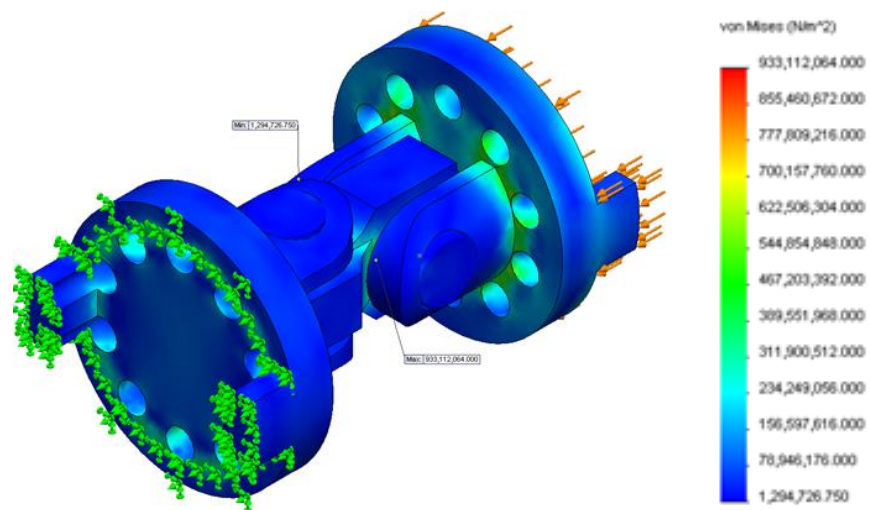


Figure 5.6 Iteration of 2DOF snake arm joint undergoing a FEA simulation.

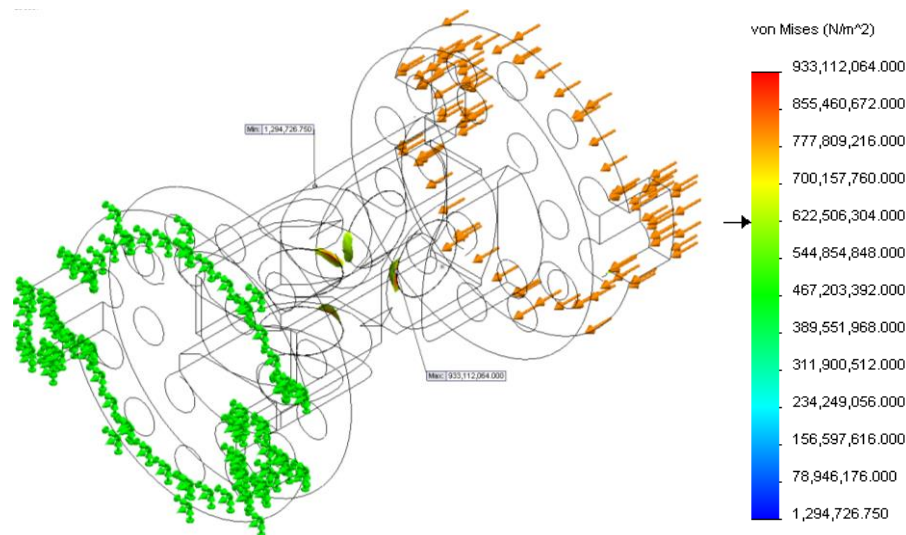


Figure 5.7 Iteration of 2DOF snake arm joint, FEA results can reveal the site for highest stress points. The above shows where the local stresses exceed the material yield stress.

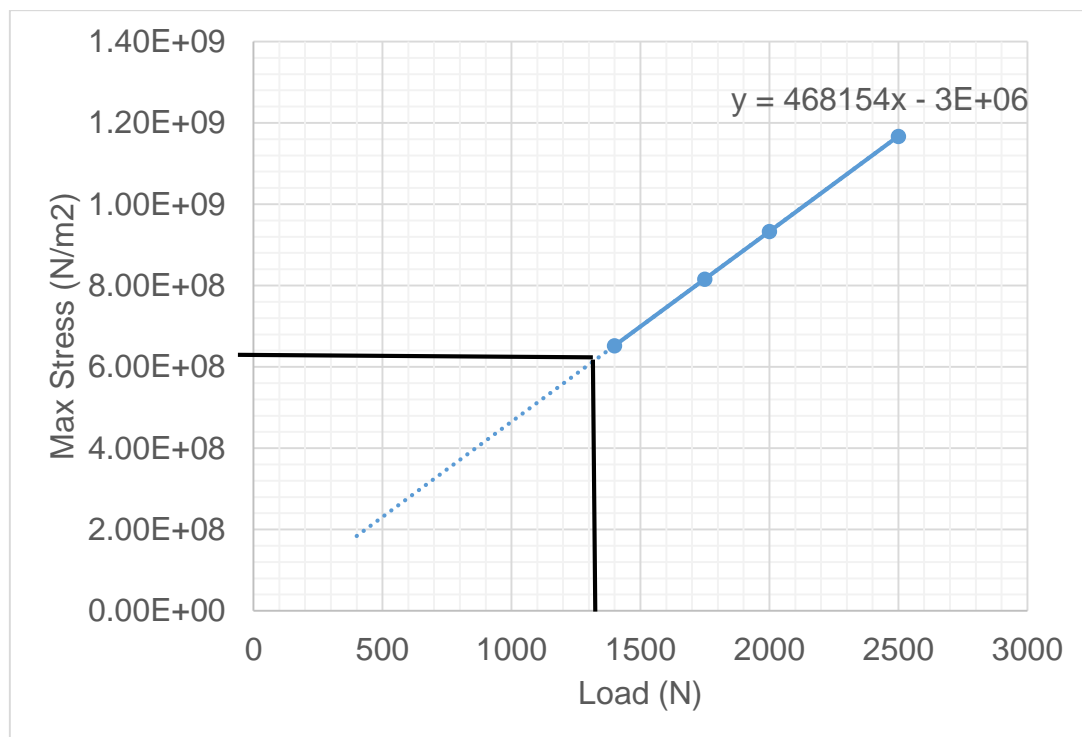


Figure 5.8 Results of multiple FEA simulations, linear trend reveals an axial load of approximately 1350N to be the absolute maximum the 2DOF joint should be subjected too.

As the axial compressive force remains unknown until the length of the snake-arm is established, the approach used for this FE analysis is similar to the pin shear and the maximum limit was to be methodically found. Plotting the results

of load versus maximum stress from multiple FEA simulations (Figure 5.8), the load value the joint can withstand before reaching its material yield stress was extrapolated to be in the region of 1332N.

Alongside compression, the joint must also sustain torque twisting from lateral joint angles. Repeating the methodology used for analysing joint compression, multiple simulations of the FE analysis was conducted with increasing increments of torque. The changing maximum von Mises stress was recorded and once interpolated; it revealed a limit to the maximum torque for the joint as 1.8Nm.

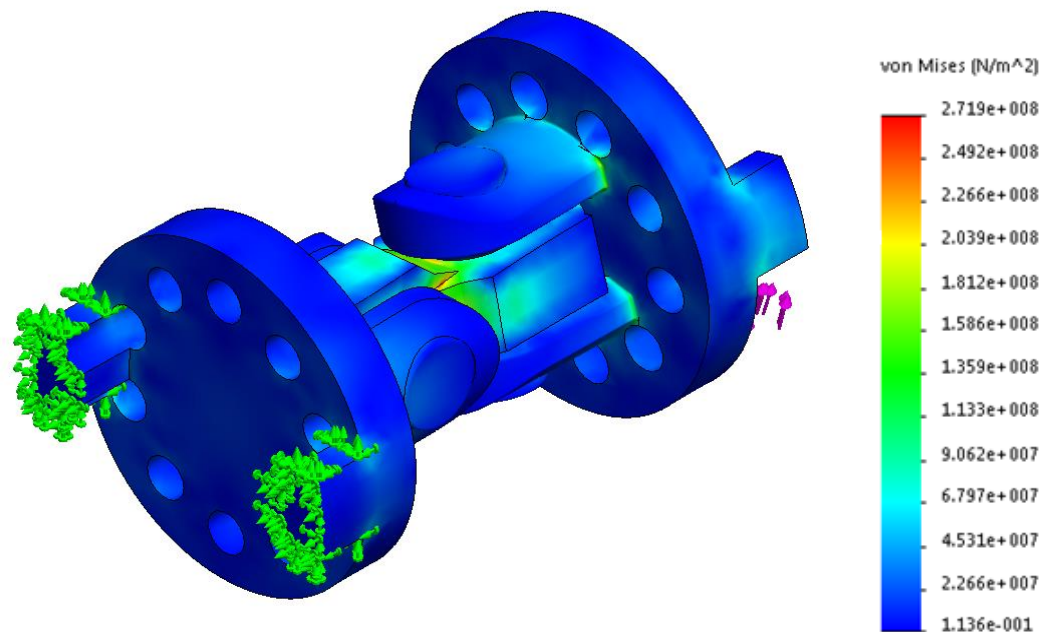


Figure 5.9 FEA simulation with 0.8Nm torque axial torque applied to joint.

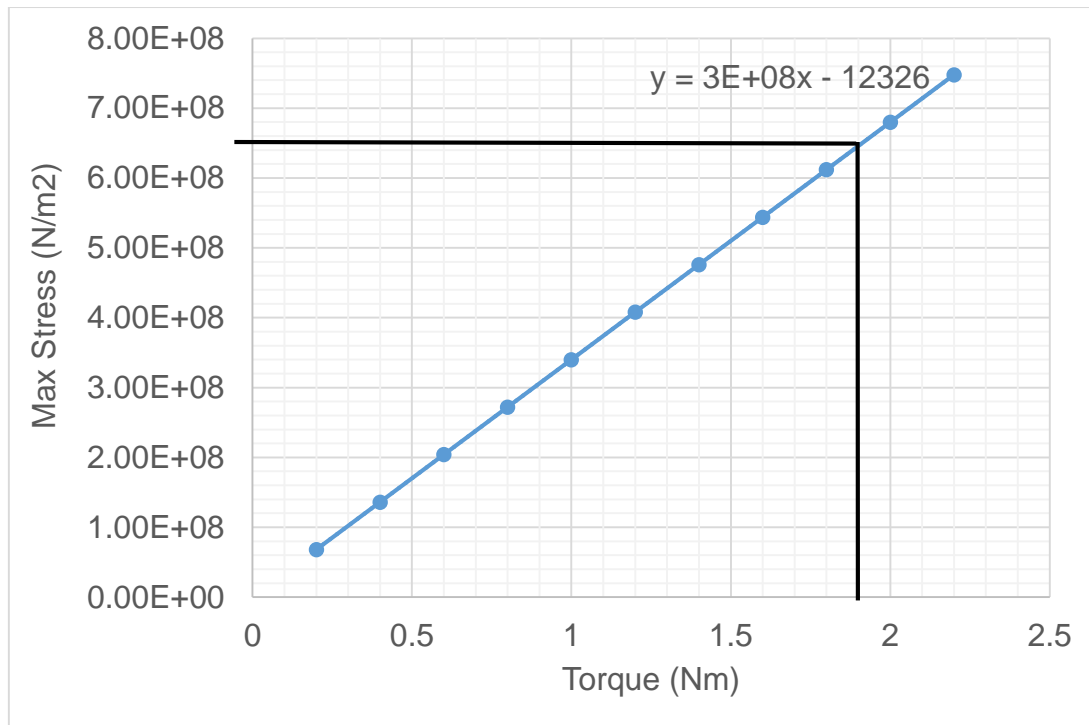


Figure 5.10 FEA simulation plot.

5.4 Cable properties

Cables are collectively responsible for maintaining the position or the movement of each joint. A cable of high yield strength will enable the creation of a snake arm with long length. Other important cable characteristics are the weight per unit length, stretch, stiffness and physical characteristics such as effective termination (attachment of a cable end to a structure).

UHMwPE (Ultra High Molecular weight Polyethylene) fibres are an attractive option for high tension cables. The properties of these fibres can be compared to steel as [2]:

- Weight for weight, the fibres are 15 times stronger than steel wire.
- Size for size, the fibre cables are 8 times lighter.
- The fibre cables are hydrophobic and do not absorb water.
- The fibre cables are chemically inert and perform in dry, wet, salty and humid environments.

Two samples of 1.5mm diameter cable from separate suppliers (<http://www.backpackinglight.co.uk/> (BPL) and Marlow) were tested on tensile testing machinery to determine the breaking loads (Figure 5.11). The

experiment was designed to subject each of the seven specimens to an increasing load through movement of 8mm/s until failure (speed from the linear actuator at Table 5.6). Each specimen was attached to the testing rig using the figure-eight loop knot, a very important prime knot used in sailing and rock climbing (Figure 5.12). Tested to destruction the recorded load and extension of the seven specimens is then plotted as shown in Figure 5.15 and Figure 5.16.

Table 5.3 Supplier stated average break loads.

Name	Average Breaking Load (N)
BPL Dyneema 1.5mm Diameter	1078.732
Marlow Excel Racing 1.5mm Diameter	1363.124

Given the cross-sectional diameter of each specimen is 1.5mm and the original lengths are known, the stress, strain and Young's Modulus can then be calculated using:

$$\sigma = \frac{F}{A} \quad 5.6$$

$$\varepsilon = \frac{\Delta L}{L_o} \quad 5.7$$

$$E = \frac{\sigma}{\varepsilon} \quad 5.8$$

Where:

σ = Stress

ε = Strain

F = Force

A = Cross sectional Area

ΔL = Change in length

L_o = Original length

The average breaking load for the BPL Dyneema rope in Figure 5.15 is 475N and the Marlow rope in Figure 5.16 is 490N. The average strain at the breaking load for the BPL Dyneema rope in Figure 5.15 is 0.146 and the Marlow rope in Figure 5.16 is 0.127. Therefore, the Marlow rope makes the better

candidate for the snake arm construction due to a greater breaking load and lower strain.

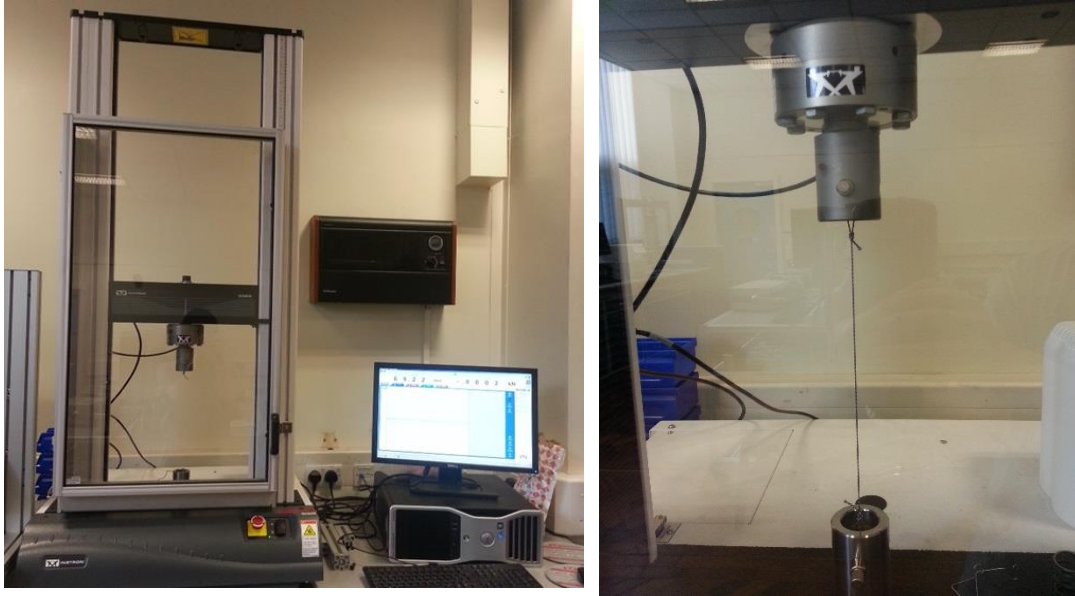


Figure 5.11 Tensile testing machine.



Figure 5.12 Figure-eight loop knot.

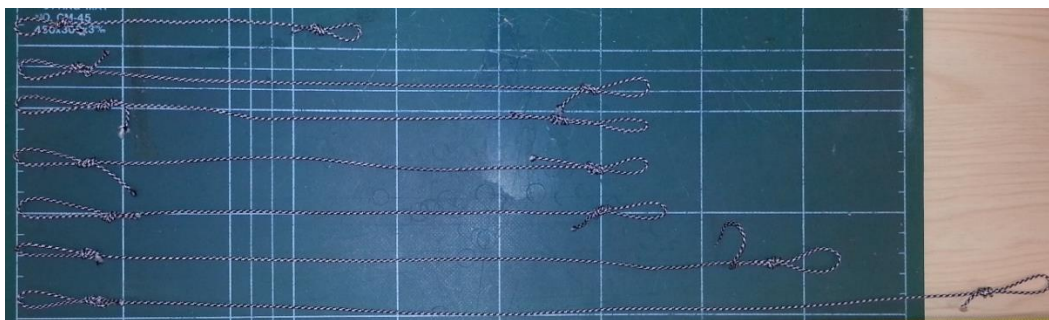


Figure 5.13 Seven specimens before testing.

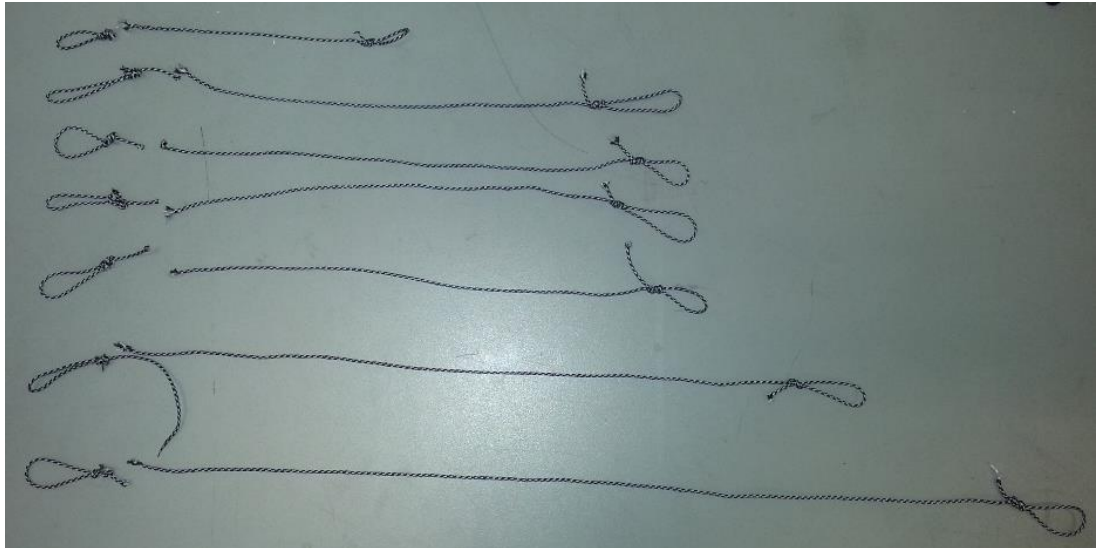


Figure 5.14 Seven specimens after testing.

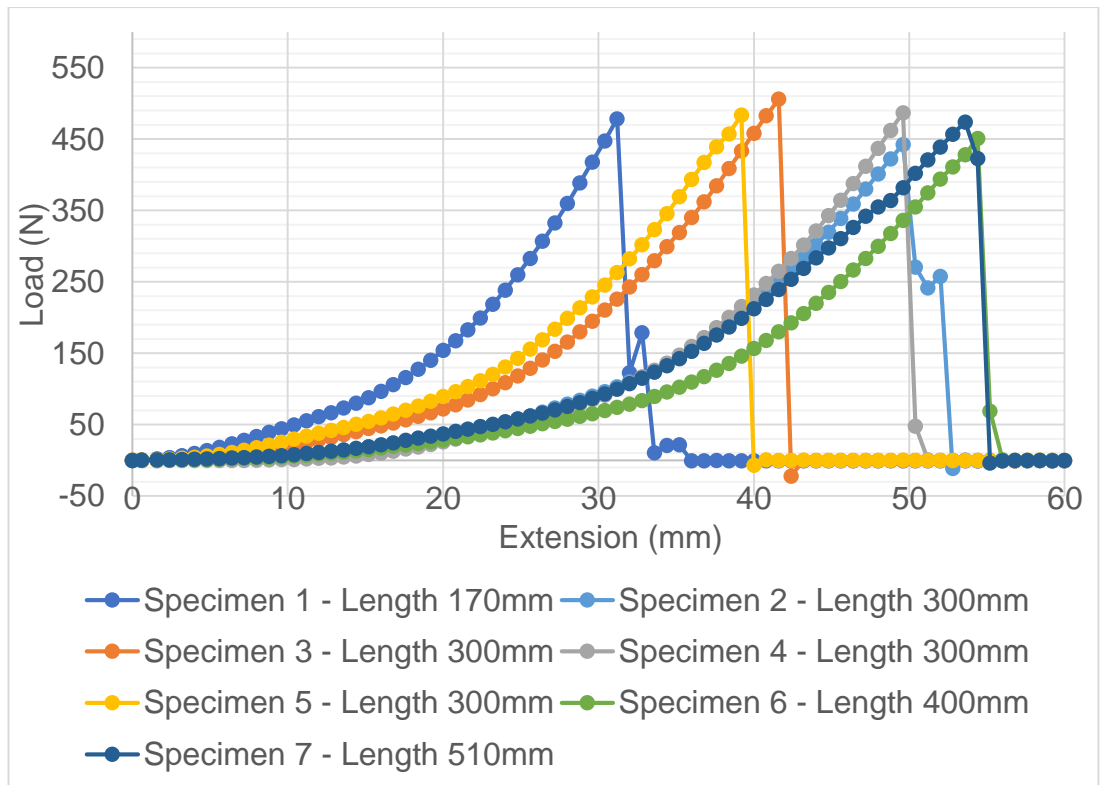


Figure 5.15 BPL 1.5mm diameter Dyneema rope.

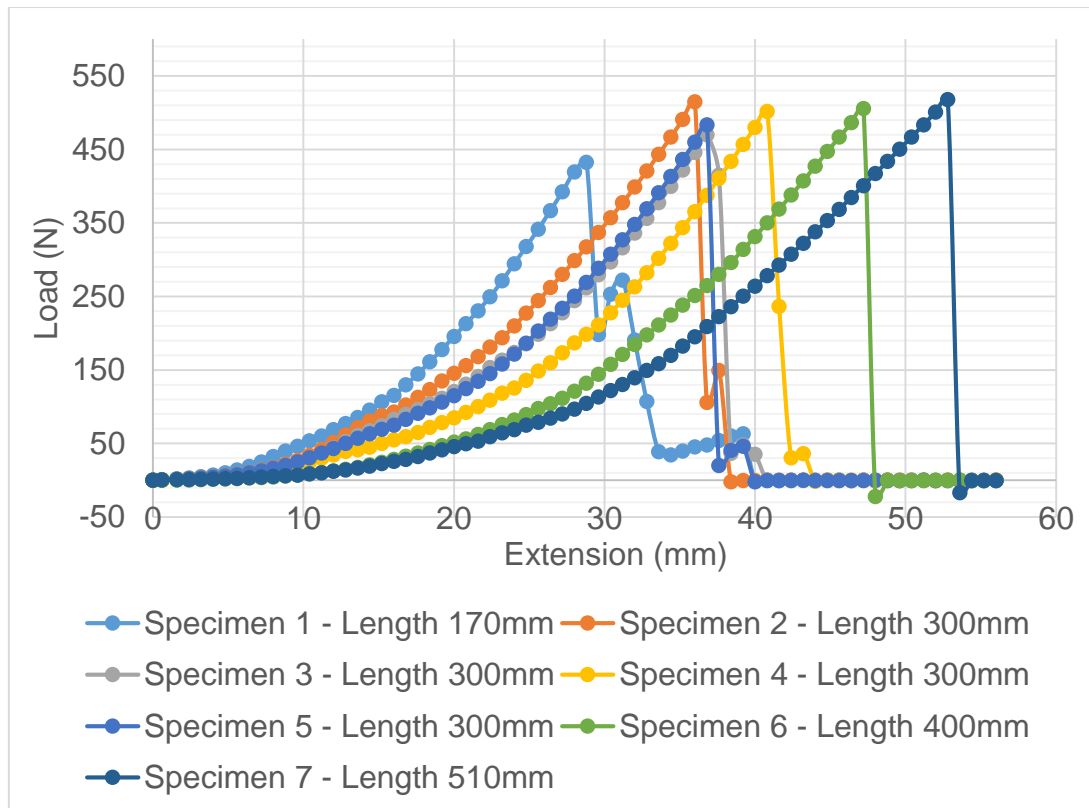


Figure 5.16 Marlow Excel Racing Dyneema rope with SK75 core and 16 plait polyester cover.

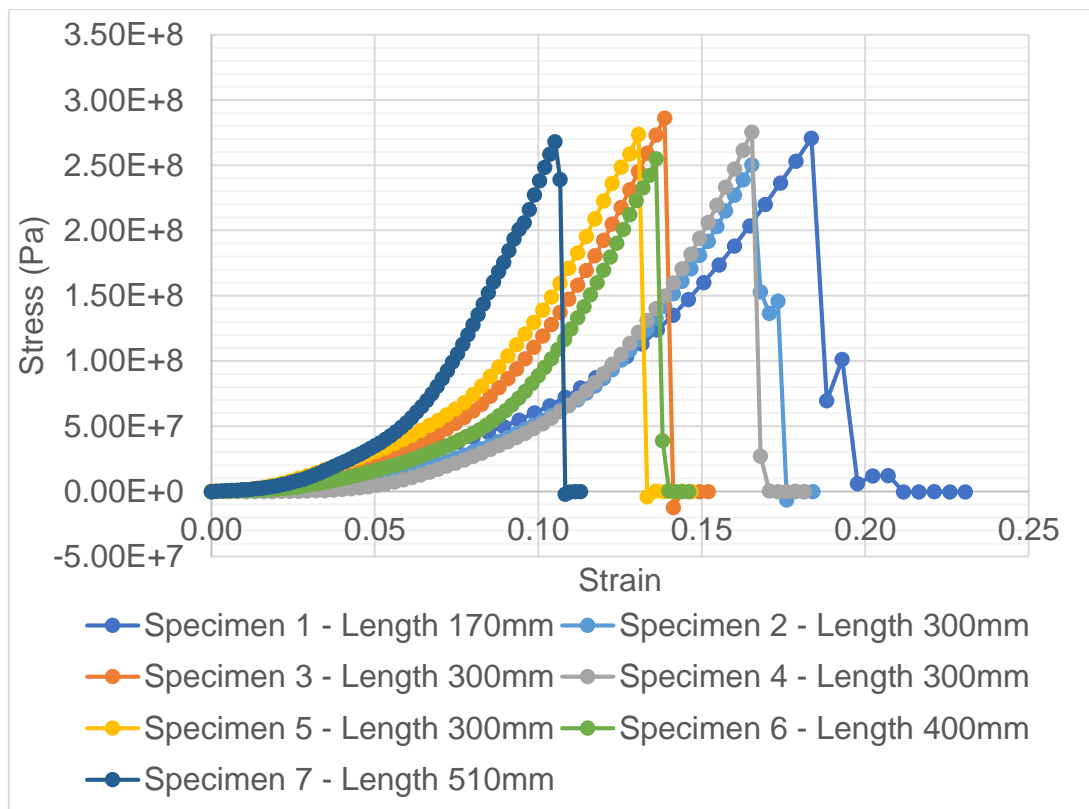


Figure 5.17 BPL 1.5mm diameter Dyneema rope.

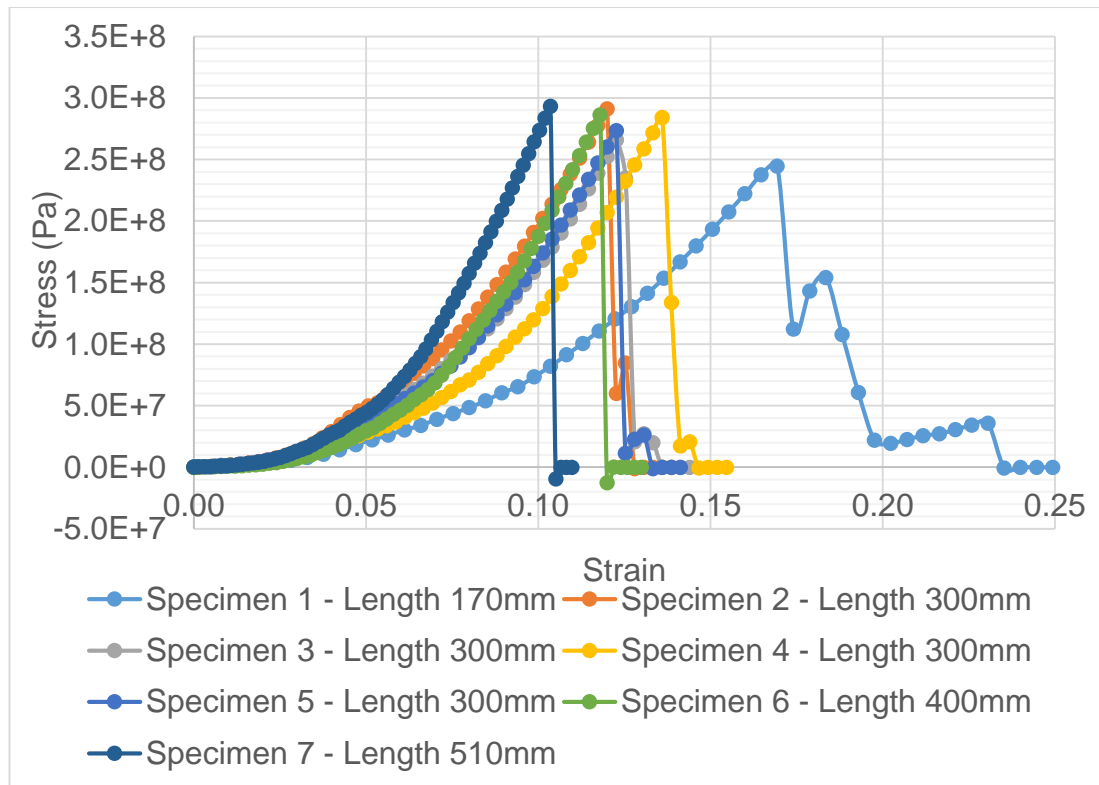


Figure 5.18 Marlow Excel Racing Dyneema rope with SK75 core and 16 plait polyester cover.

Comparing the breaking loads to the supplier's listed values, a decrease of 44% was noted for the BPL Dyneema rope and 36% for the Marlow Excel Racing rope. These results are consistent with the findings of Adam Long et al [114] in their investigation into the effect of ten different knots against the manufacturers stated strength for ropes of nominal 10.5mm diameter at lengths of 200mm. The test consisted of extending the ropes at a rate of 500mm/minute to destruction and recording the maximum force sustained. The presented results show there is little variation of strength with respect to the knot used. Whilst in some cases one knot displayed greater strength over another, the large variance between individual tests results demonstrates that one knot cannot be guaranteed to be stronger than the other. Overall no knot reduced the strength to <55% of its absolute strength. Indeed, the figure-eight loop knot managed to retain between 66% and 77% of the rope's full strength. Given the strength of a knot depends on largely on the radius of the first bend [114], the smaller 1.5mm diameter ropes used in our own experiments (in comparison to the 10.5mm diameter ropes by Adam Long et al) does explain the drop from 66% to 36%.

5.5 Base actuation design

The role of the base component is to control the movement of all the actuation cables and provide a support structure for the snake arm to resist against reaction forces (Figure 5.20). To control the snake arm, precise calculation of each cable length (Chapter 5.5.1) is required along with simultaneous control of nine linear actuators. A human operator will specify the angle of six joints and a computer controller will then translate this to individual cable length to be implemented through closed loop feedback control (Figure 5.19).

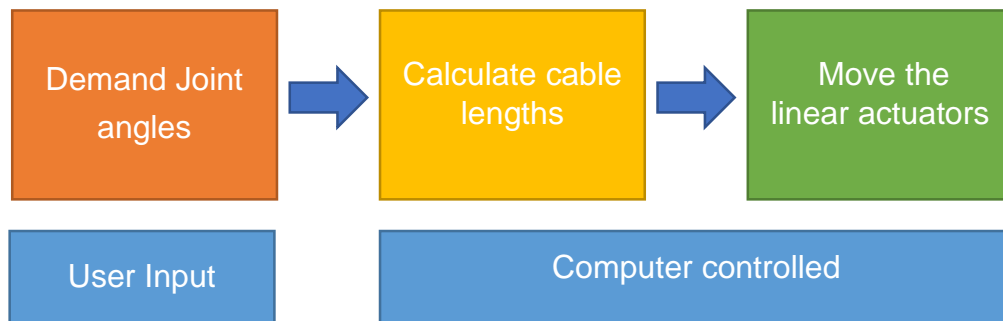


Figure 5.19 Proposed cable length control method.

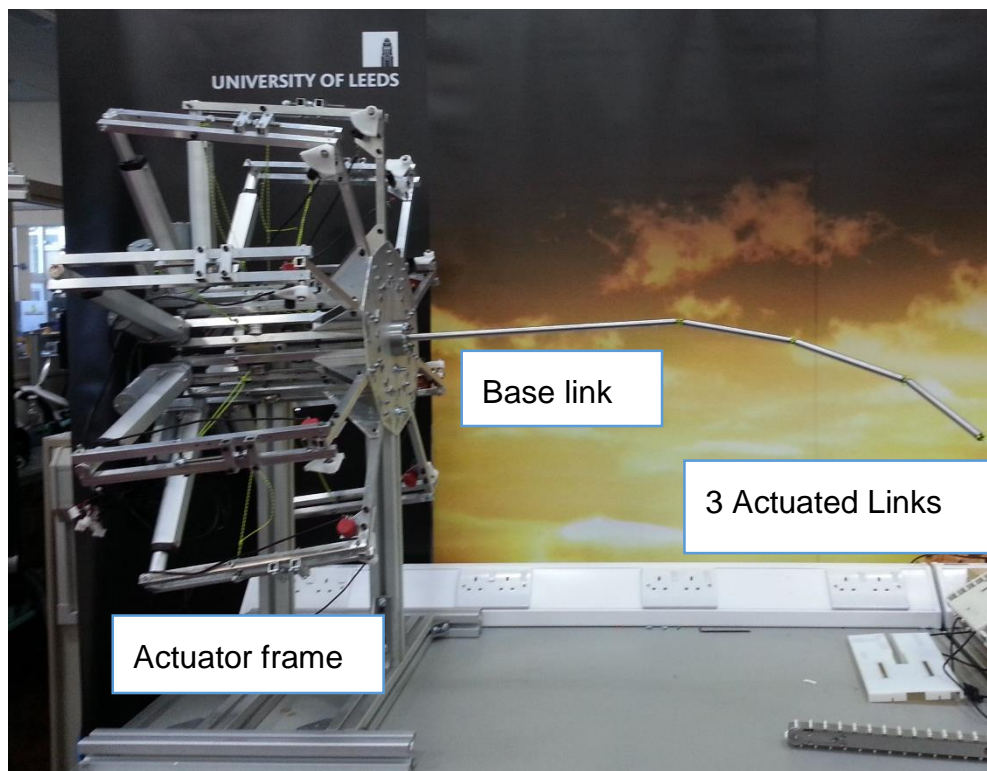


Figure 5.20 Complete snake arm assembly with base mechanism on left.

5.5.1 Tendon forces and control

Assuming no cable stretching, all changes in cable length within the snake arm will directly result in rotation of joints. The length of each individual cable can be found using forward kinematics of each joint to attain the transformation matrix and multiplying it by the cables positional coordinates. Figure 5.21 represents the joint shown in Figure 5.3 indicating degrees of freedom and link lengths.

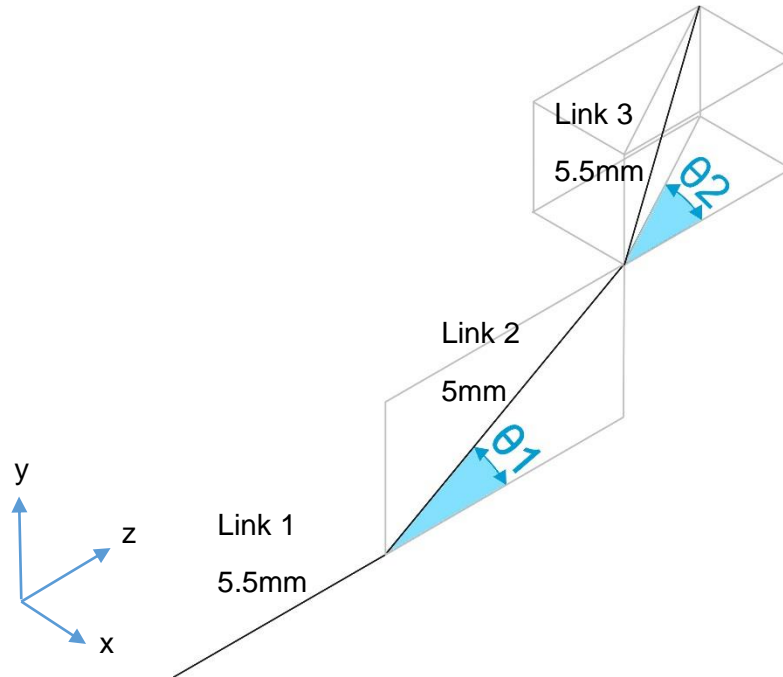


Figure 5.21 Simplified kinematic model of the 2DOF joint.

The calculation to find the position and orientation at the end of the joint, the transformation matrix can be written as the product of individual transformation matrices for links 1 to 3:

$$T = \text{Trans}(0,0,5.5) \text{Rot}(x,\theta_1) \text{Trans}(0,0,5) \text{Rot}(y,\theta_2) \text{Trans}(0,0,5.5) \quad 5.9$$

$$\text{Trans}(0,0,5.5) = \begin{bmatrix} 1 & 0 & 0 & 0 \\ 0 & 1 & 0 & 0 \\ 0 & 0 & 1 & 5.5 \\ 0 & 0 & 0 & 1 \end{bmatrix} \quad 5.10$$

$$\text{Rot}(x,\theta_1) = \begin{bmatrix} 1 & 0 & 0 & 0 \\ 0 & \cos\theta_1 & -\sin\theta_1 & 0 \\ 0 & \sin\theta_1 & \cos\theta_1 & 0 \\ 0 & 0 & 0 & 1 \end{bmatrix} \quad 5.11$$

$$Trans(0,0,5) = \begin{bmatrix} 1 & 0 & 0 & 0 \\ 0 & 1 & 0 & 0 \\ 0 & 0 & 1 & 5 \\ 0 & 0 & 0 & 1 \end{bmatrix} \quad 5.12$$

$$Rot(y, \theta_2) = \begin{bmatrix} \cos\theta_2 & 0 & \sin\theta_2 & 0 \\ 0 & 1 & 0 & 0 \\ -\sin\theta_2 & 0 & \cos\theta_2 & 0 \\ 0 & 0 & 0 & 1 \end{bmatrix} \quad 5.13$$

Which equates to:

$$T = \begin{bmatrix} c\theta_2 & 0 & s\theta_2 & 5.5(s\theta_2) \\ (-s\theta_1)(-s\theta_2) & c\theta_1 & (-s\theta_1)(c\theta_2) & 5.5(-s\theta_1)(-c\theta_2) + 5(-s\theta_1) \\ (c\theta_1)(-s\theta_2) & s\theta_1 & (c\theta_1)(c\theta_2) & 5.5(c\theta_1)(c\theta_2) + 5(c\theta_1) + 5.5 \\ 0 & 0 & 0 & 1 \end{bmatrix} \quad 5.14$$

Where:

$s = \sin, c = \cos$

Given the spacing of each cable is known as coordinates in the X-Y plane (Figure 5.22 and Table 5.4), the joint transformation matrix (Equation 5.14) multiplied by the coordinates in vector form will output the position of each cable at the end of the joint, using the start of the joint as the frame of reference.

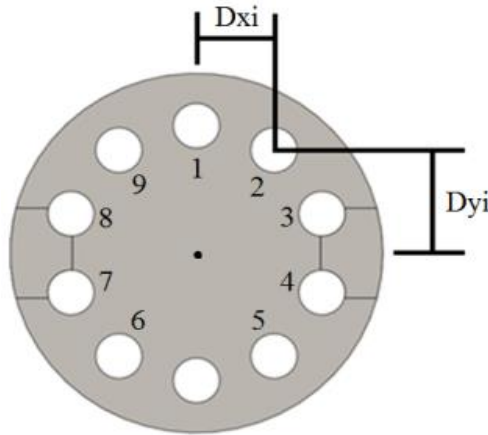


Figure 5.22 Arrangement of actuation cables in the joint vertebrae. Dxi denotes the horizontal position and Dyj denotes the vertical position of the ith cable.

Table 5.4 Coordinates of each actuation cable w.r.t the centroid.

Cable i	Dxi (mm)	Dyi (mm)
1	0	4.25
2	2.5	3.44
3	4.04	1.31
4	4.04	-1.31
5	2.5	-3.44
6	-2.5	-3.44
7	-4.04	-1.31
8	-4.04	1.31
9	-2.5	3.44

So for joint 2 and given joint angle values of $\theta_1=15$ and $\theta_2=20$, the position of the cable at the far end of the joint is calculated as:

$$\begin{bmatrix} c\theta_2 & 0 & s\theta_2 & 5.5(s\theta_2) \\ (-s\theta_1)(-s\theta_2) & c\theta_1 & (-s\theta_1)(c\theta_2) & 5.5(-s\theta_1)(-c\theta_2) + 5(-s\theta_1) \\ (c\theta_1)(-s\theta_2) & s\theta_1 & (c\theta_1)(c\theta_2) & 5.5(c\theta_1)(c\theta_2) + 5(c\theta_1) + 5.5 \\ 0 & 0 & 0 & 1 \end{bmatrix} \quad 5.15$$

$$\times \begin{bmatrix} 2.5 \\ 3.44 \\ 0 \\ 1 \end{bmatrix} = \begin{bmatrix} 4.2303 \\ 0.9123 \\ 15.3863 \\ 1 \end{bmatrix} \quad 5.16$$

Where:

$$s = \sin$$

$$c = \cos$$

Using the two positional vectors, the difference can be found as:

$$\begin{bmatrix} 4.2303 \\ 0.9123 \\ 15.3863 \\ 1 \end{bmatrix} - \begin{bmatrix} 2.5 \\ 3.44 \\ 0 \\ 1 \end{bmatrix} = \begin{bmatrix} 1.7303 \\ -2.5277 \\ 15.3863 \\ 0 \end{bmatrix} \quad 5.17$$

In addition, the individual cable length is calculated as its hypotenuse.

$$cable\ 2\ length = \sqrt{1.7303^2 + -2.5277^2 + 15.3863^2} = 15.6882mm \quad 5.18$$

Applying same joint angles to all other cables provides:

Table 5.5 Sample cable lengths for joint angles $\theta_1=15$ and $\theta_2=20$.

Cable i	Cable Length (mm)
1	16.761
2	15.688
3	14.605
4	13.926
5	13.906
6	15.633
7	16.717
8	17.395
9	17.414

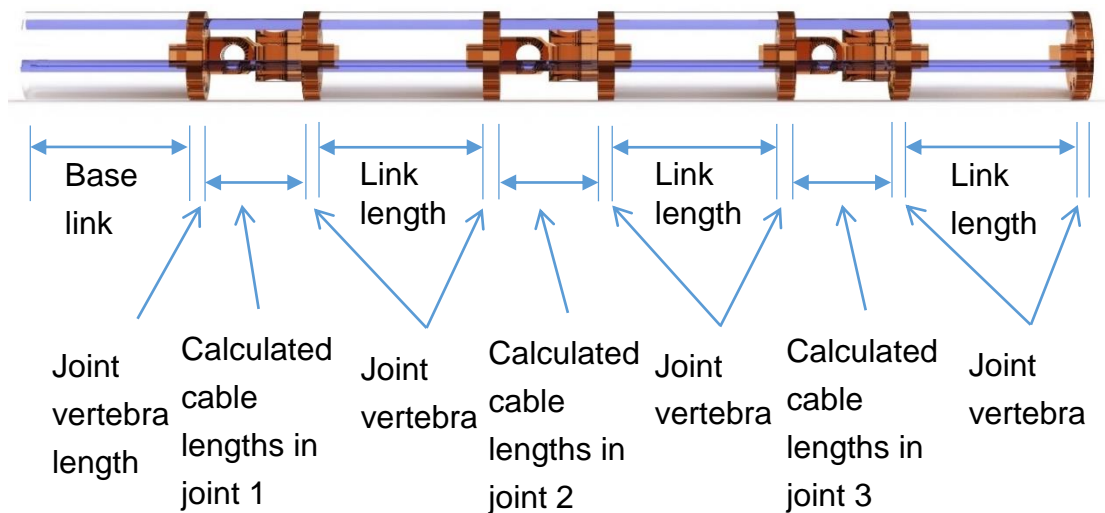


Figure 5.23 Illustration of the different part lengths required to calculate each cable length.

Applying this methodology to the complete snake arm as shown in Figure 5.23 can therefore output the length of each cable at any joint orientation. This can be computed quickly using the sum of each known part length however not all cables pass through the length of the whole snake arm as illustrated in Figure 5.24 which show which links and joints each cable passes through the snake arm and where the cables terminate.

		Joint 1				Joint 2				Joint 3				
Cable i	Base link	Joint vertebra	Joint 1 Cable lengths	Joint Vertebra	Link Length	Joint Vertebra	Joint 2 Cable lengths	Joint Vertebra	Link Length	Joint Vertebra	Joint 3 Cable lengths	Joint Vertebra	Link Length	Joint Vertebra
1														
2														
3														
4														
5														
6														
7														
8														
9														

Figure 5.24 The three groups of cables and where each is expected to span the snake arm.

5.5.2 Actuator frame

Mounting the linear actuators with the configuration illustrated in Figure 5.25 benefits the system by:

- Increasing the maximum force supplied to the actuation cables.
- Improving accuracy of the actuation cable lengths.
- Supplying a means to attach a sensor for measuring the cable length.

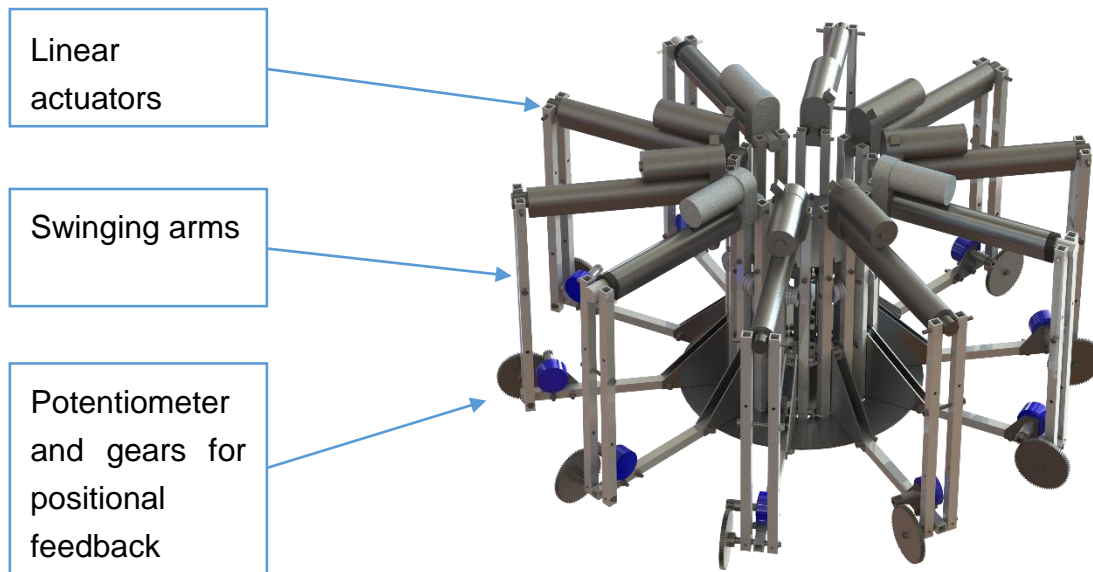


Figure 5.25 The base actuator frame assembly.

Changing the stroke length of the linear actuator mounted in its individual frame allows for the actuation cable lengths to be altered and controlled. The range of motion is illustrated in Figure 5.26. Through leverage a large displacement of the linear actuator will produce a smaller displacement for the cables and in return the force supplied is increased.

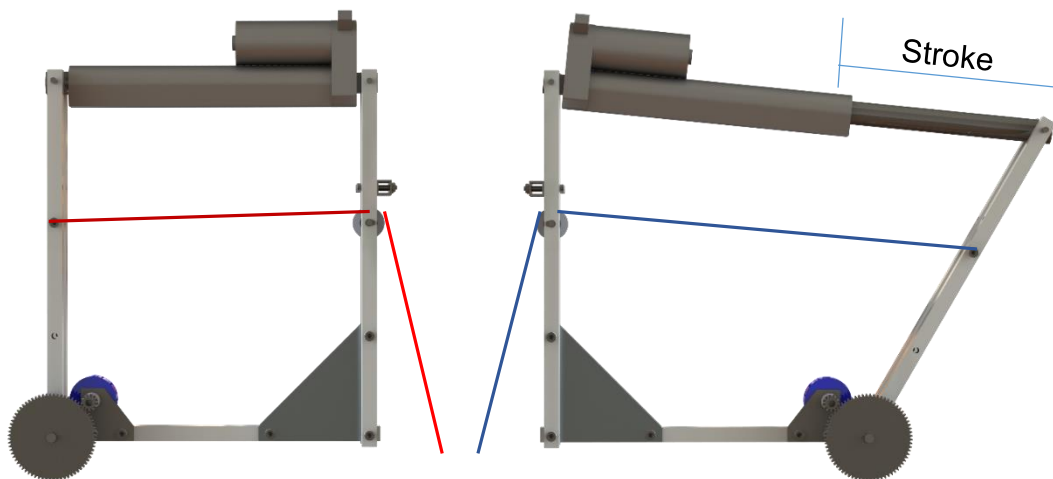


Figure 5.26 Illustration of change in actuation cable length. (left) The red actuation cable will be at its shortest length, (right) the blue actuation will be at its longest length.

5.1.1.1 Force supplied

Selection of the linear actuator required a combination of large force and stroke length. Large force to supply the predicted forces necessary for each cable and the large stroke to increase the accuracy in combination with the frame for supplying the correct changes in cable length. As the Marlow cables have a maximum tension limit of 490N, the force supplied by the linear actuator should be equal or greater. Future-proofing for later platforms that can utilise a cable of larger breaking load will aid the reusability of the base actuator frame, so a linear actuator that can be mounted on the frame (Figure 5.26) and is capable of supplying at least 3 times the spec cable tension was required.

Table 5.6 Firgelli Automation Light Duty Linear Actuator [115].

Specification – FA-240-S-12-12”	
Gear Ratio	30:1
Input Voltage	12v
Load Capacity	200lbs (890N)
Static Load	400lbs (1779N)
Stroke Length	12” (305mm)
Speed at No load	0.3 inch/s (8mm/s)
Current consumption 12v DC	5A
Operating Temperature Range	-26°C to +65°
Protection	IP54

From the actuator specifications (Table 5.6) and the geometry of the actuator frame, the maximum values of tension supplied on the cables can be calculated as a function of arm angle θ with the variables shown in Figure 5.26. Figure 5.27 illustrates the change in max tension supplied to range from 1454N to 1603N as the linear actuator extends towards its maximum stroke length of 12”.

The arm angle θ is limited from 90° to 120° due to the linear actuator stroke length. At the minimum angle of 90°, forces F_L will equal F_L and F_T will equal T , at this instance, the force transmitted from the linear actuator to the cable

will be parallel and the leverage will create the occurrence of a larger force creating the drop in the force curve in Figure 5.28 as arm angle begins to swing.

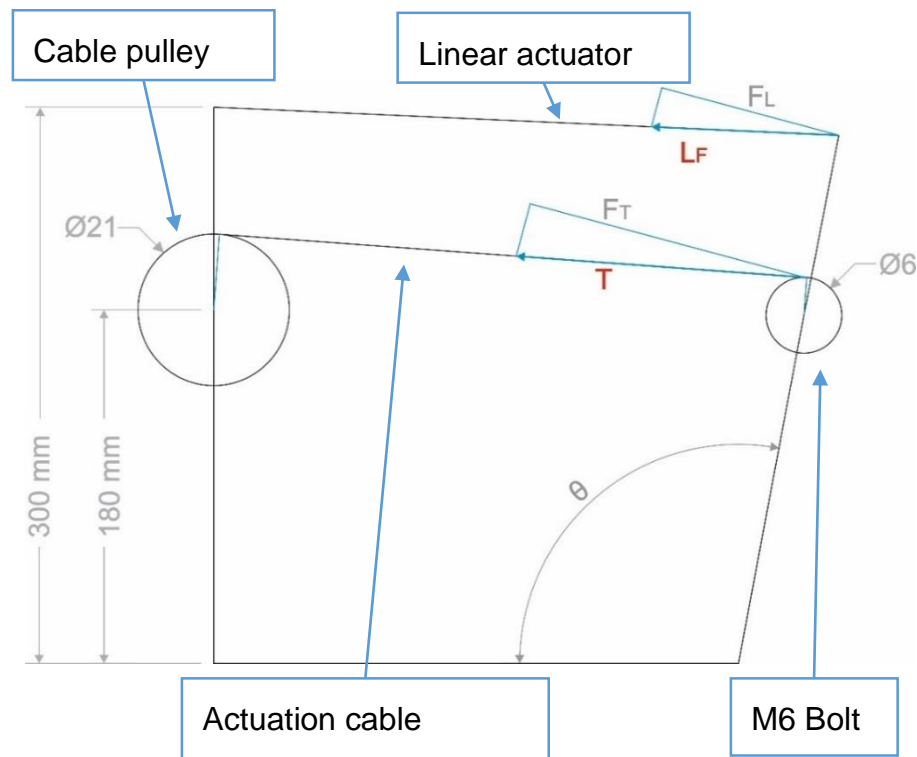


Figure 5.27 Graphical model of the actuator frame assembly as seen in Figure 5.26.

Where:

L_F = Load capacity of linear actuator

F_L = Perpendicular force exerted by linear actuator

F_T = Perpendicular force experienced on cable

T = Tension force exerted by linear actuator

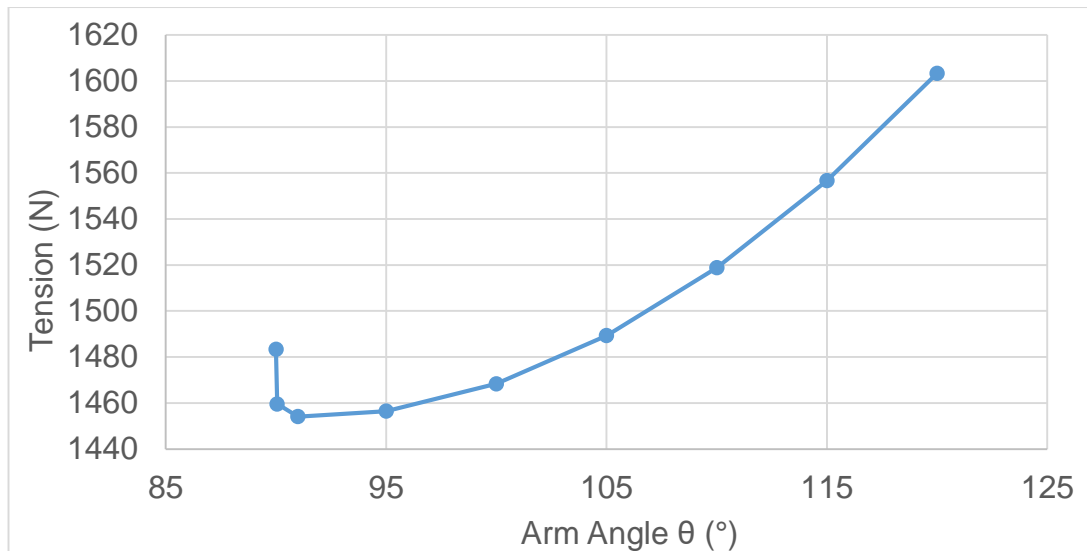


Figure 5.28 Maximum possible cable tension changes with the arm angle in the actuator frame.

5.1.1.2 Beam bending

The aluminium beams that form the actuator frame are required to withstand loads of up to 1603N (the maximum force that can be supplied to the cables). Focusing on the sections where the actuation cables terminate (Figure 5.30), the beam sections comprises of twin parallel beams (Figure 5.29) of constant cross section meaning each is only subjected to half of the 1603N load.

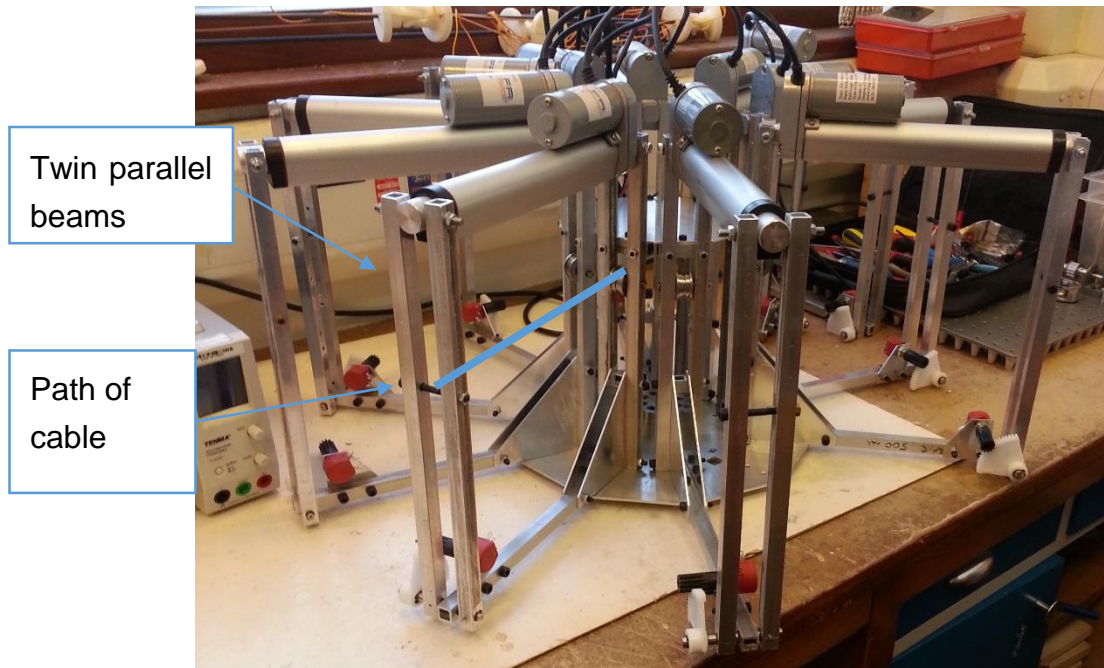


Figure 5.29 Actuator frame beams and cable path.

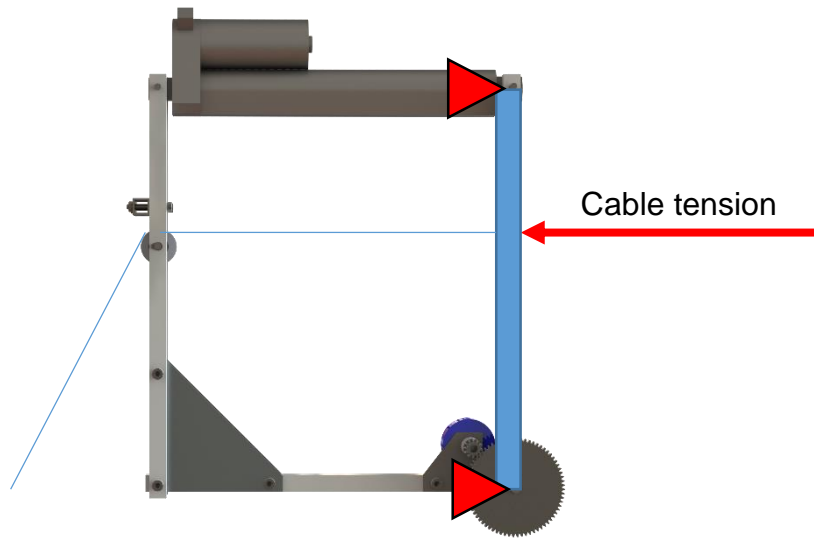


Figure 5.30 Actuator frame beam bending.

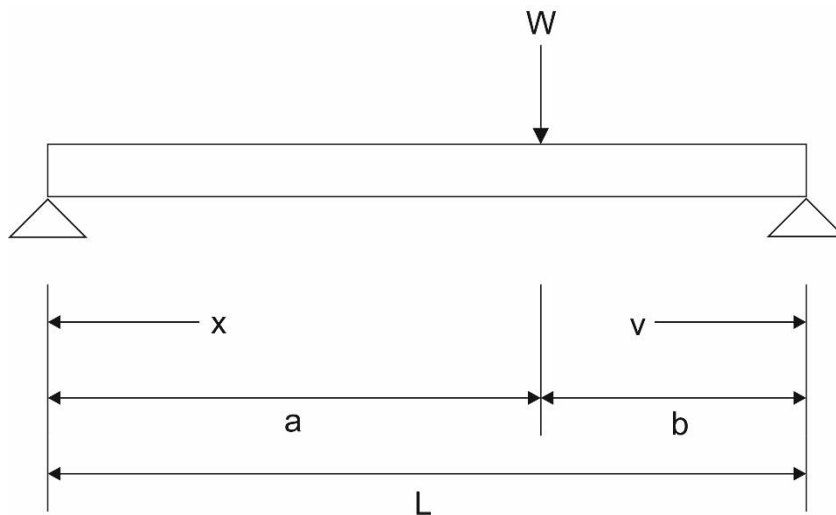


Figure 5.31 Actuator frame loading condition simplifies to beam bending problem.

Forces acting on a beam causes bending and deflection, this affects the control of the cable lengths. By calculating the maximum deflection expected the design of the beam was verified before manufacture. Ideally, the calculated deflection of the beam should be small and insignificant.

The deflection of the beam at the point of load is defined as [116]:

$$\frac{W a^2 b^2}{3 E I L} \quad 5.19$$

Whereas the maximum deflection is defined as [116]:

$$\frac{Wa(v_1^3)}{3EIL} \quad 5.20$$

Which occurs at [116]:

$$v_1 = b \sqrt{\frac{1}{3} + \frac{2a}{3b}} \quad 5.21$$

Where:

W = Load

E = Modulus of Elasticity

I = Moment of Inertia

L = Total length

The Moment of Inertia of a single aluminium beam of constant cross-section is calculated as [117]:

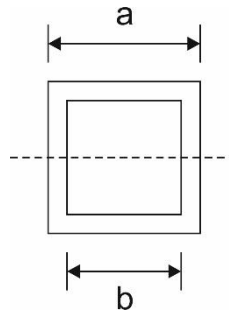


Figure 5.32 Moment of inertia for square aluminium beam.

$$I = \frac{a^4 b^4}{12} = \frac{12.7^4 \times 9.3^4}{12} = 1.5445 \times 10^9 m^4 \quad 5.22$$

Using $W=801.5\text{N}$, $a=0.18\text{m}$, $b=0.12\text{m}$, $L=0.3\text{m}$ and $E_{\text{aluminium}} = 69 \times 10^9 \text{N/m}^2$ the deflections are.

Deflection at the load point:

$$\frac{Wa^2 b^2}{3EIL} = \frac{801.5 \cdot 0.18^2 \cdot 0.12^2}{3 \cdot 69 \times 10^9 \cdot 1.5445 \times 10^9 \cdot 0.3} = 3.899 \times 10^{-21} m \quad 5.23$$

Maximum deflection at:

$$v_1 = b \sqrt{\frac{1}{3} + \frac{2a}{3b}} = 0.12 \sqrt{\frac{1}{3} + \frac{2 \cdot 0.18}{3 \cdot 0.12}} = 0.139 m \quad 5.24$$

Maximum deflection:

$$\frac{Wa(v_1^3)}{3EIL} = \frac{801.5 \cdot 0.18(0.139^3)}{3 \cdot 69 \times 10^9 \cdot 1.5445 \times 10^9 \cdot 0.3} = 4.0396 \times 10^{-21}m \quad 5.25$$

Given the small value of maximum deflection, the frame structure is expected to perform adequately within the expected loading conditions.

5.1.1.3 Arm angle

The relationship between the actuation cable length and the angle of the arm can be found by simplifying the model (Figure 5.33).

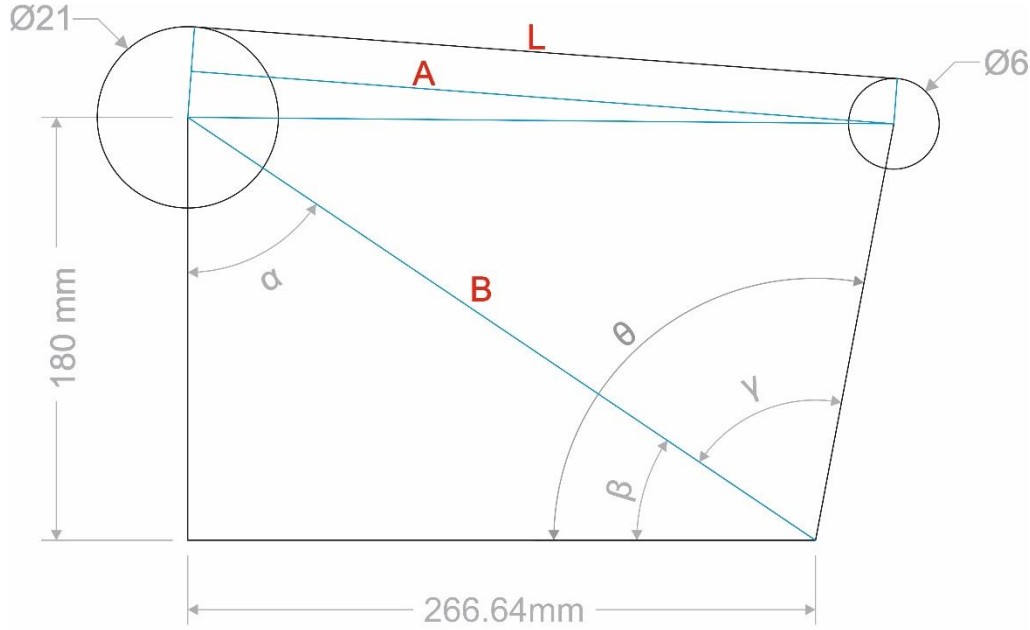


Figure 5.33 Graphical model of the actuator frame assembly without a linear actuator.

$$A = \sqrt{L^2 + \left(\frac{21}{2} - \frac{6}{2}\right)^2} \quad 5.26$$

$$B = \sqrt{180^2 + 266.64^2} \quad 5.27$$

$$\alpha = \tan^{-1} \left[\frac{266.64}{180} \right] \quad 5.28$$

$$\beta = 90 - \alpha \quad 5.29$$

$$\gamma = \cos^{-1} \left[\frac{B^2 + 180^2 - A^2}{360 \times B} \right] \quad 5.30$$

$$\theta = \beta + \gamma \quad 5.31$$

Where:

L = length of cable in the frame

θ = angle of arm in association with the potentiometer

Therefore, the total change in cable length can be calculated by subtracting the cable length when the linear actuator is at maximum length by the cable length when the linear actuator is at minimum length.

Table 5.7 Cable lengths in actuator frame.

Angle θ	Cable length L
90°	266.534mm
120°	357.376mm
Maximum change in cable length	90.842mm

5.1.1.4 Gearing selection

The arm rotates through 30 degrees (from 90 degrees to 120 degrees) to achieve the desired change in cable length. It is important to measure the actual joint angle so that feedback control can be implemented. A potentiometer is a simple and low-cost sensor capable of measuring rotation through a change in resistance. If a potentiometer were mounted directly at the arm pivot point, only approximately 20% of measurable signal range would be used resulting in poor sensor resolution.

The use of spur gears between the swinging arm and the potentiometer can increase the range of motion. Potentiometers typically have an active range of 280 degrees, therefore an optimum rotational range of 180° was selected to allow a small measurable overshoot at the end of each range. Equation 5.32 calculates the gear ratio required to scale from 30 degrees to 180 degrees.

$$\frac{180^\circ}{30^\circ} = \frac{6}{1} \text{ratio} \quad 5.32$$

Figure 5.34 illustrates the gears chosen for scale the potentiometer motion, 1 gear of 12 teeth and one of 72 teeth. Teeth of module 1 were chosen as the gears only transmit torque to rotate the potentiometer.

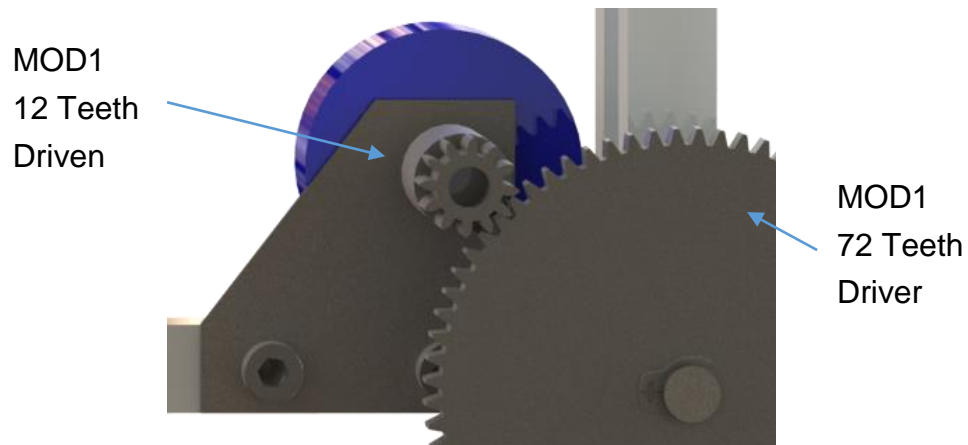


Figure 5.34 Gear assembly on the actuator frame.

5.6 Iterative solver

The design of an optimally long snake arm involves many interdependent variables. Table 5.8 and Table 5.9 presents the known and unknown variables to design a snake arm.

Due to a large number of unknowns, there is not an algorithmically solvable solution to determine the optimal length of snake arm. Therefore, an interactive solver was developed to search potential solutions for an optimal case.

Table 5.8 Known variables for iterative solver.

Known variable	Value	Unit
Number of joints	3	
Length of joint	0.0055	m
Length of end vertebrae	0.002	m
Length of joint link	0.005	m
Position of yaw joint centroid	0.00321	m
Position of pitch joint centroid	0.00229	m
Position of end vertebrae centroid	0.00081	m
Payload mass	0.02	kg

Payload length	0.06	m
Mass of joint	0.00252	kg
Mass of joint link	0.0008	kg
Mass of end vertebrae	0.00147	kg
Density of electrical wire	8940	kg/m ³
Diameter of electrical wire	0.0015	m
Diameter of actuation cable	0.0015	m
Density of actuation cable	955	kg/m ³
Breaking load of actuation cable	490	N
Breaking load of joint	1332	N
Breaking twisting torque of joint	1.8	Nm
Cable FOS	6	
Joint FOS	4	
Joint twist torque FOS	4	
Tube FOS	4	

Table 5.9 Unknown variables for iterative solver.

Unknown variable	Value	Unit
Base link length	-	m
Link length	-	m

5.6.1 Optimisation strategy

As represented in Figure 5.33, the approach was to firstly determine the maximum length of the links and thereafter determine the length of the base link. This is because the base link length does not affect the actuation cable tensions, the calculations for the buckling failure of the three links or the forces acting into the 2DOF joints. However, the axial stress resulting from the cable tensions acting through the Base link and weight of the unsupported snake arm does affect the likelihood of buckling for the base link.

MATLAB was used as a numerical solver to find the maximum lengths for both the link types of the self-supported snake arm design. The design for a

discrete 12mm diameter snake arm was built and parts such as the joints were designed to conform to the size constraints. The aluminium tubing was selected for its properties on buckling resistance, density and size. The actuation cables were chosen for its high yield strength and low strain so the only unknown factors were the lengths of the links and base link. To simplify the study, the length of the three link are kept the same under the single variable.

A model was written to take two variables (length of link and base link) and calculate the tensions for nine actuation cables using the methods defined in Chapter 4.3. A full breakdown of the code used for the solver can be found in Appendix D. Assumptions made for the model include friction to be negligible and the snake arm to remain static and not affected by any external forces other than gravity.

Once the tensions were calculated, the next stage was to sequentially perform checks to ensure no parts are anticipating failure. These checks consisted of:

- Comparing the cable tensions to the experimentally found yield load of 490N.
- Analysing the axial stress through the links for buckling utilising buckling theory already available for thin-walled cylinders in axial compression [111, 112].
- Comparing the axial load with the shearing load of 4240N on the joint pins.
- Comparing the axial load with the joints material failure load of 1332N.
- Comparing the torque generated by the snake arm against the joints torque twist limit of 1.8Nm.

Design factors of safety (FOS) were implemented into the study for each of the failure modes, as allowing the tension of the cables to equal or surpass its breaking stress, for example, would severely harm the durability and performance of the snake arm whilst still allowing the snake arm to be at its physical maximum length. The application of any appropriate FOS will, therefore, aid overcome any uncertainties in applied loads or variations in material properties [118].

Based on recommended values supplied from manufacturers and values chosen to represent where materials used are reliable but used under difficult and environmental conditions.

The FOS values designated were:

Table 5.10 Factors of safety.

Part	FOS	Source
Actuation cable	6	[119]
Link buckling	4	[120]
Joints	4	[120]

MATLAB was used to determine the maximum length of snake arm by algorithmically incrementing the length of the base link and all links by 1mm whilst simultaneously ensuring the imposed design safety constraints are conserved.

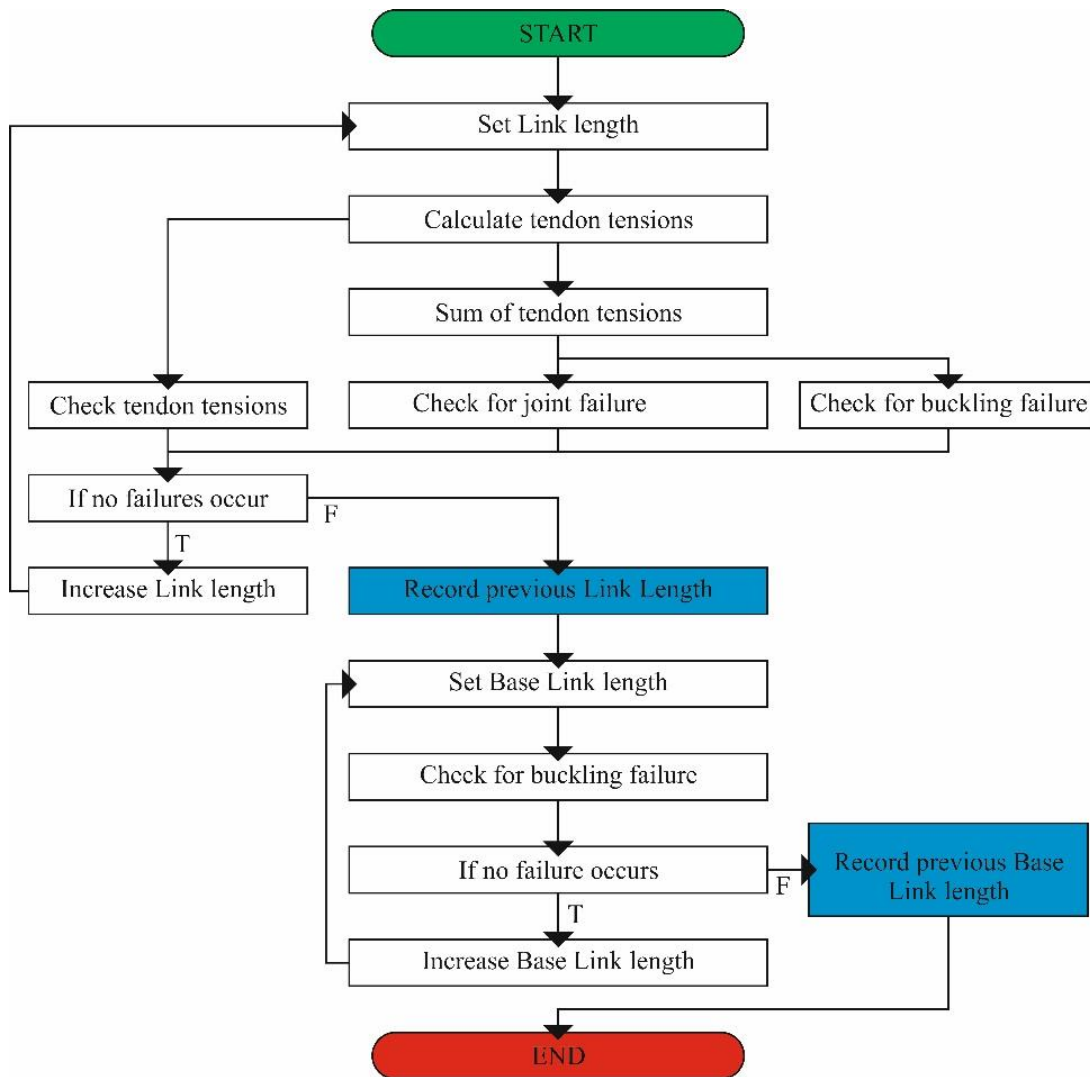


Figure 5.35 Graphical representation of MATLAB code to determine the maximum length of the snake arm.

As represented in Figure 5.35, the approach was to firstly determine the maximum length of the links and thereafter determine the length of the base link. This is because the base link length does not affect the actuation cable tensions, the calculations for the buckling failure of the three links or the forces acting into the 2DOF joints. However, the axial stress resulting from the cable tensions acting through the Base link and weight of the unsupported snake arm does affect the likelihood of buckling for the base link.

5.6.2 Solver results

This approach yielded a snake arm of total length 1.149m with a link length of 0.1850m and base link of 0.5440m for the 12mm diameter snake arm, the effective length being 0.605m. Extracting information from the solver at the

final solution provides can inform what components of the snake arm risk failure and limits the growth of the snake arm.

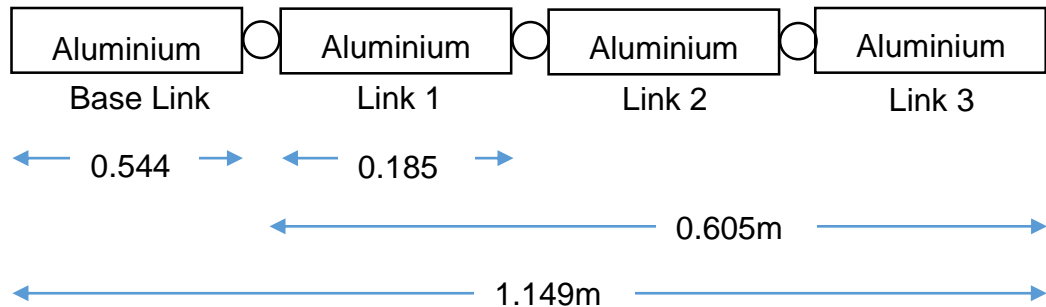


Figure 5.36 Snake arm lengths.

Table 5.11 Actuation cable tension results.

Cable Number	Tension (N)	Limit (N)	FOS
1	78.975	490	6.205
2	50.866	490	9.633
3	14.779	490	33.155
4	0.000	490	-
5	0.000	490	-
6	0.000	490	-
7	0.000	490	-
8	31.476	490	15.567
9	23.883	490	20.517

The results from the predicted cable tensions (Table 5.11) shows cable 1 approach the FOS limit of 6. This was expected as the cables 1, 4 and 7 are tasked with actuating joint 1 (with the highest torque requirements). However, as cables 4 and 7 are positioned below the centroid as shown in Figure 5.22, these cables are kept slack as per the cable tension theory (Chapter 4.4); therefore, cable 1 remains to provide the largest torque required to support the rest of the snake arm.

Table 5.12 Joint compression results.

Joint Number	Axial Compression Force (N)	Limit (N)	FOS
1	199.980	1332	6.661
2	121.004	1332	11.008
3	38.662	1332	34.453

Table 5.13 Joint shear results.

Total axial load (N)	Limit (N)	FOS
199.979	4240	21.20

Table 5.14 Maximum torque twist at joint 1

Maximum Torque Twist (Nm)	Limit (Nm)	FOS
0.449	1.8	4.012

The joints display a surplus tolerance to axial compression (Table 5.12) with a FOS value of 6.661 and pin shearing with a FOS of 21.2 (Table 5.13). However, for the torque twisting of joint 1 (where greatest torque occurs), the limited FOS of 4 was met.

Table 5.15 Flexural buckling results.

Link	Axial stress (N)	Elastic buckling stress (N/m ²)	FOS
Base	5786900	23178000	4.005
1	5786900	110140000	19.033
2	3501500	110140000	31.455
3	1118800	110140000	98.445

Table 5.16 Local buckling results.

Link	Axial stress (N)	Local buckling stress (N/m ²)	FOS
Base	5786900	4453300000	769.549
1	5786900	4453300000	769.549
2	3501500	4453300000	1271.826
3	1118800	4453300000	3980.426

As intended, the FOS of the base link reached the limit of 4 as to maximise its length at 0.544m. Given the short link lengths of 0.185m, the calculated elastic buckling stress for flexural buckling to occur was large (Table 5.15), resulting in a FOS as low as 19.033. The likelihood of local buckling occurring in the snake arm is very low given the FOS values of minimum 769.549 as shown in Table 5.16.

The complex interconnection of each part made constructing a long length snake arm difficult. The results of the algorithm used to calculate the 1.149m snake arm has shown in this case the likelihood of torque twisting to be the main culprit in hindering the reality of a truly long snake arm with small diameter. If the FOS for the joint were to be relaxed, this would allow for increased link lengths, the results of the joint compression and buckling show enough excess capacity to allow such increases. However, the longer link lengths would by association increase cable tensions wherein lies a problem as the FOS is already in close proximity to the cable FOS limit, so any increases in length would be small (reducing the joint FOS to 3 results in a small length increase to 1.15m).

5.6.3 Further strategies

To further increase the length of the snake arm beyond the current 1.149m length, the analysis of the solver results revealed the yield limit of the cables and the maximum allowable joint torque twist must both be strengthened. One possible solution would be to increase the diameter of the snake arm (going against the specification); this allows the cables to be displaced further from the centroid therefore providing greater torque and less tension.

Another approach however would be to reduce the forces acting through the snake arm by reducing the torque required at each joint. This is possible without going against the specification by altering the weight of each link. Until now each of the three links has been kept identical by using the same construction materials for each link tubing, the buckling results of the solver (Table 5.15 and Table 5.16) does show each link from 1 to 3 progressively increase its FOS as the axial compressive forces decrease as it approaches the end of the arm. By swapping links currently using aluminium for a weaker but lighter carbon fibre alternative of same size, the length of the snake arm can be improved.

For example, using carbon fibre tubing for the third link increases the total length to 1.529m and effective length 0.281m (Figure 5.37). In consequence, the length of each link is reduced by 41.62% to just 0.077m due to the decrease in elastic buckling stress leading to an earlier occurrence of flexural buckling.

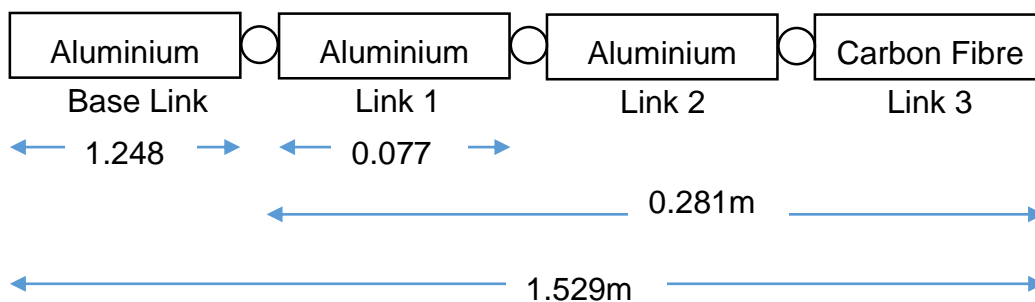


Figure 5.37 Snake arm lengths.

A result of the shorter link lengths, the torque requirements are reduced resulting in an increase to the calculated cable FOS with a minimum of 31 (Table 5.17).

Table 5.17 Actuation cable tension results.

Cable Number	Tension (N)	Limit (N)	FOS
1	15.360	490	31.902
2	9.483	490	51.670
3	4.061	490	120.665
4	0.000	490	-
5	0.000	490	-
6	0.000	490	-
7	0.000	490	-
8	5.868	490	83.498
9	6.562	490	74.669

The implications of the shorter link lengths are also seen in the joint results with a minimum FOS of 14 occurring with the joint twisting (Table 5.20). This leaves the buckling of the links to be the main source of failure. Table 5.21 shows the Base link length to be maximised until the FOS limit is reached, but the carbon fibre link also risks flexural buckling failure due to the reduced elastic buckling stress.

Table 5.18 Joint compression results.

Joint Number	Axial Compression Force (N)	Limit (N)	FOS
1	41.334	1332	32.225
2	25.975	1332	51.281
3	10.623	1332	125.387

Table 5.19 Joint shear results.

Total axial load (N)	Limit (N)	FOS
41.334	4240	102.578

Table 5.20 Maximum torque twist at joint 1.

Maximum Torque Twist (Nm)	Limit (Nm)	FOS
0.121	1.8	14.925

Table 5.21 Flexural buckling results.

Link	Axial stress (N)	Elastic buckling stress (N/m ²)	FOS
Base	1196100	4791300	4.006
1	1196100	150000000	125.408
2	751640	150000000	199.564
3	307400	1268300	4.126

Table 5.22 Local buckling results.

Link	Axial stress (N)	Local buckling stress (N/m ²)	FOS
Base	1196100	4453300000	3723.184
1	1196100	4453300000	3723.184
2	751640	4453300000	5924.778
3	307400	4110200	13.371

Going further and introducing more carbon fibre tubing for links two and three (Figure 5.38) reveals the trend of longer total snake arm length at the compromise of a shorter effective snake arm length.

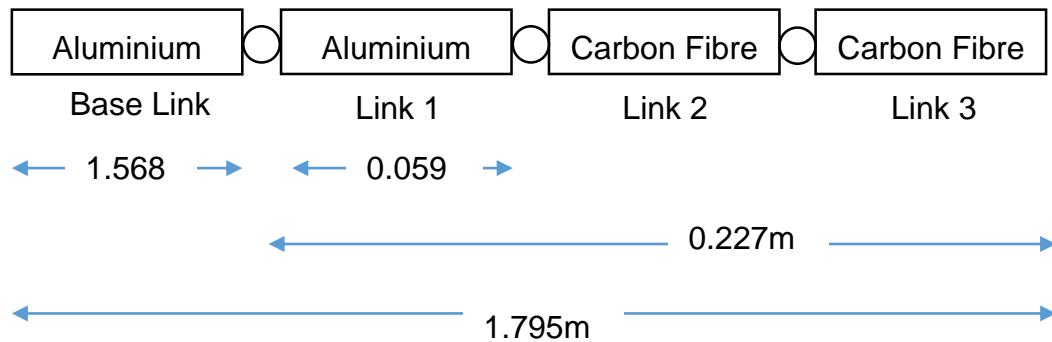


Figure 5.38 Snake arm lengths.

Table 5.23 Actuation cable tension results.

Cable Number	Tension (N)	Limit (N)	FOS
1	8.444	490	58.026
2	5.738	490	85.399
3	3.360	490	145.854
4	0.000	490	-
5	0.000	490	-
6	0.000	490	-

7	0.000	490	-
8	3.551	490	138.004
9	5.429	490	90.256

Table 5.24 Joint compression results.

Joint Number	Axial Compression Force (N)	Limit (N)	FOS
1	26.521	1332	50.224
2	18.077	1332	73.685
3	8.789	1332	151.561

Table 5.25 Joint shear results.

Total axial load (N)	Limit (N)	FOS
26.521	4240	159.871

Table 5.26 Maximum torque twist at joint 1.

Maximum Torque Twist (Nm)	Limit (Nm)	FOS
0.086	1.8	20.930

Table 5.27 Flexural buckling results.

Link	Axial stress (N)	Elastic buckling stress (N/m ²)	FOS
Base	767460	3071500	4.002
1	767460	154930000	201.874
2	523100	2159800	4.129
3	254320	2159800	8.493

Table 5.28 Local buckling results.

Link	Axial stress (N)	Local buckling stress (N/m ²)	FOS
Base	767460	4453300000	5802.648
1	767460	4453300000	5802.648
2	523100	4110200	7.857
3	254320	4110200	16.162

The results of the cable and joint FOS show the forces acting on the parts are well within the bounds of the FOS limits. Just as the carbon fibre link was the limiting factor to the snake arm in Figure 5.37, the results in Table 5.27 show

the carbon fibre link undergoing the greater amount of axial stress to be the limiting component.

Interchanging all three links for the carbon fibre tubing (Figure 5.39) further increases the overall snake arm length to be 1.894m whilst reducing the effective length to 0.209m.

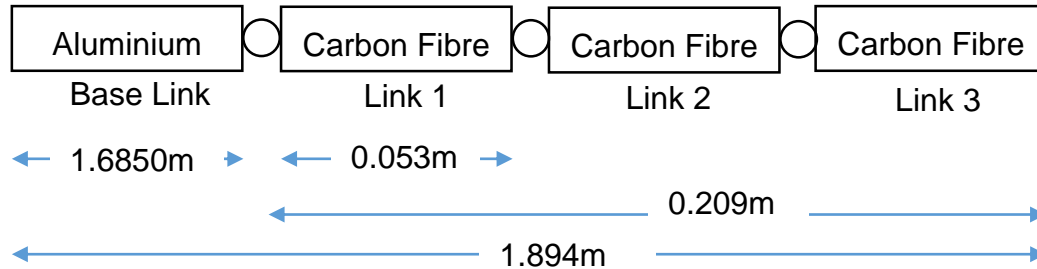


Figure 5.39 Snake arm lengths.

Table 5.29 Actuation cable tension results.

Cable Number	Tension (N)	Limit (N)	FOS
1	6.461	490	75.836
2	5.175	490	94.683
3	3.132	490	156.439
4	0.000	490	-
5	0.000	490	-
6	0.000	490	-
7	0.000	490	-
8	3.202	490	153.008
9	5.062	490	96.806

Table 5.30 Joint compression results.

Joint Number	Axial Compression Force (N)	Limit (N)	FOS
1	23.033	1332	57.831
2	16.572	1332	80.379
3	8.194	1332	162.561

Table 5.31 Joint shear results.

Total axial load (N)	Limit (N)	FOS
23.033	4240	184.086

Table 5.32 Maximum torque twist at joint 1.

Maximum Torque Twist (Nm)	Limit (Nm)	FOS
0.076	1.8	23.747

As was the case for replacing one (Figure 5.36) or two links (Figure 5.37) for carbon fibre tubes, the shortened link lengths result in the design of the joints and cables to be fully capable of withstanding the tension and axial compressive forces. Table 5.33 reveals Link 1 to be the reason for the shorter link lengths.

Table 5.33 Flexural buckling results.

Link	Axial stress (N)	Elastic buckling stress (N/m ²)	FOS
Base	666510	2668200	4.003
1	666510	2676100	4.015
2	479530	2676100	5.581
3	237110	2676100	11.286

Table 5.34 Local buckling results.

Link	Axial stress (N)	Local buckling stress (N/m ²)	FOS
Base	666510	4453300000	6681.520
1	666510	4110200	6.167
2	479530	4110200	8.571
3	237110	4110200	17.335

The increasing reliance on lighter carbon fibre links with the aim of an ever increasing snake arm length has revealed the compromise of a longer snake arm resulting in a shorter manoeuvrable length and hence a smaller workspace as illustrated in Figure 5.40. This is due to the increased likelihood of flexural buckling for the carbon fibre links. Given the compromise and the aim of investigating within a restricted access void, in this instance, the greater workspace volume is more beneficial than the long reach and as such, the 1.149m snake arm was chosen.

Issues will arise if the restricted access borehole is longer than the base link length of 0.544m as the borehole will interfere with the movement of the joints. On the other hand, the length of a borehole will effectively confine the base link and support the structure, thus reducing the chance of flexural buckling and instead increasing the likelihood of local buckling. Therefore, this would allow the total snake arm length to increase but the effective length to remain the same with the same construction design.

Due to the resulting short lengths presented, another means of increasing the exploration workspace beyond the 1.149m is required to increase the scope of exploration. Similar to a snake robot, if a robotic tool can traverse the borehole entirely then the tool should be able to utilise an alternative form of locomotion to continue the exploration.

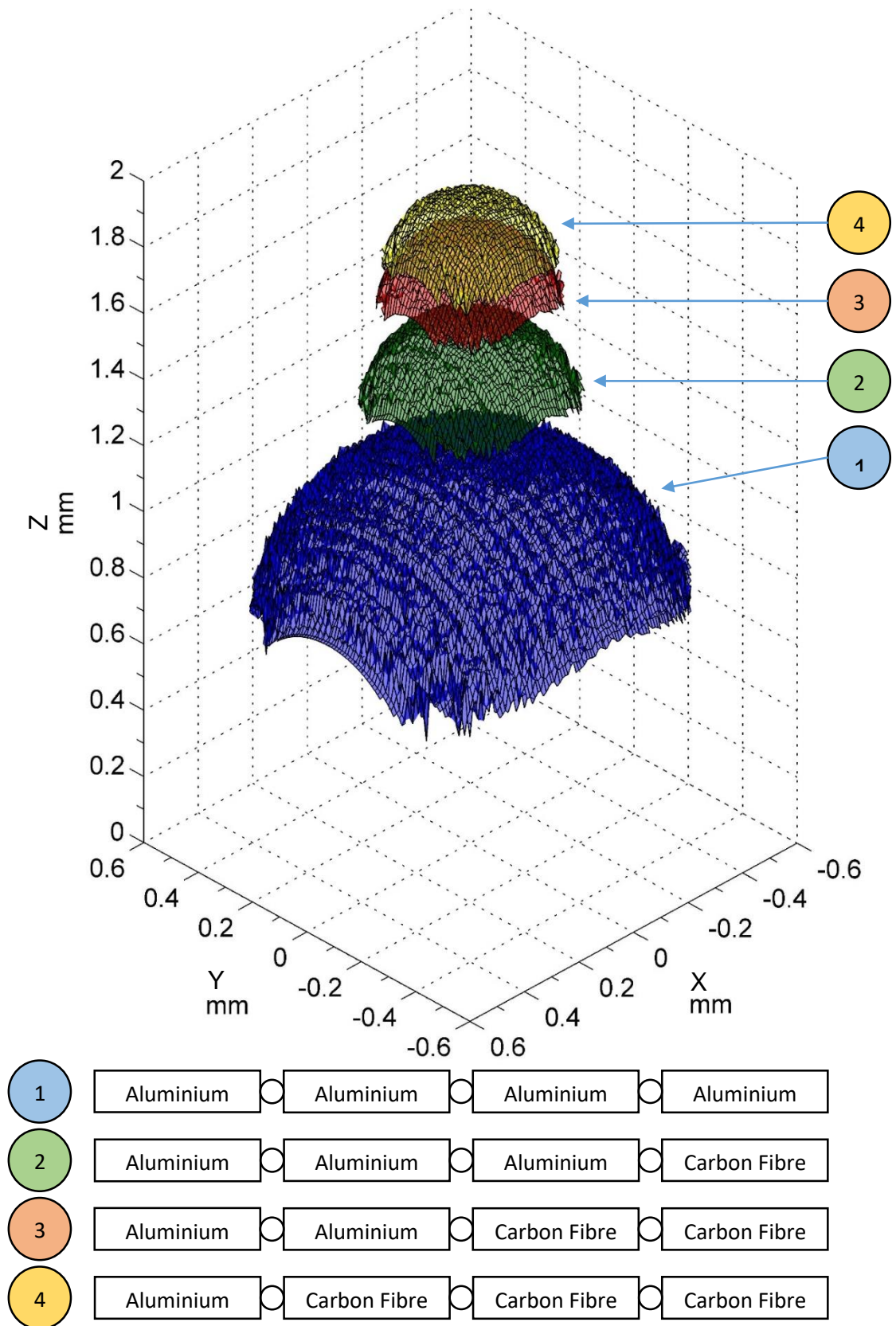


Figure 5.40 Workspace for snake arms of different link materials.

5.7 Experiment

An experiment to observe the response of the snake arm to a change in cable length was conducted. In Figure 5.19 the proposed control process involved demanding two joint angles for each joint (pitch and yaw) as the user input and the controlling software will then calculate the ideal cable lengths for all cables and adjust the stroke of the linear actuators to match the ideal cable lengths.

Observing the relationship between the change in cable length provided by the actuator frame (from Section 5.5.2) and the joint angle output will allow the accuracy of the snake arm to be graded.

5.7.1 Methodology

Cable 1 of the snake-arm is responsible for much of the heavy lifting for the snake arm. The cable terminates after Joint 1 (Figure 5.24) and carries the largest amount of tension whilst under the horizontal cantilever position (Table 5.11). It is ideally located laterally centred to the joint (Figure 5.22) where distance D_y is greatest and any displacements to the cable will result in no lateral angle changes to the snake arm. This makes Cable 1 an ideal candidate for this experiment as only the arm movements in the longitudinal plane needs to be monitored.

The set up for the experiment is shown in Figure 5.41 from the vantage point of a dedicated camera to film the changes to the joint angles as Cable 1 is actuated to lift the snake arm. The side view perspective allows the three joint angles to be measured post-experimentation for analysis but the stroke of the linear actuator is measured directly and recorded during the procedure. Power to the linear actuator is supplied through a bench power supply at 6V and activating the linear actuator is done through the power supply onboard switch.

Measuring the joint angles is performed before, during and after the activation of the linear actuator to pull Cable 1 (Figure 5.42) and the measured angles are paired with the measured stroke length changes for further analysis.

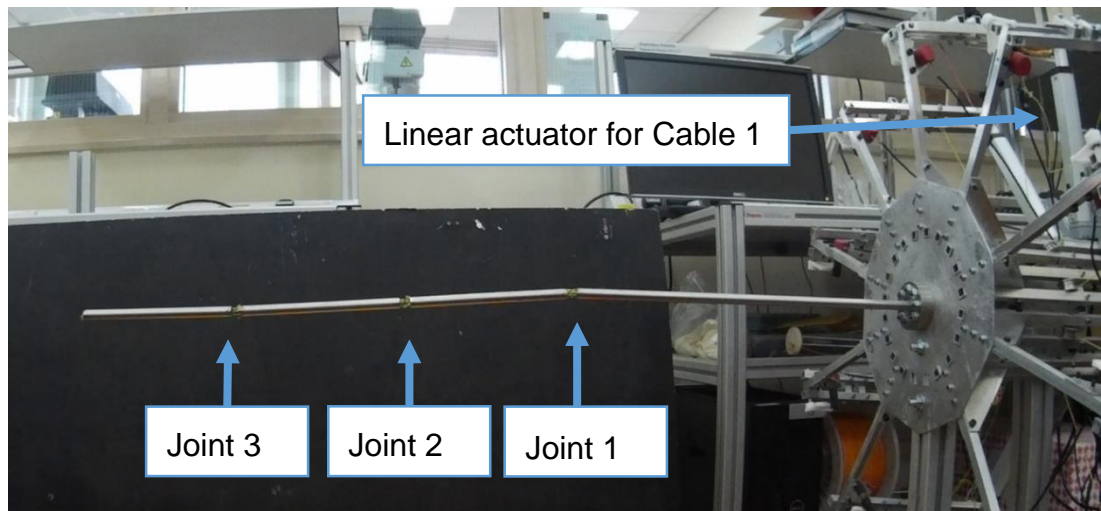


Figure 5.41 Experimental test rig set up.

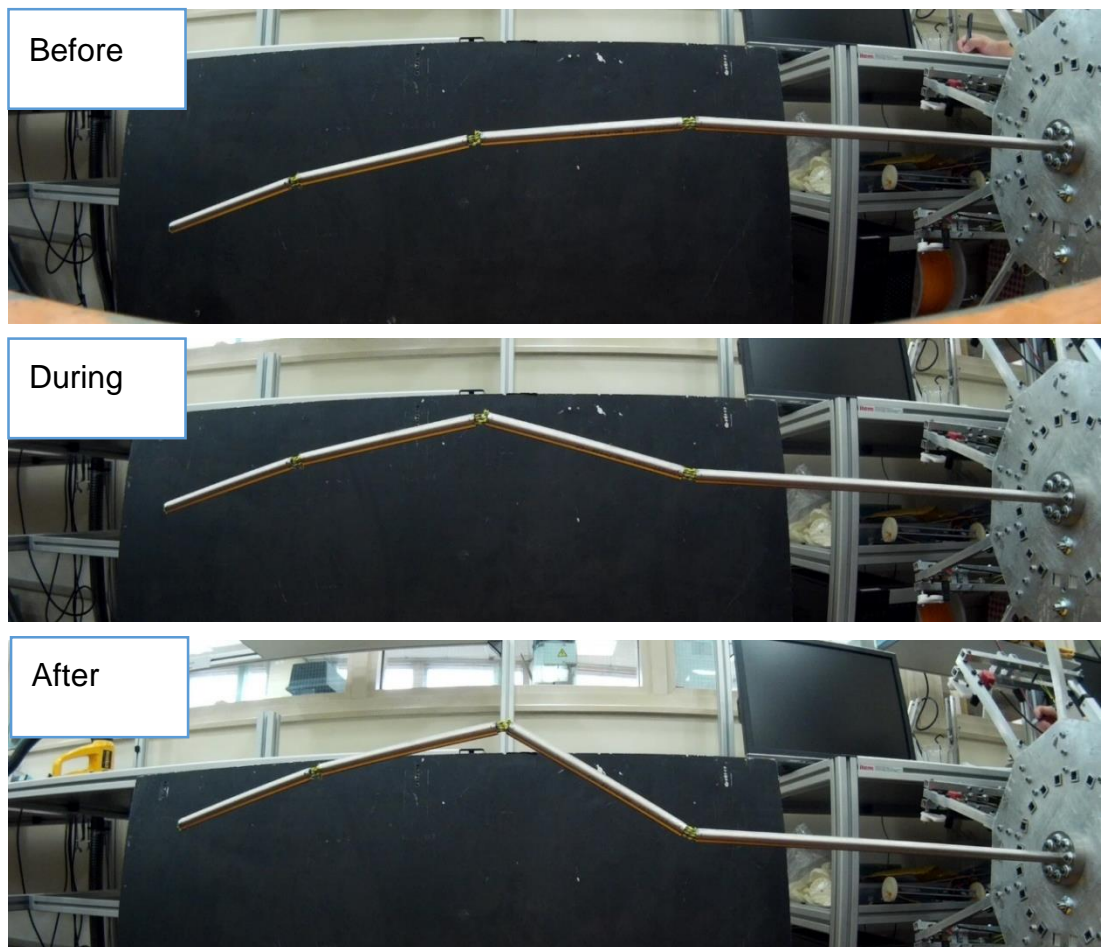


Figure 5.42 Results of actuating only Cable 1.

5.7.2 Results

The effect of actuating just Cable 1 does produce changes to the arm angles for joints 2 and 3. This is due to the cables that terminate at Joints 2 and 3 being subjected to small changes to length at Joint 1. If the pitch of Joint 1 is increased, the calculations for cable lengths in Section 5.5.1 would reveal the cables above the centre is reduced in length but the cables below the centre is increased. Therefore it was expected from the experimental results that whilst the pitch of Joint 1 will increase, the pitch of Joint 2 should decrease and the changes to the length of cables for Joint 3 should be mostly unchanged as the individual cables are shortened at Joint 1 but lengthened at Joint 2.

The experiment method was repeated ten times and the results for each plotted in Figures 5.43, 5.44 and 5.45 (full results are found in Appendix E). The manually controlled displacement of the linear actuator ranged from 0mm to 18mm and the arm positions and linear actuator is reset after each test, this left small deviations to the initial starting joint angles prior to each test.

As shown in Figure 5.43 the pitch angle of Joint 1 was increased as expected, and the linear actuators target displacement of 12mm resulted in joint pitch angles of approximately 33°.

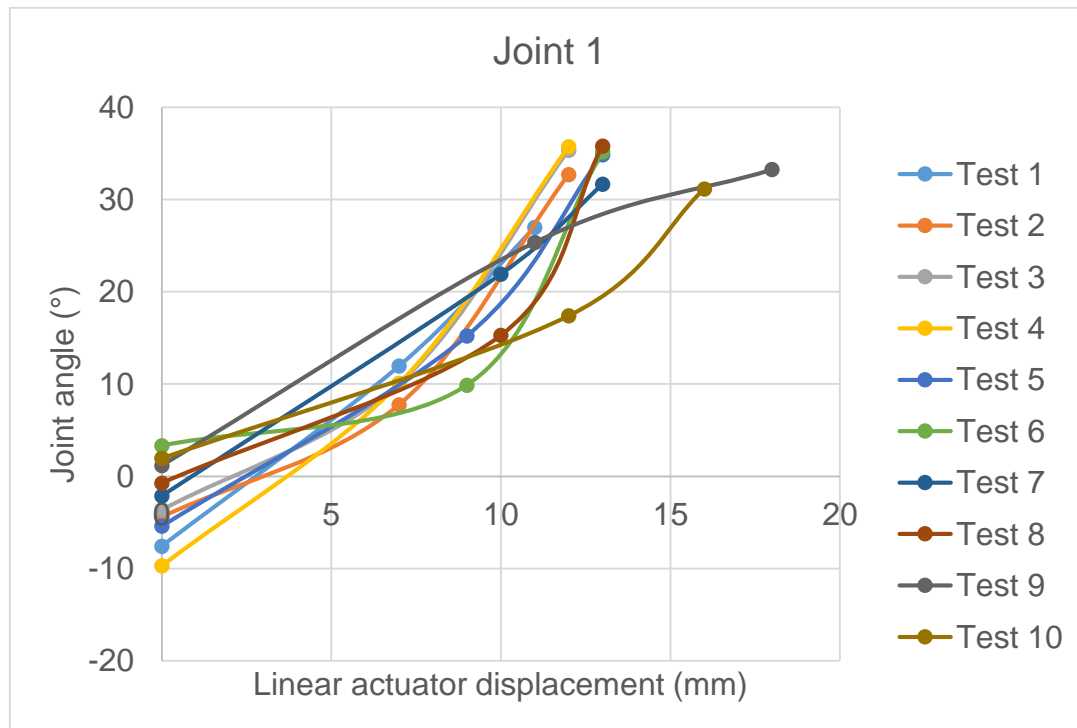


Figure 5.43 Experimental results for Joint 1.

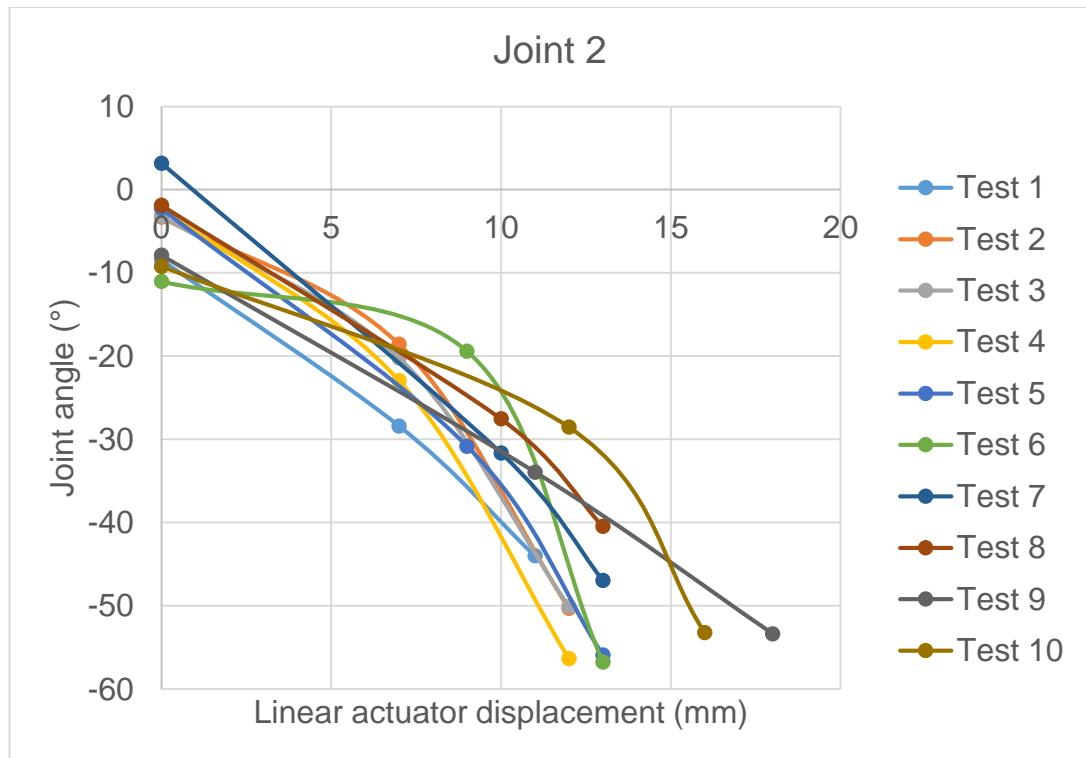


Figure 5.44 Experimental results for Joint 2.

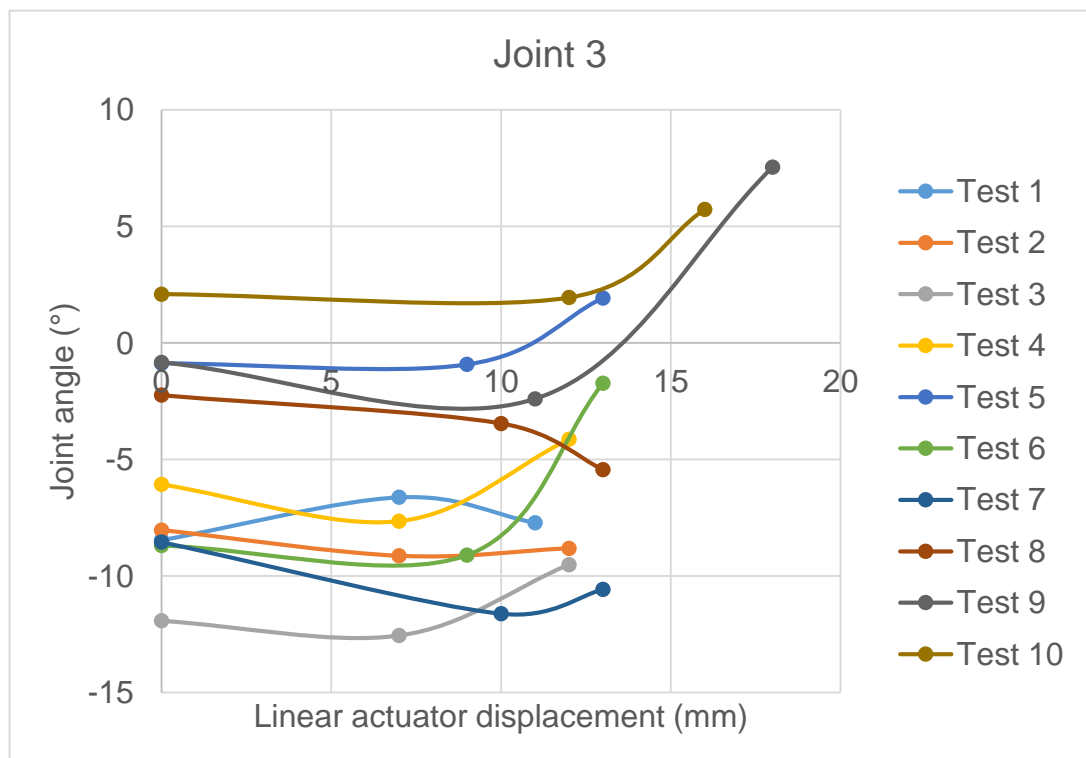


Figure 5.45 Experimental results for Joint 3.

It was anticipated Joint 2 will demonstrate a reduction in the joint pitch angle as Joint 1 was actuated, Figure 5.44 shows the average pitch angle for Joint 2 to be -51°. The difference in joint angles between Joints 1 at 33° and Joint 2 at -51°, therefore, has an effect on Joint 3 that can be seen in Figure 5.45.

Small cable length changes occur as the Joint 3 cables pass through the other joints, the changes due to the difference in angles result in Joint 3 exhibiting an increase in the pitch angle.

The variance and standard deviation (SD) of the experimental results in Table 5.35 allows the accuracy of the snake arm to be graded. From the standard deviation of individual joints 76% of all the angles occur within one standard deviation indicating confidence in the experimental results, but the deviation values are widely spread with 2.79° for Joint 1, 5.51° for Joint 2 and 6.46° for Joint 3. Interpreting the SD values shows the positional error from this method of control can be large and requires further refinement.

Table 5.35 Experimental accuracy.

Test	Cable Displacement (mm)	Joint 1 angle (°)	Joint 2 angle (°)	Joint 3 angle (°)
1	11	26.98	-43.99	-7.71
2	12	32.72	-50.31	-8.81
3	12	35.35	-50.1	-9.51
4	12	35.73	-56.35	-4.13
5	13	34.86	-55.9	1.93
6	13	35.17	-56.74	-1.73
7	13	31.65	-46.94	-10.57
8	13	35.81	-40.45	-5.43
9	18	33.25	-53.36	7.55
10	16	31.16	-53.2	5.73

Average	33.27	-50.73	-3.27
Variance	7.77	30.39	41.72
Standard deviation (sample)	2.79	5.51	6.46

5.8 Discussion and conclusion

The tension of each actuation cable is related to the length of the overall snake arm. As the overall length and cable tensions increase, the potential for component failure also increases. Along with link buckling as analysed in Section 4.3, there is the risk of cable and joint failure. Each potential failure mode limits the maximum length of snake arm possible.

To find the maximum length a snake arm of 12mm diameter is capable of, an iterative solver was formed to check for each failure mode as the snake arm length was gradually increased. The tensile strength of the actuation cables was found experimentally by pulling several samples of cable until failure. This type of experiment is common for discovering the force at which cables tend to fail and are accurate and reproducible. A non-destructive approach towards predicting the failure of the joints was implemented using FE analysis to remove the need to destroy the custom joints.

Overall, the iterative solver produced a snake arm of 1.149m in length with the joint being the limiting component. A length that the snake arm would be sufficient for inspecting environment 1, but not enough for the end effector to reach from one wall to another opposing wall. As the weight of each link can drastically affect the force required to maintain a snake arm in the horizontal cantilever position, the steel construction of each link was replaced with a lighter carbon fibre alternative of equal size to discover whether a longer snake arm can be achieved.

Replacing the steel links for carbon fibre in the iterative solver does achieve a longer snake arm length, however, at the cost of its workspace volume and reduced effective arm length. This compromise for longer overall length would not benefit the exploration of a subterranean tomb of historical significance and the use of steel links was held.

An experiment to measure how the snake arm responds to changes in a cable length was performed. Pulling a single cable by a known length produced a reproducible change in joint angle with slight variance. This variance is likely caused by stretching of each cable whilst under load. The indication of cable stretching would therefore interfere with the model for controlling the snake

arm through changes in the actuator cable lengths and additional controls will need to be implemented for any control software.

Chapter 6

Reconfigurable Dual Track Robot

This chapter investigates the use of reconfigurable mobile robots, deployed through boreholes, as an alternative technology to the use of robotic snake arms. The expected distance and weight requirements of the robot is calculated alongside the forces the robot is required to generate in order to achieve them. The whegged design incorporated into the tracks is also analysed to measure the capability of the robot over rough terrain. Finally, the experiments to find the actual driving forces of the tracks are performed to calculate the actual range of the robot in comparison to the target range.

6.1 Introduction

To explore a mineshaft up to 200m long and located approximately 9m from the entrance through a borehole. The 1.149m length of the snake arm developed in Chapter 5 becomes unsuitable for performing inspections at the distances required. However, this result was anticipated and the decision matrix and discussions in Chapter 3 revealed an alternative mobile robotic device is an attractive option to explore large distances beyond the initial entry point. Deciding upon a non-modular reconfigurable robot using wheel-leg profiles to improve its locomotion capabilities, the development of a reconfigurable dual-track robot is investigated here to conduct explorations beyond the range of conventional snake arms.

6.2 Specifications

As presented in Chapter 3, environment 2 was to conduct a visual survey of an underground mine, where the mine entrance is collapsed and sealed. In many situations, the quickest method of entry would be through a vertical borehole from an accessible mine shaft into the sealed shaft. In this scenario, the following specification was developed in Chapter 3.

The specifications given were:

- The robot will be deployed vertically downwards in a borehole of length 30ft (9.144m) 41mm diameter hole.
- The robot will have the ability to travel 200m on a slight 2° incline.

- The robot will be tethered to transmit power and assist in extraction of the device
- Illumination from a small light, such as a single Cree XLamp module will provide sufficient illumination [106].
- Tapered at rear for withdrawal.
- The robot weight needs to be sufficiently high to generate traction forces sufficient to pull the cable.
- The robot is required to be deployed from an entrance tunnel of up to height/width 2.5m.

6.3 Design theory

Initially the theory of tracked vehicles will be developed without regard for reconfiguration constraints to understand the required performance of mobile robots beyond the entrance point. Assuming a tracked configuration instead of wheels as the method of locomotion due to a greater ability to obtain footholds over higher obstacles and increased surface contact as described in Chapter 2.3.1.

There is no ideal distance for the separation of the tracks. The ratio or aspect ratio between wheelbase and track width (Figure 6.1) differs according to the purpose of a vehicle. For vehicles designed for speed where aerodynamics for reduced drag calls for a small track width and large wheelbase ratio, lateral stability is sacrificed for the reduced track width and increases the likelihood of toppling over.

A small wheelbase with large track width contributes to a vehicle with smaller turning radius and enhanced resistance to lateral weight transfer and body lean.

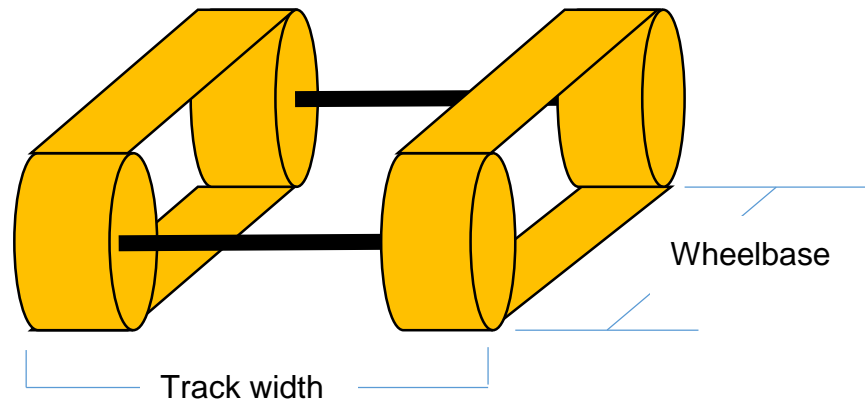


Figure 6.1 Illustrating track width and wheelbase.

6.3.1 Robot Mass

The mass of the robot serves to produce the required tractive force to travel the specified length. The mass can be calculated when assuming the robot on an incline (Figure 6.2) is static but at the point of moving and is located at the furthest point. At this point, the forces acting to drag the robot down the incline would be highest due to the tether drag and assuming a smooth surface.

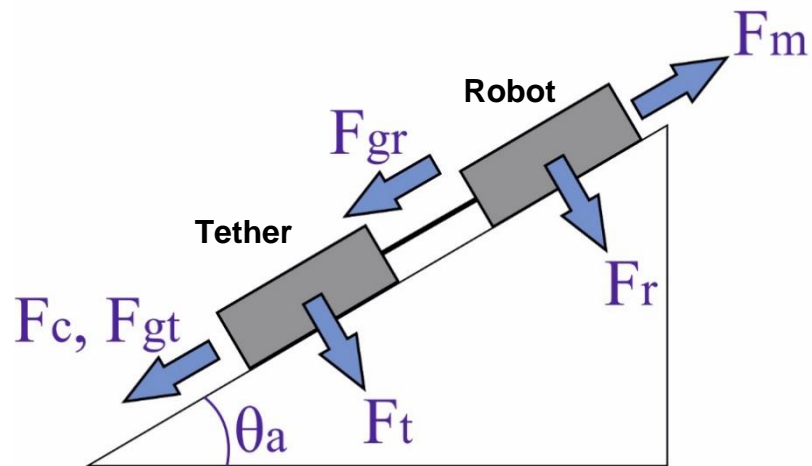


Figure 6.2 Free body diagram of robot and tether on an incline.

Where:

F_m = Robot static friction

F_r = Robot normal force

F_{gr} = Robot mass acting down incline

F_c = Tether static friction

F_t = Tether normal force

F_{gt} = Tether mass acting down incline

These equations are valid for the free body diagram:

$$F_m = \mu_r \cdot M_r \cdot g \cdot \cos(\theta_a) \quad 6.1$$

$$F_{gr} = M_r \cdot g \cdot \sin(\theta_a) \quad 6.2$$

$$F_c = \mu_t \cdot C_m \cdot x_c \cdot g \cdot \cos(\theta_a) \quad 6.3$$

$$F_{gt} = C_m \cdot x_c \cdot g \cdot \sin(\theta_a) \quad 6.4$$

Assuming the mass of the robot is sufficiently high so that F_m is equal or greater to the sum of the forces acting down the incline.

$$F_m \geq F_{gr} + F_c + F_{gt} \quad 6.5$$

$$\begin{aligned} \mu_r \cdot M_r \cdot g \cdot \cos(\theta_a) \\ \geq M_r \cdot g \cdot \sin(\theta_a) + \mu_t \cdot C_m \cdot x_c \cdot g \cdot \cos(\theta_a) + C_m \cdot x_c \cdot g \cdot \sin(\theta_a) \end{aligned} \quad 6.6$$

$$\begin{aligned} \mu_r \cdot M_r \cdot g \cdot \cos(\theta_a) - M_r \cdot g \cdot \sin(\theta_a) \\ \geq \mu_t \cdot C_m \cdot x_c \cdot g \cdot \cos(\theta_a) + C_m \cdot x_c \cdot g \cdot \sin(\theta_a) \end{aligned} \quad 6.7$$

Rearranging,

$$M_r \geq \frac{C_m \cdot x_c (\mu_t \cdot \cos(\theta_a) + \sin(\theta_a))}{\mu_r \cdot \cos(\theta_a) - \sin(\theta_a)} \quad 6.8$$

Where:

μ_r = Static coefficient of friction between robot and slate floor

μ_t = Static coefficient of friction between tether and slate floor

θ_a = Angle of incline

C_m = Mass of tether per metre

x_c = Length of tether (distance travelled up the incline)

Using the values:

$$\mu_r = 0.9 \text{ (rubber to dry concrete) [121]}$$

$$\mu_t = 0.9 \text{ (rubber to dry concrete) [121]}$$

$$\theta_a = 2^\circ$$

$$C_m = 0.03344 \text{ kg/m}$$

$$x_c = 200\text{m}$$

From Equation 6.8 and the values defined here, the required mass of the robot is calculated to be at least 7.229kg. However, the actual weight of the robot after manufacturing was 2.372kg. Adding additional weight was problematic

given the diameter of 36mm and lack of available space. Given the density of grade 316 stainless steel is 8.0 g/cm^3 [122], to make up the additional 4.857kg weight, a 36mm diameter stainless steel bar must be 0.6m long. Consequently, the specified 200m distance may not be achieved. Despite this, the presence of rough terrain could aid traction that in combination with sufficient driving force would increase the distance possible.

If the length of tether (x_c) is indicative of the distance travelled by the robot, then rearranging Equation 6.8 for x_c will provide the maximum distance possible assuming a smooth surface. The variable x_c therefore equates to 65.629m.

6.3.2 Driving Force

For the robot to climb an incline of angle of known mass M_r , the robot must generate sufficient pulling force F_p to overcome gravitational force F_{gr} and F_{gt} , and the forces required to overcome the drag from the tether F_c .

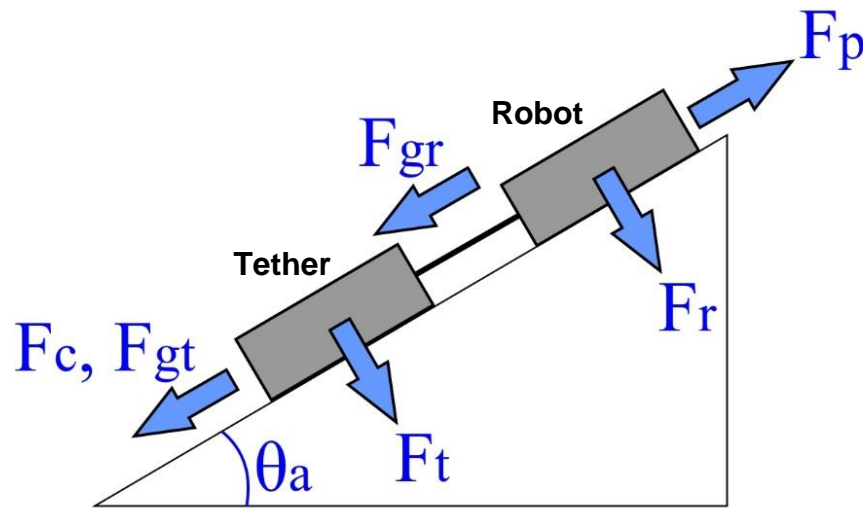


Figure 6.3 Free body diagram of the robot on an incline.

These equations are valid for the free body diagram:

$$F_r = M_r \cdot g \cdot \sin(\theta_a) \quad 6.9$$

$$F_{gr} = M_r \cdot g \cdot \cos(\theta_a) \quad 6.10$$

Force F_p is also highest when located at the furthest point up the incline due to the tether friction and mass.

$$F_p \geq F_{gr} + F_c + F_{gt} \quad 6.11$$

$$F_p \geq M_r \cdot g \cdot \cos(\theta_a) + \mu_t \cdot C_m \cdot x_c \cdot g \cdot \cos(\theta_a) + C_m \cdot x_c \cdot g \cdot \sin(\theta_a) \quad 6.12$$

Therefore, in order to climb the incline, the required pulling force is:

$$F_p \geq M_r \cdot g \cdot \sin(\theta_a) + C_m \cdot x_c \cdot g \cdot [\sin(\theta_a) + \mu_c \cdot \cos(\theta_a)] \quad 6.13$$

Using the values:

$$\mu_r = 0.9 \text{ (rubber to dry concrete) [121]}$$

$$\mu_t = 0.9 \text{ (rubber to dry concrete) [121]}$$

$$\theta_a = 2^\circ$$

$$C_m = 0.03344 \text{ kg/m}$$

$$x_c = 200\text{m}$$

From Equation 6.8, the required force of the robot of ideal weight 7.229kg is calculated to be $\geq 8.724\text{N}$.

6.4 Robot design

To fabricate an experimental robot similar to the Hitachi shape changing robot concept (from Section 6.4) the design of the robot was broken down into three modules, two locomotion and a single deployment module.

Preserving the differential steering tracks as the locomotion method for its ability to navigate rough terrain and small size, the robot concept assumes a U-like shape once deployed (Figure 6.4) but can configure into a slender straight line throughout the deployment process (Figure 6.5). The finished dimensions and weights are shown in Table 6.1.

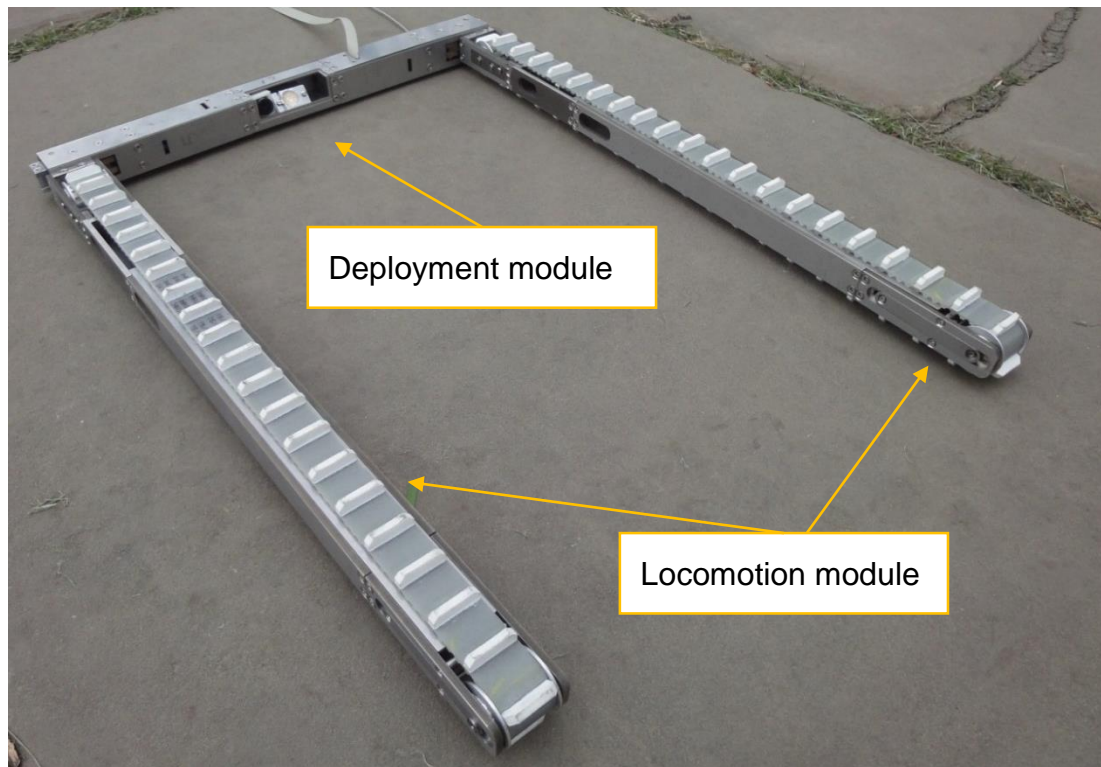


Figure 6.4 The mine exploration robot in the deployed configuration.



Figure 6.5 The mine exploration robot in the un-deployment configuration.

Table 6.1 Mine exploration robot specifications.

Mass	2.372	kg
Deployed size (H x W x L)	33 x 335 x 455	mm
Un-deployed size (H x W x L)	33 x 31 x 1199.5	mm

6.4.1 Locomotion Module

For the robot to be deployed the diameter of the robot must be less than the specified 41mm diameter, leaving 2.5mm room each side for clearance, the diameter becomes 36mm (Figure 6.6). The length of the un-deployed robot was only limited by the height of the shaft at approximately 2.5m meaning although the diameter was restricting, the available length provided the volumetric space to successfully house all the internal components by extending the robot.

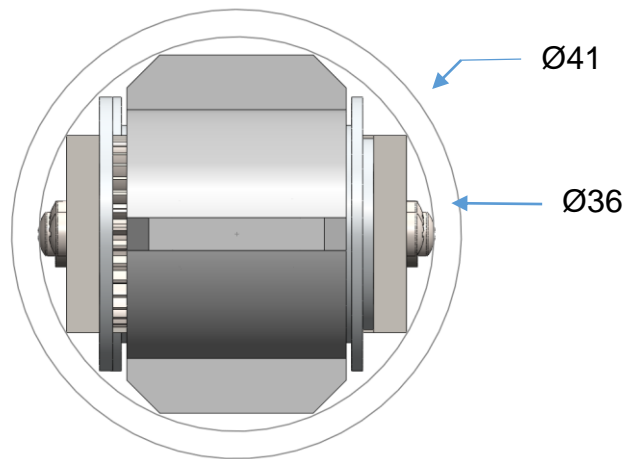


Figure 6.6 Front view of the locomotion module and the diameter limits.

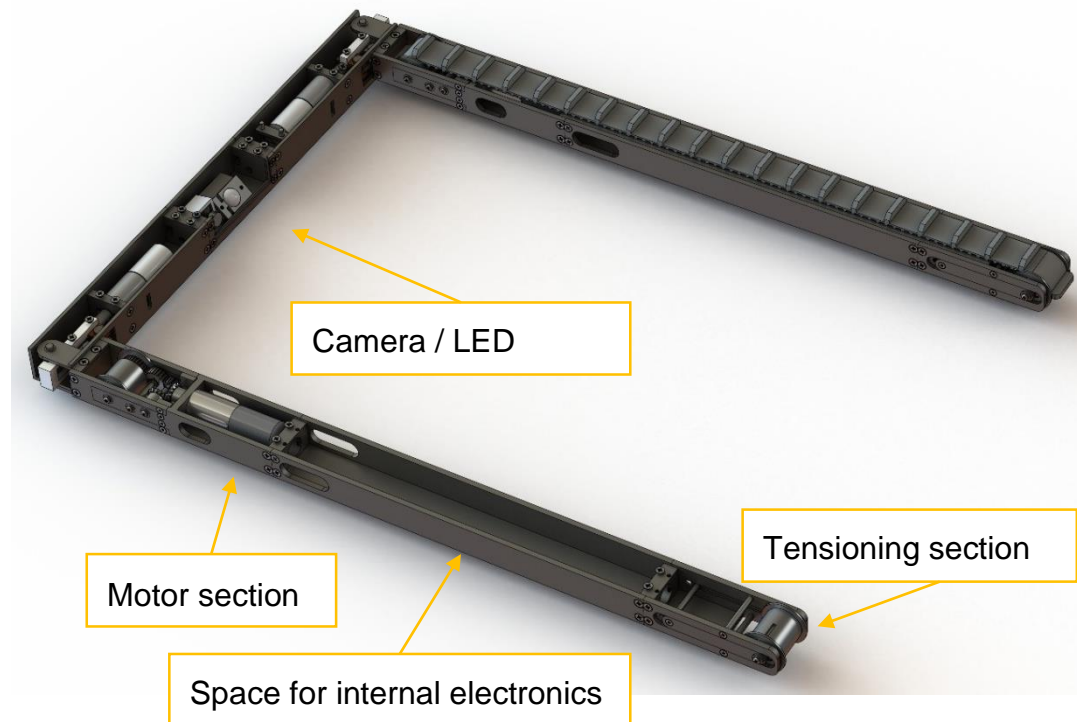


Figure 6.7 Locomotion module.

The locomotion module is constructed from three sections, one end houses the motor and gearbox and the other maintains the belt tension of the tracks (Figure 6.7). The tension is supplied through a sliding platform and capacity for containing variable stiffness extension springs to adjust the tension of the tracks.

6.1.1.1 Gearbox

The force exerted from the tracks is supplied from a specially designed low profile gearbox (Table 6.3) and motor (Table 6.2) that fits entirely within the tracks as shown in Figure 6.8.

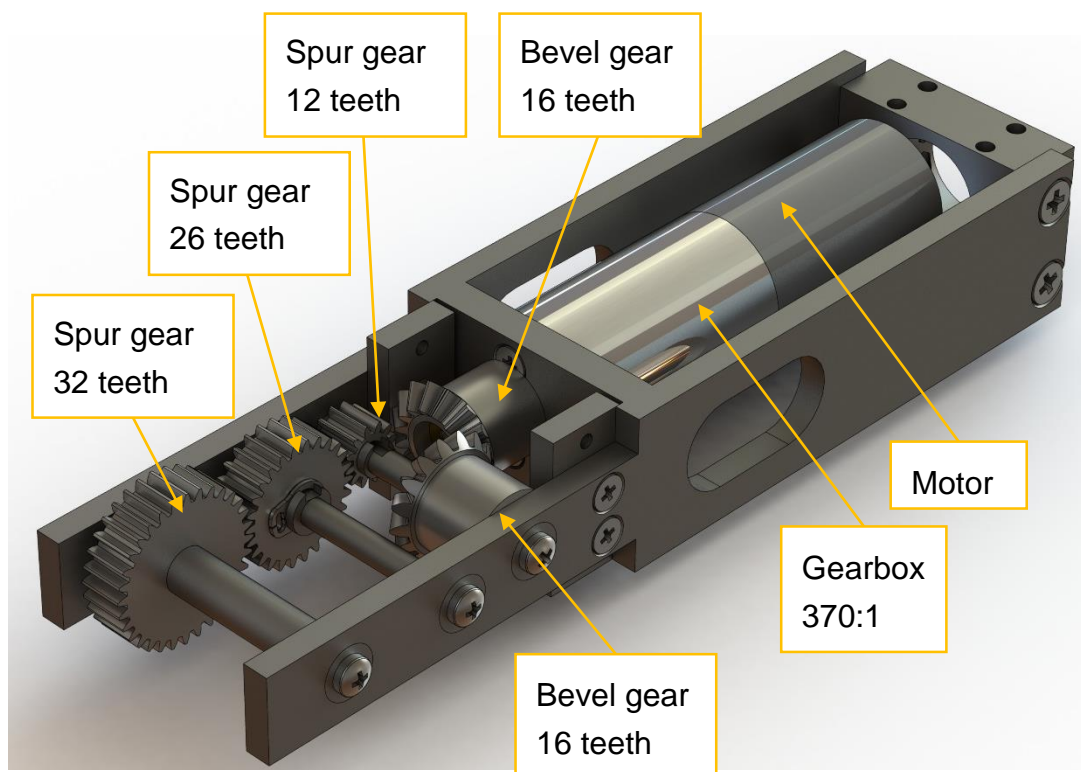


Figure 6.8 Motor and gearbox section for locomotion module.

Table 6.2 Maxon motor specification.

Brand	Maxon Motor
Part number	110044
Nominal torque (Nm)	0.00219
Nominal speed (rpm)	6700
No load speed (rpm)	12300

Table 6.3 Maxon motor planetary gearbox specification.

Brand	Maxon Motor
Part number	110324
Reduction	370:1
Max continuous torque at gearbox output (Nm)	0.25

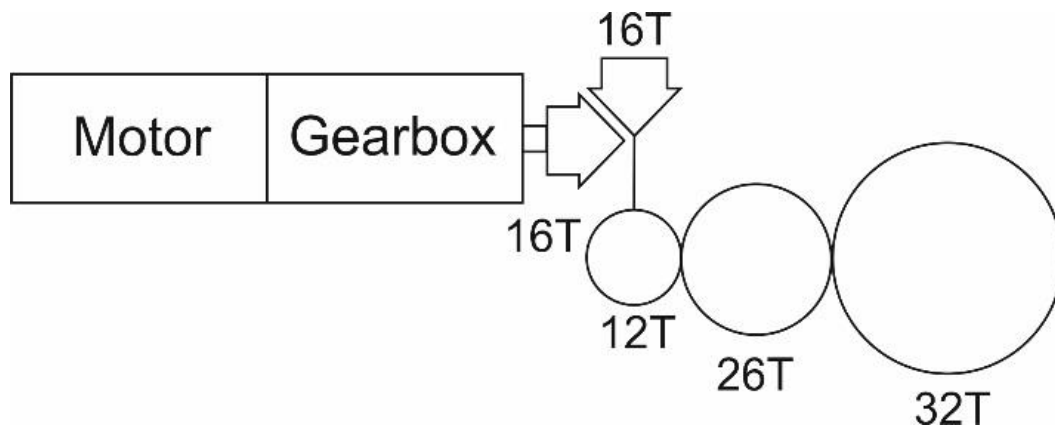


Figure 6.9 Track gear train.

The maximum output torque was calculated from the gear train in Figure 6.9. These calculations were necessary during the design phase prior to manufacturing to ensure the force output is adequate to meet the demands from the driving force calculations in Section 6.3.2. The calculated torque produced is shown in Table 6.4.

Table 6.4 Maximum torque from track gearbox.

Motor output	0.00219 Nm
Gearbox output	0.810 Nm
Track output	2.161 Nm

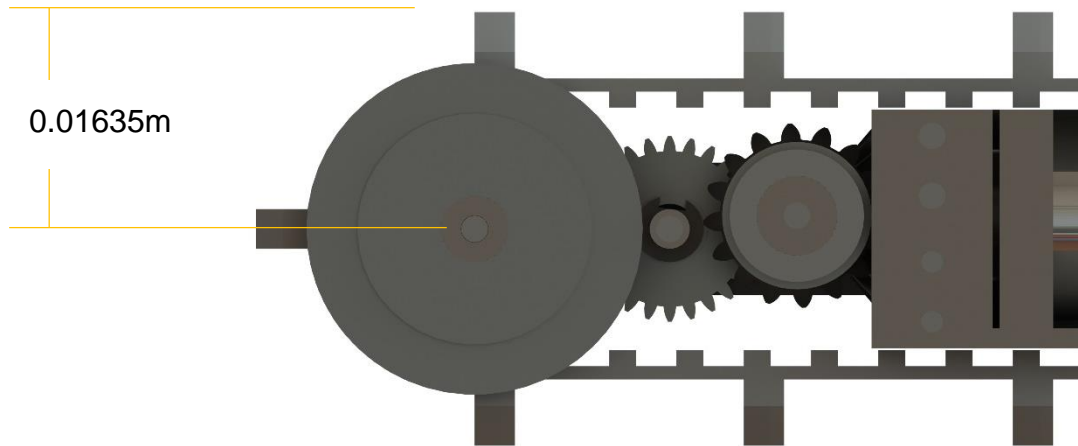


Figure 6.10 Side view of the track.

Using the perpendicular distance between the centre and track (Figure 6.10), the maximum force produced was calculated as:

$$Force = \frac{Torque}{Distance} \quad 6.9$$

$$Force = \frac{2.1608}{0.01635} \quad 6.10$$

$$Force = 132.159N \quad 6.11$$

However, the Maxon motor gearbox is only rated for a maximum continuous torque of 0.25Nm (from Table 6.3). Substituting this value as the gearbox output in Table 6.4 results in a torque of 0.667Nm and 40.775N of force. This provides a factor of safety of:

$$\frac{Force\ produced}{Force\ required} = \frac{40.775}{8.724} = 4.674 \quad 6.12$$

Assuming a mechanical efficiency of 50% that doubles the force required. The calculated factor of safety will remain larger than one; this result indicates the system is still sufficient for driving the robot.

The maximum speed of the track and ultimately the speed of the robot can also be calculated from the gearbox ratio and track geometry.

Table 6.5 Maximum speed from track gearbox.

Motor nominal output	6700 rpm
Gearbox output	18.108 rpm
Track output	6.7905 rpm

Therefore:

$$\text{Theoretical max speed} = \text{circumference} \cdot \text{rpm} \quad \mathbf{6.13}$$

$$\text{Theoretical max speed} = 2 \cdot \pi \cdot r \cdot \text{rpm} \quad \mathbf{6.14}$$

$$\text{Theoretical max speed} = 2 \cdot \pi \cdot 0.0164 \cdot \frac{6.791}{60} \quad \mathbf{6.15}$$

$$\text{Theoretical max speed} = 0.0116 \text{ m/s} \quad \mathbf{6.16}$$

6.1.1.2 Step-Climbing

Assuming rough terrain within the mineshaft, the robot would be expected to climb over steps and obstacles. The function of the 5mm high profiles in a 20mm pitch on the tracks serves two purposes, to provide ground clearance to the robot and also the characteristics of a whegged robot [16]. The whegs can allow the robot to maintain a discontinuous foothold on irregular terrain, similar to legs [37]. Additionally, the whegs enable such robots to climb and negotiate terrain that are usually impassable for wheeled robots.

The maximum step height of the tracks is calculated from 20mm pitch of the whegs, 3mm thickness and 16.35mm radius.

$$\text{arc length} = \frac{\theta}{360} \cdot \text{circumference} \quad \mathbf{6.17}$$

$$\text{arc length} = \frac{\theta}{360} \cdot 2 \cdot \pi \cdot r \quad \mathbf{6.18}$$

$$20 = \frac{\theta}{360} \cdot 2 \cdot \pi \cdot 16.35 \quad \mathbf{6.19}$$

Rearranging,

$$\theta = \frac{20 \cdot 360}{2 \cdot \pi \cdot 16.35} \quad \mathbf{6.20}$$

$$\theta = 70.087^\circ \quad \mathbf{6.21}$$

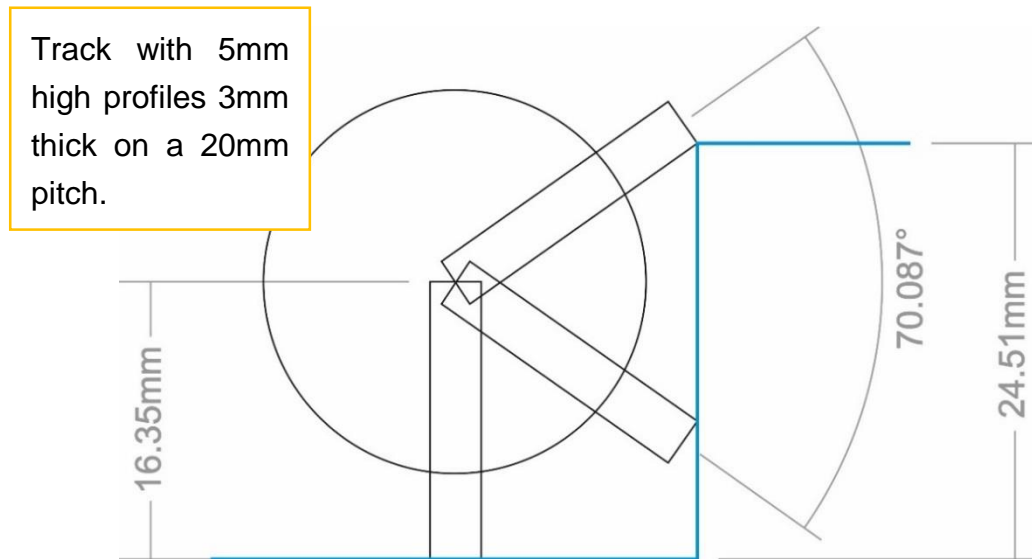


Figure 6.11 Whegged tracks climbing steps.

From the equations and Figure 6.11, the maximum step height the robot can climb is 24.51mm.

6.4.2 Deployment Module

The role of the deployment module is to connect the two locomotion modules and change the configuration of the robot when required. To complete the survey of the shaft, the module also contains the single Cree XLamp alongside an analogue camera.

To find the torque required in order to deploy the locomotion modules, the deployment module and a single locomotion module was modelled as a two-link arm moving from 0° to 90° (Figure 6.12). When at 0°, the torque is expected to peak due to the greater gravity effect.

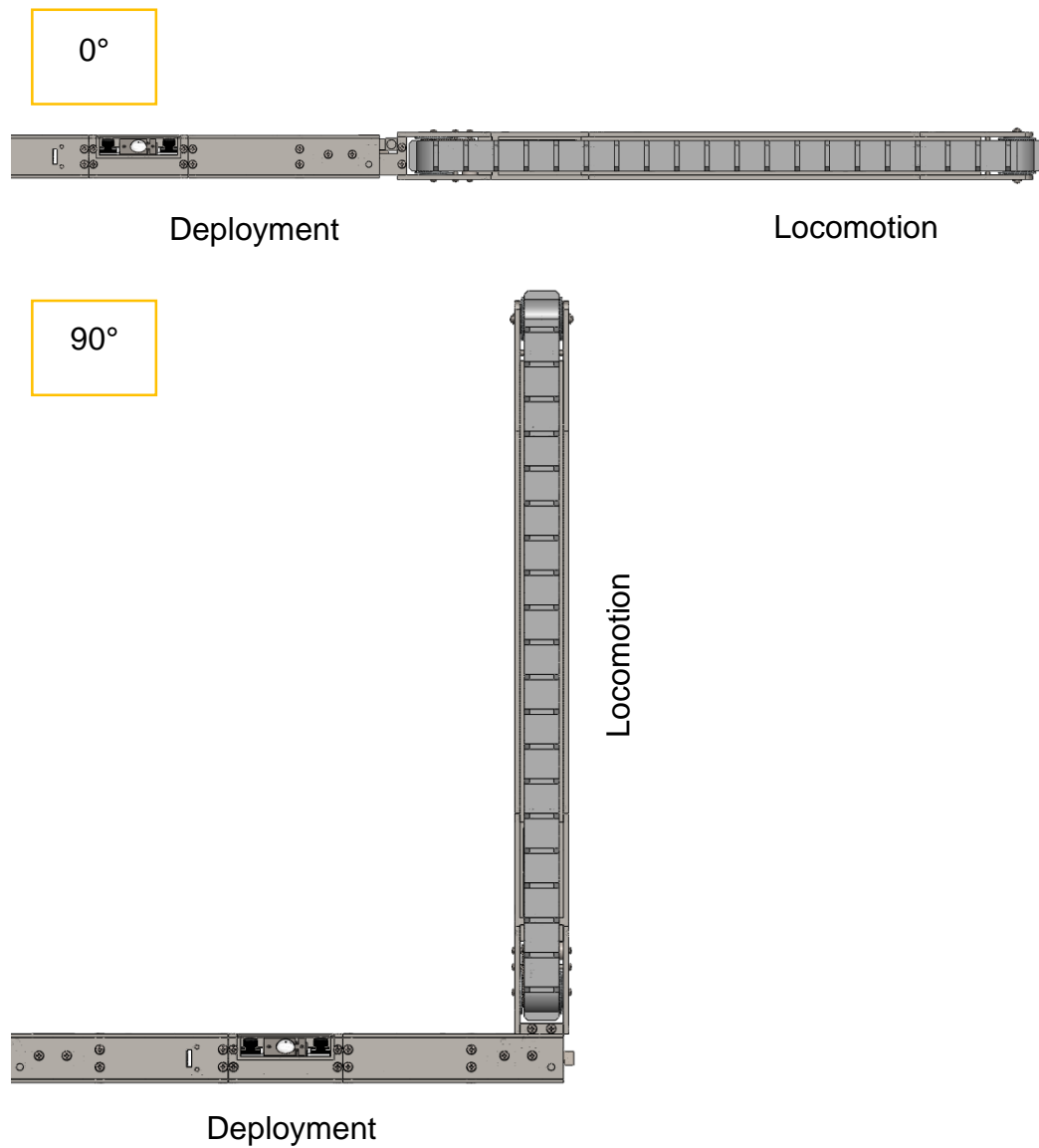


Figure 6.12 Two modules as a two-link arm at both angle extremes.

Table 6.6 Deployment module properties.

Length (m)	0.306
Actual mass (kg)	0.69
Centroid position (m)	0.153

Table 6.7 Locomotion module properties.

Length (m)	0.441
Actual mass (kg)	0.789
Centroid position (m)	0.222

Using the Recursive Newton-Euler methodology as used in Chapter 4.2, the torques required to actuate the arm using the link properties at table 6.6 and Table 6.7 as a function of the arm angle was computed and the results in Figure 6.13 show a peak of 1.6928Nm when at 0° to 0Nm at 90°.

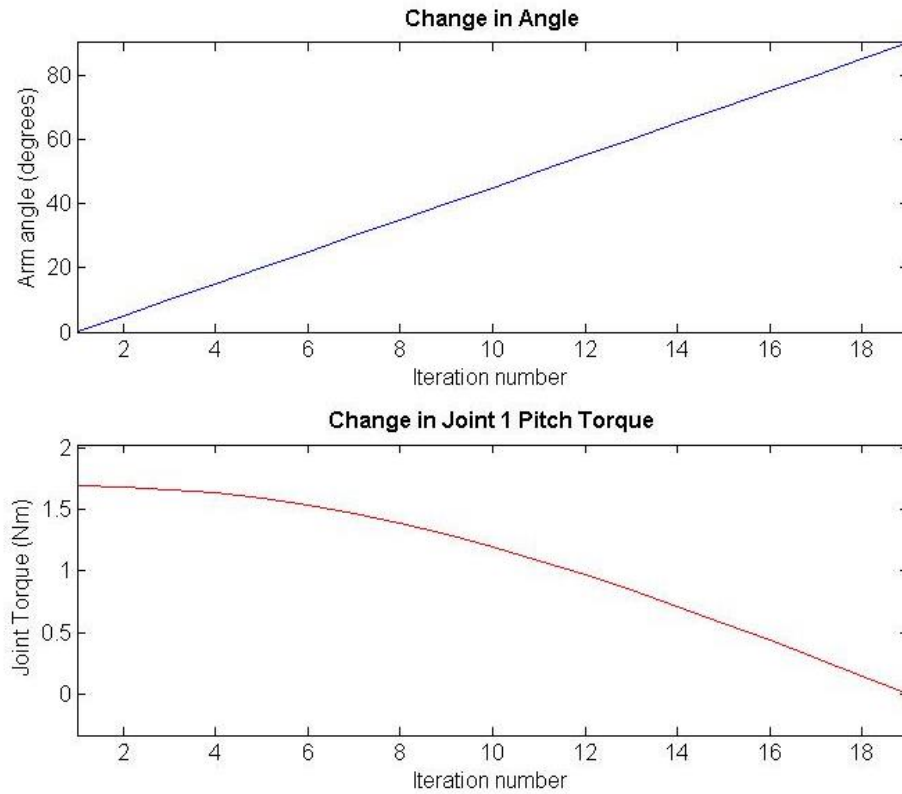


Figure 6.13 Change in joint torque versus arm angle.

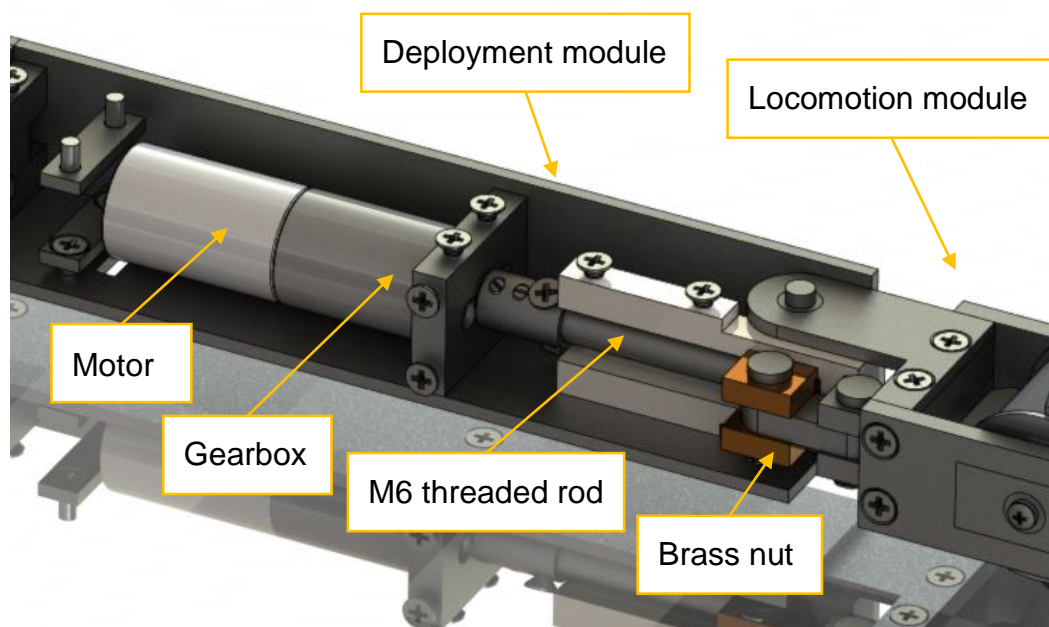


Figure 6.14 Inside deployment module.

Production of the large torque requirements rests upon the linear actuator mechanism within the deployment module (Figure 6.14). Utilising the same gearbox (Table 6.3) and motor (Table 6.2) combination as the locomotion module the torque generated is non-linear and a function of the arm angle.

The power screw assembly (Figure 6.15) converts the motor's torque into a reciprocating linear force and is calculated as:

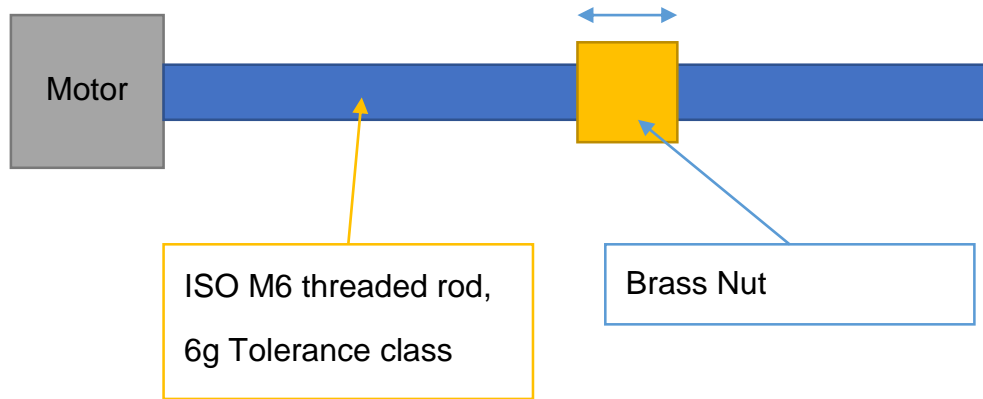


Figure 6.15 Power screw components.

Table 6.8 Power screw properties.

Motor torque, T		0.8103	Nm	
Pitch, P		0.001	m	
Lead, L		0.001	m	
Nominal diameter, D		0.005312	m	
Root diameter, Di		0.004596	m	
Pitch diameter, d	$d = \frac{D + D_i}{2}$	0.004954	m	6.22
Helical angle, θ	$\theta = \tan^{-1}\left(\frac{L}{\pi \cdot d}\right)$	3.6764	°	6.23
Coefficient of friction, μ		0.19		
Friction angle, ℓ	$\ell = \tan^{-1}(\mu)$	10.758	°	6.24
Thread angle, α	$\alpha = \frac{\alpha}{2}$	30	°	6.25

Specifications for the power screw assembly are shown in Table 6.8. The force produced by the power screw is dependent on whether it is raising (90° to 0°) or lowering (0° to 90°).

$$F_{raise} = \frac{2 \cdot T}{d \left(\frac{\mu \cdot \sec(\alpha) + \tan(\theta)}{1 - \mu \cdot \sec(\alpha) \cdot \tan(\theta)} \right)} = 1137.5667N \quad 6.26$$

$$F_{lower} = \frac{2 \cdot T}{d \left(\frac{\mu \cdot \sec(\alpha) - \tan(\theta)}{1 + \mu \cdot \sec(\alpha) \cdot \tan(\theta)} \right)} = 2140.1842N \quad 6.27$$

Working with the smaller force produced, the torque produced can be calculated simplifying the mechanism into a 4-bar linkage force analysis with the forces labelled in Figure 6.16.

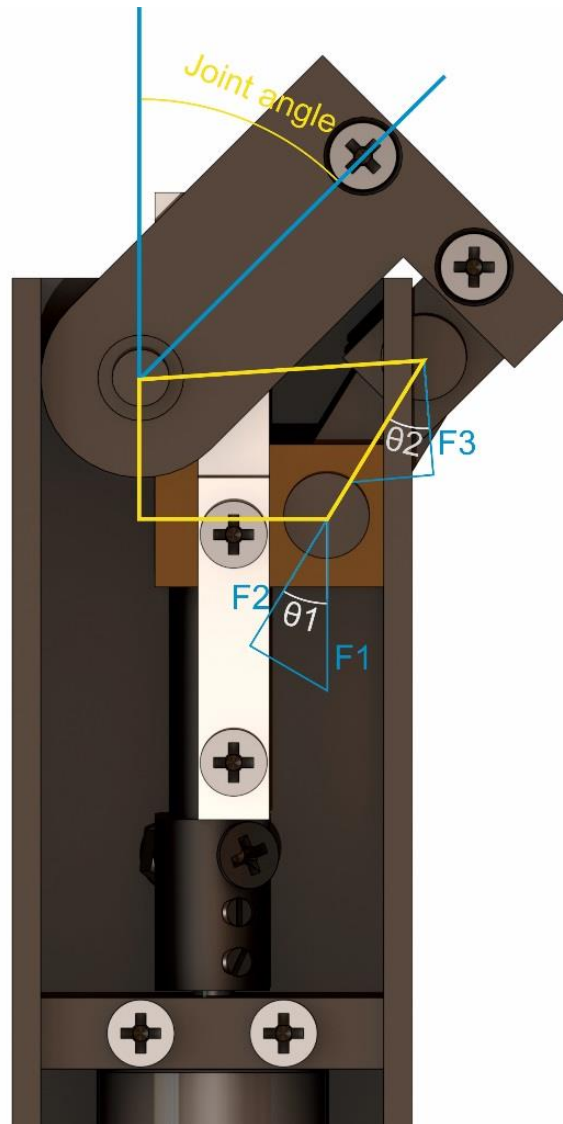


Figure 6.16 Deployment mechanism.

Figure 6.17 shows the torque produced by the power screw assembly and the torque required to lift the locomotion module as calculated in Figure 6.13. As the torque produced is consistently greater than the torque required, the assembly should be able to lift the locomotion module with no external assistance.

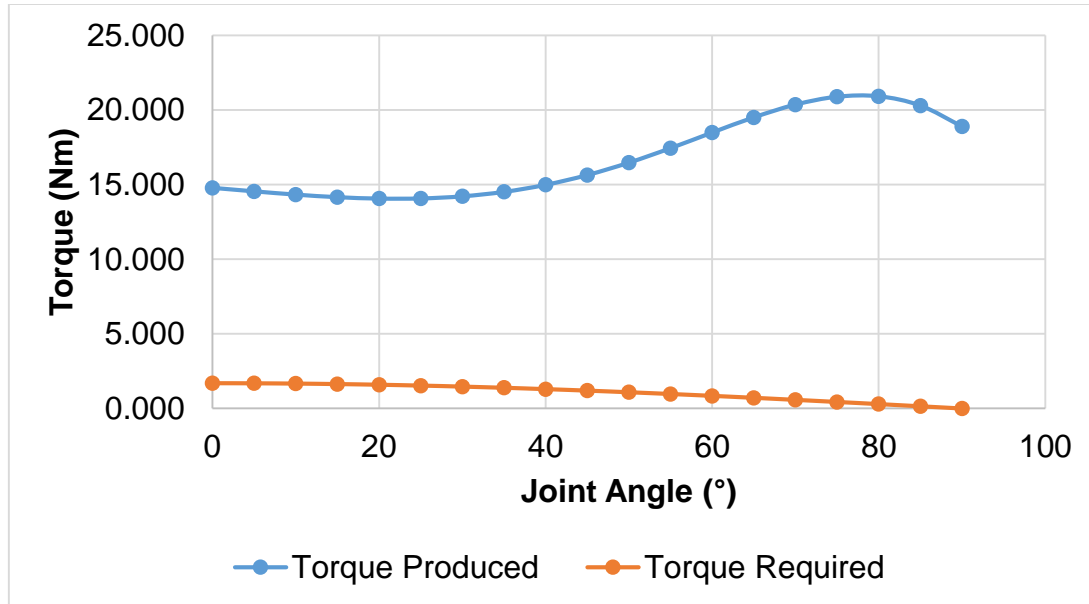


Figure 6.17 Torque results.

Reducing the motor/gearbox output to the 0.25Nm gearbox operating limit, the force produced by the power screw assembly is reduced to 350.97N. Recalculating the torque results reveal the mechanism still provides the required torque with a minimum FOS of 2.7 (Figure 6.18). Accordingly, the deployment system remains fully capable of actuating the locomotion modules in the horizontal cantilever position where the torque requirements are at its peak.

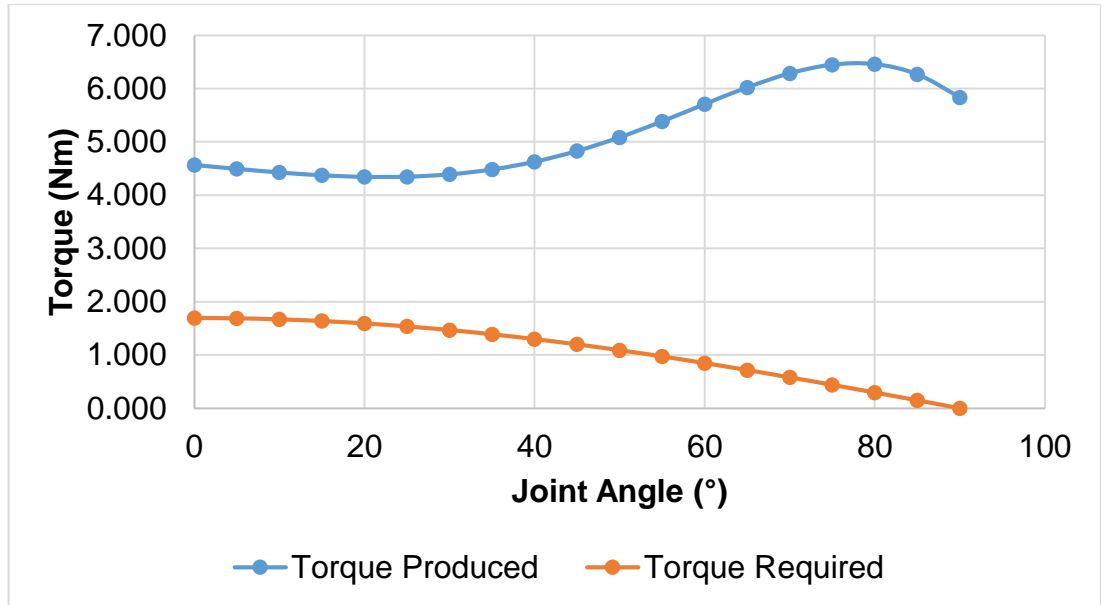


Figure 6.18 0.25Nm Gearbox output torque results.

6.5 Experimentation

6.5.1 Speed

The speed of the robot was theoretically calculated as 1.16cm/s, to establish the actual speed the robot was tested to displace 0.6m in a straight line and manually timed as shown in Figure 6.19.



Figure 6.19 Experimental set up for timed distances.

The test was repeated for both deployment states and the speed calculated as:

$$v = \frac{s}{t} \quad 6.28$$

Where:

v = Velocity (m/s)

s = Distance (m)

t = Time (s)

Table 6.9 Velocity results.

Distance	Joint angle 0°	Joint angle 90°
0.6	39.99	40.92
0.6	39.64	39.58
0.6	39.71	39.92
0.6	39.70	39.84
0.6	39.80	39.55
0.6	39.64	39.55
0.6	39.60	39.74
0.6	39.72	39.53
0.6	39.60	40.13
0.6	39.59	39.84
Average	39.70	39.86

The velocity of the robot in the un-deployed straight line configuration is, therefore:

$$v = \frac{0.6}{39.70} = 1.51 \text{ cm/s} \quad \mathbf{6.29}$$

The velocity of the robot in the deployed U-like configuration is, therefore:

$$v = \frac{0.6}{39.86} = 1.51 \text{ cm/s} \quad \mathbf{6.29}$$

This results in the experimental speed being greater than the theoretical speed, a difference of 26.0479%. This can be explained due to the theoretical speeds being calculated from the motors nominal speed that would normally vary under different loading conditions. The results in Table 6.9 also shows the speeds to be consistent.

6.5.2 Track force

Analysis of a robot climbing an incline revealed the force required by the locomotion drive to be 8.724N. To investigate whether the robot can supply the force a test rig was built to allow different loads to be attached to the drive (Figure 6.20).

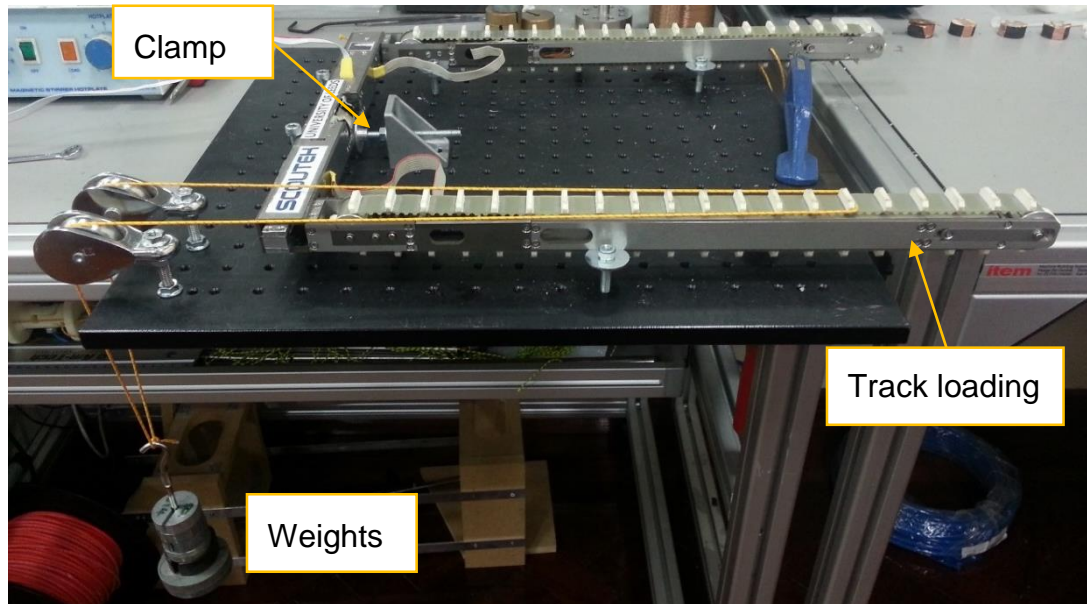


Figure 6.20 Track force experimental set up.

As shown in Figure 6.20 the test procedure involved attaching weights to the tracks in increments of 0.1 and 0.5kg and driving the tracks forward to lift the weights upwards. It was observed that overloading the tracks would cause the belts to slip due to the belt-tensioning component being overcome and unable to maintain non-slip contact between timing pulley and belt. A solution was found by increasing the spring stiffness of the tensioning component, this overall increases the tension throughout the belt and also increased the force required for the belt slip to occur.

The aim of this experiment was not to find the absolute force output, but rather a sufficient amount of force to be supplied for the robot to climb the 2° incline at 200m and at which point does the track slippage start to occur without further increasing the tensioning spring stiffness.

Table 6.10 Testing robot at 2° incline.

Distance (m)	200	Incline (°)	2
μ_r	0.9	μ_t	0.9
Required mass (kg)	7.2285	Required force (N)	8.7242
Applied force (N)	9.32	Verdict	Pass

The results of Table 6.10 shows the locomotion module capable of providing the torque required to drive a 7.229kg robot up 200m on a 2° incline. The next

step was to incrementally increase the load on the tracks until slippage occurred. At a load of 12.86N, no slippage had occurred. It was observed at a load of 13.36N slippage was becoming a frequent occurrence.

From Equation 6.13, the incline the robot can no longer climb the 200m distance can be found as 4.9° however the robot mass must be increased to 8.0969kg.

6.6 Discussion and conclusion

The theory developed with the two track locomotion system with wheel-leg profiles would allow the robot to climb over small obstacles and generate sufficient force to climb the 200m distance. However, for the necessary traction to be generated the weight of the manufactured robot is insufficient without substantial modifications to incorporate additional mass. These weight requirement calculations on an incline does assume a smooth surface where only the weight provides the static friction force, however a mineshaft floor is rarely ever smooth. An advantage of using tracks with the whegged profiles is it will allow the robot to gain additional traction to further increase the distance travelled.

The analysis and experimentation with the robot has shown it to be capable of contributing a driving force of up to 13.36N on the 2.372kg platform to a distance of 65.629m on a 2° incline. At this distance, the robot is only employing 2.863N driving force according to Equation 6.13. If the robot was to fully utilise the driving force with the same mass, Equations 6.8 and 6.13 also show the robot to be capable of achieving 10.813m on a 33.5° incline.

Ground clearance for the robot is limited to the height of the track profiles at 5mm. The length of the deployment module dictates the size of the track width. As the dimensions of the robot are known (Table 6.1), the aspect ratio of the robot can be calculated as 1.36:1. This track width contributes towards resistance to lateral weight transfer and body lean. The low ground clearance would result in obstacles being caught in the space between the two tracks resulting in a build-up of debris. Likewise, this issue will also occur with the Hitachi shape changing robot and can be resolved if the ground clearance of

the locomotion modules is either increased for the deployment modules raised higher through additional mechanisms.

Chapter 7

Feasibility of Self-Folding Robots

The potential of reconfigurable mobile robots for deployment through boreholes is limited by the requirement for conventional gears, motors, and joints. This chapter explores the use of smart materials and innovative manufacturing techniques to form a novel concept of a self-folding robotic joint for a self-assembling robotic system. The design uses shape memory alloys fabricated in laminate structures with heaters to create folding structures.

7.1 Introduction

Programmable self-folding machines (similar to folded paper origami) could enable the creation of a more complex and capable robotic structure. Shin, B., et al. have demonstrated the fabrication of folding laminate structures [56].

Research has developed self-folding hinges for irreversible assembly structures only [55, 58, 123]. The folds are actuated using thermoplastic film layers of pre-stretched polystyrene (PSPS) or shape memory alloys (SMA). The PSPS activated fold is permanent and non-reversible, whereas the SMA fold can be reversible through external manipulation but not permanent [59, 60].

The ability of an SMA actuated fold to work in two directions without manually resetting the state after each use will be hugely beneficial, enabling the deployment, recovery and cyclic operation for locomotion. Thus removing the need for traditional motors and other bulky electronics and mechanisms. The development of self-reconfigurable and self-folding laminates can therefore introduce an alternative platform for smaller miniature mobile borehole exploration robots.

The implementation of a true self-reversible bi-directional fold is a significant milestone for self-folding robotics. The research conducted in this chapter aims to develop a true self-reversible bi-directional fold using SMA and drawing from the results of manufactured samples, form a decision on the feasibility of using these actuated folds for actuating robots.

7.2 Specifications

A self-folding robot should start fully flat without externally embedded electronics. By using shape memory alloys, each fold should produce enough torque to actuate its hinge, be self-reversible and non-permanent. The creation of a self-reversible fold allows the simple concept of a basic inchworm mechanism to be proposed that can assemble and actuate itself fully.

7.3 Layer design

SMA folds can be activated by heating the alloy above its activation temperature where the metal structure transforms from martensite to austenite phase. When activated, the SMA fold will actuate to a preprogrammed shape on the other hand when left below the activation temperature, the SMA is ductile and stays at its previous shape [124].

Activation can be accomplished by any means of applying heat to the alloys, the common methods are using joule heating [59] or by attaching a flexible heater to the alloy and activating by heat conduction [60]. For the hinge folds to be bi-directional and reversible, attempts have been made training an alloy to remember both two separate actuation directions and selectively activating one portion when required [60]. This solution, however, is not reversible and cannot be used repeatedly.

It is proposed that by introducing two individually activated SMA sheets into a single fold (Figure 7.1), the fold will be fully bi-directional and reversible through selective heating with a capable heat insulating layer separating them (Figure 7.2).

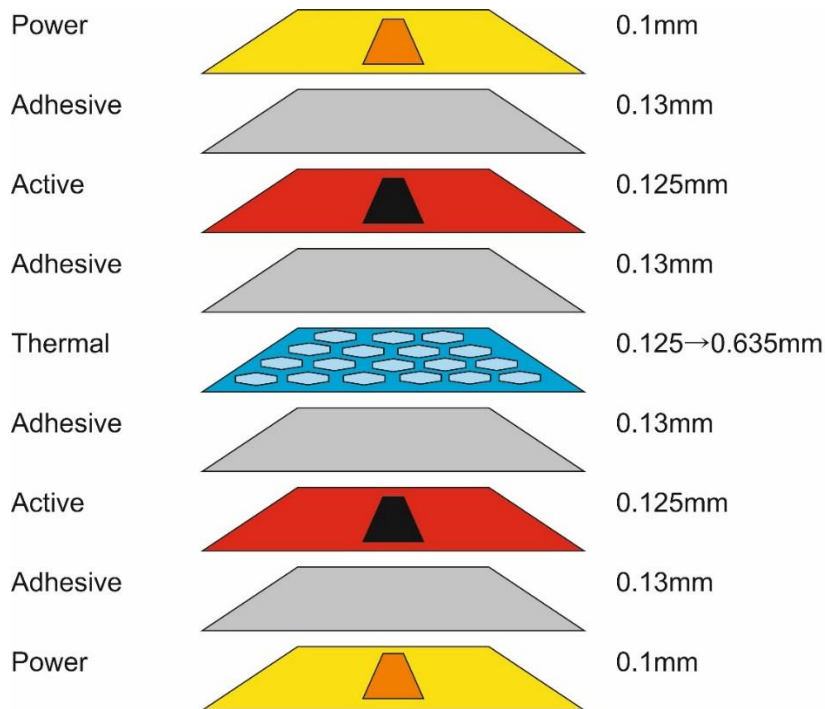


Figure 7.1 Layer composition.

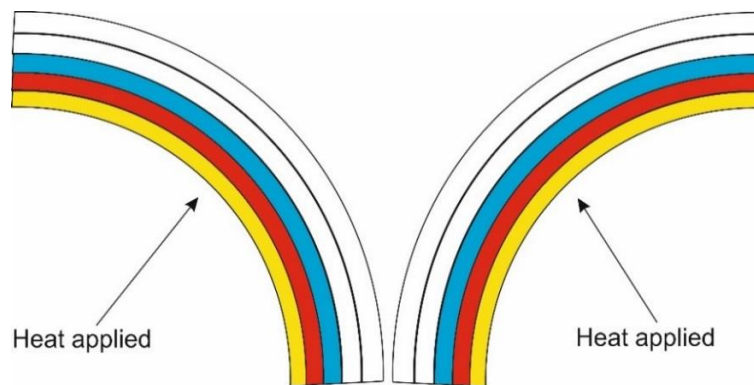


Figure 7.2 Selectively heating one side changes fold direction.

The role each layer plays is defined in Table 7.1.

Table 7.1 Layer roles.

Layer	Role
Power	Contains the embedded flexible heating circuit, used to activate the SMA.
Adhesive	Binds the two adjoining layers together.
Active	Contains the embedded SMA sheet, preprogrammed to fold the hinge.
Thermal	Thermally insulating layer to reduce heat conduction through the other layers. Allows SMA activation on only one side.

The parts supplied for each layer is provided in Table 7.2. The selected copper-polyimide laminate was chosen as these are commonly sourced for flexible circuitry and the thin thickness was intentional to more effectively conduct heat to the SMA layer. In general, the thickness of each layer was important due to its effects on the bend radius and overall stiffness. Although the selection of the thermal layer was a compromise between thickness and its heat transfer properties.

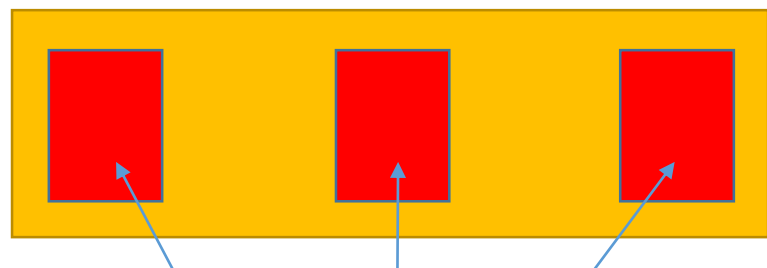
Table 7.2 Layer parts sourced.

Layer	Thickness	Material	Brand	Mfr-reference
Power	0.1	Copper-Polyimide Laminate	Goodfellow	283-280-25
Adhesive	0.13	Acrylic sheet	3M	3M 7955
Active	0.1	NiTi alloy sheet	Memry	Nitinol Alloy M
Thermal	0.125	Polyimide film	Goodfellow	667-985-89

It is proposed the self-folding hinges be used to actuate a basic inchworm mechanism as illustrated in Figure 7.3.

Top View:

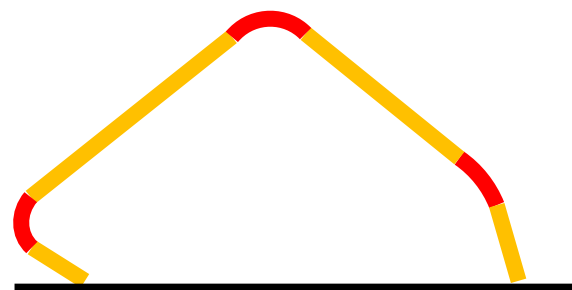
Stored flat when in storage and unused.



Three SMA actuated folds

Side View:

Activated folds creates the inchworm mechanism with angled feet for asymmetric friction. The active centre fold will actuate the mechanism for locomotion.



Direction of travel

Figure 7.3 Proposed self-folding inchworm mechanism.

7.3.1 Bend radius

The thickness of the total layer composition affects the bend diameter and force required to actuate the folds. When a fold is actuated, one-half is under compression and the other under extension. This change in length can be measured as strain and is important for parts such as the NiTi alloy that have a 10% limit [125].

If the design is for a bidirectional fold of 360°, the SMA strain can be found as:

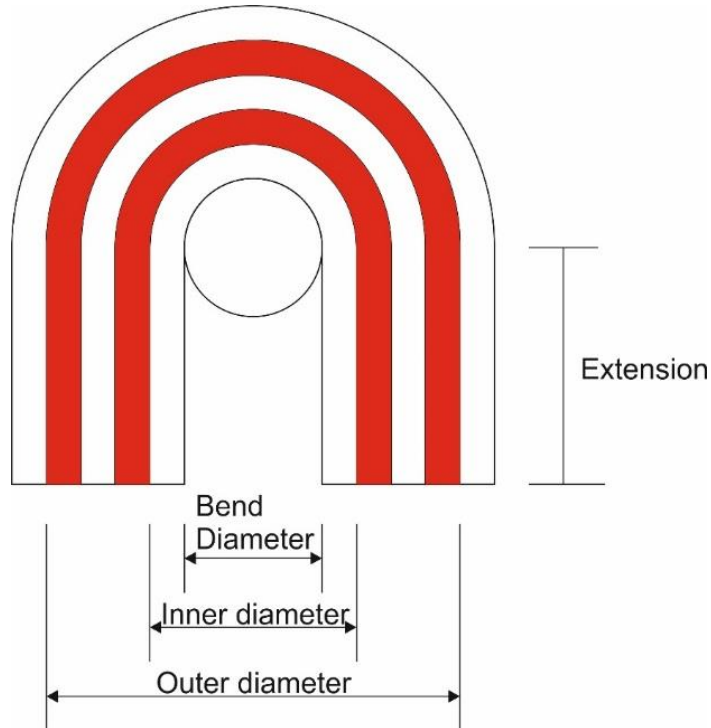


Figure 7.4 SMA strain.

Where:

B = Bend diameter

ID = Inner diameter

OD = Outer diameter

EX = Extension

$$IA = \frac{\pi \cdot ID}{2} + (2 \cdot EX) \quad 7.1$$

$$OA = \frac{\pi \cdot OD}{2} + (2 \cdot EX) \quad 7.2$$

$$SMA \text{ strain} = \frac{OA - IA}{IA} \quad 7.3$$

This would then inform whether the SMA strain limits are exceeded.

7.3.2 Active Af Experiment

The austenite finish temperature (A_f) is the temperature at which the transformation from martensite to austenite finishes on heating i.e. the temperature when the SMA has fully transformed. The transformation curve of the SMA in combination with the insulating abilities of the thermal layer is vital for the bidirectional fold to work. A common method for determining the transformation temperatures of an alloy whilst being slowly heated is the active A_f -test. It is conducted by bending a sample and submerging it into a cold bath initially to ensure no transformation are present from the start. The bath water is slowly heated while the shape recovery and temperature is monitored. This method has been demonstrated to achieve accurate and repeatable results if performed carefully [126].

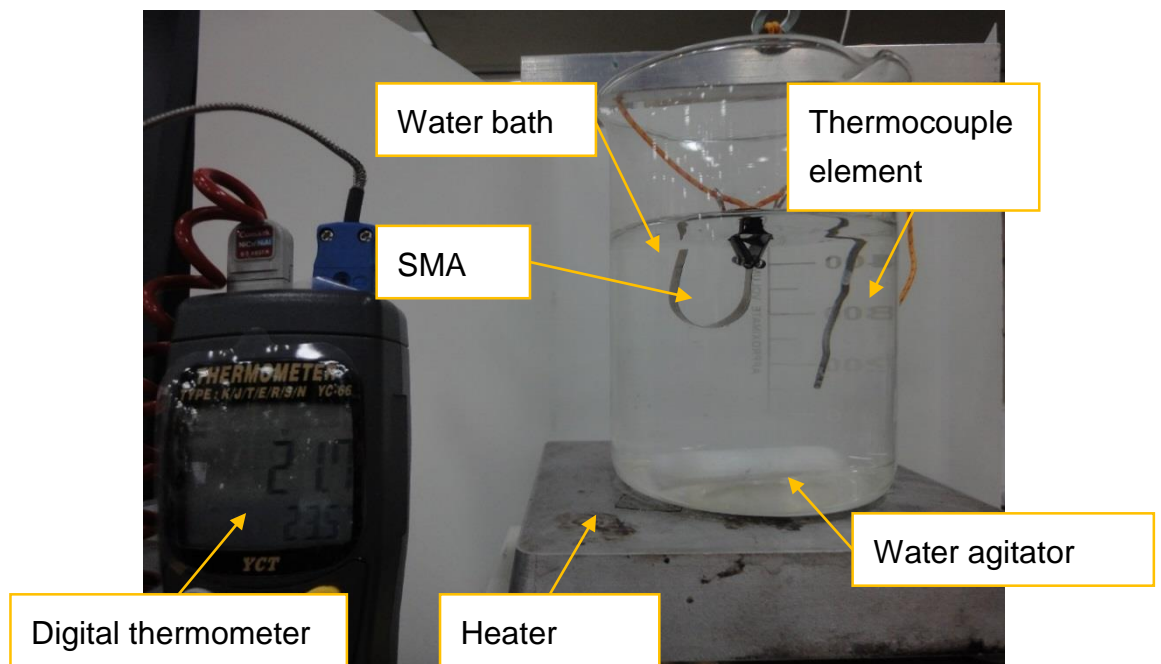



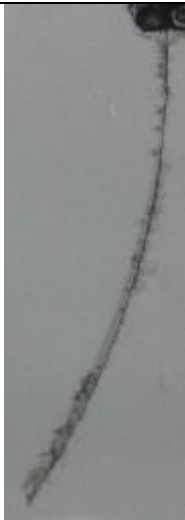


Figure 7.5 Active A_f -test.

The experimental procedure involved fully submerging the SMA alloy pre-deformed into a U shape. The combination of a heater and water agitator results in the water temperature being uniform, minimising temperature differences between the SMA and thermometer. As the water temperature rose, an image was taken of the SMA at regular intervals until no more changes were observed. The water is then replaced with cold water to remove heat effects and then the experiment repeated 7 times. Post-processing of

each image was performed to measure the angle of the SMA in each frame to be correlated with water temperature.

Table 7.3 Active Af measurement experiment 1.

Temperature (°C)	Image	Angle (°)
22	 A photograph of a thin, light-colored SMA wire held by a black clip. The wire is curved into a shallow U-shape, indicating a low deflection angle.	-14.83
50	 A photograph of the SMA wire at a higher temperature. It is curved more sharply than at 22°C, with a more pronounced U-shape.	17.01
60	 A photograph of the SMA wire at 60°C. The wire is significantly more curved, forming a deep arc.	83.94
70	 A photograph of the SMA wire at 70°C. The wire is almost straight, showing a very sharp deflection angle.	145.92

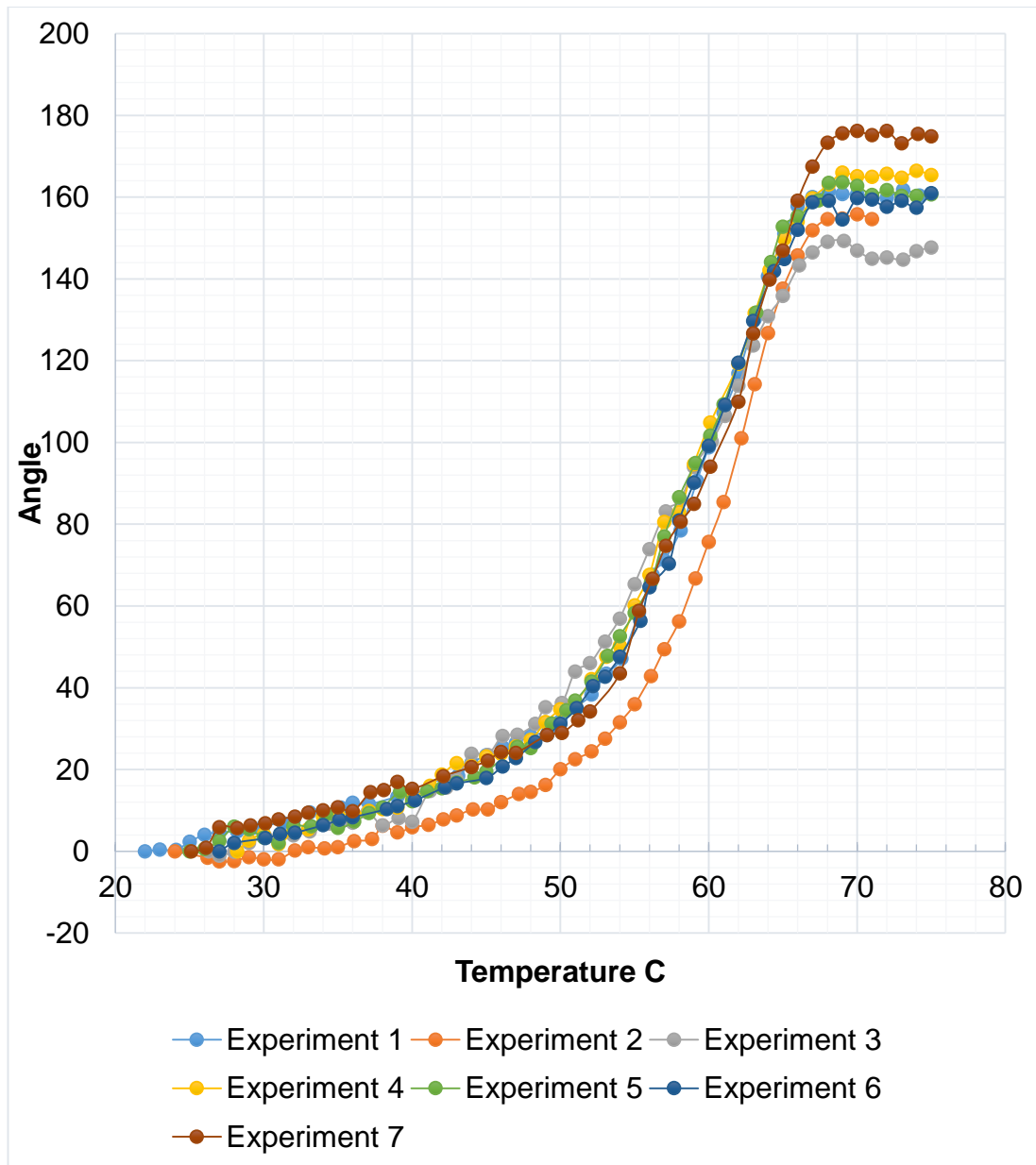


Figure 7.6 Active Af measurement results.

The transformation curve illustrated in Figure 7.6 shows that between 25°C to 52°C the SMA response is small and slow, and the large changes occur from 52°C to 68°C where the alloy assumes its pre-programmed state. From 52°C to 68°C, this 16°C difference is important for the development of the thermal layer (Figure 7.7).

The role of the thermal layer is to thermally separate both SMA actuators. When the flexible heater heats one side the temperature should reach 70°C to fully activate its adjacent SMA actuator. However, if this heat was to continue conducting through the other layers, the other SMA actuator will also activate causing no net angle change to the hinge.

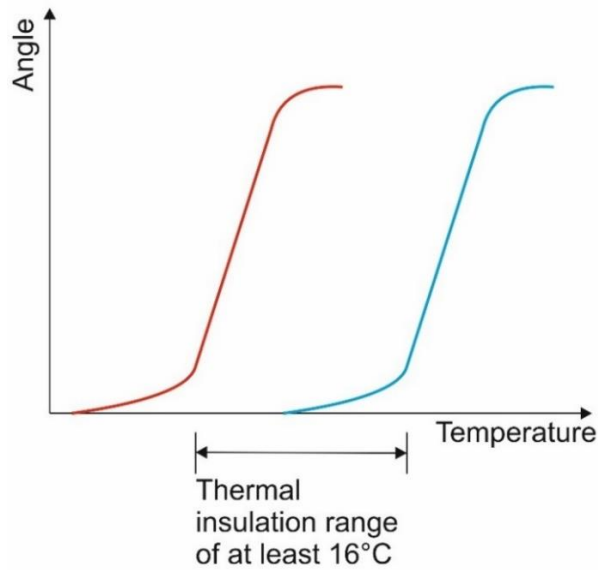


Figure 7.7 Thermal damping range.

7.3.3 Thermal Layer

The thermal insulating properties of air (Table 7.5) can be taken advantage of to assist the layer. As the layer cannot entirely consist of only air, the polyimide film (Table 7.4) must still be used to provide a structure small enough to limit heat conduction but enough to support the pockets of air. Comparing the coefficient of thermal conductivity between the two materials, it is clear the larger the percentage of air in the layer the better the thermal damping range. It is unknown what performance the single layer can have or how many layers are needed.

Table 7.4 Polyimide thermal properties at 25°C

Density	ρ	1420 kg/m ³
Coefficient of thermal conductivity	k	0.12 w/mk
Specific heat	c	1090 J/kg.k
Thermal diffusivity	α	0.0775x10 ⁻⁶ m ² /s

Table 7.5 Air thermal properties at 25°C

Density	ρ	1.1 kg/m ³
Coefficient of thermal conductivity	k	0.027 w/mk
Specific heat	c	1000 J/kg.k
Thermal diffusivity	α	24.5454x10 ⁻⁶ m ² /s

7.3.3.1 Thermal Analysis

Thermal layers with air pockets of different sizes (Figure 7.8) were analysed using SolidWorks Thermal Analysis. Setting the temperature of the heating elements to the target 70°C as part of a transient study (Table 7.6) as shown in Figure 7.9, the temperatures of both SMA sheets were measured and the temperature differences extracted post processing. For completeness, the presence of no air and only air was also analysed. At the cost of additional thickness, the thermal layer can also be composed of multiple layers of the air pockets and adhesive layers in-between in order to increase the thermal insulation.

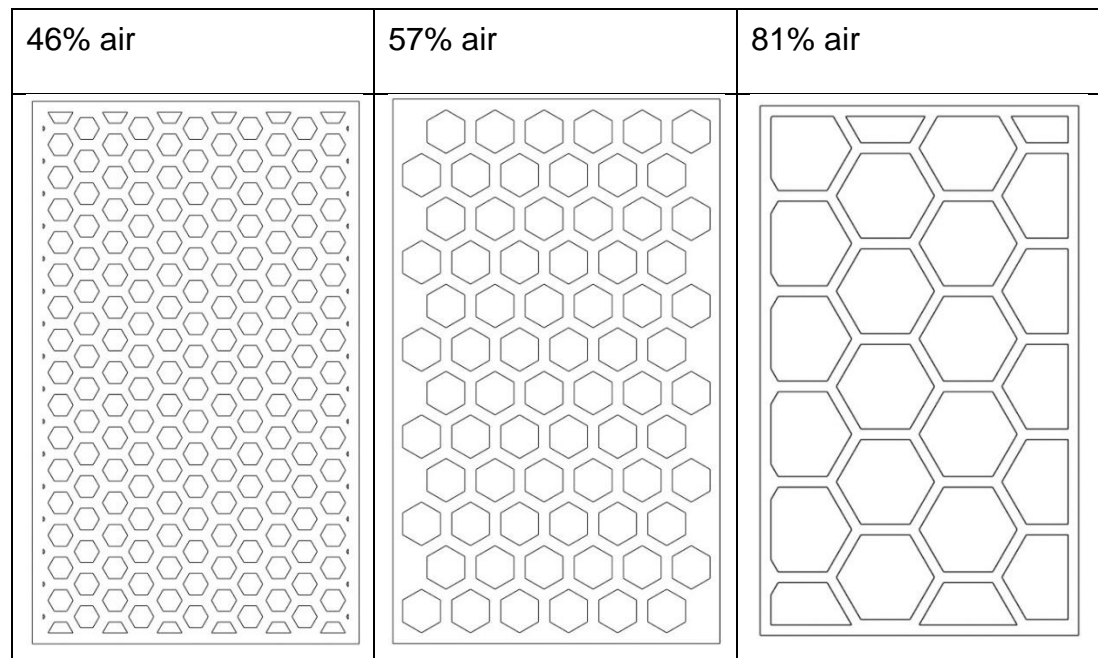


Figure 7.8 Different sized air pockets.

Table 7.6 Thermal Analysis Parameters.

Heat Power	1 W
Heat Power Limits	69°C - 71°C
Convection	10 W/m ² .k
Initial temperature	25°C

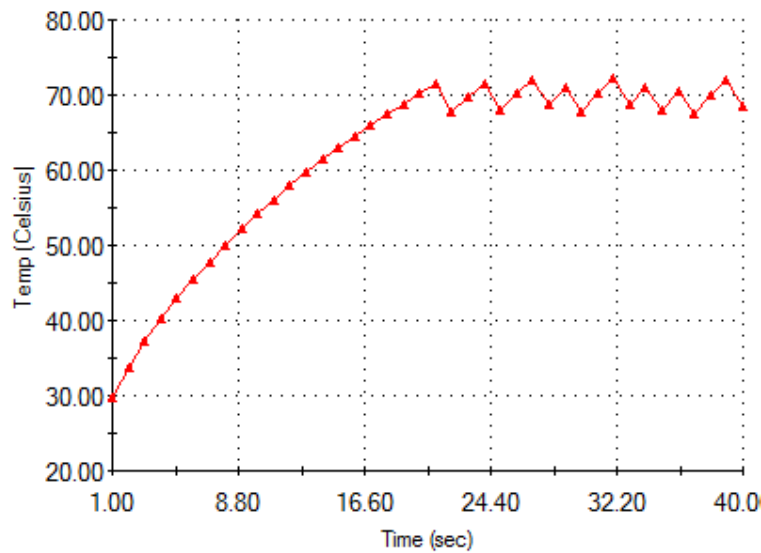


Figure 7.9 SolidWorks thermal analysis heating curve maintains the temperature at 70°C.

The following results display the surface heat maps of the two active SMA layers as the target temperature is met and illustrates the temperature differences between them. The greater the average temperature difference the larger the proposed effectiveness of the thermally insulating layer. Only the results of 57% air are shown, the results for other layers with different sized air pockets are found in Appendix G.

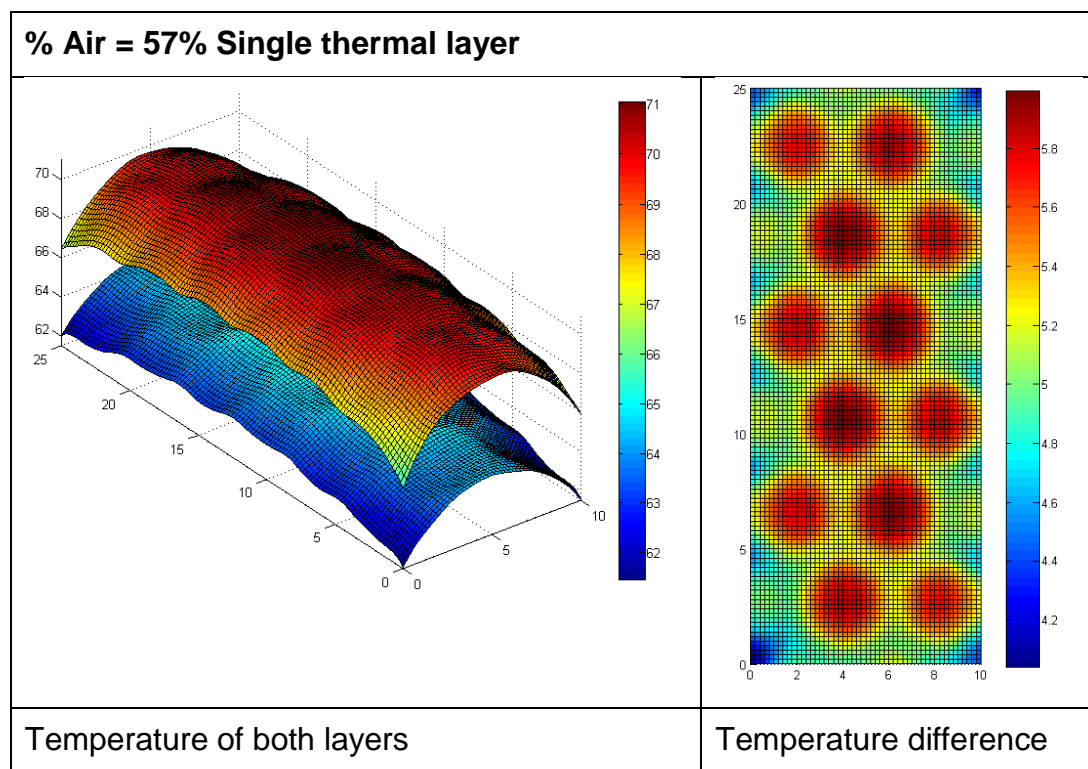


Figure 7.10 Thermal analysis results.

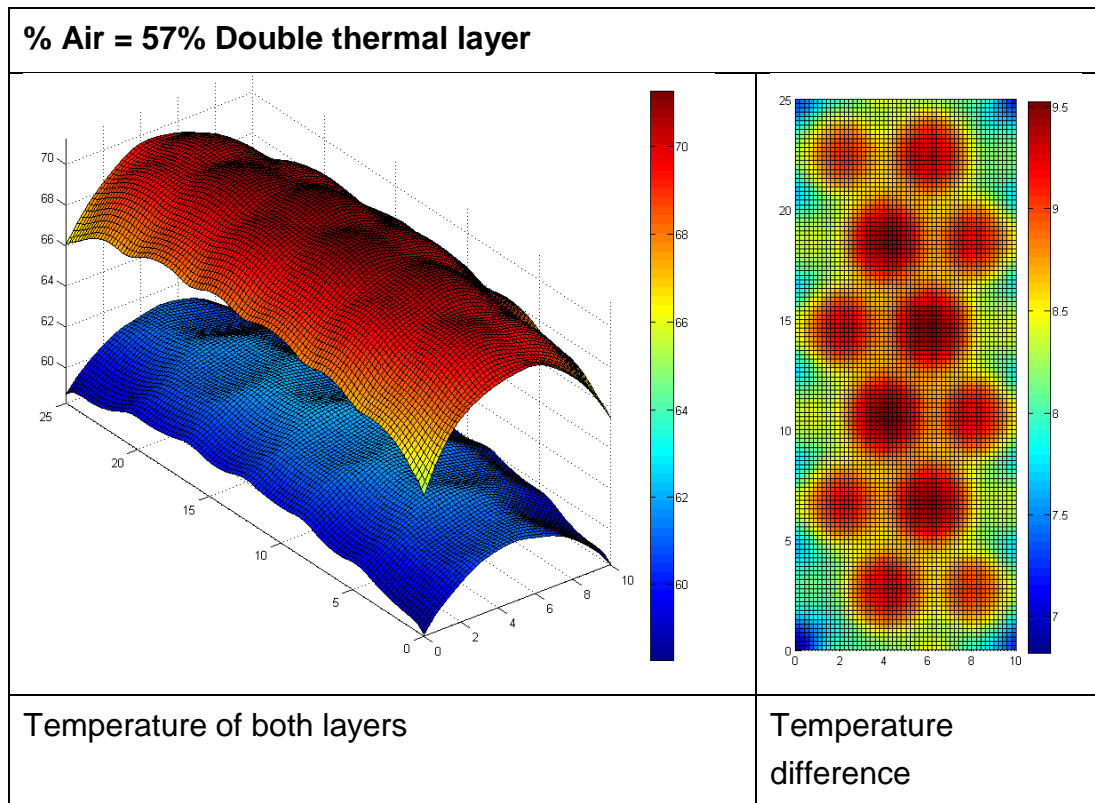


Figure 7.11 Thermal analysis results.

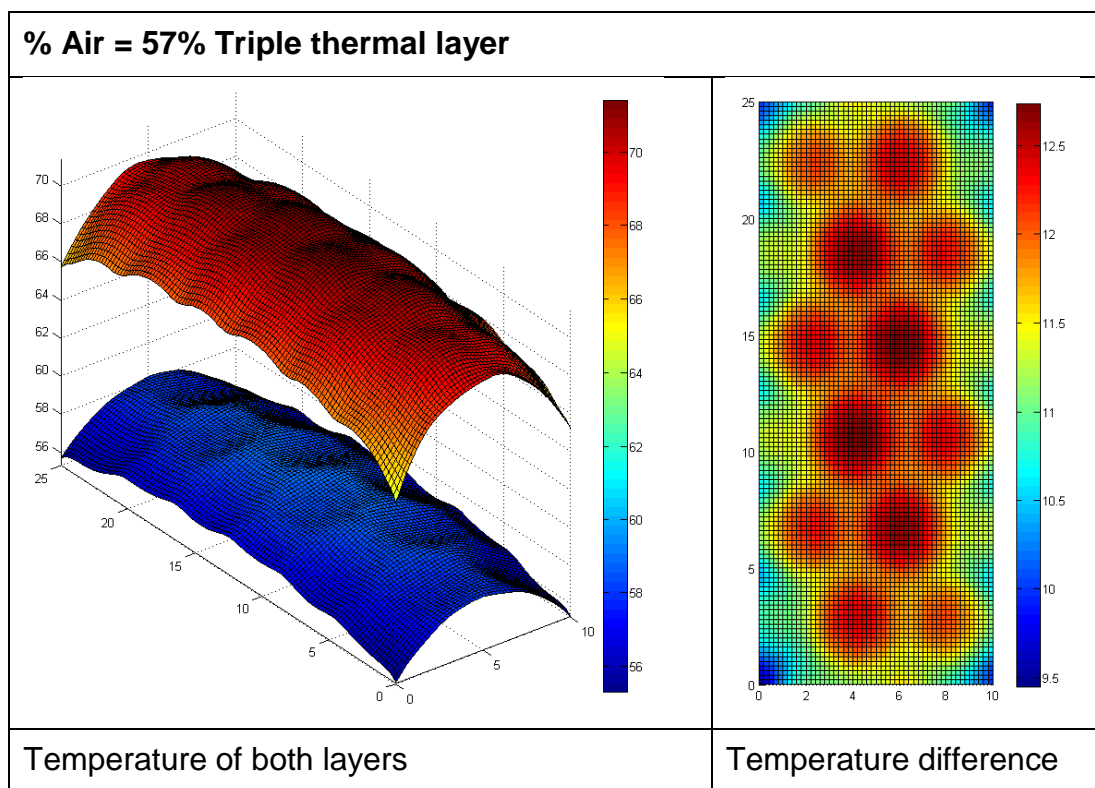


Figure 7.12 Thermal analysis results.

Table 7.7 Thermal analysis results comparison.

			% Air				
			0%	46%	57%	81%	100%
Layer Arrangement	Single	Time	40	37	37	37	34
		Average U Temp	69.0403	69.1086	69.5093	69.3891	69.8795
		Average L Temp	65.6183	64.3722	64.1988	62.4800	61.0487
		Difference	3.422	4.7364	5.3105	6.9091	8.8308
	Double	Time	54	46	42	42	38
		Average U Temp	70.6394	70.6035	69.5361	74.1346	70.3677
		Average L Temp	65.2953	62.9727	30.9122	61.7015	56.0091
		Difference	5.3441	7.6309	8.6239	12.4331	14.3586
	Triple	Time	58	52	48	44	38
		Average U Temp	68.5165	70.9055	70.5117	74.0903	69.4574
		Average L Temp	61.3006	60.5608	58.8309	57.2722	50.3634
		Difference	7.2159	10.3446	11.6808	16.8181	19.0941

The results of the thermal analysis (Table 7.7) has shown for the 16°C difference to be achieved, the closest match would be to use three layers of the 81% air pockets. The results are as expected due to the smaller coefficient of thermal conductivity for air in comparison to the polyimide film. To further increase the effectiveness of the thermal layer, it can be proposed that the medium is altered so that the air is replaced with a material with a smaller coefficient of thermal conductivity.

Using Equations 7.1, 7.2 and 7.3, the minimum bend diameter gave the combined layer thicknesses of 1.6mm is calculated to be 4.05mm for 10% strain.

7.4 Experiment

To test the abilities of the bi-directional SMA actuated folds, several samples were produced for testing using the triple thermal layers with 81% air. The tests involved hinges with different sized SMA sheets embedded of different lengths and widths with the aim to find how the size of the SMA affects the hinges performance.

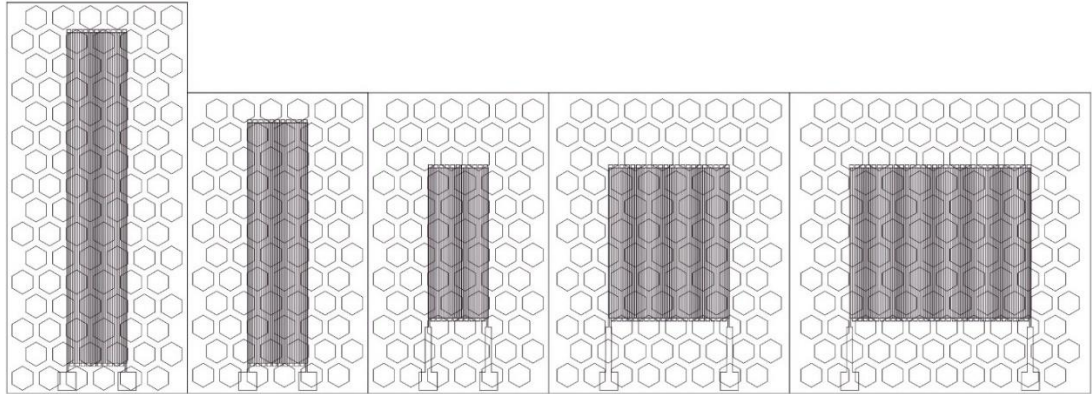


Figure 7.13 Several samples of different sized embedded SMA sheets.

The SMA sizes chosen for the experiment are listed in Table 7.2. From strip 1 to 5, the length and width values are varied to allow for the effects of SMA size and its effects on the performance of the fold to be observed.

Table 7.8 Different sized SMA strips used.

SMA number	Length (mm)	Width (mm)
1	55	10
2	40	10
3	25	10
4	25	20
5	25	30

7.4.1 Methodology

Five different samples were produced each with a unique SMA size. Activation of the hinge relies on the combined effort of several layers and the failure of any will result in the failure of the joint to move. For each sample, a series of tests were performed to check the functionality and performance. Table 7.9 lists the tests performed, what was expected and indications the layer has failed.

Table 7.9 Experimental checks.

Test performed	Success	Failure
Does the heating layer produce enough heat to activate the SMA layer?	<p>If the heating layer functions correctly and the SMA activation temperature is met, a change in the shape of the hinge should be noticeable.</p> <p>A digital thermometer will be able to accurately read the temperature at the surface.</p>	<p>Manufacturing complications could result in a heater that does not produce sufficient heat.</p> <p>Faults in the copper tracks create areas of abnormally high resistance resulting in hot spots that can cause the heater to burn.</p>
Does the SMA produce enough torque?	Generating sufficient torque to overcome internal stiffness will be revealed with a change to the angle of the fold.	No change to the shape of the fold will occur if the internal stiffness of the combined layers is too high.
Does the thermal layer function as intended?	<p>The thermal layer can only delay the temperature rise so only one SMA layer is activated before the other. Measuring the temperature delay of the layer at both sides is difficult as direct access is obstructed by other layers.</p> <p>Indications the layer is performing as intended can be witnessed through the fold being actuated and reversed when the opposite layer is activated after (assuming</p>	Just as the successful functionality of the thermal layer can be observed through the actions of the SMA layer. The failure of the thermal layer can be observed if no or slight folding occurs.

	the SMA layer produces sufficient torque).	
--	--	--

7.4.2 Results

Table 7.10 Experimental results for SMA strip 1.


<p>SMA Strip 1</p> <p>55 x 10mm</p> 	<p>Does the heating layer produce enough heat to activate the SMA layer?</p>
	<p>Measuring the temperature rise with a digital thermometer, the 70°C target can be reached and maintained by controlling the supply of power to the heater.</p>
	<p>Does the SMA produce enough torque?</p>
	<p>No noticeable change to the fold angle was observed during heating. This would indicate the stiffness of the fold could not be overcome for fold actuation to occur.</p>
	<p>Does the thermal layer function as intended?</p> <p>No actuation of the fold was observed, it is unclear whether the thermal layer functioned or not. As the design of the thermal layer is repeated for the other samples and the thermal layer does work in those cases, it can be assumed the thermal layer in this sample would also be functional.</p>

Table 7.11 Experimental results for SMA strip 2.

<p>SMA Strip 2</p> <p>40 x 10mm</p>	<p>Does the heating layer produce enough heat to activate the SMA layer?</p>
	<p>Measuring the temperature rise with a digital thermometer, the 70°C target can be reached and maintained by controlling the supply of power to the heater.</p>
	<p>Does the SMA produce enough torque?</p>



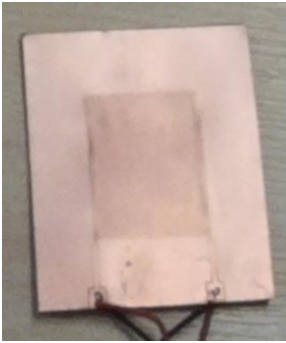
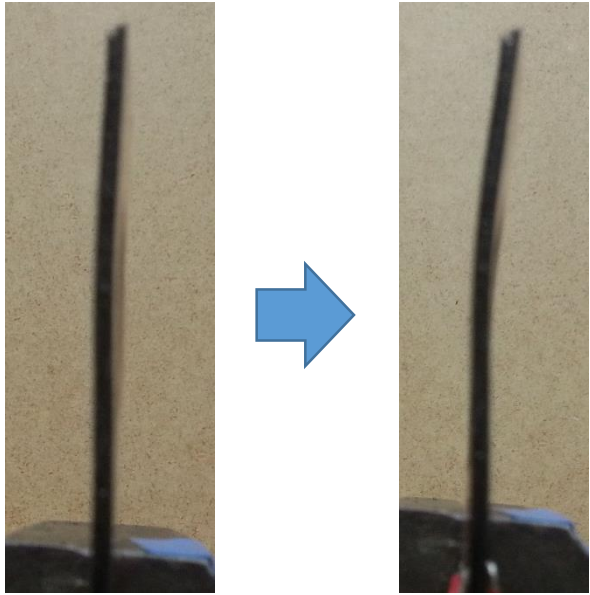
	<p>No noticeable change to the fold angle was observed during heating. This would indicate the stiffness of the fold could not be overcome for fold actuation to occur.</p>
	<p>Does the thermal layer function as intended?</p>
	<p>No actuation of the fold was observed, it is unclear whether the thermal layer functioned or not. As the design of the thermal layer is repeated for the other samples and the thermal layer does work in those cases, it can be assumed the thermal layer in this sample would also be functional.</p>

Table 7.12 Experimental results for SMA strip 3.

<p>SMA Strip 3 25 x 10mm</p> 	<p>Does the heating layer produce enough heat to activate the SMA layer?</p>
	<p>Measuring the temperature rise with a digital thermometer, the 70°C target can be reached and maintained by controlling the supply of power to the heater. The activation of the SMA layer was demonstrated before the full assembly in Figure 7.15 showing the maximum fold angle that can be achieved with the SMA.</p>
	<p>Does the SMA produce enough torque?</p>
	<p>No noticeable change to the fold angle was observed during heating. This would indicate the stiffness of the fold could not be overcome for fold actuation to occur.</p>
	<p>Does the thermal layer function as intended?</p> <p>Once the initial fold was observed showing the SMA layer can actuate the fold, the power was swapped to heat the opposing side. Successful activation of the opposing layers was observed as the fold</p>

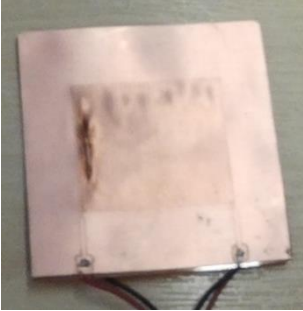
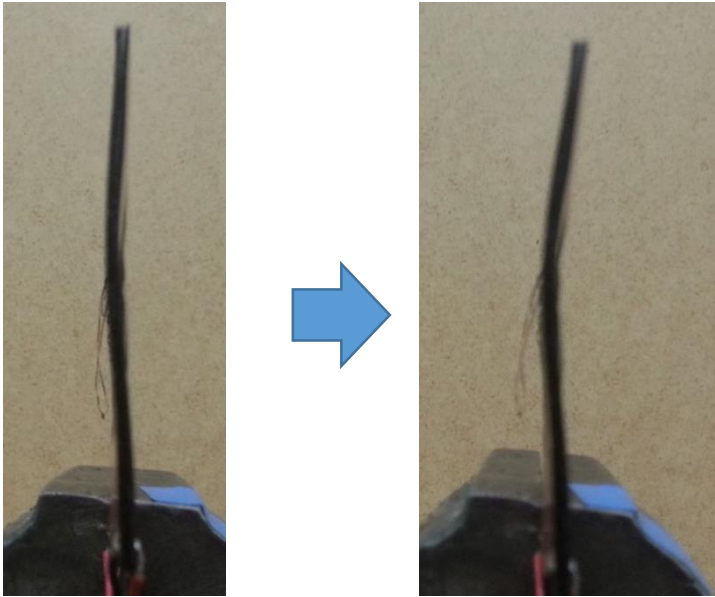
	actuated in the opposite direction to restore the fold angle.
--	---

Table 7.13 Experimental results for SMA strip 4.

<div>SMA Strip 4</div> <div>55 x 20mm</div> <div></div>	Does the heating layer produce enough heat to activate the SMA layer?
	Measuring the temperature rise with a digital thermometer, the 70°C target can be reached and maintained by controlling the supply of power to the heater.
	Does the SMA produce enough torque?
	<p>A change to the fold angle was recorded when the heating layer was powered. The deformation is illustrated below.</p> <div></div>
	Does the thermal layer function as intended?
	Once the initial fold was observed showing the SMA layer can actuate the fold, the power was swapped to heat the opposing side. Successful activation of the

	opposing layers was observed as the fold actuated in the opposite direction to restore the fold angle.
--	--

Table 7.14 Experimental results for SMA strip 5.

<p>SMA Strip 5 55 x 30mm</p> 	<p>Does the heating layer produce enough heat to activate the SMA layer?</p> <p>The heating element eventually failed and a section of the copper track delaminated. However, the activation temperature of the SMA layer was achieved when activation of the SMA layer occurred. The delamination can be seen in Figure 7.14.</p>
	<p>Does the SMA produce enough torque?</p> <p>A change to the fold angle was recorded when the heating layer was powered. The deformation is illustrated below.</p>
	
	<p>Does the thermal layer function as intended?</p> <p>Once the initial fold was observed showing the SMA layer can actuate the fold, the power was swapped to heat the opposing side. Successful activation of the opposing layers was observed as the fold</p>

	actuated in the opposite direction to restore the fold angle.
--	---

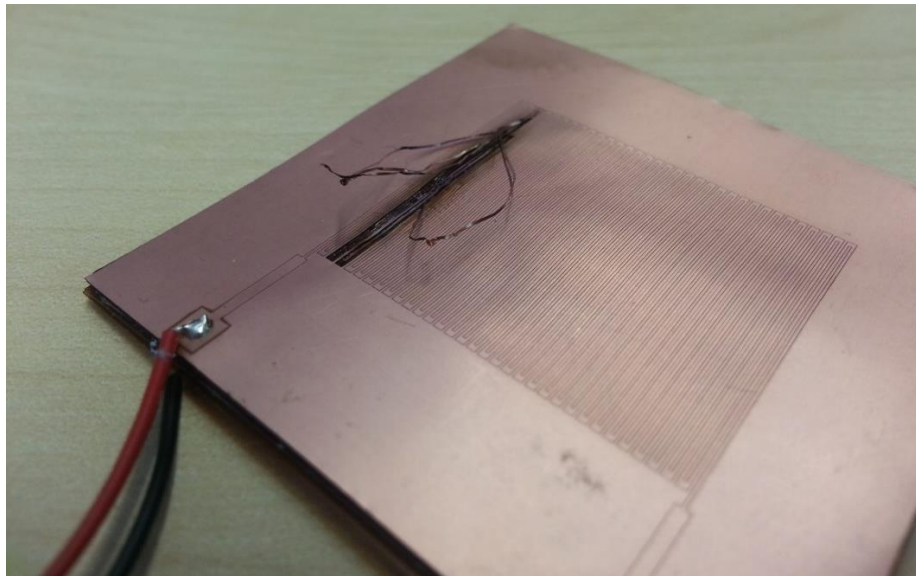


Figure 7.14 Flexible heating layer failure.

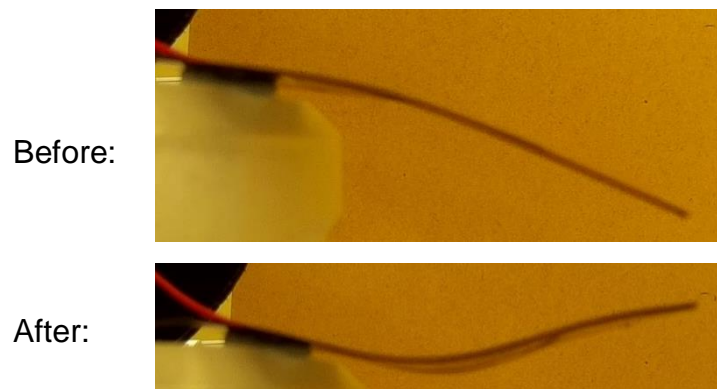


Figure 7.15 Heat activation of strip 3 with just the heating element and SMA (size 25 x 10mm).

The results of testing five samples of different SMA sizes has shown the width of the SMA to be more important than the length in supplying the torque necessary for fold actuation. The stiffness of the combined layers is an obstacle that limits the achievable fold angle range. Reducing the overall thickness will reduce the stiffness of the fold allowing the SMA to actuate the folds with the same torque.

Figure 7.15 can represent the achievable fold angle if the layer stiffness was minimal. Ideally, the fold angle should be 180°, but the annealing step (400°C for 30 minutes then water quench) to program the SMA requires further work to improve the memorised angle.

7.5 Discussion and conclusion

A self-folding robot is ideally capable of remote, autonomous assembly that could be easily transported when packed flat for applications such as satellites in space or rapid deployment of shelters during natural disasters [58]. These robots are easy to manufacture and the versatility of folds necessitates the creation of complex three-dimensional structures from two-dimensional structures.

Printed inchworm robots capable of self-assembly found in literature, such as those by Felton, S.M., et al. [55] are reliant on assembly machines to pick and place electrical components during manufacturing to provide the printed inchworm robot the means to actuate its main fold for locomotion. These servomotors, linkages and batteries are bulky constructs that remove the ability for self-folding robots to be flat, easily stored and transported.

The incorporation of SMA strips to power the structural folds and actuation folds allows a fully flat machine to be built. The development of a true bidirectional SMA folding actuator with collinear rotational axis is the key to allowing such self-folding robots to function without external manipulation to reverse any folds. The layout of the parallel SMA strips for the actuated fold in this chapter relies on a novel heat-insulating barrier to isolate the activation of each SMA strip from another. The experimentation conducted reveals the direction of the fold can be controlled through selective heating of the flexible PCB to its associated SMA strip in combination with the insulating barrier.

The displacement range of the sample fold was small for a situation where a 90° fold should be a minimum. This was due to complications in the programming of the SMA strips to 'remember' large bend angles. The torque generated at each fold is also small and was expected with SMA materials. From experimentation, a SMA strip of larger width (55 x 30mm) produced more displacement on the joint in comparison to a thinner strip (55 x 10mm). Therefore, the width of a fold plays a crucial part in the operation of a fold. It is unlikely, however, the fold can generate sufficient torque to move the main actuation fold needed for the inchworm configuration shown in Figure 7.3. The feasibility of self-folding robots is possible and already exist. The use of SMA

strips to construct a version without any external electrical components does require additional study to increase the force output of the SMA actuated folds.

Chapter 8

Conclusions and future work

This chapter details conclusions drawn from the findings of three case studies. Before finally summarising the research and its findings. It discusses benefits of using the proposed systems and make recommendations for further research.

8.1 Assessment of research objectives

Four research objectives were outlined in Section 1.3. This section identifies the extent to which they have been fulfilled during this study:

8.1.1 Investigate the length limitations to snake arms

The design of long reach snake arms has been demonstrated in Chapters 4 and 5. The effects of long reach snake arms on the actuation cables were demonstrated with calculations and experiments to predict the cable tensions in Section 4.4. The actuation cables provide acceptable movement to the snake arm joints (Section 5.7). The limitations to the snake arm links (Section 4.3) and joints (Section 5.3) were explored for buckling modes that contributes to the length limit for the snake arm device.

8.1.2 Develop an algorithmic approach to producing a snake arm of optimal length

The iterative solver demonstrated the ability to optimise the length of a snake arm design in Section 5.6. The snake arm of optimised length was successfully designed and fabricated based on the solver's output reducing the risk of component failure, improving the longevity of the snake arm.

8.1.3 Extend the range capabilities of borehole robots using reconfigurable robot techniques

A three module reconfigurable robot has been successfully designed and fabricated based on established actuation and manufacturing techniques. The robot is capable of assuming two configurations (one for deployment and the other for exploring). Experiments have verified that the robot is capable of applying the forces (Section 6.6.2) to drive the robot and drag the tether in a

hypothetical tunnel of distances greater than the reach of a similar reconfigurable robot (Section 6.4).

8.1.4 Investigate advanced actuation and fabrication technologies

The design uses shape memory alloys fabricated in laminate structures with heaters to create folding structures. The performance of SMA is experimentally verified in Section 7.3.2 that formed the basis for a thermally insulating layer vital for a self-reversible fold to be made possible (Section 7.3.3).

A (limited) study has been performed to evaluate the feasibility of folds with different size SMA strips. The study shows the concept of a single self-reversible actuated fold that has potential applications for a self-assembling flexible robot; however, the force generated by the SMA is small. For the inchworm mechanism to be feasible, the torque generated at the actuated folds needs to be more substantial.

8.2 Conclusions

The following conclusions relate to the specific elements of work performed:

8.2.1 Snake arm

- Minimally invasive exploration of restricted access and confined spaces requires bespoke designed hardware for each scenario. As the terrain and environment vary from one scenario to the next, the changing constraints used to develop one robot will generate a different robot for the next.
- The length of the snake-arm is dependent on the destination of the deployment. The forces used in the snake arm analysis focused on the position being the highly demanding horizontal cantilever position, where the cable tensions and axial compressive forces are at its peak. Without any external supports for the Base Link, the snake arm length was calculated to be 1.149m with an effective length of 0.605m. However, those values are only valid for a horizontal deployment.

- Given another scenario for a 12mm diameter snake arm that would be deployed vertically down into a subterranean chamber; the changed constraints will result in different lengths for the Base Link and Links. The distribution of actuation cables around the joints will not require any changes, meaning the effects of the changed deployment direction will only result in a minor change to the orientation of the Denavit-Hartenberg notation used to describe the snake arm. This results in different torques calculated by the recursive Newton-Euler method and the remaining method for the algorithmically calculated snake arm length largely remains the same.
- The experiments to verify the cable tension theory highlighted inaccuracies due to friction in the experimental test rig that deviated the experimental results from the theoretical. The experimentally found cable tensions are larger than the theoretical. Additional tests to measure friction in the test rig was performed and the experimental data was updated to accommodate for friction that brought the theoretical and experimental data closer together.
- Terminating the Dyneema cables required the simple solution of a small knot, which has worked effectively, and taking very little space, therefore, allowing the cables to be distributed about the largest diameter. The use of steel cables was considered but the proper termination of steel cables required bulky ferrules or crimps that drastically affected the diameter of the snake arm.
- Usually, in universal joints, the two pivots are collinear to better transmit rotation, however, to strengthen the load the snake arm joints can withstand the two pivots were offset in the fabricated build. The results of the snake arm experiment to observe the effects of cable length on the joints revealed the offset did not affect the performance of the joints.

8.2.2 Reconfigurable Dual Track Robot

- Reconfigurable robots with at least two configurations (one for deploying and the other for completing its objective) can be utilised to perform an exploration with greater reach. The robot detailed in this paper can navigate through a borehole of just 41mm and equipped with a camera and light be able to perform the initial surveying of a hypothetical mine shaft to a range of approximately 65m. The key issue with the robot was its lightweight of 2.372kg being inadequate for supplying the required traction to drive the full 200m distance and the low ground clearance that would struggle under the rough terrain.
- For small borehole diameter deployments, the weight requirement for tethered robots to travel large distances exhibit diminishing returns as heavier robots must result in a longer bulkier system during the deployment.
- When driving the robot, the low ground clearance resulted in a constant need for awareness of the surroundings and path planning to avoid obstacles and unwanted build-up of debris at the deployment module where the camera and lights are located. Without a means to increase the ground clearance or lift the deployment module further away from the ground, travelling long distances can be problematic.
- In order to compact the gears and electronics into the void between the track, parts were successfully mounted in series allowing the small deployment diameter to be achieved. This left unwanted issues with exposed electrical wiring to connect the modules together.
- The tensioning system responsible for maintaining the tension through the tracks and protecting the driving gears when slip occurs also serves other useful functions that are not previously mentioned. The mechanism allows for quick access to the internal compartments where the electronics are stored and aids the disassembly of the module where the track is usually the first part to be removed. Without the

system, the lips on the timing belt pulleys that secure the tracks from the unwanted lateral movement will also result in more complicated disassembles and builds.

8.2.3 Self-Folding Robot

- The novel robotic self-assembling mechanism is unique. To the author's current knowledge, there have been no attempts at constructing a fully self-reversible, self-folding robot using embedded SMA actuators and flexible heating circuitry for a locomotion system and support structure. The implicit use of flexible materials results in the robot capable of being manually deformed for deployment purposes, yet given enough SMA actuators, can self-assemble as required post-deployment.
- Programming the SMA was problematic during the annealing stages as memory loss caused the SMA to only transform into a fraction of the intended shape. To compensate, it was required the SMA be shaped prior to heat treatment with more extreme angles than needed. This method restored some functionality to the SMA layers but offers less control of the final shape.
- To reduce the internal stiffness during the material selection process, the thickness of the sourced materials was always of concern. The small thicknesses eventually became a problem during the fabrication of the flexible heater, as the copper layer in the copper-polyimide laminate was thicker than the polyimide. This resulted in a laser etcher struggling to isolate copper tracks without cutting or burning the polyimide layer underneath.
- The thermal layer was developed using thermal analysis software to estimate the thermal insulation range. Increasing the size of the air pockets improved the thermal layer as additional air (with smaller thermal conductivity) was introduced.

8.3 Future work

This research has provided a starting point for research into borehole exploration robots. This section looks forward to future work that might be undertaken to further improve the designs.

8.3.1 Snake arm

- The cables are subjected to large tensions and selecting stronger cables will result in longer snake arms, however, this will offload the forces onto other components such as the joints and links that may then require further strengthening. The iterative solver will only optimise the snake arm length by changing the length of the links and all the parts running through them. It cannot, however, vary the thickness of the tubes to improve the buckling resistance or increase the diameter of the cables to better optimise the components as they reach the FOS targets.
- The base actuator frame relies on potentiometers and gearing to monitor and control the length of each cable. The cable length calculations, however, reveal the changes to the ideal cable length to be a few millimetres and requires accuracy the current setup cannot provide due to backlash in the gears and resolution of the potentiometer. A better alternative would be the installation of optical encoders directly onto the linear actuator motor to vastly improve resolution and accuracy.
- Cable stretching was an occurrence seen in the cable testing in Chapter 5.4. Under load, the cables will also experience a stretch in the snake arm during the initial set up pre-loading, however, when the snake arm has actuated the state of the cable stretch is unknown. Modelling cable stretch into the control software should improve decrease the deviation found during testing.
- Friction in the system is problematic for the control of the snake arm as was observed with the experimental cable tension test rig. Improving

the snake arm design to reduce friction at the joints where friction is most prominent would enable the arm to be better predicted and controlled.

- Measuring the joint angles is completed with a time intensive method of taking still imagery from a side or top view and using image manipulation software to read the joint angles. This method is not adequate for live monitoring of the arm orientation. Without the known joint angles, forward kinematics cannot be used to compute the exact position of the end effector. Mounting additional sensors to the joints should vastly improve the control of the snake arm. Although space around the joints is already limited.
- It can be possible to periodically monitor the structural integrity of the snake arm during use if the cable tensions can be measured directly with strain gauges mounted between the cables and the actuator frame. With all cable tensions known, the axial compression can be calculated from the snake arm orientation and cable tensions where the values can then be compared to the failure modes previously researched.

8.3.2 Reconfigurable dual track robot

- A major obstacle for the robot is the low ground clearance at the middle deployment module where debris can be caught and obstruct the camera and light. A mechanism is needed that can raise the module further from the ground.
- Connecting the three modules together resulted with electrical cables being routed externally to bypass structural components. This left the exposed wiring to the terrain with low ground clearance. Some form of cable protection or a method to route the cabling internally is required to better protect the robot.

8.3.3 Self-folding robot

- The flexible heater uses copper tracks of 0.23mm for joule heating and is fabricated using laser etching. To ease the fabrication of this component, the track width can be increased (as power consumption is not an issue) to allow for standard lithography manufacturing techniques to be used. This should improve the quality and reliability for the flexible heater.
- A method to measure the temperature at both SMA layers will assist in the actuation of the fold. It can be made to turn off the heaters when the SMA activation temperature is approached for the opposing layer.
- Further study into better optimising the thermal layer will benefit the system. Thicker sheets of polyimide are available which will reduce the number of adhesive layers required in between. A better performing thermal insulating layer could also be thinner resulting in a reduced internal stiffness that can enhance the folding angle and torque generated.

List of References

1. Trivedi, B., *Search-and-Rescue Robots Tested at New York Disaster Site in National Geographic Today* 2001: National Geographic.
2. Morris, A., et al., *Recent developments in subterranean robotics*. Journal of Field Robotics, 2006. **23**(1): p. 35-57.
3. Guizzo, E. *Robots Enter Fukushima Reactors, Detect High Radiation* IEEE Spectrum [Web Blog] 2011 18/4/2011 [cited 2013 23 January]; Available from: <http://spectrum.ieee.org/automaton/robotics/industrial-robots/robots-enter-fukushima-reactors-detect-high-radiation>.
4. Pauley, E., T. Shumaker, and B. Cole. *Black Wolf Coal Company, Inc. Quecreek No. 1 Mine*. 2002 [cited 2014; 64]. Available from: <http://www.elibrary.dep.state.pa.us/dsweb/Get/Document-44211/5800-RE-DEP3100.pdf>.
5. BBCNews. *Scores rescued from flooded Chinese mine*. 2010 [cited 2014 3 April]; Available from: <http://news.bbc.co.uk/1/hi/world/asia-pacific/8603102.stm>.
6. Murphy, R.R., et al., *Mobile robots in mine rescue and recovery*. Robotics & Automation Magazine, IEEE, 2009. **16**(2): p. 91-103.
7. Adelman, J. *Japan Taps U.S. Robots For Nuclear Reactor Cleanup Help* [Web News Article] 2011 [cited 2013 23 January]; Available from: http://www.huffingtonpost.com/2011/04/18/japan-reactor-cleanup-us-robots_n_850344.html.
8. iRobot. *iRobot 510 PackBot*. [Website] 2012 [cited 2014 2 April]; Available from: <http://www.irobot.com/en/us/robots/defense/packbot.aspx>.
9. Matunhire, I., *Design of Mine Shafts*. Department of Mining Engineering, University of Pretoria, Pretoria, South Africa <http://www.infomine.com/publications/docs/Matunhire2007.pdf>, 2007.
10. Thrun, S., et al., *Autonomous exploration and mapping of abandoned mines*. Robotics & Automation Magazine, IEEE, 2004. **11**(4): p. 79-91.
11. Hawass, D.Z. *Keeping the Great Sphinx's Paws Dry*. Zahi Hawass 2009 [cited 2014; Available from: <http://www.drhawass.com/blog/keeping-great-sphinx%E2%80%99s-paws-dry>.
12. Aydan, Ö. and R. Ulusay, *Geotechnical and geoenvironmental characteristics of man-made underground structures in Cappadocia, Turkey*. Engineering Geology, 2003. **69**(3-4): p. 245-272.
13. Schoenbaum, S., *William Shakespeare: a compact documentary life*. 1987: Oxford University Press, USA.
14. Company, S.T. *SHAW TOOL*. [Website] 2011 [cited 2016 13 April]; Available from: <http://www.backpackdrill.com/>.
15. Takahashi, K., et al. *A study of locomotion mechanism based on gravitational environment*. in *Intelligent Robots and Systems, 2004. (IROS 2004). Proceedings. 2004 IEEE/RSJ International Conference on*. 2004.
16. Taylor, B.K., et al., *Design and validation of a Whegs robot in USARSim*, in *Proceedings of the 2007 Workshop on Performance Metrics for Intelligent Systems* 2007, ACM: Washington, D.C. p. 105-112.

17. Thomson, T., I. Sharf, and B. Beckman. *Kinematic control and posture optimization of a redundantly actuated quadruped robot*. in *Robotics and Automation (ICRA), 2012 IEEE International Conference on*. 2012.
18. Morozovsky, N., C. Schmidt-Wetekam, and T. Bewley. *Switchblade: An agile treaded rover*. in *Intelligent Robots and Systems (IROS), 2011 IEEE/RSJ International Conference on*. 2011.
19. Jueyao, W., et al. *Design of a modular robotic system for archaeological exploration*. in *Robotics and Automation, 2009. ICRA '09. IEEE International Conference on*. 2009.
20. Song, S.-M. and K.J. Waldron, *Gaits for Irregular Terrain*, in *Machines that walk: the adaptive suspension vehicle*. 1988, MIT press. p. 99-150.
21. Wang, Z. and H. Gu, *A review of locomotion mechanisms of urban search and rescue robot*. *Industrial Robot: An International Journal*, 2007. **34**(5): p. 400-411.
22. Tokuda, K., et al. *Concept and development of general rescue robot CUL*. in *Intelligent Robots and Systems, 1999. IROS '99. Proceedings. 1999 IEEE/RSJ International Conference on*. 1999.
23. Matthies, L., et al., *A portable, autonomous, urban reconnaissance robot*. *Robotics and Autonomous Systems*, 2002. **40**(2-3): p. 163-172.
24. Luk, B., et al. *An arthropodous robot for working in hazardous environments*. in *2nd IFAC International Conference on Intelligent Autonomous Vehicles (IAV'95)*. 1995.
25. Rollinson, D., et al. *Design and architecture of a series elastic snake robot*. in *Intelligent Robots and Systems (IROS 2014), 2014 IEEE/RSJ International Conference on*. 2014.
26. Erkmen, I., et al., *Snake robots to the rescue!* *IEEE Robotics & Automation Magazine*, 2002. **9**(3): p. 17-25.
27. Iwamoto, T. and H. Yamamoto, *Mechanical Design of Variable Configuration Tracked Vehicle*. *Journal of Mechanical Design*, 1990. **112**(3): p. 289-294.
28. Moosavian, S.A.A., H. Semsarilar, and A. Kalantari. *Design and Manufacturing of a Mobile Rescue Robot*. in *Intelligent Robots and Systems, 2006 IEEE/RSJ International Conference on*. 2006.
29. Marques, C., et al., *A search and rescue robot with tele-operated tether docking system*. *Industrial Robot: An International Journal*, 2007. **34**(4): p. 332-338.
30. Yamauchi, B.M. *PackBot: A versatile platform for military robotics*. in *Defense and Security*. 2004. International Society for Optics and Photonics.
31. iRobot. *iRobot 110 FirstLook*. [Website] 2013 [cited 2013 7 February]; Available from: <http://www.irobot.com/us/robots/defense/firstlook.aspx>.
32. Silva, M.F. and J.A.T. Machado, *A historical perspective of legged robots*. *Journal of Vibration and Control*, 2007. **13**(9-10): p. 1447-1486.
33. Menon, C., et al. *Abigaille-I: Towards the development of a spider-inspired climbing robot for space use*. in *Biomedical Robotics and*

- Biomechatronics*, 2008. *BioRob 2008. 2nd IEEE RAS & EMBS International Conference on*. 2008.
34. Clark, J.E., et al. *Biomimetic design and fabrication of a hexapedal running robot*. in *Robotics and Automation*, 2001. *Proceedings 2001 ICRA. IEEE International Conference on*. 2001.
 35. Arena, P., et al. *An autonomous mini-hexapod robot controlled through a CNN-based CPG VLSI chip*. in *Cellular Neural Networks and Their Applications*, 2006. *CNNA '06. 10th International Workshop on*. 2006.
 36. Eich, M., F. Grimmering, and F. Kirchner. *A Versatile Stair-Climbing Robot for Search and Rescue Applications*. in *Safety, Security and Rescue Robotics*, 2008. *SSRR 2008. IEEE International Workshop on*. 2008.
 37. Saranli, U., M. Buehler, and D.E. Koditschek, *Rhex: A simple and highly mobile hexapod robot*. *The International Journal of Robotics Research*, 2001. **20**(7): p. 616-631.
 38. SPIRITO, C.P. and D.L. MUSHRUSH, *Interlimb coordination during slow walking in the cockroach: I. Effects of substrate alterations*. *The Journal of Experimental Biology*, 1979. **78**(1): p. 233-243.
 39. Morrey, J.M., et al. *Highly mobile and robust small quadruped robots*. in *Intelligent Robots and Systems*, 2003. (*IROS 2003*). *Proceedings. 2003 IEEE/RSJ International Conference on*. 2003.
 40. Lambrecht, B.G.A., A.D. Horschler, and R.D. Quinn. *A Small, Insect-Inspired Robot that Runs and Jumps*. in *Robotics and Automation*, 2005. *ICRA 2005. Proceedings of the 2005 IEEE International Conference on*. 2005.
 41. Morris, A., et al., *Case Studies of a Borehole Deployable Robot for Limestone Mine Profiling and Mapping*, in *Field and Service Robotics*, S.i. Yuta, et al., Editors. 2006, Springer Berlin Heidelberg. p. 189-198.
 42. Carsey, F., et al., *A borehole camera system for imaging the deep interior of ice sheets*. *Journal of Glaciology*, 2002. **48**(163): p. 622-628.
 43. Voyles, R.M. and A.C. Larson, *TerminatorBot: a novel robot with dual-use mechanism for locomotion and manipulation*. *Mechatronics, IEEE/ASME Transactions on*, 2005. **10**(1): p. 17-25.
 44. Yim, M., et al., *Modular Self-Reconfigurable Robot Systems [Grand Challenges of Robotics]*. *Robotics & Automation Magazine, IEEE*, 2007. **14**(1): p. 43-52.
 45. Yim, M., D.G. Duff, and K.D. Roufas. *PolyBot: a modular reconfigurable robot*. in *Robotics and Automation*, 2000. *Proceedings. ICRA '00. IEEE International Conference on*. 2000.
 46. Salemi, B., M. Moll, and W.-M. Shen. *SUPERBOT: A deployable, multi-functional, and modular self-reconfigurable robotic system*. in *Intelligent Robots and Systems*, 2006 *IEEE/RSJ International Conference on*. 2006. IEEE.
 47. Yim, M., et al., *Connecting and disconnecting for chain self-reconfiguration with PolyBot*. *Mechatronics, IEEE/ASME Transactions on*, 2002. **7**(4): p. 442-451.
 48. Duff, D., M. Yim, and K. Roufas. *Evolution of polybot: A modular reconfigurable robot*. in *Proc. of the Harmonic Drive Intl. Symposium*, Nagano, Japan. 2001. Citeseer.

49. Chiu, H.C., M. Rubenstein, and W.-M. Shen. *Multifunctional superbots with rolling track configuration*. in *IROS 2007 Workshop on Self-Reconfigurable Robots & Systems and Applications*. 2007.
50. Schempf, H. *Houdini: In-tank mobile cleanup robot*. in *Robotics for Challenging Environments*. 1994.
51. Granosik, G., M. Hansen, and J. Borenstein, *The OmniTread serpentine robot for industrial inspection and surveillance* *Industrial Robot: An International Journal*, 2005. **32**(2): p. 139.
52. Hitachi. *Submersible and shape-changing robots developed for Fukushima inspection*. [Website] 2014 [cited 2016 27th April]; Available from: <http://phys.org/news/2014-03-submersible-shape-changing-robots-fukushima.html>.
53. Russon, M.-A. *Fukushima: Robot 'dies' 3 hours after entering Japan's radioactive reactor*. [Website] 2015 [cited 2016 27th April]; Available from: <http://www.ibtimes.co.uk/fukushima-robot-dies-3-hours-after-entering-japans-radioactive-reactor-1496126>.
54. Schempf, H. *Houdini: Site and locomotion analysis-driven design of an in-tank mobile cleanup robot*. in *Paper delivered at American Nuclear Society Winter Meeting, San Francisco, November*. 1995.
55. Felton, S.M., et al. *Robot self-assembly by folding: A printed inchworm robot*. in *Robotics and Automation (ICRA), 2013 IEEE International Conference on*. 2013.
56. Shin, B., et al., *Self-assembling Sensors for Printable Machines*. 2014.
57. Felton, S.M., et al., *Self-folding with shape memory composites*. *Soft Matter*, 2013. **9**(32): p. 7688-7694.
58. Felton, S., et al., *A method for building self-folding machines*. *Science*, 2014. **345**(6197): p. 644-646.
59. Paik, J.K., E. Hawkes, and R.J. Wood, *A novel low-profile shape memory alloy torsional actuator*. *Smart Materials and Structures*, 2010. **19**(12): p. 125014.
60. Paik, J.K. and R.J. Wood, *A bidirectional shape memory alloy folding actuator*. *Smart Materials and Structures*, 2012. **21**(6): p. 065013.
61. Onal, C.D., R.J. Wood, and D. Rus, *An Origami-Inspired Approach to Worm Robots*. *Mechatronics, IEEE/ASME Transactions on*, 2013. **18**(2): p. 430-438.
62. Onal, C.D., R.J. Wood, and D. Rus. *Towards printable robotics: Origami-inspired planar fabrication of three-dimensional mechanisms*. in *Robotics and Automation (ICRA), 2011 IEEE International Conference on*. 2011.
63. Je-Sung, K. and C. Kyu-Jin. *Omegabot : Biomimetic inchworm robot using SMA coil actuator and smart composite microstructures (SCM)*. in *Robotics and Biomimetics (ROBIO), 2009 IEEE International Conference on*. 2009.
64. Je-Sung, K. and C. Kyu-Jin. *Omegabot: Crawling robot inspired by Ascotis Selenaria*. in *Robotics and Automation (ICRA), 2010 IEEE International Conference on*. 2010.
65. Je-sung, K. and C. Kyu-jin, *Omega-Shaped Inchworm-Inspired Crawling Robot With Large-Index-and-Pitch (LIP) SMA Spring Actuators*. *Mechatronics, IEEE/ASME Transactions on*, 2013. **18**(2): p. 419-429.

66. Kesner, S., et al. *A Hopping Mobility Concept for a Rough Terrain Search and Rescue Robot*. in *Advances in Climbing and Walking Robots - Proceedings of 10th International Conference*. 2007.
67. Aoyama, H., et al. *Micro hopping robot with IR sensor for disaster survivor detection*. in *Safety, Security and Rescue Robotics, Workshop, 2005 IEEE International*. 2005.
68. Hirose, S., *Biologically inspired robots : snake-like locomotors and manipulators*. 1993: Oxford University Press. 220.
69. Technology, T.I.o. *Hirose receives the 2009 Engelberger Robotics Award*. 2009 [cited 2012 17 October]; Available from: http://www.titech.ac.jp/english/news-topics/detail_98.html?id=news-topics.
70. Hirose, S. and M. Mori. *Biologically Inspired Snake-like Robots*. in *Robotics and Biomimetics, 2004. ROBIO 2004. IEEE International Conference on*. 2004.
71. Hirose, S. and H. Yamada, *Snake-like robots [Tutorial]*. *Robotics & Automation Magazine, IEEE*, 2009. **16**(1): p. 88-98.
72. Yamada, H. and S. Hirose. *Study of a 2-DOF joint for the small Active Cord Mechanism*. in *Robotics and Automation, 2009. ICRA '09. IEEE International Conference on*. 2009.
73. Granosik, G. and J. Borenstein, *Integrated joint actuator for serpentine robots*. *Mechatronics, IEEE/ASME Transactions on*, 2005. **10**(5): p. 473-481.
74. Buckingham, R.O. and A.C. Graham. *Dexterous manipulators for nuclear inspection and maintenance - Case study*. in *Applied Robotics for the Power Industry (CARPI), 2010 1st International Conference on*. 2010.
75. Sung, G.T. and I.S. Gill, *Robotic laparoscopic surgery: a comparison of the da Vinci and Zeus systems*. *Urology*, 2001. **58**(6): p. 893-898.
76. Lum, G.Z., et al. *Design and motion control of a cable-driven dexterous robotic arm*. in *Sustainable Utilization and Development in Engineering and Technology (STUDENT), 2010 IEEE Conference on*. 2010.
77. Yisheng, G., et al. *1-DoF robotic joint modules and their applications in new robotic systems*. in *Robotics and Biomimetics, 2008. ROBIO 2008. IEEE International Conference on*. 2009.
78. Bartow, A., A. Kapadia, and I. Walker. *A novel continuum trunk robot based on contractor muscles*. in *Proceedings of the 12th WSEAS International Conference on Signal Processing, Robotics, and Automation*. 2013.
79. Li, C. and C.D. Rahn, *Design of Continuous Backbone, Cable-Driven Robots*. *Journal of Mechanical Design*, 2002. **124**(2): p. 265-271.
80. Minor, M. and R. Mukherjee. *A dexterous manipulator for minimally invasive surgery*. in *Robotics and Automation, 1999. Proceedings. 1999 IEEE International Conference on*. 1999.
81. Martinez, R.V., et al., *Robotic Tentacles with Three-Dimensional Mobility Based on Flexible Elastomers*. *Advanced Materials*, 2013. **25**(2): p. 205-212.
82. Tsukagoshi, H., A. Kitagawa, and M. Segawa. *Active Hose: an artificial elephant's nose with maneuverability for rescue operation*. in

- Robotics and Automation, 2001. Proceedings 2001 ICRA. IEEE International Conference on.* 2001.
83. Camarillo, D.B., et al., *Mechanics Modeling of Tendon-Driven Continuum Manipulators*. Robotics, IEEE Transactions on, 2008. **24**(6): p. 1262-1273.
84. Simaan, N., R. Taylor, and P. Flint, *High Dexterity Snake-Like Robotic Slaves for Minimally Invasive Telesurgery of the Upper Airway Medical Image Computing and Computer-Assisted Intervention – MICCAI 2004*, C. Barillot, D. Haynor, and P. Hellier, Editors. 2004, Springer Berlin / Heidelberg. p. 17-24.
85. Wei, W., X. Kai, and N. Simaan. *A Compact Two-armed Slave Manipulator for Minimally Invasive Surgery of the Throat*. in *Biomedical Robotics and Biomechatronics, 2006. BioRob 2006. The First IEEE/RAS-EMBS International Conference on.* 2006.
86. Du, Z., W. Yang, and W. Dong, *Kinematics Modeling of a Notched Continuum Manipulator*. Journal of Mechanisms and Robotics, 2015. **7**(4): p. 041017-041017.
87. Zheng, L. and D. Ruxu. *Expanding workspace of underactuated flexible manipulators by actively deploying constraints*. in *Robotics and Automation (ICRA), 2014 IEEE International Conference on.* 2014.
88. Dong, X., et al., *A Novel Snake Arm Robot Using Twin-Pivot Compliant Joints: Design, Modeling and Validation*. Journal of Mechanisms and Robotics.
89. Tianjiang, Z., et al. *Dynamic continuum arm model for use with underwater robotic manipulators inspired by octopus vulgaris*. in *Robotics and Automation (ICRA), 2012 IEEE International Conference on.* 2012.
90. Junhu, H., et al. *The mechanical design of snake-arm robot*. in *Industrial Informatics (INDIN), 2012 10th IEEE International Conference on.* 2012.
91. Cheng, N.G., et al. *Design and Analysis of a Robust, Low-cost, Highly Articulated manipulator enabled by jamming of granular media*. in *Robotics and Automation (ICRA), 2012 IEEE International Conference on.* 2012.
92. Niu, G., et al., *A novel design of aircraft fuel tank inspection robot*. TELKOMNIKA Indonesian Journal of Electrical Engineering, 2013. **11**(7): p. 3684-3692.
93. Buckingham, R., et al., *Snake-arm robots: a new approach to aircraft assembly*, 2007, SAE Technical Paper.
94. Lu, C., et al. *Design of a portable snake-like search and rescue apparatus used in the gap*. in *Mechatronic Science, Electric Engineering and Computer (MEC), 2011 International Conference on.* 2011.
95. Chalfoun, J., et al. *Design and flexible modeling of a long reach articulated carrier for inspection*. in *Intelligent Robots and Systems, 2007. IROS 2007. IEEE/RSJ International Conference on.* 2007.
96. Chalfoun, J., et al. *Flexible Modeling of a Long Reach Articulated Carrier: Geometric and Elastic Error Calibration*. in *Computational Intelligence in Robotics and Automation, 2007. CIRA 2007. International Symposium on.* 2007.

97. Horigome, A., et al. *Development of a coupled tendon-driven 3D multi-joint manipulator*. in *Robotics and Automation (ICRA), 2014 IEEE International Conference on*. 2014.
98. Perrot, Y., et al. *Long reach articulated robots for inspection in hazardous environments, recent developments on robotics and embedded diagnostics*. in *Applied Robotics for the Power Industry (CARPI), 2010 1st International Conference on*. 2010.
99. Robotics, O. *Snake-arm robots, Robots for confined spaces*. 2012 [cited 2012 23 October]; Available from: <http://www.ocrobotics.com/>.
100. Buckingham, R. and A. Graham, *Link Assembly for a Snake Like Robot Arm*, O.C.R. Limited, Editor 2009, Oliver Crispin Robotics Limited: United States.
101. Perrot, Y., et al., *Long-reach articulated robots for inspection and mini-invasive interventions in hazardous environments: Recent robotics research, qualification testing, and tool developments*. *Journal of Field Robotics*, 2012. **29**(1): p. 175-185.
102. Tran, L.D., et al. *Control of a cable-driven 2-DOF joint module with a flexible backbone*. in *Sustainable Utilization and Development in Engineering and Technology (STUDENT), 2011 IEEE Conference on*. 2011.
103. Simaan, N. *Snake-Like Units Using Flexible Backbones and Actuation Redundancy for Enhanced Miniaturization*. in *Robotics and Automation, 2005. ICRA 2005. Proceedings of the 2005 IEEE International Conference on*. 2005.
104. Wolf, A., et al. *A mobile hyper redundant mechanism for search and rescue tasks*. in *Intelligent Robots and Systems, 2003. (IROS 2003). Proceedings. 2003 IEEE/RSJ International Conference on*. 2003.
105. Li, B., et al., *AMOEBa-I: A Shape-Shifting Modular Robot for Urban Search and Rescue*. *Advanced Robotics*, 2009. **23**(9): p. 1057-1083.
106. Cree. *XLamp MP-L EasyWhite*. [Website] 2016 [cited 2016 13 march]; Available from: <http://www.cree.com/LED-Components-and-Modules/Products/XLamp/Arrays-Directional/XLamp-MPL-EasyWhite>.
107. Lowe, K.M., et al., *Ground-penetrating radar and burial practices in western Arnhem Land, Australia*. *Archaeology in Oceania*, 2014. **49**(3): p. 148-157.
108. Buckingham, R., *Snake-Arm Robots*, in *Ingenia Online* 2006, Royal Academy of Engineering: Ingenia Online. p. 35 - 40.
109. Morecki, A., et al. *Synthesis and control of the anthropomorphic two-handed manipulator*. in *Proceedings of the 10th international symposium on industrial robots*. 1980.
110. Asada, H. and J. Leonard, *Dynamics*, in *Introduction to Robotics*. 2005: MIT Open Courseware. p. 1.
111. Hunter, D.F., *ESDU 88034 Avoidance of buckling of some engineering elements (struts, plates and gussets)*. 1988: IHS ESDU.
112. Howard Allen, P.B., *Cylindrical Shell in Axial Compression, in Background to Buckling*. 1980, McGraw-Hill Book Company (UK) Limited. p. 515 -524.
113. Conry, T.F., *Machine design theory and practice: A.D. Deutschman, W.J. Michels and C.E. Wilson: Macmillan, New York, 1975, 932 pp. Mechanism and Machine Theory*, 1976. **11**(4): p. 304-305.

114. Long, A., M. Lyon, and G. Lyon, *Industrial rope access - Investigation into items of personal protective equipment*, 2001, Health & Safety Executive.
115. Automations, F. *Light Duty Linear Actuators*. [Webpage] 2016 [cited 2016 23rd March]; Available from: <https://www.firgelliauto.com/products/light-duty-rod-actuator>.
116. Oberg, E. and C.J. McCauley, *Machinery's handbook: a reference book for the mechanical engineer, designer, manufacturing engineer, draftsman, toolmaker, and machinist*. 2012, Industrial Press: New York. p. 257.
117. Matthews, C., *IMechE Engineers' Databook*. 2011, John Wiley & Sons. p. 75.
118. Tyson, F., *ESDU SS1 Guide to the use of the Stress and Strength Series*, 2003: IHS ESDU.
119. GOPE, P.C., *MACHINE DESIGN: FUNDAMENTALS AND APPLICATIONS*. 2012, PHI Learning. p. 811.
120. Toolbox, E. *Factors of Safety*. [Website] 2016 [cited 2016 8th April]; Available from: http://www.engineeringtoolbox.com/factors-safety-fos-d_1624.html.
121. Jong, I.C. and B.G. Rogers, *Engineering mechanics*. 1991, Saunders College Pub.: Philadelphia. p. 354.
122. aalco. *Stainless Steel - Austenitic - 1.4401 Bar and Section*. [Website] 2016 [cited 2016 14 March]; Available from: http://www.aalco.co.uk/datasheets/Stainless-Steel-14401-Bar-and-Section_37.ashx.
123. Hawkes, E., et al., *Programmable matter by folding*. Proceedings of the National Academy of Sciences, 2010. **107**(28): p. 12441-12445.
124. Fremond, M. and S. Miyazaki, *Shape memory alloys*. Vol. 351. 2014: Springer.
125. Technologies, C.M. *Shape Memory Nitinol Alloys*. [Online Datasheet] 2016 [cited 2016 15 March]; Available from: <https://confluentmedical.com/wp-content/uploads/2016/01/Material-Data-Sheet-Shape-Memory.pdf>.
126. Components, J.M.M. *Measuring Transformation Temperatures in Nitinol Alloys*. [Website] 2016 [cited 2016 15 March]; Available from: <http://jmmedical.com/resources/211/Measuring-Transformation-Temperatures-in-Nitinol-Alloys.html>.

Appendix A

Papers published

This section contains published work from this thesis.

1. Liu, J., et al., Exploration Robots for Harsh Environments and Safety. IFAC-PapersOnLine, 2015. 48(10): p. 41-45.
2. Liu, J., et al., Mechanical Design of Long Reach Super Thin Discrete Manipulator for Inspections in Fragile Historical Environments, in Towards Autonomous Robotic Systems: 16th Annual Conference, TAROS 2015, Liverpool, UK, September 8-10, 2015, Proceedings, C. Dixon and K. Tuyls, Editors. 2015, Springer International Publishing: Cham. p. 155-160.

Exploration Robots for Harsh Environments and Safety

J. Liu*, B.-Y. Ma*, N. Fry*, A. Pickering*, S. Whitehead***, N. Somjit**, R. C. Richardson*, I. D. Robertson**

* School of Mechanical Engineering, University of Leeds, LS2 9JT, UK (e-mail: {mn07jhw, mnbm, el10nrf, A.D.Pickering, R.C.Richardson}@leeds.ac.uk)

** School of Electronic and Electrical Engineering, University of Leeds, LS2 9JT, UK (Tel: +44 (0) 113 343 8207; e-mail: {N.Somjit, I.D.Robertson@leeds.ac.uk}).

*** Scoutek Ltd., Leeds, UK (e-mail: shaun@creationeer.co.uk)

Abstract: In this paper the development and demonstration of various robotic systems for safety applications and harsh environments are presented. These robotic systems assist human to monitor and explore various types of spaces and measure physical parameters of these spaces. Each individual robot can be equipped with 3D ceramic-packaged multi-purpose sensors/actuators, smart navigation systems, and reconfigurable high-speed wireless communication networking. The targeted applications are real-time monitoring/rescuing in various kinds of harmful environments e.g. deep mines, pipe and tube systems, dramatically reducing risk of life and economic damage.

Keywords: Robotic exploration, harsh environments, safety and security, co-operative robot.

1. INTRODUCTION

This paper presents the design and demonstration of three novel compact robotic systems, which can be integrated with 3D ceramic-packaged, multi-purpose micro-sensors and high-speed ad-hoc wireless communication systems. The targeted application is for real-time monitoring and exploring folded spaces under possible harmful conditions e.g. chemical leakages, pressure level, temperature and gas concentration in harsh environments as well as for security and archaeological applications; decreasing the risk of life and economic damage.

2. DJEDI ROBOT: A PYRAMID EXPLORATION ROVER

The Great Pyramid of Giza is the last remaining wonder of the ancient world. The pyramid contains three chambers, including the king's and queen's chamber. Airshafts have been discovered in both chambers, however the queen's shaft has no obvious purpose nor does it breach the outer face of the pyramid structure, unlike the king's chamber. Exploration of the northern and southern airshafts to answer the mysteries of its purpose and construction required the use of specialised mobile robotic tools, such as the Djedi Pyramid Explorer Robot (Figure 1) which in May 2010 performed a video survey successfully, by climbing the full length of the southern air shaft.

Produced from soft limestone of varying surface roughness, the air shafts are approximately 210 mm x 210 mm and spans through different configurations for the northern and southern shaft. The southern shaft begins running horizontally for approximately 2 m before rising at an incline of 40° from the horizontal, spanning approximately a further 62 m in length from the chamber entrance. Additional obstacles exist within the shafts such as a lateral step at about 30 m or the 40 mm vertical step at 59 m and at the top of the shaft are the main objectives, which consists of two limestone blocking stones of 60 mm approximate thickness for the first stone and an unknown thickness for the second; each spaced approximately 200 mm apart.

The specifications for the Djedi robot required the robot to climb the air shafts with minimal or no damage to the pyramid walls, yet retain the capacity to obtain sufficient tractive force to safely navigate the steep inclines, smooth surfaces and counter the resultant forces from the on-board drill. Building upon the testing of three prototypes using different variations of an inch worm mechanism, the latest design of the Djedi robot had two independently driven pinion carriages on the same rack, with one carriage for driving the robot through the shafts and the other for driving the on-board drill.

To brace against the shaft walls and provide the necessary traction to climb and provide stability during drilling, custom linear actuators were created with a silicon rubber brace pad mounted at the end. The points of

contact between the brace actuators and the wall from each inchworm step during the shaft ascent does not move (Figure 2), also the applied force is perpendicular to the wall surface. These features combined with the soft silicon pads resulted in a large reduction to the risk of damaging the air shaft walls. The four wheels were left unpowered and served only to allow Djedi to climb the vertical step and to prevent dragging on the shaft floor.

The use of 3D printing technology was used almost exclusively for the manufacture of the carriages. Enabling rapid productions of chassis parts with complex features, which allowed for increasingly compact carriages to be reduced in weight and size and therefore increase step and drill length of the robot.

Embedded into the carriage chassis are eleven composite cameras with an additional snake arm camera attachment to replace the drill. Each camera is strategically positioned to provide a full field of view for all sides of the air shafts and vital components of the Djedi robot for visual monitoring. The findings from the climb revealed red ochre markings or hieratic characters previously unseen for thousands of years (Richardson, R 2013).

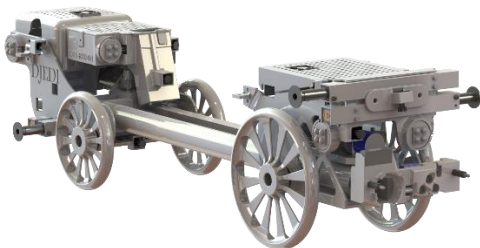


Fig. 1. Djedi Southern Shaft Rover.

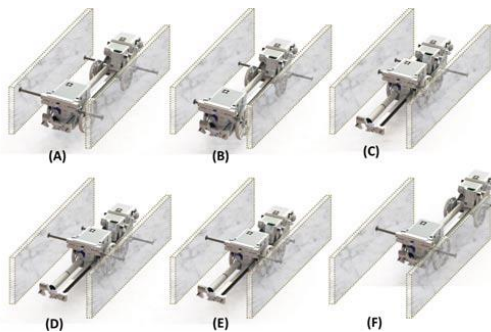


Fig. 2. Rendered images of the Djedi rover during different stages of the inchworm locomotion.

3. MINEBOT: A DUAL-TRACK RECONFIGURABLE ROBOT

The subterranean environments such as mines and tunnels are remote, inaccessible, and dangerous for human entry. Inherent dangers in environments motivate the use of robotic

technology for addressing such challenges (Morris, A 2006). In order to inspect subterranean environment, it is common to drill small boreholes from the surface into what is expected to be the exploration area. The idea is to insert a small robot through the borehole, lower the robot into the subterranean space, and explore the area. However, there are still many challenges in terms of limited diameter of borehole and lack of illumination posed by boreholes exploration.

In response to these challenges, a dual-tracked reconfigurable robot with on-board camera and Cree LED light, named Minebot, was developed at the University of Leeds. The Minebot is an imaging mobile system that can be lowered down through narrow passages, such as boreholes, for subterranean exploration. It can establish a remote, subterranean presence without unnecessary risk to humans. The Minebot is capable of reconfiguring to move inside the tunnel, using dual-tracked mobility system to move in parallel (as shown in Figure 3).

When the situation requires the robot to be inserted into boreholes or navigate obstacles, it can transform into a snake-like configuration (as shown in Figure 4). The Minebot is designed to be deployable and retrievable through a 9.1m long, 41 mm diameter borehole into tunnels and to operate at long ranges in tunnels of approximately 200m long on a slight incline over rough terrain.

Table 1. Minebot measurements

Weight	2.7 kg
Fully deployed size	33 x 335 x 455 mm
Snake-like size	33 x 1199.5 x 31 mm
Maximum speed	11.4 mm/s



Fig. 3. Fully deployed configuration of the Minebot.



Fig. 4. Snake-like configuration of the Minebot.

Provided with some approximate environmental specifications, the locomotion and deployment systems of the Minebot were developed. The diameter of the borehole was a fixed variable supplied from a portable borehole drilling device used to gain entry into the mine. Considering the small diameter of the borehole and its length, a limit of 35mm diameter for the entire Minebot during the deployment phase was agreed upon. This allowed for a value of torque to be calculated to compensate for the robots mass on an incline and frictional drag forces from the tether. Without the ability to replicate the Djedi robots ability to brace on two sections of wall, the Minebot relies on the weight to produce the required traction to travel the long distances.

Extraction of the Minebot was also considered as essential for the mission brief. This resulted in the need for a high torque reversible joint capable of changing between the fully deployed state and the snake-like configuration with no assistance.

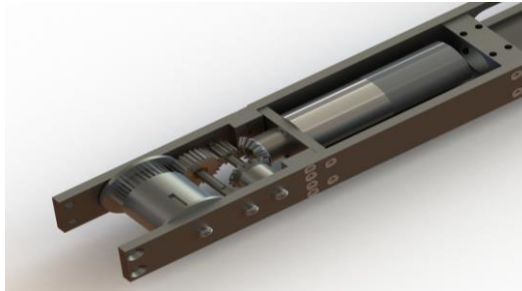


Fig. 5. Gearbox housing within track section.



Fig. 6. High torque with slender profile joint.

4. LETTERBOT: A FOLDED BUILDING EXPLORATION ROBOT

The Police and other authorities often have to search buildings without prior knowledge of what hazards may be present. Large robots currently in use require a door or window to be broken before it can enter the building. LetterBot was designed to enable quick deployment into any building without requiring tools or damage.

In the majority of locked properties the only damage free way to insert a robot is through the letterbox. The standard BS EN 13724:2002 (BSI 2002) gives the minimum dimensions of the slot to be 230x30mm. This gives a very tight height constraint requiring careful actuator selection. For the robot to provide information beyond that of a pole camera it is important that it can overcome stairs as reported by Nguyen et al. (Nguyen 2000).

To ensure the robot is capable of ascending all regular stairs, UK building regulations (HM Government 2013) were reviewed. Giving the requirement that the robot length is $\geq 443\text{mm}$ to span two steps, it will have to overcome step heights of over 7 times its height, and produce enough torque to climb up stairs angled up to 42° .

A variety of robotic methods have been developed for stair climbing, such as a rack and pinion arm to lift itself up each step (Wende, G 2004), a tri-wheeled design that interlocks with the stairs (Hirose, S 2001), a multilink mechanism with six driven wheels (Michaud, S 2002) or various humanoid designs. While these have all been shown to climb stairs they all rely on the robot being larger than an individual step.

A tracked design with two separate sections and an actuated link joint was developed. Liu et al. (2005) analysed fundamental kinematics and dynamics for a tracked robot to climb stairs. The process is split into Riser Climbing, Riser Crossing, and Nose Line Climbing. A tall angled front is often used to aid riser climbing (Tao, Ou and Feng et al. 2012) but cannot be used in this case due to the height restriction.

The two sections allow the robot to ascend the stairs without the Riser Climbing stage (Figure 5).

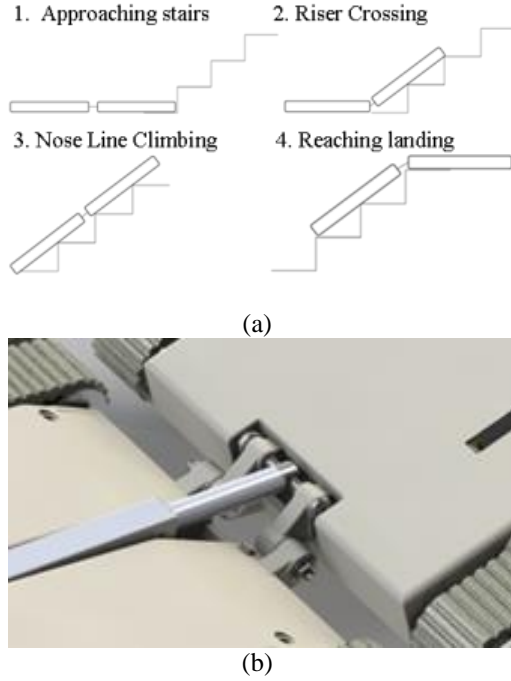


Fig. 5: (a) Sequence for a two sectioned robot to climb stairs. (b) Version 1 mechanism.

Two versions of LetterBot have now been created. The mechanism used in the first was designed to be simple and robust. A very short lever arm and a 200N linear actuator make the front section lift around a one degree of freedom revolute joint as shown in Figure 5. The second version uses an adaptation of a “little-known” gear slider mechanism, Figure 6, (Chironis et al. 1996). To aid weight optimisation and complex geometries 3D printing was used for the first design. Version 2 used a steel base plate as a thin rigid base, with aluminium modules building up the rest of the chassis.

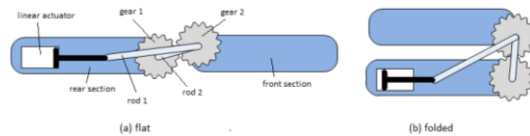
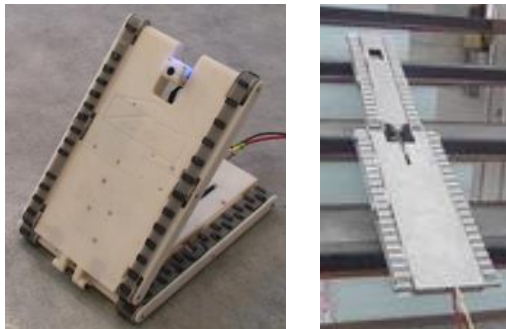


Fig. 6. Modified gear slider mechanism.

Continuous tracks were chosen as they can be used with a smaller diameter driving wheel than sectioned tracks. The tracks were custom



designed to enable the robot to grip the noses of steps while climbing and reduce the friction when turning. When climbing the angle reduces the friction force, the contact area is also much smaller. Therefore welded on profiles were designed to mesh with the steps like teeth of a gear. They also help keep the robot perpendicular to the stairs. Using analysis by Rastan et al. (2011) the pitch was found to be optimal at 20mm. As the robot uses a differential drive system to steer, large sideways frictional forces are generated during turning which can remove the tracks. The angled profiles reduce this drag as does hinging the robot in the middle to shorten the track length in contact.

Fig. 7. Left, LetterBot v1 folded up and looking around. Right, v2 climbing stairs.

5. CLIMBING IDEAL INCLINES

For a compact exploration robot to climb an incline of angle θ_a , a robot of mass M_r must generate sufficient pulling force F_p to overcome gravitational force F_g , frictional drag forces F_d , and the forces required to drag the tether F_c . The gravitational force can be resolved into a two components of force, one parallel to the ground and the other perpendicular to the ground.

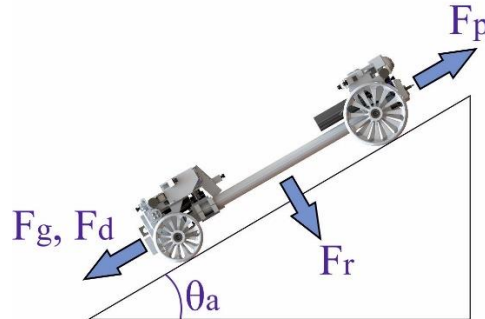


Fig. 8. Free body diagram of robot on an incline.

These equations are valid for the free body diagram:

$$F_r = M_r \cdot g \cdot \sin(\theta_a), \quad (1)$$

$$F_g = M_r \cdot g \cdot \cos(\theta_a). \quad (2)$$

The pulling force F_p exerted by the robot is limited by the frictional coefficient between the robot and the floor surface (μ_n) and the normal force (F_r),

$$F_p \leq F_r \cdot \mu_n. \quad (3)$$

In order to overcome the frictional drag from the tether (F_c), the sum of the forces due to the

cable need to be considered. If the friction coefficient between the cable and floor is (μ_c), the cable weight is C_m and x_c is the length of the tether in meters. The force required to overcome the cable frictional drag is then calculated as:

$$F_c = C_m \cdot x_c \cdot g \cdot \sin(\theta_a) + \mu_c \cdot C_m \cdot x_c \cdot g \cdot \cos(\theta_a). \quad (4)$$

Therefore, in order to climb the incline, the required pulling force is:

$$F_p = M_r \cdot g \cdot \sin(\theta_a) + C_m \cdot x_c \cdot g \cdot [\sin(\theta_a) + \mu_c \cdot \cos(\theta_a)]. \quad (5)$$

The most straightforward method to increase the robots capability to climb steep inclines is to increase the friction coefficient between the robot and floor (μ_n) and decrease the friction coefficient between tether and floor (μ_c).

In the case of the Djedi robot, the tether was custom made with a thin, low friction, sheath. As a result of the inch-worm mechanism the weight of the robot was designed for minimal weight (M_r) as the four linear actuators can exert the required normal force (F_r) to overcome the opposing forces. On the other hand, the Minebot and Letterbot with the tracked configurations will rely on the mass of the robot to provide the necessary force for sufficient traction.

6. CONCLUSIONS

The Djedi robot operated as intended and reached the top of the southern shaft. The findings from the video survey provided valuable evidence towards the purpose and construction of the pyramid. The locomotion system was successful in protecting the pyramid from damage, as no surface marks in the shaft walls were observed after repeated climbs.

The use of rapid prototyped bodywork proved to have sufficient strength to endure the forces experienced during manoeuvring in the shaft. A noticeable drawback to the inch worm locomotion was the robots low climbing speed. Taking up to four hours to ascend the shafts, this time was acceptable when just one or two ascents are planned, but if future surveys require the use of multiple tools, then the ascent time would be a serious issue.

Deployment of the Minebot through a 3m long tube of 40mm diameter has been demonstrated successfully. Further testing in lab spaces has shown the Minebot to be capable of changing its deployments states with no assistance and

also able to drive effortlessly in the dual track configuration on a wooden floor.

However to achieve the operational distance of 200m to fully survey the proposed mine tunnel, the Minebot will require a large increase in weight to 6kg in order to supply the necessary traction. The current weight of 2.7kg allows the Minebot to survey up to a theoretical distance of 92m. A consequence of increasing the weight to 6kg is the robots un-deployed length must also be increased which will affect either the deployed length or width. This could possibly affect the robots ability to navigate and this trade-off will require further study.

LetterBot has successfully been deployed through a letter box and has climbed sets of stairs while returning HD video. The mechanism is robust, simple to maintain and has proven reliable over many test deployments. Version 2's mechanism (Figure 6) gives a greater mechanical advantage and allows the front section to be both longer and heavier, so larger steps can be negotiated. However due to its added complexity there is a trade off in reliability.

7. FUTURE WORK

Whilst the Minebot has been successfully tested in lab environments, future work will involve field testing in more realistic real world environments to find its capabilities to overcome rough terrain with debris and also its effective range in the mine environment. The inclusion of debris could allow for a larger coefficient of friction between robot and floor which would result in a greater range without the increase in robot mass however the low ground clearance may play a significant role in limiting range.

Building upon the experiences and techniques used in the Minebot for condensing the electronics and mechanisms into smaller spaces, these techniques can be applied to further improve the next iteration of LetterBot. At which point the LetterBot will be improved for easier deployments through higher and/or vertically orientated letterboxes with the capacity for additional sensor packages.

REFERENCES

- BSI. 2002. BS EN 13724:2002 *Postal services. Apertures of private letter boxes and letter plates. Requirements and test methods*. BSI.
- Chironis, N. P. 1996. *Mechanisms and mechanical devices sourcebook*. 2nd ed. London: McGraw-Hill
- Hirose, S. 2001. Super Mechano-System: New Perspective for Versatile Robotic System. In: RUS, D. & SINGH, S. (eds.)

- Experimental Robotics VII*. Springer Berlin Heidelberg. pp.249-258.
- HM Government. 2013. *The Building Regulations 2010*, 2013 edition. Newcastle Upon Tyne: NBS.
- Liu, J. et al. 2005. Analysis of stairs-climbing ability for a tracked reconfigurable modular robot. *Safety, Security and Rescue Robotics, Workshop, 2005 IEEE International*, 6-9 June 2005, pp.36-41.
- Michaud, S. et al.. 2002. SOLERO: Solar powered exploration rover. *Proceedings of the 7th ESA Workshop on Advanced Space Technologies for Robotics and Automation (ASTRA2002)*, Noordwijk, The Netherlands: Citeseer,
- Morris, A., Ferguson, D., Omohundro Z., Bradley D., Silver D., Baker C., et al. 2006. Recent developments in subterranean robotics. *Journal of Field Robotics*, vol. 23, pp. 35-57.
- Nguyen, H. G. and J. P. Bott. 2000. Robotics for law enforcement: Applications beyond explosive ordnance disposal. *SPIE Proc. 4232: Technologies for Law Enforcement*, pp.433-454.
- Rastan H. 2011. Mechanical Design for Track Robot Climbing Stairs. *MASc thesis*, University of Ottawa,
- Richardson R., Whitehead S., Ng T. C., Hawass Z., Pickering A, Rhodes S., et al.. 2013. The “Djedi” Robot Exploration of the Southern Shaft of the Queen's Chamber in the Great Pyramid of Giza, Egypt. *Journal of Field Robotics*, vol. 30, pp. 323-348
- Tao, W., Ou Y. and Feng H.. 2012. Research on Dynamics and Stability in the Stairs-climbing of a Tracked Mobile Robot. *Int J Adv Robotic Sys*, 9(146)
- Wende, G.. StairBot 2004 [online]. [Accessed 06/12/2014].
http://www.stairbot.de/en_beschreib.htm.

Mechanical Design of Long Reach Super Thin Discrete Manipulator for Inspections in Fragile Historical Environments

Jason Liu¹, Robert Richardson¹, Rob Hewson² and Shaun Whitehead³

¹ School of Mechanical Engineering, University of Leeds, Leeds, United Kingdom
{mn07jhw1, r.c.richardson}@leeds.ac.uk

² Faculty of Engineering, Imperial College, London, United Kingdom
r.hewson@imperial.ac.uk

³ Scoutek Ltd., Saltburn-by-the-Sea, United Kingdom
shaun@scoutek.com

Abstract. Long reach and small diameter manipulators are ideal for borehole deployments into search and rescue scenarios and fragile historical environments. Small diameter passageways impose constraints on a snake arm manipulator which severely limit its performance and capabilities. This work investigates the effects of tendon tensions on the maximum working length of a snake arm under tight size constraints and how the maximum length is achieved through an algorithmic approach and consideration of how and when key parts fail.

Keywords: Exploration, Long reach, Discrete backbone, Robot archaeology, Snake arm, Tendon tension, Minimally invasive, Small Diameter

Introduction

The application of robotic devices has been widely used in exploration and search and rescue (SAR) scenarios [1]. Ideally deployed where human risk is considered too high [2], tools such as the snake arm are often important for examining confined space environments where humans and some robots struggle. These robotic platforms are profoundly influenced by their intended environments and most exploit a single locomotion mechanism to operate in the complex terrains [3-5].

Different environments vary greatly from one to another, and produces a level of uncertainty and challenges for the end user [4]. It can be desirable for small boreholes to be used as means of access. Small boreholes will be faster to drill and reduces secondary collapse hazards; they are also less destructive and aid to preserve a site. Snake arms already have all the necessary locomotion parts anchored to a mobile platform outside the borehole [6-8], this allows the snake arm to fully utilize a boreholes diameter which plays a vital role in the snake arm's length.

The length of a snake arm is representative of the maximum working distance possible with a manipulator. Current small diameter snake arms include the continuous DTRA arm by OC Robotics with a reach of 610 mm and an outer diameter of 12.5 mm [9]. On the other hand long reach snake arms with large diameters already exist where

mechanisms to compensate for gravity are possible to achieve unsupported lengths of 6 m with a 100 mm diameter [9].

In this paper the design of a triple jointed snake arm manipulator that conforms to a very restrictive small diameter constraint is firstly introduced, and then an analysis of the snake arm theory is discussed. Lastly, an algorithmic approach is used to determine the maximum working length for the snake arm.

Description of the Basic Snake Arm

A discrete backbone snake arm simplifies kinematic formulations and motion control over its continuous backbone counterpart. Formed from a series of links and joints and actuated by a minimum of three tendons per joint, these tendons run through each link and terminate at each joint it is assigned to control. Assuming the boreholes are straight, the snake arm is not expected to maneuver around obstacles until it breaches through the borehole into a target chamber.

A snake arm capable of self-supporting the full length of its own arm in the deployed environment is advantageous for surveying fragile and historically important tomb-like chambers because there would be no need for any contact between the arm and surfaces for any risk of damage to occur. Fig. 1 shows a 12 mm diameter snake arm consisting of a base link (of length B), three two degrees of freedom (DOF) joints (of length J) and three links of identical length (of length L). The diameter places physical constraints on the number of cables controlling the snake arm joints, the thickness of the tubing that makes the links and the diameter of the two DOF joints.

Increasing link length L to create a longer snake arm has the effect of increasing the tendon tensions required to maintain the snake arms horizontal cantilever position. These forces result in greater axial compressive forces acting through the snake arm and possibly leading to joint failure and/or buckling of the links.

As a consequence, a method was required to theoretically calculate the tendon tensions from the snake arms kinematics and analyze the values to determine whether any anticipated failure modes will occur.

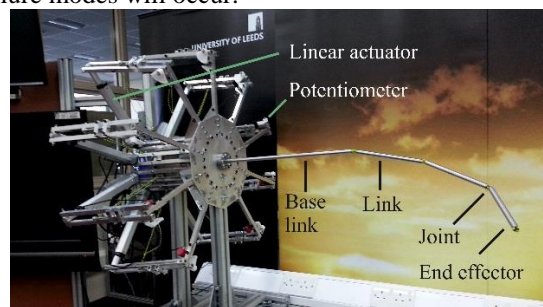


Fig. 1. 12 mm diameter snake arm

Discrete Snake Arm Kinematics and Statics

The position of the end effector with respect to the base frame is computed with forward kinematics using transformation matrices produced from joint angles and link lengths. Combined with the Recursive Newton-Euler (RNE) method the torque at each joint is computed and carried over to calculate the cable tensions.

The RNE joint torques reaches a maximum when the snake arm is at a horizontal cantilever position without additional external forces other than gravity acting upon it; therefore at this point it is assumed the associated tendon tensions are also at its maximum. This horizontal state should then be where failure of the snake arm is most likely to occur and is where this analysis is focused on.

Calculating tendon tensions from joint torques can be performed if tensions are assumed constant throughout with negligible friction and all joint angles are known. For a snake arm with two joints and two tendons of link length L , weight W , payload weight P and perpendicular tendon distance of D_y as shown in Fig. 2, multiple tendons cannot occupy the same space for all joints, therefore some tendons are displaced radially about the center. This creates an undesirable lateral load and requires the introduction of additional tendons to counteract the loads.

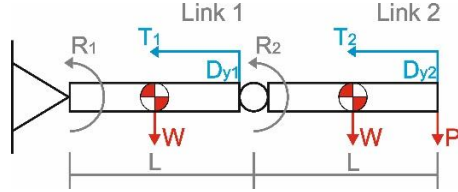


Fig. 2. Simplified snake arm with two joints and two tendons

The RNE method is used to calculate the joint torques R_1 and R_2 and the tendon tensions calculated for the i th joint is expressed as:

$$R_{xyi} = \sum_{j=i}^N T_j D_{xyj} \quad (1)$$

Where R_{xyi} is the torque generated at joint i for both yaw (R_x) and pitch (R_y) joint directions. T_j is the tension of each tendon that passes through or terminates at joint j . D_{xyj} is defined as the distance between tendon j and the neutral axis of joint i , it can also be a negative value dependent on the direction the tendon j transmits its force on joint i . Applying equation (1) to the double jointed snake arm as shown on Fig. 2, the equations relating torques to tensions can be produced and solved using matrices.

$$\begin{bmatrix} 0 & D_{y2} \\ D_{y1} & D_{y2} \end{bmatrix} \begin{bmatrix} T_1 \\ T_2 \end{bmatrix} = \begin{bmatrix} R_{y2} \\ R_{y1} \end{bmatrix} \quad (2)$$

Where the tensions T_1 and T_2 can be solved as:

$$\begin{bmatrix} T_1 \\ T_2 \end{bmatrix} = \begin{bmatrix} \frac{R_{y1}}{D_{y1}} - \frac{R_{y2}}{D_{y1}} \\ \frac{R_{y2}}{D_{y2}} \end{bmatrix} \quad (3)$$

For a three jointed snake arm with six DOF and nine control tendons, equation (1) creates a system of linear equations with infinite solutions.

$$\begin{bmatrix} 0 & 0 & D_{x3} & 0 & 0 & D_{x6} & 0 & 0 & D_{x9} \\ 0 & 0 & D_{y3} & 0 & 0 & D_{y6} & 0 & 0 & D_{y9} \\ 0 & D_{x2} & D_{x3} & 0 & D_{x5} & D_{x6} & 0 & D_{x8} & D_{x9} \\ 0 & D_{y2} & D_{y3} & 0 & D_{y5} & D_{y6} & 0 & D_{y8} & D_{y9} \\ D_{x1} & D_{x2} & D_{x3} & D_{x4} & D_{x5} & D_{x6} & D_{x7} & D_{x8} & D_{x9} \\ D_{y1} & D_{y2} & D_{y3} & D_{y4} & D_{y5} & D_{y6} & D_{y7} & D_{y8} & D_{y9} \end{bmatrix} \begin{bmatrix} T_1 \\ T_2 \\ T_3 \\ T_4 \\ T_5 \\ T_6 \\ T_7 \\ T_8 \\ T_9 \end{bmatrix} = \begin{bmatrix} R_{y3} \\ R_{x3} \\ R_{y2} \\ R_{x2} \\ R_{y1} \\ R_{x1} \end{bmatrix} \quad (4)$$

As the tendons with a negative D_y would not contribute to overcoming the gravity acting on the snake arm, these can be given pre-tension values and this action results in a solvable matrix and the necessary equations for a theoretical tendon tensions.

$$\begin{bmatrix} 0 & 0 & D_{x3} & 0 & 0 & D_{x9} \\ 0 & 0 & D_{y3} & 0 & 0 & D_{y9} \\ 0 & D_{x2} & D_{x3} & 0 & D_{x8} & D_{x9} \\ 0 & D_{y2} & D_{y3} & 0 & D_{y8} & D_{y9} \\ D_{x1} & D_{x2} & D_{x3} & D_{x4} & D_{x8} & D_{x9} \\ D_{y1} & D_{y2} & D_{y3} & D_{y4} & D_{y8} & D_{y9} \end{bmatrix} \begin{bmatrix} T_1 \\ T_2 \\ T_3 \\ T_4 \\ T_8 \\ T_9 \end{bmatrix} = \begin{bmatrix} R_{y3} - T_6 D_{x6} \\ R_{x3} - T_6 D_{y6} \\ R_{y2} - T_5 D_{x5} - T_6 D_{x6} \\ R_{x2} - T_5 D_{y5} - T_6 D_{y6} \\ R_{y1} - T_5 D_{x5} - T_6 D_{x6} - T_7 D_{x7} \\ R_{x1} - T_5 D_{y5} - T_6 D_{y6} - T_7 D_{y7} \end{bmatrix} \quad (5)$$

The tensions T_5 , T_6 and T_7 in (5) are the pre-tension values assigned, where a value of zero would represent the tendon left slack.

Cable Tension Experiment

To measure the tension of the tendons in multiple configurations, a test rig modelled after Fig. 2 was assembled with two single DOF joints and links of constant length with capacity for five joints and fifteen tendons at three different diameters.

The methods consisted of holding the arm at a horizontal cantilever position and incrementally attach weights to each tendon. When the arm is released and maintains its position with no change to joint angles the weight is recorded and the process repeated. If inadequate tension is supplied to the tendons the arms would collapse and if too much tension is supplied the arm will rise beyond the horizontal starting position. To alter the torque at each joint only the payload was incremented.

The results shown on Fig. 3 show a close trend between the theoretical equation (3) and the experimental results. Further investigation revealed the zero-shift in the data was the result of friction in the test rig between the tendon, vertebra and pulleys and the theoretical calculations which were assumed to have negligible. To compensate for the error, the relationship between the load acting on the tendons and friction for the test rig was measured with the experimental values adjusted for the additional friction forces dependent on the load on the tendons.

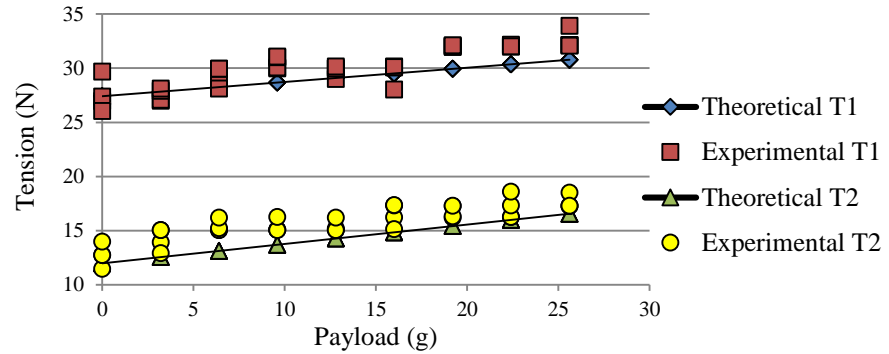


Fig. 3. Comparison between theoretical and experimental tendon tensions for a double jointed snake arm with two tendons.

Maximum working length

MATLAB was used to determine the maximum length of snake arm by algorithmically increasing the length of both links whilst at each step checking against the anticipated failure modes (Table 1). The implementation of factors of safety (FOS) reduces the lengths as a compromise for increased reliability.

The approach was to firstly determine the maximum length of the Links and thereafter determine the length of the Base link. This is because the Base link length does not affect the tendon tensions, the calculations for buckling failure of the three Links or the forces acting onto the 2DOF joints. However the axial stress resulting from the tendon tensions acting through the Base link and weight of the unsupported snake arm does affect the likelihood of buckling for the Base link.

Strongly dependent on the design of the snake arm, the order the failure modes will materialize is difficult to determine and so each mode was analysed individually in the design.

Table 2. Anticipated snake arm failure modes and Factors of Safety

Failure Mode	Check	FOS
Tendon	Each calculated tendon tension was compared to the tendons experimentally found yield stress.	6
Joints	Using Finite element analysis to find the load required for joint failure and compare to the predicted compressive axial loads.	4
Link Buckling	Axial stress through the links was analyzed for buckling using buckling theory for thin walled cylinders in axial compression [10,11].	4

This approach yielded a snake arm of total length 1.011m with a Link length of 0.161m and Base link of 0.478m for the 12mm diameter snake arm.

Conclusion and Future Work

The limiting factors for the design of the snake arm were the tendons and link buckling. A length of 1.676 m is achieved if the FOS is set to the point of failure. However a better approach would be to increase the yield stress of the tendons and design links capable of greater compressive loads. The outcome of the algorithmic approach to find the maximum length resulted in a length of 1.011m making this design not ideal for SAR scenarios where much greater lengths are crucial but possible for archaeology.

In future, the snake arm will be examined to increase reach. Including an investigation into the effect of axial, bending, and twisting forces through the joints and lastly, further tests by performing fielded experiments in real world situations.

References

1. Jueyao, W., Xiaorui, Z., Fude, T., Tao, Z., Xu, X.: Design of a modular robotic system for archaeological exploration. In: Robotics and Automation, 2009. ICRA '09. IEEE International Conference on, 12-17 May 2009 2009, pp. 1435-1440
2. Guizzo, E.: Robots Enter Fukushima Reactors, Detect High Radiation <http://spectrum.ieee.org/automaton/robotics/industrial-robots/robots-enter-fukushima-reactors-detect-high-radiation> (2011)
3. Daler, L., Lecoeur, J., Hahlen, P.B., Floreano, D.: A flying robot with adaptive morphology for multi-modal locomotion. In: Intelligent Robots and Systems (IROS), 2013 IEEE/RSJ International Conference on, 3-7 Nov. 2013 2013, pp. 1361-1366
4. Morris, A., Ferguson, D., Omohundro, Z., Bradley, D., Silver, D., Baker, C., Thayer, S., Whittaker, C., Whittaker, W.: Recent developments in subterranean robotics. *Journal of Field Robotics* **23**(1), 35-57 (2006)
5. Murphy, R.R., Kravitz, J., Stover, S., Shoureshi, R.: Mobile robots in mine rescue and recovery. *Robotics & Automation Magazine*, IEEE **16**(2), 91-103 (2009)
6. Hirose, S.: Biologically inspired robots : snake-like locomotors and manipulators. Oxford University Press, (1993)
7. Buckingham, R.O., Graham, A.C.: Dexterous manipulators for nuclear inspection and maintenance - Case study. In: Applied Robotics for the Power Industry (CARPI), 2010 1st International Conference on, 5-7 Oct. 2010 2010, pp. 1-6
8. Junhu, H., Rong, L., Ke, W., Hua, S.: The mechanical design of snake-arm robot. In: Industrial Informatics (INDIN), 2012 10th IEEE International Conference on, 25-27 July 2012 2012, pp. 758-761
9. Chalfoun, J., Bidard, C., Keller, D., Perrot, Y., Piolain, G.: Design and flexible modeling of a long reach articulated carrier for inspection. In: Intelligent Robots and Systems, 2007. IROS 2007. IEEE/RSJ International Conference on, Oct. 29 2007-Nov. 2 2007 2007, pp. 4013-4019
10. Howard Allen, P.B.: Cylindrical Shell in Axial Compression. In: Background to Buckling. pp. 515 -524. McGraw-Hill Book Company (UK) Limited, (1980)
11. Hunter, D.F.: ESDU 88034 Avoidance of buckling of some engineering elements (struts, plates and gussets). In: IHS ESDU, (1988)

Appendix B

Results for Tension Experiments

This section contains the raw theoretical and experimental data from the single cable tension experiments.

To validate the theoretical calculations for cable tensions of the snake arm in the horizontal cantilever position, experiments were conducted for comparison. The raw data is provided as is.

B.1 Theoretical Results of a Single Cable on Single Joint

Dw	Payload (Kg)					
	0	0.02	0.042	0.058	0.08	0.1
50	2.02	2.82	3.67	4.28	5.13	5.90
42	2.41	3.35	4.36	5.10	6.11	7.03
34	2.97	4.14	5.39	6.30	7.55	8.68

This data appears in Figure 4.13.

B.2 Experimental Results of a Single Cable on Single Joint

Dw	Payload (Kg)					
	0	0.02	0.042	0.058	0.08	0.1
50	1.99	2.83	3.64	4.37	5.07	
	1.99	2.92	3.54	4.47	5.15	
	2.00	2.92	3.64	4.47	5.08	
	2.00	2.83	3.53	4.38	5.20	
42	2.41	3.25	4.35	4.98		
	2.40	3.34	4.27	4.97		
	2.41	3.25	4.28	4.97		
	2.40	3.24	4.27	5.00		
34	2.93	4.15	5.09			
	2.93	3.95	5.39			
	2.93	3.95	5.27			
	2.92	3.96	5.30			

This data appears in Figure 4.13.

B.3 Theoretical and Experimental Results of a Double Cable on Double Joint

	Cable 1		Cable 2	
Payload (g)	Theoretical (N)	Experimental (N)	Theoretical (N)	Experimental (N)
0	27.4068	25.5060	11.9825	9.8100
		22.8573		10.8891
		23.2497		10.8891
		21.9744		11.9682
3.2	27.8307	22.8965	12.5550	11.9192
		22.9652		12.8707
		23.7696		12.8707
		23.9658		11.0559
6.4	28.2546	24.8291	13.1274	12.8903
		23.9855		12.8903
		25.7709		13.0375
		25.7905		13.8910
9.6	28.6785	25.8003	13.6999	12.9100
		25.8886		12.9100
		26.8402		12.8903
		26.9088		13.9302
12.8	29.1024	24.8389	14.2723	12.8903
		25.8297		12.9983
		25.8003		12.8903
		25.9769		13.8812
16	29.5263	25.8984	14.8447	13.9106
		25.9769		12.9492
		23.8874		14.8720
		25.9278		14.9014

19.2	29.9502	27.8212	15.4172	14.8229
		27.8114		13.8910
		27.9095		13.9989
		27.9585		14.8425
22.4	30.3741	27.8310	15.9896	13.9302
		27.9095		13.9400
		27.9977		14.8720
		27.8604		16.0001
25.6	30.7978	27.9781	16.5621	14.8327
		27.9683		14.8523
		29.8126		15.9216
		27.9291		14.8622

This data appears in Figure 4.14 and Figure 4.15.

Force (N)	Length (m)	Force (N)	Length (m)	Force (N)	Length (m)
0.0000	0.0000	0.0000	0.0000	0.0000	0.0000
0.9810	0.0010	0.9908	0.0010	0.9908	0.0010
1.9718	0.0030	1.9620	0.0020	1.9424	0.0030
2.9430	0.0040	2.9528	0.0030	2.9332	0.0040
3.9142	0.0060	3.9338	0.0040	3.9044	0.0060
4.8756	0.0070	4.9148	0.0060	4.8952	0.0070
5.8566	0.0100	5.8860	0.0070	5.8762	0.0090
6.8474	0.0120	6.8670	0.0080	6.8376	0.0100
7.8186	0.0130	7.8382	0.0100	7.8186	0.0110
8.8094	0.0160	8.8094	0.0115	8.7996	0.0130
9.7708	0.0180	9.7806	0.0130	9.7806	0.0140
10.7518	0.0190	10.7518	0.0140	10.3692	0.0150
10.9480	0.0200	11.3404	0.0150	10.9578	0.0160
11.9192	0.0220	11.9290	0.0160	11.9192	0.0170
12.9002	0.0230	12.9002	0.0170	12.8903	0.0180
13.8910	0.0250	13.8910	0.0190	13.8713	0.0190
14.8425	0.0260	14.8818	0.0195	14.8622	0.0210

15.8235	0.0280	15.8530	0.0215	15.8432	0.0230
16.8045	0.0300	16.8340	0.0220	16.8045	0.0250
17.7757	0.0320	17.8052	0.0240	17.7855	0.0270
18.7567	0.0330	18.7763	0.0260	18.7665	0.0280
19.7279	0.0350	19.7475	0.0270	19.7377	0.0290
20.8855	0.0370	20.9247	0.0285	20.9149	0.0300
21.8665	0.0380	21.8861	0.0300	21.8763	0.0320
22.8475	0.0400	22.8671	0.0320	22.8573	0.0340
23.8285	0.0420	23.8481	0.0340	23.8383	0.0350
24.7997	0.0430	24.8291	0.0345	24.8193	0.0370
25.7709	0.0450	25.8003	0.0370	25.8003	0.0390
26.7617	0.0470	26.7813	0.0410	26.7715	0.0410

This data appears in Figure 4.17.

C.2 Force Applied Against Friction for Cable 1 and Cable 2

Force (N)	Friction Force on C1 (N)	Force (N)	Friction Force on C2 (N)
0.0000	0.2117	0.0000	0.2117
0.9908	0.6417	0.9908	0.6417
1.9620	1.0521	1.9424	0.4716
2.9528	1.4821	2.9332	0.9016
3.9338	1.9022	3.9044	0.7512
4.9148	1.7616	4.8952	1.1812
5.8860	2.1720	5.8762	1.0405
6.8670	2.5921	6.8376	1.4411
7.8382	2.4417	7.8186	1.8613
8.8094	2.5717	8.7996	1.7206
9.7806	2.7016	9.7806	2.1408
10.7518	3.1120	10.3692	2.1686
11.3404	3.1398	10.9578	2.1964
11.9290	3.1675	11.9192	2.5969
12.9002	3.5779	12.8903	3.0073
13.8910	3.4471	13.8713	3.4275
14.8818	4.1575	14.8622	3.2966
15.8530	4.0070	15.8432	3.1560
16.8340	4.7076	16.8045	2.9957
17.8052	4.5572	17.7855	2.8551
18.7763	4.4067	18.7665	3.2753
19.7475	4.8171	19.7377	3.6856
20.9247	5.1531	20.9149	4.3020
21.8861	5.2732	21.8763	4.1418
22.8671	5.1326	22.8573	4.0011
23.8481	4.9919	23.8383	4.4213

24.8291	5.6925	24.8193	4.2807
25.8003	5.2617	25.8003	4.1400
26.7813	3.9994	26.7715	3.9896

This data appears in Figure 4.18 and Figure 4.19.

C.3 Theoretical and Corrected Experimental Results of a Double Cable on Double Joint

	Cable 1		Cable 2	
Payload (g)	Theoretical (N)	Experimental (N)	Theoretical (N)	Experimental (N)
0	27.4068	30.6028	11.9825	11.9707
		27.7989		13.2416
		28.2193		13.2416
		26.8469		14.5053
3.2	27.8307	27.8411	12.5550	14.4480
		27.9147		15.5566
		28.7736		15.5566
		28.9820		13.4374
6.4	28.2546	29.8937	13.1274	15.5794
		29.0028		15.5794
		30.8788		15.7503
		30.8992		16.7390
9.6	28.6785	30.9094	13.6999	15.6022
		31.0013		15.6022
		31.9853		15.5794
		32.0559		16.7844
12.8	29.1024	29.9040	14.2723	15.5794
		30.9401		15.7048
		30.9094		15.5794
		31.0930		16.7277
16	29.5263	31.0115	14.8447	16.7617
		31.0930		15.6478
		28.8987		17.8698
		31.0420		17.9037

19.2	29.9502	32.9892	15.4172	17.8134
		32.9792		16.7390
		33.0790		16.8637
		33.1288		17.8360
22.4	30.3741	32.9991	15.9896	16.7844
		33.0790		16.7957
		33.1687		17.8698
		33.0291		19.1629
25.6	30.7978	33.1488	16.5621	17.8247
		33.1388		17.8473
		34.9938		19.0732
		33.0989		17.8586

This data appears in Figure 4.20 and Figure 4.21.

Appendix D

Matlab .m files

This section contains the .m files developed and used throughout the thesis.

D.1 Algorithmic solver for snake arm length

The purpose of the solver as presented in Chapter 5.7 was to iteratively increase the 'Link' length or the 'Base Link' length to maximise the feasible length of a snake arm. During each iterative step the cable tensions are calculated using the method presented in Chapter 4.4 and a series of safety checks are made to ensure the failure modes do not occur.

D.2 run_me.m

This section of code iteratively increases both link lengths and stops when failure conditions are met.

```
clear
clc
tic

continue_function=1;
while continue_function==1

    for tle=0.001:0.001:1

        b=0.01;
        [ROBOT_check,snl]=test_code(b,tle);

        if ROBOT_check(1,1)==1 || ROBOT_check(3,1)==1 ||
ROBOT_check(5,1)==1 || ROBOT_check(6,1)==1
            continue_function=0;
            break
        else
            final_tle=tle;
        end
    end
end

continue_function=1;
while continue_function==1
    for b=0.001:0.001:10
        tle=final_tle;
        [ROBOT_check,snl]=test_code(b,tle);
        if ROBOT_check(4,1)==1
            continue_function=
            break
        else
            final_b=b;
        end
    end
end
```

Clears any current held variables and visible lines on the Command window.

Link length is increased in 0.001m increments from 0.001m to 1m.

At each step the function test_code is recalled to calculate the cable tensions and perform the safety checks. Once a failure mode is reached the loop is broken and the Link length is brought forward.

Using the recorded Link length, the loop is repeated with the Base link length increased in 0.001m increments from 0.001m to 10m, this continues until any failure conditions are met.

```
final_b  
final_tle
```

The maximum Link and Base link lengths are displayed.

```
% Number of joints  
number_of_joints=3;  
% Length of base link (m)  
base_tube_link_length=final_b;  
% Length of links (m)  
tube_link_length=final_tle;  
% Length of joint (m)  
joint_length=0.0055;  
% Length of end vertebrae (m)  
end_vert_length=0.002;  
% Length of link in joint (m)  
joint_link_length=0.005;
```

The total snake arm length is calculated and displayed.

```
snl=base_tube_link_length+(tube_link_length*number_of_joints)+(joint  
_length*(2*number_of_joints))+end_vert_length+(joint_link_length*num  
ber_of_joints)
```

```
toc
```

D.3 test_code.m

This section of code contains the variables forming the snake arm model.

```
% new algorithm for searching snake arm length
```

```
function [ROBOT_check,snl]=test_code(b,tle)
```

```
x(1)=b;  
x(2)=tle;
```

Assigns the new link length values each step.

```
gravity=9.81;  
% Number of joints  
number_of_joints=3;  
% Length of base link (m)  
base_tube_link_length=x(1);  
% Length of links (m)  
tube_link_length=x(2);  
% Length of joint (m)  
joint_length=0.0055;  
% Length of end vertebrae (m)  
end_vert_length=0.002;  
% Length of link in joint (m)  
joint_link_length=0.005;  
% Maximum diameter of Snake Arm (m)  
arm_max_diameter=0.012;
```

Specification of the snake arm.

```
% Length of joint yaw centroid  
joint_yaw_centroid=0.00321;  
% Length of joint pitch centroid  
joint_pitch_centroid=0.00229;  
% Length of end vertebrae centroid (m)  
end_vert_centroid=0.00081;
```

Centroid locations of the joint parts and end vertebrae.

```
% Payload weight (kg)  
payload_kg=0.02;
```

Payload conditions are specified here.


```
% Payload Length (m)
payload_length=0.06;
```

```
% Weight of joint (kg)
weight_joint=0.00252;
% Weight of link in joint (kg)
weight_joint_link=0.0008;
% Weight of end vert (kg)
weight_end_vert=0.00147;
```

Known constant weights of parts.

```
% Density of electrical wire (kg/m^3)
wire_density=8940;
% Electrical wire diameter (m)
wire_diameter=0.0015;
% Tendon outer diameter (m)
tendon_diameter=0.0015;
% Tendon density (kg/m^3)
tendon_density=955;
```

Values required to calculate the weight of parts as the length increases.

```
% Arm angles (degrees)
arm_angle=[0 0 0 0 0 0 0 0];
```

Initialises the joint angles for the snake arm.

```
% Yield Stress of Cable
safety_cable_yield=490;
% Compression limit of joint
safety_joint=1332;
% Joint torque twist limit
safety_twist=1.8;
% Cable Factor of Safety
cable_fos=6;
% Joint Factor of Safety
joint_fos=4;
% Joint twist Factor of Safety
twist_fos=4;
% tube Factor of Safety
tube_fos=4;
```

The safety constraints associated with the snake arm.

```
% Selection of tubes for each link including base tube
% Default tube selection is 1 for all links
tselect_array=[1; 1; 1; 1];
```

```
%% File workings
```

```
% Use Robotics Toolbox?
USE_robotics=1;
% See Plot?
USE_plot=0;
```

This array allows the material of the links to be easily interchanged, but cannot be changed during the iterative process.

```
% Length of Snake arm
snl=base_tube_link_length+(tube_link_length*number_of_joints)+(joint_length*(2*number_of_joints))+end_vert_length+(joint_link_length*number_of_joints);
inv_snl=1/snl;
disp(['Length of Snake arm set at ' num2str(snl) ' meters.']);
```

```
%% Tendons
```

Calculates the length of the snake arm

```
teor=tendon_diameter/2;
ewor=wire_diameter/2;
```

```
% Number of tendons in each section
for i=1:number_of_joints
    tendon_array(i,1)=(number_of_joints-1)
end
```

With 3 cables per joint, this For loop calculates the number of number of cables in each of the 3 links.

```
% Imports where tendons stop at each section
joint_tendon_array=[1 1 4 7; 2 2 5 8; 3 3 6 9];
```

```
% Import the position of each tendon
```

```
tendon_position =
[1,0,0.00425;2,0.0025,0.00344;3,0.00404,0.00131;4,0.00404,-
0.00131;5,0.0025,-0.00344;6,-0.0025,-0.00344;7,-0.00404,-0.00131;8,-
0.00404,0.00131;9,-0.0025,0.00344];
```

Termination point for each cable.
From Figure 5.24

```
Dx1=tendon_position(1,2);
Dy1=tendon_position(1,3);
Dx2=tendon_position(2,2);
Dy2=tendon_position(2,3);
Dx3=tendon_position(3,2);
Dy3=tendon_position(3,3);
Dx4=tendon_position(4,2);
Dy4=tendon_position(4,3);
Dx5=tendon_position(5,2);
Dy5=tendon_position(5,3);
Dx6=tendon_position(6,2);
Dy6=tendon_position(6,3);
Dx7=tendon_position(7,2);
Dy7=tendon_position(7,3);
Dx8=tendon_position(8,2);
Dy8=tendon_position(8,3);
Dx9=tendon_position(9,2);
Dy9=tendon_position(9,3);
```

Coordinate position of each cable.
From Table 5.4.

```
%% Initialise Arrays
```

```
disp('Start-up arrays initialised. ');
weight_array=zeros([2*number_of_joints+2,2]);
distance_array=zeros([number_of_joints,number_of_joints]);
counter_array=zeros([number_of_joints,1]);
tension_temp=zeros([1,3]);
arm_angle_rad=zeros([1,2*number_of_joints+2]);
arm_angle_rad_reverse=zeros([1,2*number_of_joints+2]);
link_length=zeros([1,2*number_of_joints+2]);
link_centroid=zeros([1,2*number_of_joints+2]);
mass_inertia=zeros([1,2*number_of_joints+2]);
link_moments_array=zeros([number_of_joints,2*number_of_joints+2]);
ROBOT_tension_array=zeros([tendon_array(1,1),4]);
joint_force=zeros([number_of_joints,1]);
ROBOT_check=zeros(6,1);
ROBOT_compression_array=zeros([number_of_joints,1]);
```

```
%% Lengths
```

```
% Length of base section
```

```
length_base_section=base_tube_link_length+joint_length;
```

```
% Length of mid section
```

```
length_mid_section=tube_link_length+(2*joint_length);
```

```
% Length of end section
```

```
length_end_section=tube_link_length+joint_length+end_vert_length;
```

Modelling each link segment begins here

```
link_length(1,1)=length_base_section;
link_length(1,2)=joint_link_length;
```

```
link_length(1,3)=length_mid_section;
link_length(1,4)=joint_link_length;
link_length(1,5)=length_mid_section;
link_length(1,6)=joint_link_length;
link_length(1,7)=length_end_section;
link_length(1,8)=payload_length;
```

Grouping individual part lengths, the length of each arm segment is calculated into an array.

```
%% Weights
```

```
% Imports the selection of usable tubes
```

```
tube_data =
[1,0.012,0.001,8000,210000000000,170000000,0.265;2,0.012,0.001,1504.
74,200000000,200000000,0.1;3,0.007,0.001,1300,10000000000,200000000,
0;4,0.007,0.001,1180,3300000000,66190080,0];
```

```
[tempa, tempb]=size(tube_data);
for i=1:tempa
    tor(i,1)=(tube_data(i,2))/2;
    twt(i,1)=tube_data(i,3);
    tde(i,1)=tube_data(i,4);
    tym(i,1)=tube_data(i,5);
    tys(i,1)=tube_data(i,6);
    tpr(i,1)=tube_data(i,7);
end
```

Tube_data contains the specifications of each link material. This includes values such as dimensions and densities.

```
% Calculates the weight of each sections and its centroid position
```

```
% Weight of Link 1 (base link)
```

```
weight_array(1,1)=1;
tube_weight=calc_tube_weight(tor(tselect_array(1,1),1),twt(tselect_
rray(1,1),1),base_tube_link_length,tde(tselect_array(1,1),1));
tendon_weight=calc_tendon_weight(teor,link_length(1,1),tendon_densit
y);
wire_weight=calc_wire_weight(ewor,link_length(1,1),wire_density);
weight_array(1,2)=(weight_joint)+tube_weight+(tendon_weight*tendon_a
rray(1))+wire_weight;
```

```
tempa=(tube_weight+(tendon_weight*tendon_array(1))+wire_weight)*(bas
e_tube_link_length/2)+(weight_joint*(base_tube_link_length+joint_pit
ch_centroid));
tempb=(tube_weight+(tendon_weight*tendon_array(1))+wire_weight)+weig
ht_joint;
link_centroid(1,1)=tempa/tempb;
```

The weight of each link segment is the sum of each component forming it.

```
% Weight of Link 2
```

```
weight_array(2,1)=2;
tendon_weight=calc_tendon_weight(teor,joint_link_length,tendon_densi
ty);
weight_array(2,2)=(tendon_weight*tendon_array(1))+weight_joint_link;
```

```
link_centroid(1,2)=joint_link_length;
```

As each part runs continuously through, the centroid is also calculated here.

```
% Weight of Link 3
```

```
weight_array(3,1)=3;
tube_weight=calc_tube_weight(tor(tselect_array(2,1),1),twt(tselect_a
rray(2,1),1),tube_link_length,tde(tselect_array(2,1),1));
tendon_weight=calc_tendon_weight(teor,link_length(1,3),tendon_densit
y);
wire_weight=calc_wire_weight(ewor,link_length(1,3),wire_density);
weight_array(3,2)=(weight_joint)+tube_weight+(tendon_weight*tendon_a
rray(1))+wire_weight;
```

```
tempa=(weight_joint*(joint_yaw_centroid))+(tube_weight+(tendon_weight*tendon_array(1))+wire_weight)*((tube_link_length/2)+joint_length)+(weight_joint*(joint_length+tube_link_length+joint_pitch_centroid));  
tempb=weight_joint+(tube_weight+(tendon_weight*tendon_array(1))+wire_weight)+weight_joint;  
link_centroid(1,3)=tempa/tempb;
```

```
% Weight of Link 4
```

```
weight_array(4,1)=4;  
tendon_weight=calc_tendon_weight(teor,joint_link_length,tendon_density);  
weight_array(4,2)=(  
tendon_weight*tendon_array(2))+weight_joint_link;
```

```
link_centroid(1,4)=joint_link_length/2;
```

```
% Weight of Link 5
```

```
weight_array(5,1)=5;  
tube_weight=calc_tube_weight(tor(tselect_array(3,1),1),tw(tselect_array(3,1),1),tube_link_length,tde(tselect_array(3,1),1));  
tendon_weight=calc_tendon_weight(teor,link_length(1,5),tendon_density);  
wire_weight=calc_wire_weight(ewor,link_length(1,5),wire_density);  
weight_array(5,2)=(weight_joint)+tube_weight+(tendon_weight*tendon_array(2))+wire_weight;
```

```
tempa=(weight_joint*(joint_yaw_centroid))+(tube_weight+(tendon_weight*tendon_array(1))+wire_weight)*((tube_link_length/2)+joint_length)+(weight_joint*(joint_length+tube_link_length+joint_pitch_centroid));  
tempb=weight_joint+(tube_weight+(tendon_weight*tendon_array(2))+wire_weight)+weight_joint;  
link_centroid(1,5)=tempa/tempb;
```

```
% Weight of Link 6
```

```
weight_array(6,1)=6;  
tendon_weight=calc_tendon_weight(teor,joint_link_length,tendon_density);  
weight_array(6,2)=(tendon_weight*tendon_array(2))+weight_joint_link;
```

```
link_centroid(1,6)=joint_link_length/2;
```

```
% Weight of Link 7
```

```
weight_array(7,1)=7;  
tube_weight=calc_tube_weight(tor(tselect_array(4,1),1),tw(tselect_array(4,1),1),tube_link_length,tde(tselect_array(4,1),1));  
tendon_weight=calc_tendon_weight(teor,link_length(1,7),tendon_density);  
wire_weight=calc_wire_weight(ewor,link_length(1,7),wire_density);  
weight_array(7,2)=(weight_joint)+tube_weight+(tendon_weight*tendon_array(3))+wire_weight+weight_end_vert;
```

```
tempa=(weight_joint*(joint_yaw_centroid))+(tube_weight+(tendon_weight*tendon_array(1))+wire_weight)*((tube_link_length/2)+joint_length)+(weight_end_vert*(joint_length+tube_link_length+end_vert_centroid));  
tempb=weight_joint+(tube_weight+(tendon_weight*tendon_array(3))+wire_weight)+weight_end_vert;  
link_centroid(1,7)=tempa/tempb;
```

```
% Weight of Link 8 (Payload)
```

```
weight_array(8,1)=8;
weight_array(8,2)=payload_kg;

link_centroid(1,8)=payload_length/2;

disp('Calculated the weight of each section.');
```

%% Tension

GRAV=[0 gravity 0];

% Arm angles

```
for i=1:numcols(arm_angle)
    arm_angle_rad(1,i)=arm_angle(1,i)*(pi/180);
end
```

The DH table is formed for the RNE calculations

% Denhavit-Hartenburg matrix

%	theta	kinematic: joint angle
%	d	kinematic: link offset
%	a	kinematic: link length
%	alpha	kinematic: link twist
%	sigma	kinematic: 0 if revolute, 1 if prismatic
%	mdh	kinematic: 0 if standard D&H, else 1
%	offset	kinematic: joint variable offset
%	qlim	kinematic: joint variable limits [min max]
%	m	dynamic: link mass
%	r	dynamic: link COG wrt link coordinate frame 3x1
%	I	dynamic: link inertia matrix, symmetric 3x3, about link COG.
%	B	dynamic: link viscous friction (motor referred)
%	Tc	dynamic: link Coulomb friction

% Links

```
link_array(1)=Link('alpha', pi/2, 'd', 0, 'a', link_length(1,1),
'offset', 0, 'qlim',[-pi/4 pi/4], 'm', weight_array(1,2), 'r',[-
link_centroid(1,1); 0; 0], 'I', [0.00000066 0.00000000 0.00000000;
0.00000000 0.00078561 0.00000000; 0.00000000 0.00000000 0.00078560],
'Jm', 0);
link_array(2)=Link('alpha', -pi/2, 'd', 0, 'a', link_length(1,2),
'offset', 0, 'qlim',[-pi/4 pi/4], 'm', weight_array(2,2), 'r',[-
link_centroid(1,2); 0; 0], 'I', [0.00000000 0.00000000 0.00000000;
0.00000000 0.00000001 0.00000000; 0.00000000 0.00000000 0.00000001],
'Jm', 0);
link_array(3)=Link('alpha', pi/2, 'd', 0, 'a', link_length(1,3),
'offset', 0, 'qlim',[-pi/4 pi/4], 'm', weight_array(3,2), 'r',[-
link_centroid(1,3); 0; 0], 'I', [0.00000102 0.00000000 0.00000000;
0.00000000 0.00005518 0.00000000; 0.00000000 0.00000000 0.00005519],
'Jm', 0);
link_array(4)=Link('alpha', -pi/2, 'd', 0, 'a', link_length(1,4),
'offset', 0, 'qlim',[-pi/4 pi/4], 'm', weight_array(4,2), 'r',[-
link_centroid(1,4); 0; 0], 'I', [0.00000000 0.00000000 0.00000000;
0.00000000 0.00000001 0.00000000; 0.00000000 0.00000000 0.00000001],
'Jm', 0);
link_array(5)=Link('alpha', pi/2, 'd', 0, 'a', link_length(1,5),
'offset', 0, 'qlim',[-pi/4 pi/4], 'm', weight_array(5,2), 'r',[-
link_centroid(1,5); 0; 0], 'I', [0.00000102 0.00000000 0.00000000;
0.00000000 0.00005518 0.00000000; 0.00000000 0.00000000 0.00005519],
'Jm', 0);
link_array(6)=Link('alpha', -pi/2, 'd', 0, 'a', link_length(1,6),
'offset', 0, 'qlim',[-pi/4 pi/4], 'm', weight_array(6,2), 'r',[-
```

```
link_centroid(1,6); 0; 0], 'I', [0.00000000 0.00000000 0.00000000;
0.00000000 0.00000001 0.00000000; 0.00000000 0.00000000 0.00000001],
'Jm', 0);
link_array(7)=Link('alpha', pi/2, 'd', 0, 'a', link_length(1,7),
'offset', 0, 'qlim',[-pi/4 pi/4], 'm', weight_array(7,2), 'r',[-
link_centroid(1,7); 0; 0], 'I', [0.00000102 0.00000000 0.00000000;
0.00000000 0.00005518 0.00000000; 0.00000000 0.00000000 0.00005519],
'Jm', 0);
link_array(8)=Link('alpha', -pi/2, 'd', 0, 'a', link_length(1,8),
'offset', 0, 'qlim',[-pi/4 pi/4], 'm', weight_array(8,2), 'r',[-
link_centroid(1,8); 0; 0], 'I', [0.00000000 0.00000000 0.00000000;
0.00000000 0.00000001 0.00000000; 0.00000000 0.00000000 0.00000001],
'Jm', 0);
```

```
Snake_Arm = SerialLink(link_array, 'name','Snake Arm Type 6');
%Snake_Arm.display()
%Snake_Arm.dyn
```

```
if USE_plot==1
    Snake_Arm.plot (arm_angle_rad, 'wrist');
    xlabel('x')
    ylabel('y')
    drawnow
end
```

```
if USE_robotics==1
    disp('Using Robotics Toolbox RNE function');
```

%TAU = R.rne(Q, QD, QDD) is the joint torque required for the robot R to achieve the specified joint position Q, velocity QD and acceleration QDD.

```
Q=arm_angle_rad;
QD= [0 0 0 0 0 0 0];
QDD=[0 0 0 0 0 0 0];
TAU = Snake_Arm.rne(Q, QD, QDD)
TAUtrans=TAU';

Rp1=TAU(1,2);
Ry1=TAU(1,3);
Rp2=TAU(1,4);
Ry2=TAU(1,5);
Rp3=TAU(1,6);
Ry3=TAU(1,7);1
```

```
end
```

```
%% Tension Calculations
```

```
% Calculate the tensions
```

```
if USE_robotics==1
```

```
T5=0;
T6=0;
T7=0;
```

The RNE function is called from the latest Robotics Toolbox addon¹.

As it is assumed the arm is held in the static horizontal lever position, the torque velocities and accelerations are kept zero.

Uses cable tension equations derived from Chapter 4.4.

The tension of each cable is calculated.

¹ Corke, P.I., *A robotics toolbox for MATLAB*. IEEE Robotics & Automation Magazine, 1996. 3(1): p. 24-32.

```

% Tendon 1
tempa=1;
ROBOT_tension_array(tempa,1)=tempa;
ROBOT_tension_array(tempa,2)=0;
ROBOT_tension_array(tempa,3)=tendon_position(tempa,3);
ROBOT_tension_array(tempa,4)=(Dx4*(Dy5*T5 - Rp1 + Dy6*T6 +
Dy7*T7))/(Dx1*Dy4 - Dx4*Dy1) - (Dy4*(Dx5*T5 - Ry1 + Dx6*T6 +
Dx7*T7))/(Dx1*Dy4 - Dx4*Dy1) - (Dx4*(Dy5*T5 - Rp2 + Dy6*T6))/(Dx1*Dy4
- Dx4*Dy1) + (Dy4*(Dx5*T5 - Ry2 + Dx6*T6))/(Dx1*Dy4 - Dx4*Dy1);

% Tendon 2
tempa=2;
ROBOT_tension_array(tempa,1)=tempa;
ROBOT_tension_array(tempa,2)=0;
ROBOT_tension_array(tempa,3)=tendon_position(tempa,3);
ROBOT_tension_array(tempa,4)=(Dx8*(Dy5*T5 - Rp2 +
Dy6*T6))/(Dx2*Dy8 - Dx8*Dy2) - (Dy8*(Dx5*T5 - Ry2 + Dx6*T6))/(Dx2*Dy8
- Dx8*Dy2) + (Dx8*(Rp3 - Dy6*T6))/(Dx2*Dy8 - Dx8*Dy2) - (Dy8*(Ry3 -
Dx6*T6))/(Dx2*Dy8 - Dx8*Dy2);

% Tendon 3
tempa=3;
ROBOT_tension_array(tempa,1)=tempa;
ROBOT_tension_array(tempa,2)=0;
ROBOT_tension_array(tempa,3)=tendon_position(tempa,3);
ROBOT_tension_array(tempa,4)=(Dy9*(Ry3 - Dx6*T6))/(Dx3*Dy9 -
Dx9*Dy3) - (Dx9*(Rp3 - Dy6*T6))/(Dx3*Dy9 - Dx9*Dy3);

% Tendon 4
tempa=4;
ROBOT_tension_array(tempa,1)=tempa;
ROBOT_tension_array(tempa,2)=0;
ROBOT_tension_array(tempa,3)=tendon_position(tempa,3);
ROBOT_tension_array(tempa,4)=(Dy1*(Dx5*T5 - Ry1 + Dx6*T6 +
Dx7*T7))/(Dx1*Dy4 - Dx4*Dy1) - (Dx1*(Dy5*T5 - Rp1 + Dy6*T6 +
Dy7*T7))/(Dx1*Dy4 - Dx4*Dy1) + (Dx1*(Dy5*T5 - Rp2 + Dy6*T6))/(Dx1*Dy4
- Dx4*Dy1) - (Dy1*(Dx5*T5 - Ry2 + Dx6*T6))/(Dx1*Dy4 - Dx4*Dy1);

% Tendon 8
tempa=8;
ROBOT_tension_array(tempa,1)=tempa;
ROBOT_tension_array(tempa,2)=0;
ROBOT_tension_array(tempa,3)=tendon_position(tempa,3);
ROBOT_tension_array(tempa,4)=(Dy2*(Dx5*T5 - Ry2 +
Dx6*T6))/(Dx2*Dy8 - Dx8*Dy2) - (Dx2*(Dy5*T5 - Rp2 + Dy6*T6))/(Dx2*Dy8
- Dx8*Dy2) - (Dx2*(Rp3 - Dy6*T6))/(Dx2*Dy8 - Dx8*Dy2) + (Dy2*(Ry3 -
Dx6*T6))/(Dx2*Dy8 - Dx8*Dy2);

% Tendon 9
tempa=9;
ROBOT_tension_array(tempa,1)=tempa;
ROBOT_tension_array(tempa,2)=0;
ROBOT_tension_array(tempa,3)=tendon_position(tempa,3);
ROBOT_tension_array(tempa,4)=(Dx3*(Rp3 - Dy6*T6))/(Dx3*Dy9 -
Dx9*Dy3) - (Dy3*(Ry3 - Dx6*T6))/(Dx3*Dy9 - Dx9*Dy3);

end

%% Safety Checks

disp('Commencing Safety Checks.');
```

The individual tension of each cable is compared to the cable yield in consideration with the cable FOS.

```
if USE_robotics==1
    % Check the ROBOT cable tensions
    tempb=0;
    for i=1:tendon_array(1,1)
        tempa=ROBOT_tension_array(i,4)*cable_fos;
        if tempa>safety_cable_yield
            tempb=1;
        end
    end

    if tempb==1
        ROBOT_check(1,1)=1;
        disp('ROBOT cable tension: FAIL.');
```

The condition of the cable is displayed in the command window.

```
    else
        ROBOT_check(1,1)=0;
        disp('ROBOT cable tension: PASS.');
```

The axial compressive force through each link segment is the sum of the cable tensions running through them.

```
    end
end

% Check the joint compression

if USE_robotics==1
    % Sum all ROBOT tensions for each joint
    for i=1:number_of_joints
        tempc=ROBOT_tension_array(joint_tendon_array(i,2),4);
        tempd=ROBOT_tension_array(joint_tendon_array(i,3),4);
        tempe=ROBOT_tension_array(joint_tendon_array(i,4),4);
        joint_force(i,1)=tempc+tempd+tempe;
    end
    for i=1:number_of_joints
        ROBOT_compression_array(i,1)=sum(joint_force(i:3,1));
    end
    % Check the joints
    tempb=0;
    for i=1:number_of_joints
        tempc=ROBOT_compression_array(i,1)*joint_fos;
        if tempc>safety_joint
            tempb=1;
        end
    end
    if tempb==1
        ROBOT_check(3,1)=1;
        disp('ROBOT 2DOF joint: FAIL.');
```

The axial compression through each joint is compared to the yield limit of the joint derived from the FE analysis in Chapter 5.4.2.

```
    else
        ROBOT_check(3,1)=0;
        disp('ROBOT 2DOF joint: PASS.');
```

The likelihood of buckling for the Base Link is checked using the function calc_tube_buckling.

```
    end
end

% Check the tube buckling

if USE_robotics==1
    tempa=0;
    tempb=0;

    % check base tubing
    tube_length=base_tube_link_length;
    % Row of tube for base on tselect_array
    i=1;
    tube_load=ROBOT_compression_array(i,1);
```



```
[tube_buckling, axialstress, axialstress_noFOS, Fb,
Fbt]=calc_tube_buckling(tor(tselect_array(i,1),1),
twl(tselect_array(i,1),1), tym(tselect_array(i,1),1),
tys(tselect_array(i,1),1), tpr(tselect_array(i,1),1), tube_length,
tube_fos, tube_load);
output_4=axialstress;
output_5=axialstress_noFOS;
output_6=Fb;
output_10=Fbt;
if tube_buckling==1 || (output_6/output_5)<tube_fos
    tempb=1;
end

if tempb==1
    ROBOT_check(4,1)=1;
    disp('ROBOT base tube buckling: FAIL.');
```

The likelihood of buckling for the three other Links is also checked.

```
else
    ROBOT_check(4,1)=0;
    disp('ROBOT base tube buckling: PASS.')
```

end

```

tube_buckling=0;
% check other tubing
for i=1:number_of_joints
    disp('tube buckling');

    tube_length=tube_link_length;
    tube_load=ROBOT_compression_array(i,1);
    [tube_buckling, axialstress, axialstress_noFOS, Fb,
Fbt]=calc_tube_buckling(tor(tselect_array(i+1,1),1),
twl(tselect_array(i+1,1),1), tym(tselect_array(i+1,1),1),
tys(tselect_array(i+1,1),1), tpr(tselect_array(i+1,1),1),
tube_length, tube_fos, tube_load);

    if i==1 %records the buckling data of link 2
        output_7=axialstress;
        output_8=axialstress_noFOS;
        output_9=Fb;
        output_11=Fbt;
    end

    if tube_buckling==1 || output_9/output_8<tube_fos
        tempa=1;
    end

    if tempa==1
        ROBOT_check(5,1)=1;
        disp('ROBOT tube buckling: FAIL.');
```

else

end

end

```

% Check joint twisting

[twist_buckling, Rtl]=joint_torque_check(b, tle, twist_fos,
safety_twist);
```

```
output_12=Rt1;  
if twist_buckling==1  
    ROBOT_check(6,1)=1;  
    disp('Joint twist: FAIL.');
```

The torque twisting of the joint is checked and compared to the FEA derived value from Chapter 5.4.2.

```
else  
    ROBOT_check(6,1)=0;  
    disp('Joint twist: PASS.')
```

```
end  
  
disp(' ')
```

```
%% Optimisation Outputs
```

```
if USE_robotics==1  
    % Grab max cable tension  
    for i=1:tendon_array(1,1)  
        tempa(i,1)=ROBOT_tension_array(i,1);  
    end  
    output_1=max(tempa);  
  
    % Grab max compression of 2DOF joints  
    for i=2:number_of_joints  
        tempa(i,1)=ROBOT_compression_array(i,1);  
    end  
    output_2=max(tempa);  
end
```

This section of code allows the function operator to output specific values to assist in debugging and development of the script.

```
% DEV_check=RNE_tension_array;  
% DEV_check2=RNE_compression_array;
```

```
constraint_array(1)=output_4; % base tube axial stress  
output_5; % base tube axial stress w. no FOS  
constraint_array(2)=output_6; % base tube flexural buckling stress  
constraint_array(3)=output_10; % base tube local buckling stress  
constraint_array(4)=output_7; % other tube axial stress  
output_8; % other tube axial stress w. no FOS  
constraint_array(5)=output_9; % other tube flexural buckling stress  
constraint_array(6)=output_11; % other tube local buckling stress  
constraint_array(7)=output_1; % max cable tension  
constraint_array(8)=output_2; % max tension on joints (sum of tendon  
forces)  
constraint_array(9)=output_12; % Joint torque at 1
```

```
FOS_check_1=safety_cable_yield/output_1; % cable  
FOS_check_2=output_6/output_5; % base tube flexural  
FOS_check_3=output_10/output_5; % base tube local  
FOS_check_4=output_9/output_8; % tube flexural  
FOS_check_5=output_11/output_8; % tube local  
FOS_check_6=safety_joint/output_2; % joint
```

D.3 calc_tube_buckling.m

This section of code calculates the flexural and local buckling stresses for the given link material. The equations involved are presented in Chapter 4.3.

```
function [tube_buckling, axialstress, axialstress_noFOS, Fb, Fbt]=calc_tube_buckling(tor, twt, tym, tys, tpr, tube_length, tube_fos, tube_load)

%% From equation 4.1 at ESDU 88034

% Fb = Elastic buckling stress N/m2
% FE = Euler buckling stress N/m2
% tym = Modulus of elasticity of material N/m2
% tys = 0.2 per cent proof stress or yield stress of material N/m2

% tle = Actual length of cylinder acting as strut m
% Le = Equivalent length of cylinder acting as strut m
% k = Radius of gyration of section m
% Do = outer diameter of cylinder m
% Di = inner diameter of cylinder m
% n = empirically determined factor accounting for imperfections

%% Variables
tod = tor*2;
tid = tod-(2*twt);

Axialload=tube_load*tube_fos;
%% Flexural buckling
Le = 2*tube_length;
k = (sqrt(tod^2+tid^2))/4;
n = (0.003*Le)/k;
FE = (pi^2)*tym*((k/Le)^2);
Area_Do=pi*((tod/2)^2);
Area_Di=pi*((tid/2)^2);
CSA=Area_Do-Area_Di;
axialstress=Axialload/CSA
axialstress_noFOS=tube_load/CSA
var_1= tys/FE;
var_2= 1+n;
formula_1= 0.5*(var_1+var_2);
formula_2= 0.25*((var_1+var_2)^2);
formula_3= sqrt(formula_2-var_1);
formula_4= formula_1-formula_3;
Fb=formula_4*FE
if axialstress<Fb
    tube_buckling=0;
else
    tube_buckling=1;
end

%% Local Buckling

% Q = simply supported
% v = poisson's ratio
% t = thickness
% R = radius of cylinder
% E = young's modulus
% Fbt = Elastic buckling stress N/m2
```

Calculates the flexural buckling stress.

Compares the buckling stress to the axial compressive load.

```
Q=0.85;

if tpr==0
    disp('WARNING: Tube missing Poissons Ratio data, ignoring
Local Buckling calculations')
else
    v=tpr;

    formula_5=Q*tym;
    formula_6=sqrt(3*(1-(v^2)));
    formula_7=twl/tor;
    Fbt_con=(formula_5/formula_6)*formula_7;
    Fbt=Fbt_con*0.25

    if axialstress<Fbt

    else
        tube_buckling=1;
    end
end
```

Calculates the local buckling stress.

Compares the buckling stress to the axial compressive load.

D.4 joint_torque_check.m

Torque twisting of the joint only occurs when there is a lateral load on the arm. Under the snake arms own weight this occurs when the arm is orientated to the far left or far right positions. This section of code is largely similar to test_code.m (Appendix D.2) however the arm angles are changed and only the torque twisting is compared.

```
function [twist_buckling, Rt1]=joint_torque_check(b, tle, twist_fos,
safety_twist)
% Single pass of the optimisation functions
% for those one off calculations or code testing

% Initialise Arm angles (degrees)
theta=30;
arm_angle=[0 90 -90 -90 theta 0 theta 0 theta 0];

%% Build Spec

x(1)=b;
x(2)=tle;

gravity=9.81;
% Number of joints
number_of_joints=3;
% Length of base link (m)
base_tube_link_length=x(1);
% Length of links (m)
tube_link_length=x(2);
% Length of joint (m)
joint_length=0.0055;
% Length of end vertebrae (m)
end_vert_length=0.002;
% Length of link in joint (m)
joint_link_length=0.005;
% Maximum diameter of Snake Arm (m)
arm_max_diameter=0.012;

% Length of joint yaw centroid (m)
joint_yaw_centroid=0.00321;
% Length of joint pitch centroid (m)
joint_pitch_centroid=0.00229;
% Length of end vertebrae centroid (m)
end_vert_centroid=0.00081;

% Payload weight (kg)
payload_kg=0.02;
% Payload Length (m)
payload_length=0.06;

% Weight of joint (kg)
weight_joint=0.00252;
% Weight of link in joint (kg)
weight_joint_link=0.0008;
% Weight of end vert (kg)
weight_end_vert=0.00147;

% Density of electrical wire (kg/m^3)
wire_density=8940;
```

```
% Electrical wire diameter (m)
wire_diameter=0.0015;
% Tendon outer diameter (m)
tendon_diameter=0.0015;
% Tendon density (kg/m^3)
tendon_density=955;

% Yield Stress of Cable
safety_cable_yield=500;
% Compression limit of joint
safety_joint=1300;
% Cable Factor of Safety
cable_fos=6;
% Joint Factor of Safety
joint_fos=4;
% tube Factor of Safety
tube_fos=4;

% Selection of tubes for each link including base tube
% Default tube selection is 1 for all links
%tselect_array=ones([number_of_joints+1,1]);
tselect_array=[1; 1; 1; 1];

% Length of Snake arm
snl=base_tube_link_length+(tube_link_length*number_of_joints)+(joint
_length*(2*number_of_joints))+end_vert_length+(joint_link_length*num
ber_of_joints);
inv_snl=1/snl;

%% Tendons

teor=tendon_diameter/2;
ewor=wire_diameter/2;

% Number of tendons in each section
for i=1:number_of_joints
    tendon_array(i,1)=(number_of_joints-(i-1))*3;
end

% Imports where tendons stop at each section
joint_tendon_array=[1 1 4 7; 2 2 5 8; 3 3 6 9];

% Import the position of each tendon
tendon_position
[1,0,0.00425;2,0.0025,0.00344;3,0.00404,0.00131;4,0.00404,-
0.00131;5,0.0025,-0.00344;6,-0.0025,-0.00344;7,-0.00404,-0.00131;8,-
0.00404,0.00131;9,-0.0025,0.00344];

Dx1=tendon_position(1,2);
Dy1=tendon_position(1,3);
Dx2=tendon_position(2,2);
Dy2=tendon_position(2,3);
Dx3=tendon_position(3,2);
Dy3=tendon_position(3,3);
Dx4=tendon_position(4,2);
Dy4=tendon_position(4,3);
Dx5=tendon_position(5,2);
Dy5=tendon_position(5,3);
Dx6=tendon_position(6,2);
Dy6=tendon_position(6,3);
```

```
Dx7=tendon_position(7,2);
Dy7=tendon_position(7,3);
Dx8=tendon_position(8,2);
Dy8=tendon_position(8,3);
Dx9=tendon_position(9,2);
Dy9=tendon_position(9,3);

%% Lengths
% Length of base section
length_base_section=base_tube_link_length+joint_length;
% Length of mid section
length_mid_section=tube_link_length+(2*joint_length);
% Length of end section

length_end_section=tube_link_length+joint_length+end_vert_length;

link_length(1,1)=length_base_section;
link_length(1,2)=joint_link_length;
link_length(1,3)=length_mid_section;
link_length(1,4)=joint_link_length;
link_length(1,5)=length_mid_section;
link_length(1,6)=joint_link_length;
link_length(1,7)=length_end_section;
link_length(1,8)=payload_length;

%% Weights

% Imports the selection of usable tubes
tube_data =
[1,0.012,0.001,8000,210000000000,170000000,0.265;2,0.012,0.001,1504.
74,200000000,200000000,0.1;3,0.007,0.001,1300,10000000000,200000000,
0;4,0.007,0.001,1180,3300000000,66190080,0];

[tempa, tempb]=size(tube_data);
for i=1:tempa
    tor(i,1)=(tube_data(i,2))/2;
    twt(i,1)=tube_data(i,3);
    tde(i,1)=tube_data(i,4);
    tym(i,1)=tube_data(i,5);
    tys(i,1)=tube_data(i,6);
    tpr(i,1)=tube_data(i,7);
end

% Calculates the weight of each sections and its centroid position
% Weight of Link 1 (base link)
weight_array(1,1)=1;

tube_weight=calc_tube_weight(tor(tselect_array(1,1),1),twt(tselect_a
rray(1,1),1),base_tube_link_length,tde(tselect_array(1,1),1));

tendon_weight=calc_tendon_weight(teor,link_length(1,1),tendon_densit
y);

wire_weight=calc_wire_weight(ewor,link_length(1,1),wire_density);

weight_array(1,2)=(weight_joint)+tube_weight+(tendon_weight*tendon_a
rray(1))+wire_weight;

tempa=(tube_weight+(tendon_weight*tendon_array(1))+wire_weight)*(bas
e_tube_link_length/2)+(weight_joint*(base_tube_link_length+joint_pit
ch_centroid));
```

```
tempb=(tube_weight+(tendon_weight*tendon_array(1))+wire_weight)+weight_joint;
link_centroid(1,1)=tempa/tempb;

% Weight of Link 2
weight_array(2,1)=2;

tendon_weight=calc_tendon_weight(teor,joint_link_length,tendon_density);

weight_array(2,2)=(tendon_weight*tendon_array(1))+weight_joint_link;

link_centroid(1,2)=joint_link_length/2;

% Weight of Link 3
weight_array(3,1)=3;

tube_weight=calc_tube_weight(tor(tselect_array(2,1),1),twt(tselect_array(2,1),1),tube_link_length,tde(tselect_array(2,1),1));

tendon_weight=calc_tendon_weight(teor,link_length(1,3),tendon_density);

wire_weight=calc_wire_weight(ewor,link_length(1,3),wire_density);

weight_array(3,2)=(weight_joint)+tube_weight+(tendon_weight*tendon_array(1))+wire_weight;

tempa=(weight_joint*(joint_yaw_centroid))+(tube_weight+(tendon_weight*tendon_array(1))+wire_weight)*((tube_link_length/2)+joint_length)+(weight_joint*(joint_length+tube_link_length+joint_pitch_centroid));

tempb=weight_joint+(tube_weight+(tendon_weight*tendon_array(1))+wire_weight)+weight_joint;
link_centroid(1,3)=tempa/tempb;

% Weight of Link 4
weight_array(4,1)=4;

tendon_weight=calc_tendon_weight(teor,joint_link_length,tendon_density);

weight_array(4,2)=(tendon_weight*tendon_array(2))+weight_joint_link;

link_centroid(1,4)=joint_link_length/2;

% Weight of Link 5
weight_array(5,1)=5;

tube_weight=calc_tube_weight(tor(tselect_array(3,1),1),twt(tselect_array(3,1),1),tube_link_length,tde(tselect_array(3,1),1));

tendon_weight=calc_tendon_weight(teor,link_length(1,5),tendon_density);

wire_weight=calc_wire_weight(ewor,link_length(1,5),wire_density);

weight_array(5,2)=(weight_joint)+tube_weight+(tendon_weight*tendon_array(2))+wire_weight;
```



```
tempa=(weight_joint*(joint_yaw_centroid))+(tube_weight+(tendon_weight*  
tendon_array(1))+wire_weight)*((tube_link_length/2)+joint_length)+  
(weight_joint*(joint_length+tube_link_length+joint_pitch_centroid));  
  
tempb=weight_joint+(tube_weight+(tendon_weight*tendon_array(2))+wire_weight)+weight_joint;  
link_centroid(1,5)=tempa/tempb;  
  
% Weight of Link 6  
weight_array(6,1)=6;  
  
tendon_weight=calc_tendon_weight(teor,joint_link_length,tendon_density);  
  
weight_array(6,2)=(tendon_weight*tendon_array(2))+weight_joint_link;  
  
link_centroid(1,6)=joint_link_length/2;  
  
% Weight of Link 7  
weight_array(7,1)=7;  
  
tube_weight=calc_tube_weight(tor(tselect_array(4,1),1),tw(tselect_array(4,1),1),tube_link_length,tde(tselect_array(4,1),1));  
  
tendon_weight=calc_tendon_weight(teor,link_length(1,7),tendon_density);  
  
wire_weight=calc_wire_weight(ewor,link_length(1,7),wire_density);  
  
weight_array(7,2)=(weight_joint)+tube_weight+(tendon_weight*tendon_array(3))+wire_weight+weight_end_vert;  
  
tempa=(weight_joint*(joint_yaw_centroid))+(tube_weight+(tendon_weight*tendon_array(1))+wire_weight)*((tube_link_length/2)+joint_length)+  
(weight_end_vert*(joint_length+tube_link_length+end_vert_centroid));  
  
tempb=weight_joint+(tube_weight+(tendon_weight*tendon_array(3))+wire_weight)+weight_end_vert;  
link_centroid(1,7)=tempa/tempb;  
  
% Weight of Link 8 (Payload)  
weight_array(8,1)=8;  
weight_array(8,2)=payload_kg;  
  
link_centroid(1,8)=payload_length/2;  
  
%% Torque  
  
GRAV=[0 9.81 0];  
  
% Denavit-Hartenburg matrix  
% theta kinematic: joint angle  
% d kinematic: link offset  
% a kinematic: link length  
% alpha kinematic: link twist  
% sigma kinematic: 0 if revolute, 1 if prismatic  
% mdh kinematic: 0 if standard D&H, else 1  
% offset kinematic: joint variable offset  
% qlim kinematic: joint variable limits [min max]  
% m dynamic: link mass
```

```
%      r      dynamic: link COG wrt link coordinate frame 3x1
%      I      dynamic: link inertia matrix, symmetric 3x3, about link
COG.
%      B      dynamic: link viscous friction (motor referred)
%      Tc     dynamic: link Coulomb friction

% Links
link_array(1)=Link('alpha', pi/2, 'd', 0, 'a', link_length(1,1),
'offset', 0, 'qlim',[-pi/4 pi/4], 'm', weight_array(1,2), 'r',[-
link_centroid(1,1); 0; 0], 'I', [0.00000066 0.00000000 0.00000000;
0.00000000 0.00078561 0.00000000; 0.00000000 0.00000000 0.00078560],
'Jm', 0);
link_array(2)=Link('alpha', -pi/2, 'd', 0, 'a', 0,
'offset', 0, 'qlim',[-pi/4 pi/4], 'm', 0, 'r',[0;
0; 0], 'I', [0 0 0; 0 0 0; 0 0 0], 'Jm', 0);
link_array(3)=Link('alpha', pi/2, 'd', 0, 'a', 0,
'offset', 0, 'qlim',[-pi/4 pi/4], 'm', 0, 'r',[0;
0; 0], 'I', [0 0 0; 0 0 0; 0 0 0], 'Jm', 0);
link_array(4)=Link('alpha', 0, 'd', 0, 'a', link_length(1,2),
'offset', 0, 'qlim',[-pi/4 pi/4], 'm', weight_array(2,2), 'r',[-
link_centroid(1,2); 0; 0], 'I', [0.00000000 0.00000000 0.00000000;
0.00000000 0.00000001 0.00000000; 0.00000000 0.00000000 0.00000001],
'Jm', 0);
link_array(5)=Link('alpha', -pi/2, 'd', 0, 'a', link_length(1,3),
'offset', 0, 'qlim',[-pi/4 pi/4], 'm', weight_array(3,2), 'r',[-
link_centroid(1,3); 0; 0], 'I', [0.00000102 0.00000000 0.00000000;
0.00000000 0.00005518 0.00000000; 0.00000000 0.00000000 0.00005519],
'Jm', 0);
link_array(6)=Link('alpha', pi/2, 'd', 0, 'a', link_length(1,4),
'offset', 0, 'qlim',[-pi/4 pi/4], 'm', weight_array(4,2), 'r',[-
link_centroid(1,4); 0; 0], 'I', [0.00000000 0.00000000 0.00000000;
0.00000000 0.00000001 0.00000000; 0.00000000 0.00000000 0.00000001],
'Jm', 0);
link_array(7)=Link('alpha', -pi/2, 'd', 0, 'a', link_length(1,5),
'offset', 0, 'qlim',[-pi/4 pi/4], 'm', weight_array(5,2), 'r',[-
link_centroid(1,5); 0; 0], 'I', [0.00000102 0.00000000 0.00000000;
0.00000000 0.00005518 0.00000000; 0.00000000 0.00000000 0.00005519],
'Jm', 0);
link_array(8)=Link('alpha', pi/2, 'd', 0, 'a', link_length(1,6),
'offset', 0, 'qlim',[-pi/4 pi/4], 'm', weight_array(6,2), 'r',[-
link_centroid(1,6); 0; 0], 'I', [0.00000000 0.00000000 0.00000000;
0.00000000 0.00000001 0.00000000; 0.00000000 0.00000000 0.00000001],
'Jm', 0);
link_array(9)=Link('alpha', -pi/2, 'd', 0, 'a', link_length(1,7),
'offset', 0, 'qlim',[-pi/4 pi/4], 'm', weight_array(7,2), 'r',[-
link_centroid(1,7); 0; 0], 'I', [0.00000102 0.00000000 0.00000000;
0.00000000 0.00005518 0.00000000; 0.00000000 0.00000000 0.00005519],
'Jm', 0);
link_array(10)=Link('alpha', pi/2, 'd', 0, 'a', link_length(1,8),
'offset', 0, 'qlim',[-pi/4 pi/4], 'm', weight_array(8,2), 'r',[-
link_centroid(1,8); 0; 0], 'I', [0.00000000 0.00000000 0.00000000;
0.00000000 0.00000001 0.00000000; 0.00000000 0.00000000 0.00000001],
'Jm', 0);

% Arm angles
for i=1:numcols(arm_angle)
    arm_angle_rad(1,i)=arm_angle(1,i)*(pi/180);
end

Snake_Arm = SerialLink(link_array, 'name',' ');
%Snake_Arm.display()
%Snake_Arm.dyn
```

```
plot_value=1;
```

```
% Arm angles
```

```
%arm_angle=[0 90+theta -90 -90 0 theta  
arm_angle=[0 90 -90 -90 theta 0 theta
```

Updated joint angles at maximum horizontal orientation.

```
for i=1:numcols(arm_angle)
```

```
    arm_angle_rad(1,i)=arm_angle(1,i)*(pi/180);
```

```
    link_animation_history(plot_value,i)=arm_angle_rad(1,i);
```

```
end
```

```
%TAU = R.rne(Q, QD, QDD) is the joint torque required for the robot  
R to achieve the specified joint position Q, velocity QD and  
acceleration QDD.
```

```
Q=arm_angle_rad;
```

```
QD= [0 0 0 0 0 0 0 0 0 0];
```

```
QDD=[0 0 0 0 0 0 0 0 0 0];
```

```
TAU = Snake_Arm.rne(Q, QD, QDD);
```

```
TAUtrans=TAU';
```

```
By1=TAU(1,1);
```

```
Rp1=TAU(1,2);
```

```
Rt1=TAU(1,3);
```

```
Rt2=TAU(1,4);
```

```
Ry1=TAU(1,5);
```

```
Rp2=TAU(1,6);
```

```
Ry2=TAU(1,7);
```

```
Rp3=TAU(1,8);
```

```
Ry3=TAU(1,9);
```

```
Ef1=TAU(1,10);
```

```
if Rt1*twist_fos >= safety_twist  
    twist_buckling = 1;
```

```
else
```

```
    twist_buckling = 0;
```

```
end
```

The twisting torque is compared to the torque limit of the joint as derived from Chapter 5.4.2.

```
end
```

D.5 calc_tendon_weight.m

This section of code was used for calculating the weight of each cable.

```
function tendon_weight=calc_tendon_weight(teor,tle,tede)
tendon_csa=pi*(teor^2);
tendon_volume=tle*tendon_csa;
tendon_weight=tede*tendon_volume;
```

D.6 calc_tube_weight.m

This section of code was used for calculating the weight of each link.

```
function tube_weight=calc_tube_weight(tor,twt,tle,tde)
tube_csa_1=tor^2-(tor-twt)^2;
tube_csa_2=pi*(tube_csa_1);
tube_volume=tle*tube_csa_2;
tube_weight=tde*tube_volume;
```

D.7 calc_wire_weight.m

This section of code was used for calculating the weight of the single wire to the end effector.

```
function wire_weight=calc_wire_weight(ewor,tle,ewd)
wire_csa=pi*(ewor^2);
wire_volume=tle*wire_csa;
wire_weight=ewd*wire_volume;
```

Appendix E

Results from the snake arm cable length changes

This section contains the results of the snake arm cable length experiment.

E.1 Joint 1

	Displacement	Joint 1 angle	Joint 2 angle	Joint 3 angle
Test 1	0	-7.58	-8.43	-8.46
Test 2	0	-4.41	-3.29	-8.03
Test 3	0	-3.63	-3.16	-11.92
Test 4	0	-9.7	-2.26	-6.06
Test 5	0	-5.41	-2.27	-0.87
Test 6	0	3.32	-11.03	-8.69
Test 7	0	-2.12	3.18	-8.54
Test 8	0	-0.73	-1.87	-2.24
Test 9	0	1.17	-7.88	-0.83
Test 10	0	1.96	-9.2	2.1

This data appears in Figure 5.43

E.2 Joint 2

	Displacement	Joint 1 angle	Joint 2 angle	Joint 3 angle
Test 1	7	11.96	-28.4	-6.62
Test 2	7	7.76	-18.57	-9.13
Test 3	7	10.07	-20.22	-12.55
Test 4	7	10.04	-22.95	-7.64
Test 5	9	15.21	-30.82	-0.92
Test 6	9	9.88	-19.4	-9.1
Test 7	10	21.91	-31.64	-11.61
Test 8	10	15.28	-27.53	-3.45
Test 9	11	25.35	-33.93	-2.4
Test 10	12	17.4	-28.53	1.95

This data appears in Figure 5.44.

E.3 Joint 3

	Displacement	Joint 1 angle	Joint 2 angle	Joint 3 angle
Test 1	11	26.98	-43.99	-7.71
Test 2	12	32.72	-50.31	-8.81
Test 3	12	35.35	-50.1	-9.51
Test 4	12	35.73	-56.35	-4.13
Test 5	13	34.86	-55.9	1.93
Test 6	13	35.17	-56.74	-1.73
Test 7	13	31.65	-46.94	-10.57
Test 8	13	35.81	-40.45	-5.43
Test 9	18	33.25	-53.36	7.55
Test 10	16	31.16	-53.2	5.73

This data appears in Figure 5.45.

Appendix F

Results from the reconfigurable robot design

This section contains the theoretical data for the power screw assembly from the reconfigurable robot design.

F.1 Maximum torque generated and torque required for the deployment module

Joint Angle (°)	F1 (N)	θ_1 (°)	F2 (N)	θ_2 (°)	F3 (N)	Torque (Nm)
0	1137.567	0.000	1137.567	49.086	745.027	14.789
5	1137.567	5.553	1132.229	49.638	733.245	14.555
10	1137.567	10.671	1117.894	49.757	722.198	14.336
15	1137.567	15.341	1097.033	49.427	713.534	14.164
20	1137.567	19.532	1072.106	48.618	708.751	14.069
25	1137.567	23.200	1045.577	47.286	709.259	14.079
30	1137.567	26.292	1019.882	45.378	716.394	14.220
35	1137.567	28.749	997.347	42.835	731.375	14.518
40	1137.567	30.512	980.038	39.598	755.155	14.990
45	1137.567	31.534	969.586	35.619	788.181	15.645
50	1137.567	31.782	967.001	30.867	830.032	16.476
55	1137.567	31.249	972.534	25.334	879.003	17.448
60	1137.567	29.951	985.647	19.037	931.742	18.495
65	1137.567	27.928	1005.084	12.013	983.072	19.514
70	1137.567	25.232	1029.032	4.317	1026.112	20.368
75	1137.567	21.922	1055.310	3.992	1052.750	20.897
80	1137.567	18.057	1081.539	12.857	1054.422	20.930
85	1137.567	13.687	1105.265	22.228	1023.130	20.309
90	1137.567	8.850	1124.024	32.065	952.555	18.908

This data appears in Figure 6.17.

F.2 Reduced torque generated and torque required for the deployment module

Joint Angle (°)	F1 (N)	θ_1 (°)	F2 (N)	θ_2 (°)	F3 (N)	Torque (Nm)
0	350.971	0.000	350.971	49.086	229.862	4.563
5	350.971	5.553	349.324	49.638	226.226	4.491
10	350.971	10.671	344.901	49.757	222.818	4.423
15	350.971	15.341	338.465	49.427	220.145	4.370
20	350.971	19.532	330.774	48.618	218.669	4.341
25	350.971	23.200	322.589	47.286	218.826	4.344
30	350.971	26.292	314.662	45.378	221.028	4.387
35	350.971	28.749	307.709	42.835	225.649	4.479
40	350.971	30.512	302.369	39.598	232.986	4.625
45	350.971	31.534	299.144	35.619	243.176	4.827
50	350.971	31.782	298.347	30.867	256.088	5.083
55	350.971	31.249	300.054	25.334	271.197	5.383
60	350.971	29.951	304.099	19.037	287.468	5.706
65	350.971	27.928	310.096	12.013	303.305	6.021
70	350.971	25.232	317.485	4.317	316.584	6.284
75	350.971	21.922	325.593	3.992	324.803	6.447
80	350.971	18.057	333.685	12.857	325.318	6.458
85	350.971	13.687	341.005	22.228	315.664	6.266
90	350.971	8.850	346.792	32.065	293.890	5.834

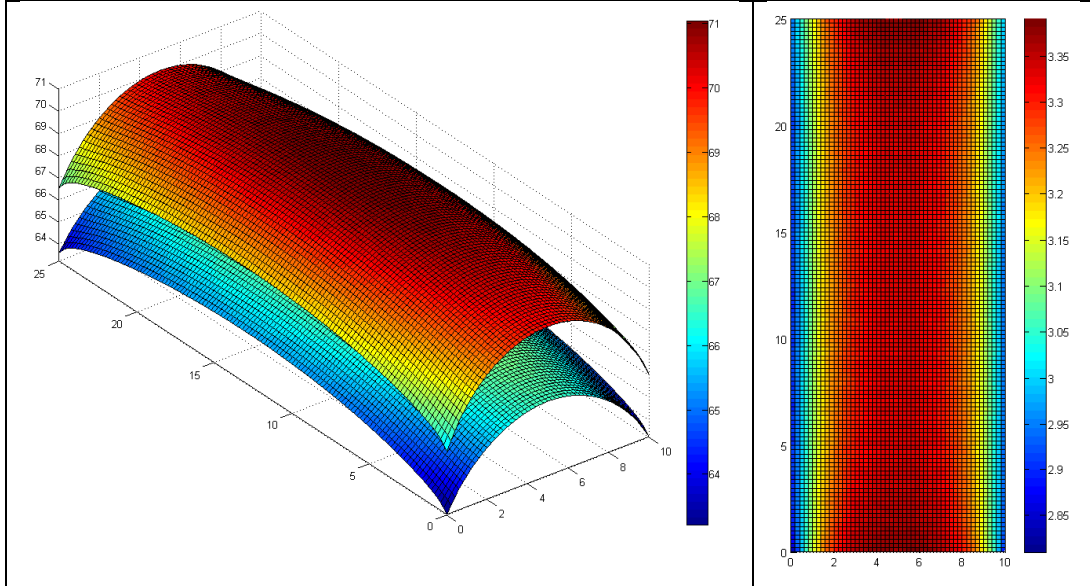
This data appears in Figure 6.18.

Appendix G

Results from transient thermal study

This section contains the thermal study results for the development of the thermally insulating barrier.

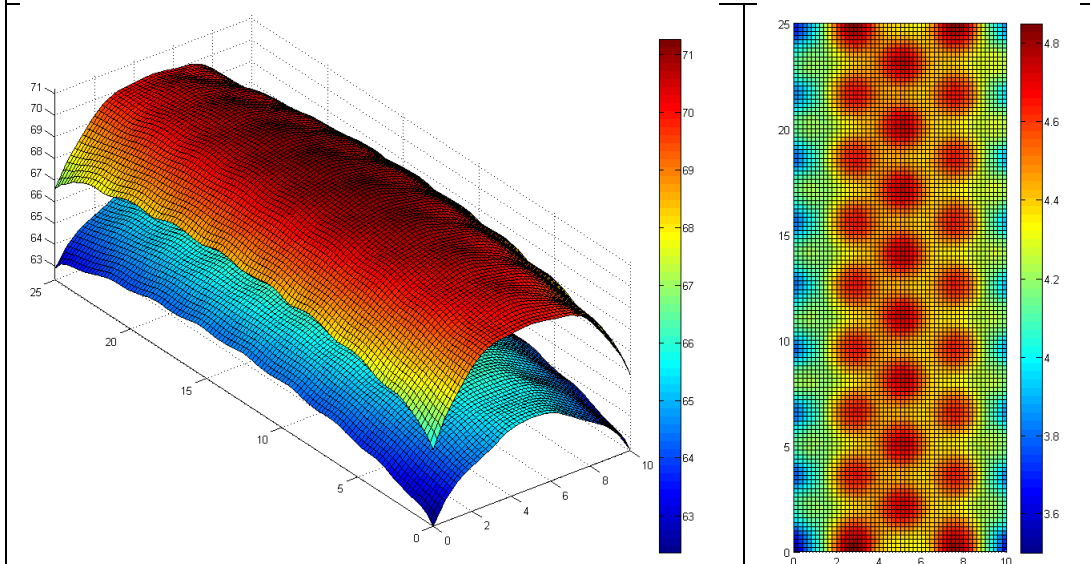
% Air = 0% Single thermal layer



Temperature of both layers

Temperature difference

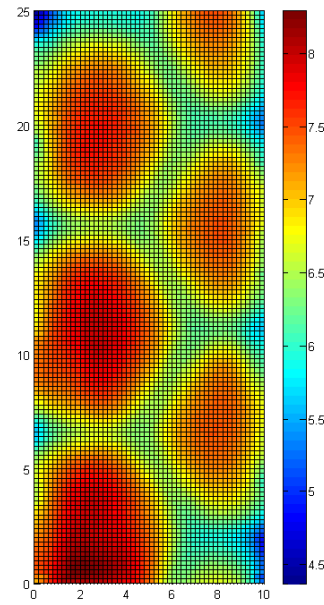
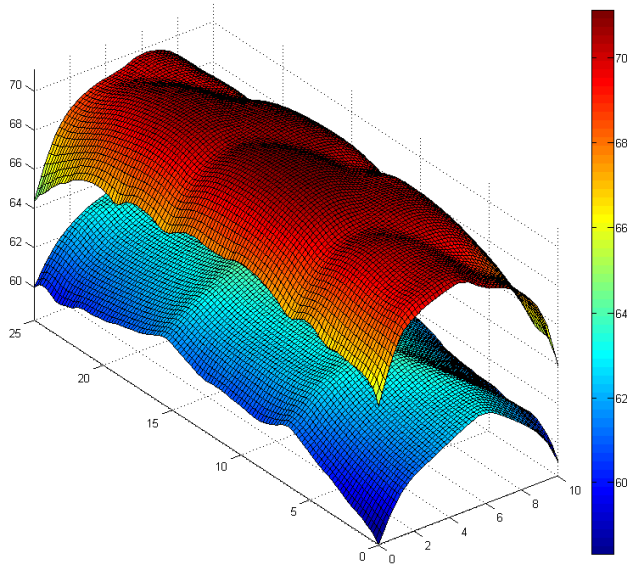
% Air = 46% Single thermal layer



Temperature of both layers

Temperature difference

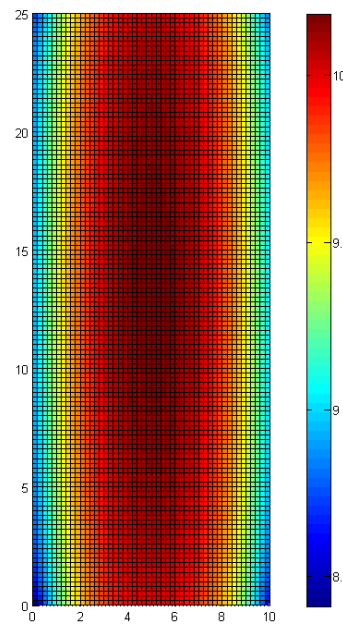
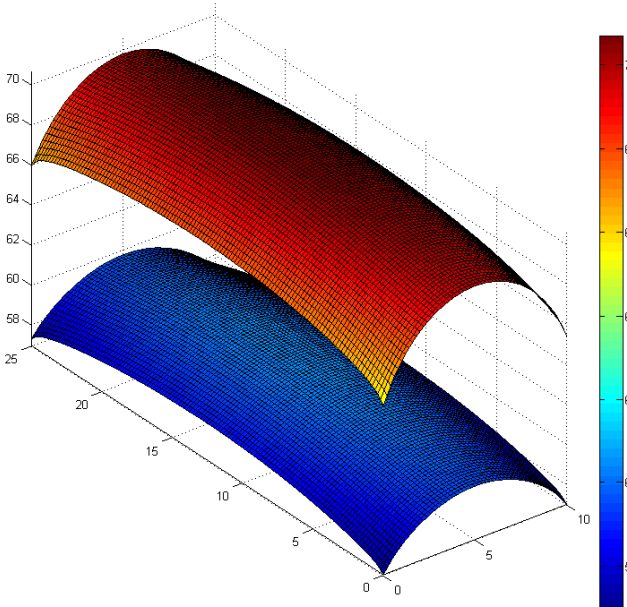
% Air = 81% Single thermal layer



Temperature of both layers

Temperature difference

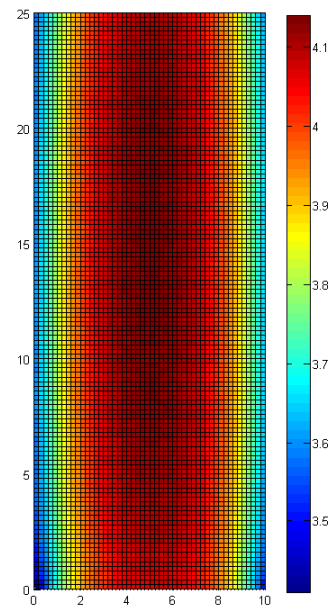
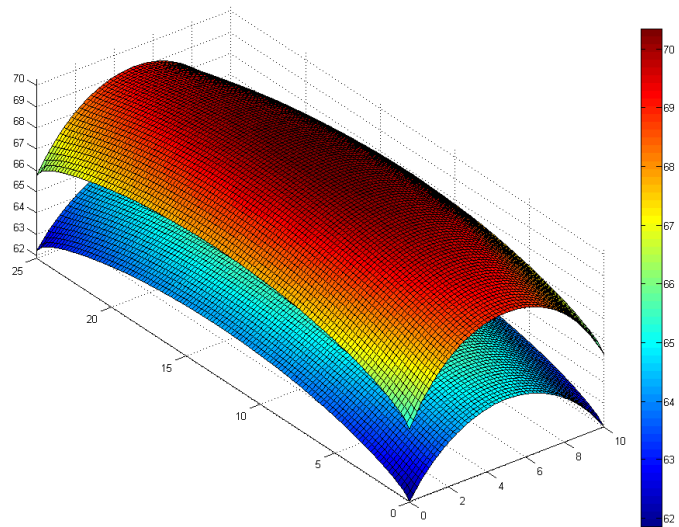
% Air = 100% Single thermal layer



Temperature of both layers

Temperature difference

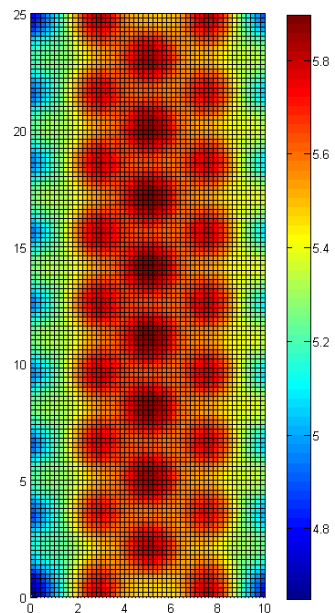
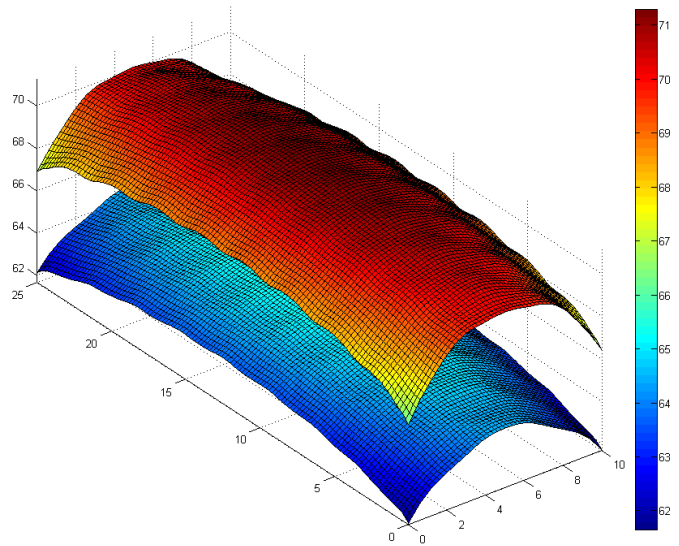
% Air = 0% Double thermal layer



Temperature of both layers

Temperature difference

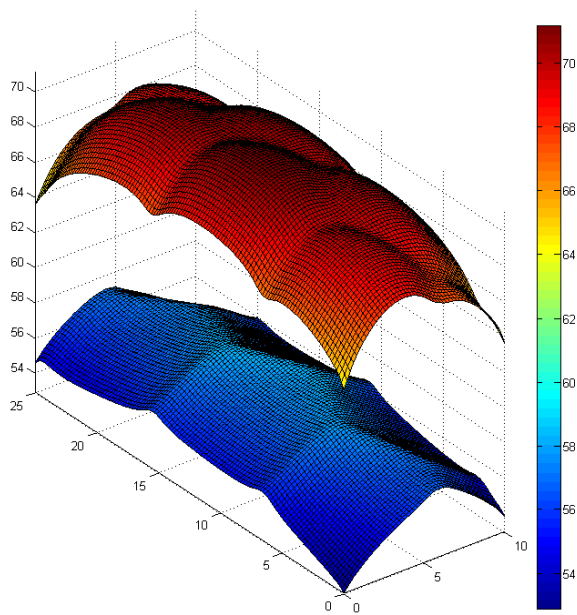
% Air = 46% Double thermal layer



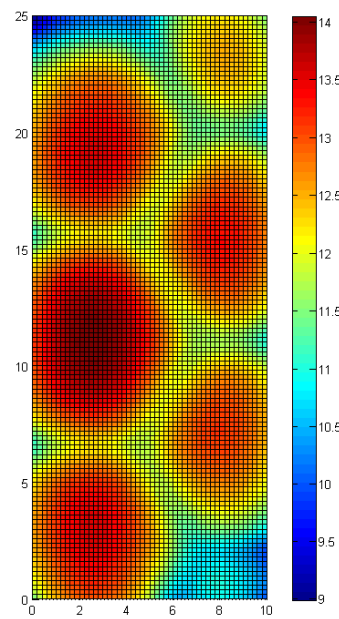
Temperature of both layers

Temperature difference

% Air = 81% Double thermal layer

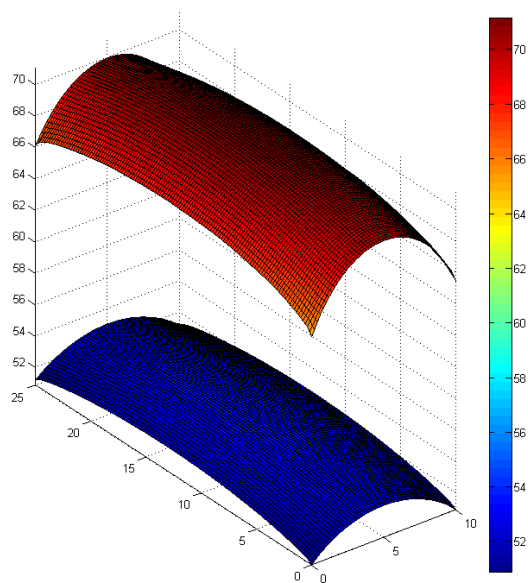


Temperature of both layers

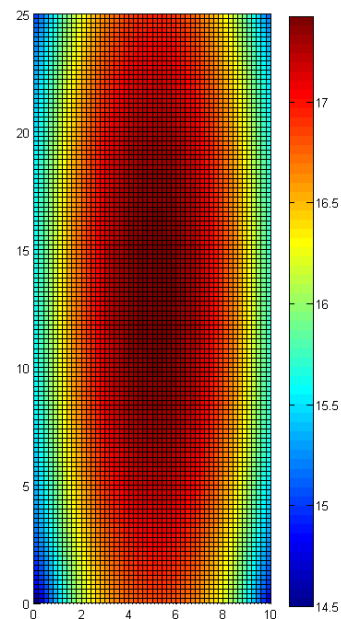


Temperature difference

% Air = 100% Double thermal layer

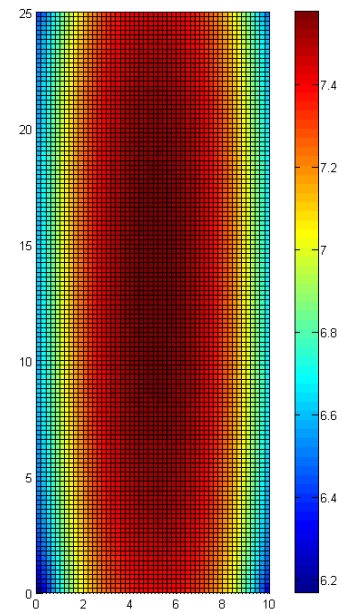
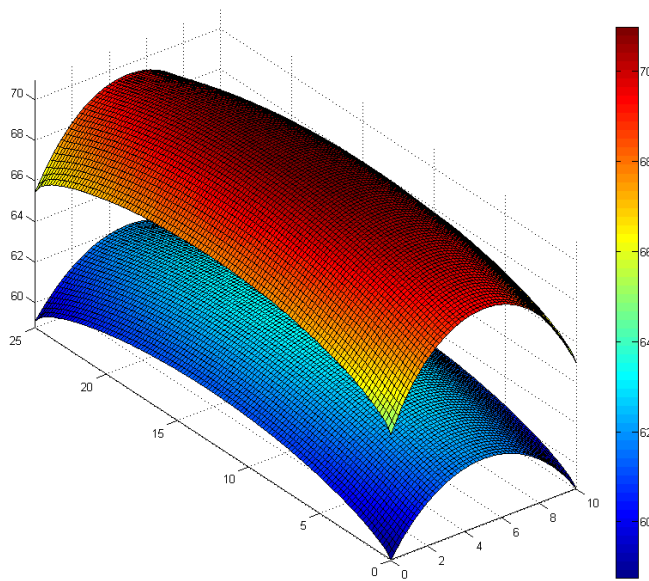


Temperature of both layers



Temperature difference

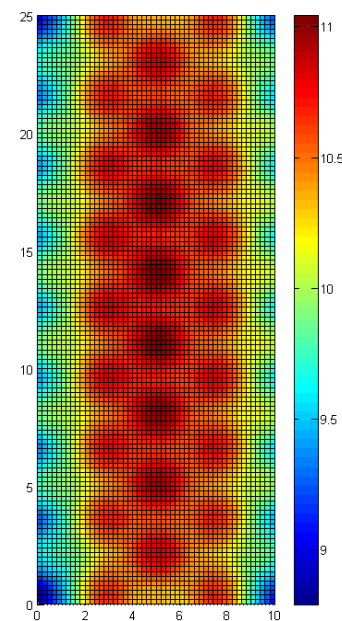
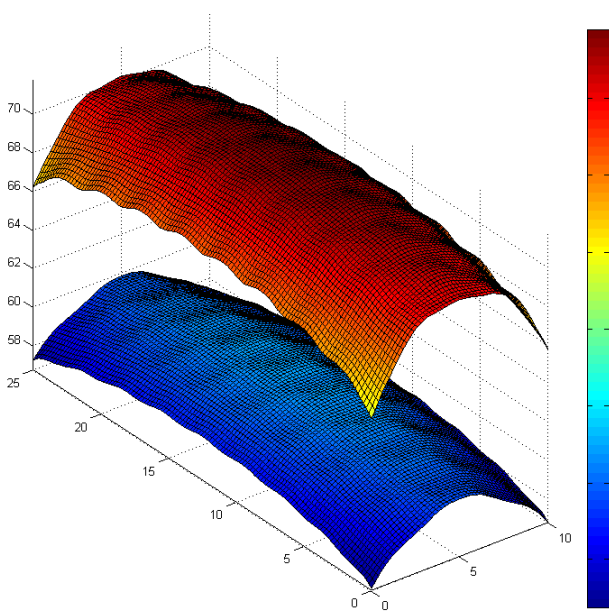
% Air = 0% Triple thermal layer



Temperature of both layers

Temperature difference

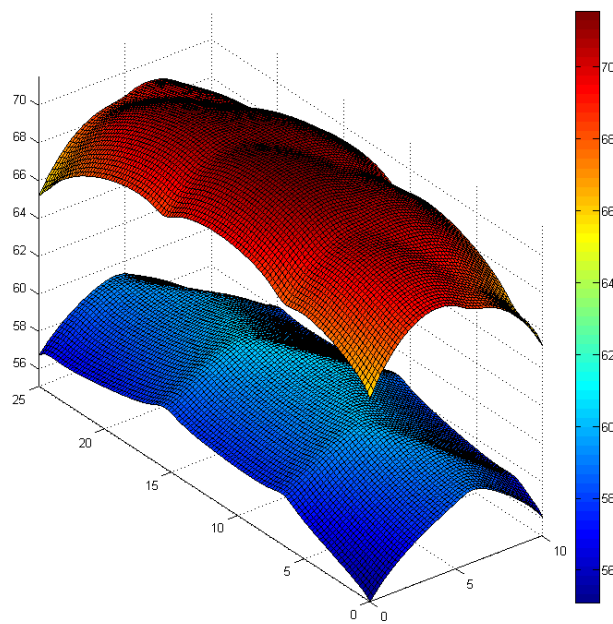
% Air = 46% Triple thermal layer



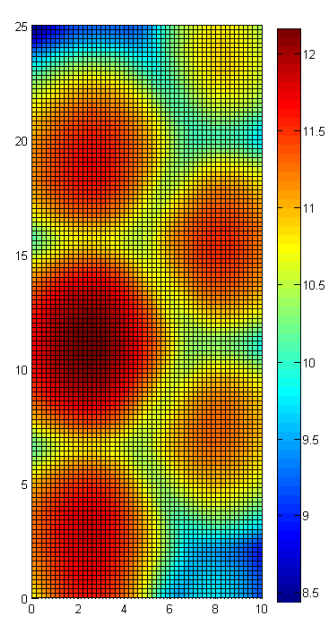
Temperature of both layers

Temperature difference

% Air = 81% Triple thermal layer

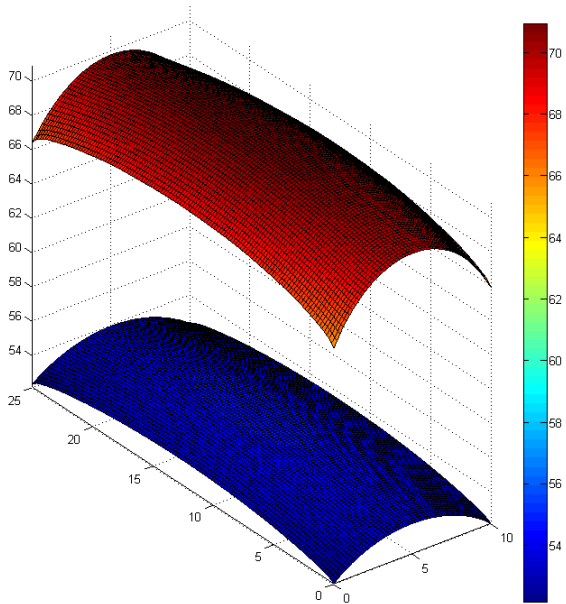


Temperature of both layers

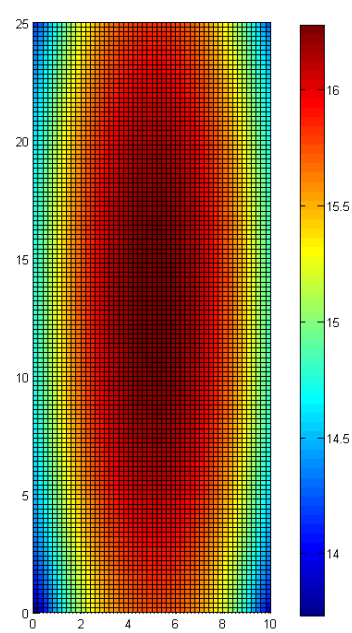


Temperature difference

% Air = 100% Triple thermal layer



Temperature of both layers



Temperature difference

